

A Cascade Analysis for the IceCube Neutrino Telescope

A THESIS SUBMITTED IN PARTIAL FULFILMENT
OF THE REQUIREMENTS FOR THE DEGREE OF
DOCTOR OF PHILOSOPHY IN PHYSICS
IN THE UNIVERSITY OF CANTERBURY

Stephanie Virginia Hickford

2012



Contents

Figures	v
Tables	x
Acronyms	xii
Acknowledgements	xv
1 Introduction	3
2 Neutrinos	6
2.1 Properties	6
2.2 Observation	9
2.2.1 Interaction with Nucleons	9
2.2.2 Cherenkov Radiation	11
2.3 Origins	12
2.3.1 Cosmic-rays and Atmospheric Neutrinos	12
2.3.2 High Energy Astrophysical Neutrinos	16
2.3.3 Low Energy Astrophysical Neutrinos	21
2.4 Analyses	23
2.4.1 Astrophysical Models and Fluxes	23
2.4.2 High Energy Cascade Analysis	26
2.5 Detectors	26
3 IceCube	29
3.1 Ice Cherenkov Detectors	29
3.1.1 Ice Properties	29

3.1.2	AMANDA	32
3.2	Construction of IceCube	33
3.2.1	Digital Optical Modules	33
3.2.2	Deployment	36
3.2.3	Data Acquisition	36
3.2.4	Subdetectors	39
4	Cascade Analysis	40
4.1	Method	41
4.2	Data	43
4.3	Simulation	44
4.3.1	Neutrino simulation	44
4.3.2	Background muon simulation	46
4.3.3	Light Propagation	49
4.3.4	Detector Simulation	51
4.4	Reconstruction	51
5	Event Selection Criteria	54
5.1	Trigger Level	55
5.2	Pole Filter	56
5.2.1	Line-fit Velocity	57
5.2.2	Tensor of Inertia Eigenvalue Ratio	59
5.3	Level 3	60
5.3.1	Zenith	61
5.3.2	Reduced log-likelihood	62
5.4	Level 4	63
5.4.1	Spatial Distance	64
5.4.2	Fill Ratio	66
5.5	Level 5	67
5.5.1	z -Containment	68
5.5.2	xy -Containment	69

5.5.3	Multivariate Analysis	71
5.6	Level 6	76
5.6.1	Optimisation	76
5.6.2	Final cuts	78
5.6.3	Final Rates	80
5.7	Expectation Of Events	83
5.7.1	Experimental Data	83
5.7.2	Signal	83
5.7.3	Background	85
6	Results	90
6.1	Final Events	90
6.1.1	Location	94
6.1.2	Direction	96
6.1.3	BDT and Energy Spectra	98
6.1.4	Classification	102
6.2	Additional Background Simulation	103
6.3	Flux Limit	107
6.4	Reconstruction Resolutions	108
6.4.1	Energy	108
6.4.2	Direction	109
6.4.3	Position	110
6.5	Systematic Uncertainties	112
6.5.1	Ice properties	113
6.5.2	DOM efficiencies	114
6.5.3	Neutrino Cross-sections	115
6.5.4	Seasonal variation	116
6.5.5	Total systematics	117
7	Muons In Hadronic Cascades	118
7.1	Hadronic Cascades	118

7.2	Theory	120
7.2.1	Electromagnetic Cascades	120
7.2.2	Hadronic Cascades	120
7.2.3	Decay	121
7.3	Simulations	122
7.3.1	CORSIKA	123
7.3.2	Pythia	124
7.3.3	GEANT	125
7.4	Muon Flux	127
7.4.1	Results	127
7.4.2	Long Range Muon	132
7.4.3	Cut Variables	133
8	Conclusion	134
A	Event Displays	136
B	Background Event Displays	144
	References	148

List of Figures

2.1	Particle travel through the interstellar medium.	8
2.2	<i>Charged-Current</i> (CC) and <i>Neutral-Current</i> (NC) neutrino interactions.	9
2.3	Event topology of tracks and cascades from Cherenkov radiation.	11
2.4	Cosmic-ray energy spectrum as observed by different experiments, from [80].	14
2.5	Atmospheric neutrino models.	17
2.6	<i>Active Galactic Nuclei</i> (AGN) made from subclasses of galactic objects.	20
2.7	Astrophysical model flux predictions.	23
2.8	IceCube analyses limits and model flux predictions.	26
3.1	Depth dependence of the effective scattering coefficient b_e measured with pulsed sources at four wavelengths, from [14].	31
3.2	Depth dependence of the absorption coefficient a measured with pulsed sources at four wavelengths, from [14].	32
3.3	The IceCube <i>Digital Optical Module</i> (DOM).	34
3.4	Photograph of a DOM mainboard and its components from [3].	35
3.5	Deployment of an IceCube string of DOMs down a hot water drilled hole into the ice.	37
3.6	The IceCube detector instrumented between 1450 m and 2450 m in the ice at the South Pole, with the Eiffel Tower shown for size perspective.	38
4.1	Energy resolution from Credo reconstruction.	41
4.2	IceCube-40 detector configuration.	44
4.3	Neutrino event topologies in IceCube, taken from [20].	45
4.4	Polygonato model, from [84], used to describe the cosmic ray composition for background simulation in CORSIKA.	47

4.5	Two-component Glasstetter model from [63].	49
5.1	Reconstructed velocities, in units of c , from a line-fit to the timing of the hit DOMs.	58
5.2	Reconstructed eigenvalue ratio from tensor of inertia.	60
5.3	Reconstructed zenith direction versus reconstructed energy.	61
5.4	Reduced log-likelihood.	63
5.5	One iteration energy reconstruction.	64
5.6	Illustration of the spatial distance reconstruction for cascade and muon events.	65
5.7	Spatial distance reconstruction.	65
5.8	Illustration of the fill ratio reconstruction for cascade and muon events.	67
5.9	Fill Ratio.	67
5.10	Reconstructed z -vertex position.	68
5.11	Reconstructed xy -vertex positions before any xy -containment cuts have been performed.	69
5.12	Reconstructed xy -vertex positions after events that do not satisfy the string containment cut have been removed.	70
5.13	Reconstructed xy -vertex positions after events that do not satisfy either the string containment cut or the DOM charge containment cut have been removed.	70
5.14	The eight input variables that are fed into the TMVA algorithm to produce a BDT response score.	74
5.15	The correlation matrices for the eight variables fed into TMVA.	75
5.16	Overtraining check of training and testing samples from TMVA.	76
5.17	BDT response score versus $\log_{10}(\text{Energy})$	77
5.18	Optimisation of final level cuts for best sensitivity and discovery potential.	79
5.19	BDT response score.	79
5.20	Four iteration reconstruction of event energy.	80
5.21	Comparison of number of signal events and number of background events from IceCube-40 and IceCube-22 filter levels.	82

5.22	IceCube-40 neutrino effective area as a function of primary neutrino energy.	84
5.23	IceCube-40 effective livetime of the muon background simulation, using the polygonato cosmic-ray spectrum, as a function of primary energy.	87
5.24	IceCube-40 effective livetime of the muon background simulation, using the two-component cosmic-ray spectrum, as a function of primary energy.	87
5.25	IceCube-40 effective livetime of the muon background simulation, using the polygonato cosmic-ray spectrum, as a function of reconstructed energy.	88
5.26	IceCube-40 effective livetime of the muon background simulation, using the two-component cosmic-ray spectrum, as a function of reconstructed energy.	88
6.1	Event 3 viewer display.	92
6.2	Event vertex depth.	95
6.3	Event vertex location in xy -coordinates.	95
6.4	Event azimuth directions.	97
6.5	BDT response score of the final 14 events.	100
6.6	Reconstructed energy of the final 14 events.	100
6.7	BDT response score of the final 14 events and the data below the final BDT response score cut.	101
6.8	Reconstructed energy of the final 14 events and the data below the final energy cut.	101
6.9	IceCube-40 effective livetime of the muon background, using the two-component spectrum, as a function of primary energy with additional simulation included.	104
6.10	IceCube-40 effective livetime of the additional muon background simulation, using the two-component spectrum, as a function of reconstructed energy.	104
6.11	BDT response score of the final 14 events and the data below the final BDT response score cut of 0.2 with additional muon background.	106
6.12	Reconstructed energy of the final 14 events and the data below the final energy cut of 25 TeV with additional muon background.	106
6.13	IceCube analyses limits and model flux predictions.	107

6.14	Energy resolution.	109
6.15	Zenith resolution.	110
6.16	Azimuth resolution.	110
6.17	x -vertex resolution.	111
6.18	y -vertex resolution.	112
6.19	z -vertex resolution.	112
6.20	Seasonal variation in rate at trigger level for IceCube-40.	116
7.1	A high energy muon produced in a hadronic cascade.	119
7.2	CORSIKA simulation. An incoming proton interacts with a proton in salt water to produce hadrons.	123
7.3	Pythia and GEANT simulation. An incoming neutrino interacts with a proton in the Antarctic ice to produce hadrons.	126
7.4	Number of muons produced in a hadronic cascade as a function of the muon energy, from the CORSIKA simulations in [114, 115].	127
7.5	Number of muons produced from pion decay as a function of the muon energy.	128
7.6	Number of muons produced from kaon decay as a function of the muon energy.	129
7.7	Number of muons produced in a hadronic cascade as a function of the muon energy.	129
7.8	Number of muons produced in a hadronic cascade as a function of the muon energy, the straight lines show the power law fits.	130
7.9	Simulation of a 10 TeV hadronic cascade.	132
A.1	Event 1 viewer display: 29.13 TeV event at $(-79.58, 322.01, 201.82)$. . .	136
A.2	Event 2 viewer display: 30.81 TeV event at $(442.29, 167.46, -427.36)$. . .	137
A.3	Event 3 viewer display: 175.28 TeV event at $(5.57, 147.82, 110.94)$	137
A.4	Event 4 viewer display: 27.14 TeV event at $(-310.92, 177.57, 24.49)$. . .	138
A.5	Event 5 viewer display: 41.36 TeV event at $(-226.14, 355.98, 300.18)$. . .	138
A.6	Event 6 viewer display: 174.09 TeV event at $(-159.49, 301.21, -230.91)$. . .	139
A.7	Event 7 viewer display: 31.20 TeV event at $(326.92, 59.76, 23.90)$	139

A.8	Event 8 viewer display: 45.33 TeV event at (303.03, 210.05, 167.72).	140
A.9	Event 9 viewer display: 144.20 TeV event at (378.63, 225.91, -303.59).	140
A.10	Event 10 viewer display: 32.06 TeV event at (352.15, -17.81, -200.99).	141
A.11	Event 11 viewer display: 46.83 TeV event at (469.60, 56.77, 254.13).	141
A.12	Event 12 viewer display: 57.19 TeV event at (-318.58, 169.02, -201.75).	142
A.13	Event 13 viewer display: 39.88 TeV event at (-225.53, 385.72, 166.87).	142
A.14	Event 14 viewer display: 27.15 TeV event at (164.71, 138.55, 300.26).	143
B.1	Simulated background muon event 1 viewer display: 25.40 TeV event at (-260.21, 213.53, 378.8).	144
B.2	Simulated background muon event 2 viewer display: 37.28 TeV event at (-325.52, 286.56, -184.91).	145
B.3	Simulated background muon event 3 viewer display: 291.67 TeV event at (-275.07, 180.27, -311.96).	145
B.4	Simulated background muon event 4 viewer display: 136.38 TeV event at (292.60, 53.14, 280.99).	146
B.5	Simulated background muon event 5 viewer display: 32.73 TeV event at (36.96, 259.93, 245.72).	146
B.6	Simulated background muon event 6 viewer display: 72.46 TeV event at (-145.00, 124.07, 326.52).	147
B.7	Simulated background muon event 7 viewer display: 26.78 TeV event at (415.18, 3.06, 373.32).	147

List of Tables

2.1	Leptons.	6
2.2	Number of events per year in the IceCube telescope from [21].	24
3.1	Hamamatsu specifications for the R7081-02 <i>PhotoMultiplier Tube</i> (PMT), from [4].	34
3.2	Year of IceCube string deployment and detector configuration. The colours correspond to those shown in Figure 3.6.	37
4.1	Simulation of neutrino events.	46
4.2	CORSIKA simulation of muon background events.	50
5.1	Rates in Hz of data, atmospheric muon background, and neutrino signal at each filter level.	81
5.2	Excess of experimental data over simulated atmospheric muon background at each filter level.	81
5.3	Expected events to be observed in unblinded experimental data.	83
5.4	Expected neutrino signal events.	85
5.5	Expected background events.	85
5.6	Comparison of number of events expected assuming various atmospheric neutrino models.	86
6.1	Summary of events: date, time, run number, event ID, and DOMs hit.	91
6.2	Location of events.	94
6.3	Direction of events.	96
6.4	Other reconstructed cut variables.	98
6.5	BDT response score and reconstructed energy of events.	99

6.6	Expected background events from additional simulation.	103
6.7	Summary of muon background events: event ID, DOMs hit, BDT re- sponse score, and reconstructed energy.	105
6.8	Systematic uncertainties.	117
7.1	Branching ratios for pion decay modes, from [66].	121
7.2	Branching ratios for kaon decay modes, from [66].	122
7.3	Values of parameter γ in the power law fits to the CORSIKA from [113] and GEANT simulations of muon production in hadronic cascades. . .	131
7.4	Number of muons produced, per cascade event, with energy greater than 10 GeV and 100 GeV in hadronic cascades.	131

List of Acronyms

AGN.....	<i>Active Galactic Nuclei</i>
AHA.....	<i>Additionally Heterogeneous Absorption</i>
AMANDA....	<i>Antarctic Muon And Neutrino Detector Array</i>
ANIS	<i>All Neutrino Interaction Simulation</i>
ANTARES ...	<i>Astronomy with a Neutrino Telescope and Abyss environmental RE- Search</i>
ASIC	<i>Application Specific Integrated Circuit</i>
ATWD	<i>Analog-to-digital Transient Waveform Digitizer</i>
BDT.....	<i>Boosted Decision Tree</i>
BLRG	<i>Broad Line Radio Galaxy</i>
CC.....	<i>Charged-Current</i>
CMB	<i>Cosmic Microwave Background</i>
CMC	<i>Cascade Monte Carlo</i>
COG.....	<i>Centre Of Gravity</i>
CORSIKA....	<i>COsmic Ray SIMulations for KAscade</i>
CTEQ.....	<i>Coordinated Theoretical-Experimental project on QCD</i>
DAQ.....	<i>Data AcQuisition</i>
DC.....	<i>DeepCore</i>
DOM	<i>Digital Optical Module</i>

DONUT *Direct Observation of the NU Tau*

DUMAND.... *Deep Underwater Muon And Neutrino Detection*

EHE..... *Extremely High Energy*

EHWD *Enhanced Hot Water Drill*

FADC..... *flash Analog-to-Digital Converter*

FSRQ..... *Flat Spectrum Radio Quasar*

GEANT *GEometry ANd Tracking*

GRB..... *Gamma Ray Burst*

GZK..... *Greisen-Zatsepin-Kuzmin*

HEP *High Energy Physics*

HV..... *High Voltage*

ICL..... *IceCube Laboratory*

IMB..... *Irvine Michigan Brookhaven*

KASCADE... *KARlsruhe Shower Core and Array DETector*

KM3NET..... *Cubic Kilometre Neutrino Telescope*

LED..... *Light Emitting Diode*

LEP *Large Electron-Positron collider*

LPM..... *Landau-Pomeranchuk-Midgal*

MDF..... *Model Discovery Factor*

MMC..... *Muon Monte Carlo*

MRF..... *Model Rejection Factor*

NC..... *Neutral-Current*

NEMO..... *NEutrino Mediterranean Observatory*

NESTOR..... *Neutrino Extended Submarine Telescope with Oceanographic Research*

NLRG *Narrow Line Radio Galaxy*
OM *Optical Module*
PDF *probability density function*
PMT *PhotoMultiplier Tube*
PNF *Processing and Filtering*
QGSP *Quark-Gluon String Precompound*
SMT *Simple Multiplicity Trigger*
SNR *SuperNova Remnant*
SPICE *South Pole ICE*
TMVA *Toolkit for MultiVariate Analysis*
UHE *Ultra High Energy*
WIMP *Weakly Interacting Massive Particle*
WMAP *Wilkinson Microwave Anisotropy Probe*

Acknowledgements

First I thank my supervisors: Dr. Jenni Adams and Dr. Suruj Seunarine. Both are always willing to give their time and knowledge and go above and beyond whenever their students need their support.

I also thank the members (past and present) of the IceCube group at Canterbury University. This includes our postdoctoral fellows Andreas Groß and Anthony Brown, and all the IceCube students: Kahae Han, Pauline Harris, Giles Reid, Sam Whitehead, Matthias Danninger, Jo McCartin, Sarah Bouckoms, Hamish Silverwood, Bart Romgens, and Oliver Auriacombe. Also thank you to the other students that shared the same department as me, especially those that helped me with proof reading my thesis (Ian Farrell and Ewan Orr), and provided computer support (Richard Graham).

Being part of a large collaboration such as the IceCube collaboration is a great experience and getting to know a diverse and fun group of people has been enlightening. I would particularly like to thank the people that I worked most closely with: those in the cascade working group and the atmospheric-diffuse working group of the IceCube collaboration.

Of course completing a PhD would not be possible without generous funding: mine came as part of Marsden grant funding from my supervisors. This allowed me to travel to collaboration meetings where I met all the great people that helped my research and it also allowed me to travel on-site to the IceCube detector at the South Pole. Working closely at the detector site and its operations personnel is an important and a very fun part of performing research in the IceCube collaboration.

Finally a special heartfelt thanks to my family and friends. Without the support of those close to us we would all be lost. Thanks to my parents and my sister for always being there for me.

Abstract

IceCube is the largest operating neutrino observatory. An array of photomultiplier tubes deployed throughout a cubic kilometre of the Antarctic ice at the South Pole detect the Cherenkov radiation from neutrino-nucleon interactions. IceCube is capable of detecting neutrinos over a large energy range. The physics manifesto includes dark matter searches, cosmic ray observation, all sky point source searches, and particle physics parameter constraints. Astrophysical neutrinos are expected to originate from hadronic interactions in some of the most energetic regions in the Universe. The detection of high energy astrophysical neutrinos will provide direct information about the astrophysical sources that produced them.

This thesis concentrates on the cascade channel for neutrino detection. Two separate studies are performed; a high energy cascade analysis and a parameterisation of the production of muons within hadronic cascades.

The experimental data for the cascade analysis was taken by IceCube from April 2008 to May 2009 when the first 40 IceCube strings were deployed and operational. The analysis was designed to isolate the astrophysical neutrino signal from the atmospheric and muon background. Fourteen cascade-like events were observed, on a background of $2.2_{-0.8}^{+0.6}$ atmospheric neutrino events and 7.7 ± 1.0 atmospheric muon events. This gives a 90% confidence level upper limit of $\Phi_{\text{lim}} E^2 \leq 7.46 \times 10^{-8} \text{ GeVsr}^{-1}\text{s}^{-1}\text{cm}^{-2}$, assuming an E^{-2} spectrum and a neutrino flavour ratio of 1 : 1 : 1, for the energy range 25.12 TeV to 5011.87 TeV.

Decay of hadronic particles in cascades produces muons. If the muons are energetic enough they can significantly alter the topology of the cascade and hence the reconstruction of the event in an analysis. The production of high energy muons within hadronic cascades was simulated and parameterised using Pythia and GEANT simulation programs.

Chapter 1

Introduction

The neutrino is a neutral particle belonging to the lepton family and was first predicted in the 1930s by Pauli and Fermi [53, 116]. It has very small mass and interacts via the electroweak force by exchange of W^\pm and Z^0 gauge bosons. Consequently the neutrino rarely interacts with ordinary matter and hence was not detected experimentally until 1956, through inverse beta-decay [42]. It is now known that there exist three active flavours of neutrino, each flavour a counterpart to one of the charged leptons: the electron neutrino, the muon neutrino, and the tau neutrino [43, 86].

Neutrinos are produced in processes such as radioactive decay on Earth, created in nuclear interactions in the Sun, and in particle showers in the Earth's atmosphere. Astrophysical objects in the universe create neutrinos in particle interactions. High energy cosmic-rays and astrophysical neutrinos are believed to originate from sources such as supernova remnants, active galactic nuclei, and gamma ray bursts. Neutrinos are neutral particles and have a small interaction cross-section with matter, interacting only via the electroweak force [66]. Consequently neutrinos travel to Earth without being absorbed by the interstellar medium, or deflected by interstellar magnetic fields. Neutrinos are a unique method for observing astrophysical sources because of their ability to provide direct information about the astrophysical phenomenon that produced them.

Many types of neutrino detectors have been constructed on Earth. Low energy and atmospheric neutrinos are detected by underground tanks of water or heavy liquid. These underground detectors are shielded from cosmic-rays by the Earth and the water or heavy liquid is the interaction medium. Neutrino-nucleon interactions in the medium produce observable particles. Astrophysical neutrino sources have a lower flux than those originating from atmospheric interactions. A larger detector volume provides a

higher probability that an astrophysical neutrino will interact to produce a detectable signal. High energy neutrino detectors are built on hundred metre scales and use natural detector media such as lakes, seas, and ice. The large and transparent natural media provide a volume that can be instrumented to detect the Cherenkov radiation that emanates from charged particles produced in neutrino-nucleon interactions [88, Ch.13].

IceCube is the largest natural medium neutrino detector and consists of photomultiplier tubes distributed in the Antarctic ice below the South Pole. The photomultiplier tubes detect Cherenkov light emitted from secondary particles produced in neutrino-nucleon interactions in the ice and surrounding bedrock. Waveforms of the events are produced and sent to the surface for analysis. IceCube can detect all flavours of neutrinos over a large energy range, from approximately 10^{11} eV and beyond [21].

Analyses are performed on each year of data, focusing on varying types of neutrino interactions and energy ranges. A muon neutrino analysis searches for a track-like signal in the detector. As only neutrinos are capable of travelling through the Earth to interact [66] the background originates from above and can be reduced by keeping only the tracks which have an upward orientation. The requirement of an upward direction is one of the most utilised methods of reducing the background in muon analyses. A cascade analysis searches for the signature of a particle shower within the detector. For the cascade stream of data at the trigger level the event rate is approximately 1500 Hz. The vast majority of these events are muons travelling through the detector from atmospheric neutrinos. Cascade analyses of the experimental data consist of isolating the cascade signal from this dominating background.

Cascade analyses are sensitive to all flavours of neutrinos and can search a 4π steradian volume in the sky. A cascade analysis has improved energy resolution over that from a muon analysis because the events can be fully contained within the detector volume. If cascades are successfully detected by IceCube they may provide information on astrophysical neutrino sources. The astrophysical neutrino spectrum is expected to be harder than that from atmospheric neutrinos so a high energy cascade analysis could observe the break in the energy spectrum of neutrino-induced cascades.

The analysis performed in this work is a high energy cascade analysis. The goal of the analysis was to observe an E^{-2} spectrum diffuse flux from astrophysical neutrinos. The analysis was performed on the IceCube-40 detector, when half of the final detector was deployed and operational. Cascade analyses have been performed on smaller datasets from earlier years and have set a limit on the diffuse flux from astrophysical

sources of $3.6 \times 10^{-7} \text{ GeVsr}^{-1}\text{s}^{-1}\text{cm}^{-2}$ [7]. The cascade analysis in this work comprises of six filter levels of cuts on the experimental data to reduce the background and detect a cascade signal. The cuts are performed on reconstructed variables that are calculated based on event parameters designed to distinguish between a track event and a cascade event. The signal is further isolated and cascade events extracted from the IceCube-40 data using machine learning techniques [83].

An additional complication in the detection of hadronic cascades is the production of muons. Although this possibility was not included in the simulations run for the analysis in this thesis it is investigated for possible inclusion in future cascade analyses. When a neutrino interacts with a nucleon in a medium the nucleon is split into its quark constituents by jet fragmentation [124]. Hadrons are formed, including charged pions and kaons which decay to muons. If a muon produced in the decay is energetic enough it can traverse through the detector leaving a track-like signal. The Cherenkov light from the muon can change the topology of the cascade and has a significant effect on the reconstruction variables in an analysis and the characterisation of observed events.

Chapter 2 introduces neutrinos, their unique properties, and their use as a probe to observe astrophysical sources. Chapter 3 describes the IceCube detector, ice properties, simulations, deployment, and experimental data. Chapter 4 introduces the high energy cascade analysis performed on the IceCube-40 experimental data, its simulations, and reconstruction algorithms. Chapter 5 describes the event selection criteria and optimisation of the cut values. Chapter 6 presents the results of the cascade analysis. Chapter 7 explains the hybrid muon-cascade events and the simulations that were performed to parameterise the muon flux in hadronic cascades. Chapter 8 concludes this work and presents future work that will be performed to continue the search for neutrino-induced cascades from astrophysical sources.

Chapter 2

Neutrinos

This chapter introduces neutrinos and their astrophysical origins. The unique properties of neutrinos means that using them as astrophysical messengers opens a new observational window to the universe.

2.1 Properties

Neutrinos belong to the leptonic family of particles. There are three generations of leptons, with each generation consisting of two particles; one charged and one neutral. The leptons that carry charge are the electron, the muon, and the tau [66]. The three flavours of neutrinos are the neutral counterparts to each of the charged leptons. This content is displayed in Table 2.1. The detection of neutrinos is a challenging task due to their small interaction cross-sections with matter [66].

Generation	1	2	3
charged	e^-	μ^-	τ^-
neutral	ν_e	ν_μ	ν_τ

Table 2.1: Leptons.

The first hint of the neutrino's existence came in 1932 when James Chadwick observed that the energy spectrum of electrons emitted in nuclear beta-decay was continuous [37], a phenomenon unexplained at the time. This observation led to the prediction, by Wolfgang Pauli, of a hypothetical particle. Pauli suggested that some

energy in beta-decay might be carried off by a neutral particle which was escaping detection [116]. A comprehensive theory of radioactive beta-decay was developed by Enrico Fermi, which included this predicted neutral particle. He called this particle the neutrino, meaning “little neutral one” in Italian [53].

Experimental discovery of the neutrino was announced in 1956 by Clyde Cowan and Fred Reines. Their experiment detected electron neutrinos from inverse beta-decay of particles from a nuclear reactor [42]. In 1962 the existence of two types of neutrinos was established by muon neutrino detection through pion decay [43]. The third leptonic particle, the tau, was discovered in 1977 [117]. Its counterpart, the tau neutrino, remained undetected until 2000 when the *Direct Observation of the NU Tau* (DONUT) experiment observed tau neutrinos in interactions with iron nuclei [86]. This completed the detection of all three flavours of active neutrinos. Prior to this, in 1991, the L3 detector at the *Large Electron-Positron collider* (LEP) was used to determine that there are only three light neutrinos [15] corresponding to the three generations of charged leptonic particles.

Neutrinos interact via the exchange of W^\pm or Z^0 gauge bosons, the charge carriers of the electroweak force [66]. The cross-section for neutrino interaction with matter is small. A *Charged-Current* (CC) interaction is mediated via the exchange of a W^\pm boson. In this interaction an incoming neutrino interacts with a nucleon to produce an outgoing charged lepton which may go on to produce an electromagnetic particle shower. A *Neutral-Current* (NC) interaction is mediated via the exchange of a Z^0 boson, and no charged lepton is produced. Both CC and NC neutrino interactions produce a hadronic cascade arising from the jet fragmentation of the nucleons constituents [124]. Neutrino experiments provided the first direct evidence for the existence of NC interactions [70].

Neutrinos have small masses. The best current limit of neutrino mass comes from the seven-year data from *Wilkinson Microwave Anisotropy Probe* (WMAP) [94], which constrains the sum of the masses of the three neutrino flavours to

$$\sum m_\nu < 0.58 \text{ eV}. \quad (2.1)$$

The neutrino flavour eigenstates are not their mass eigenstates, so as neutrinos propagate through a medium they oscillate between electron, muon, and tau flavours. Evidence for neutrino oscillation has been observed in neutrinos originating from reactor accelerator, solar, and atmospheric sources [19, 57].

Due to the neutrino’s unique properties, they provide a method for observing the Universe that has advantages over electromagnetic radiation and charged parti-

cles. Traditional observation methods rely on the detection of photons. The original wavelength used was optical light. In the last century the observation with optical wavelengths of light have been complimented by observation using other regions of the electromagnetic spectrum including radio waves, microwaves, infrared, ultraviolet, gamma-rays, and X-rays. However, the use of photons to observe astrophysical objects has disadvantages because photons may be absorbed near their source or by the intergalactic medium before reaching Earth. In addition to photons the detection of charged particles such as protons and heavier nuclei can give further information about the Universe. However, because particles that carry charge are affected by magnetic fields throughout the interstellar medium it has not been possible to identify the cosmic-ray origins from their detection.

Neutrinos are neither absorbed by opaque matter, nor their trajectory bent by magnetic fields, so neutrinos produced at an astrophysical source travel to Earth without interference by the interstellar medium. Figure 2.1 illustrates the advantage of neutrinos over photons and charged particles as a method for observing astrophysical objects.

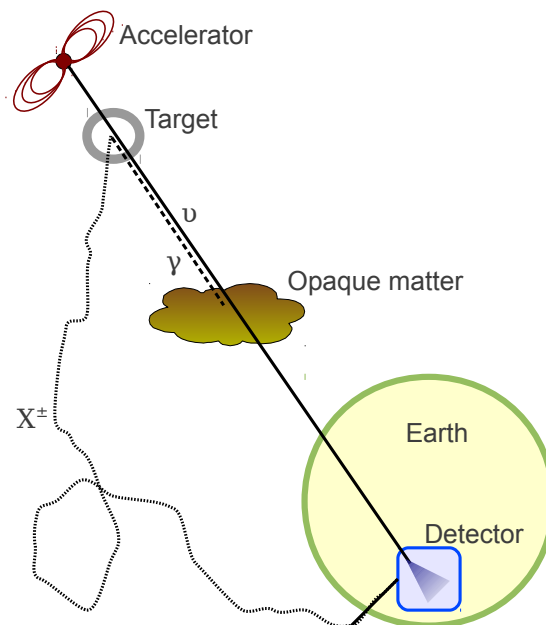


Figure 2.1: Particle travel through the interstellar medium. Photons may be absorbed by opaque matter, charged particle trajectories are affected by magnetic fields. Neutrinos travel directly from their source to Earth without interference.

2.2 Observation

Neutrino-nucleon interactions result in secondary particles which produce Cherenkov radiation. Light detectors distributed in a transparent medium can be used to observe this Cherenkov radiation allowing information about the primary neutrino to be deduced. In this section the characteristics of neutrino-nucleon interactions and the ice properties are outlined.

2.2.1 Interaction with Nucleons

All three flavours of neutrinos interact with nucleons via *Charged-Current* (CC) and *Neutral-Current* (NC) interactions. In a CC interaction, exchange of a W^\pm gauge boson occurs and the charged lepton associated with the neutrino is produced. In a NC interaction, exchange of a Z^0 gauge boson occurs and a neutrino remains present after the interaction. This is shown in Figure 2.2.

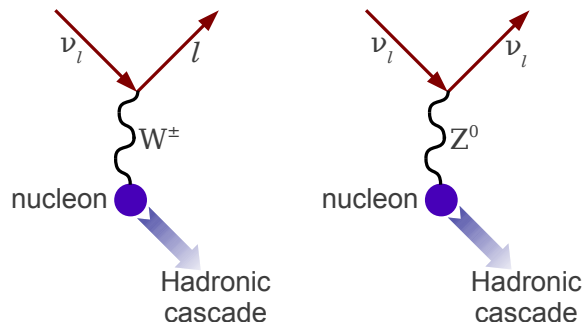


Figure 2.2: *Charged-Current* (CC) and *Neutral-Current* (NC) neutrino interactions with nucleons via exchange of W^\pm and Z^0 gauge bosons.

The direction of the charged lepton produced in a CC interaction is close to the initial direction of the neutrino [137]. The small deviation from the initial direction comes from the scattering angle of the neutrino-nucleon interaction which is on the order of one degree, and there is a contribution from the deflection by the Earth's magnetic field. The latter is on the order of less than one tenth of a degree.

All neutrino interactions produce a hadronic cascade. This occurs as the nucleon splits into its quark constituents, which produce hadrons by jet fragmentation [124]. The energy transferred to the hadronic cascade is typically 20% of the neutrino's incoming energy, with fluctuations of up to 90% of the neutrino's energy transferred into the hadronic cascade [60]. The charged leptons produced in CC interactions result in

distinct event topologies depending on their flavour. The event topologies are described below.

Electron Neutrino CC Interaction

The outgoing electron from a CC interaction will produce an electromagnetic cascade containing electrons, positrons, and photons. The primary interactions within the electromagnetic cascade are bremsstrahlung and pair production [110]. The spread of an electromagnetic cascade is narrower than a hadronic cascade and the particle tracks are more tightly contained. The total track length of an electromagnetic cascade is proportional to the energy of the cascade. The total track length is therefore also proportional to the energy of the initial electron neutrino ejected from the CC interaction. A 100 TeV electromagnetic cascade is approximately 8.5 m in length [131].

Muon Neutrino CC Interaction

In contrast to the electron the outgoing muon from a CC interaction propagates a significant distance. A 1 TeV muon travels approximately 3 km [131]. Its energy loss is due to ionization and radiative processes such as bremsstrahlung, pair production, and multiple scattering. These processes cause the muon to lose kinetic energy at a lower rate than that of an electron because of the muon's smaller interaction cross-section with matter arising from its larger mass. The muon energy loss as a function of path length dx can be described using

$$-\frac{dE}{dx} = a(E) + b(E)E \quad (2.2)$$

where $a(E)$ is the energy loss from ionization, and $b(E)$ is the combined energy loss due to the radiative processes [131]. To the approximation that these slowly varying functions are constant the mean range of a muon x_0 with initial energy E_0 is

$$x_0 = \frac{1}{b} \ln \left(1 + \frac{E_0}{E_{\mu c}} \right) \quad (2.3)$$

where $E_{\mu c} = \frac{a}{b}$ is the critical energy at which the ionization loss equals the energy loss due to other processes [110]. In ice a and b are largely independent of energy with $a = 0.2 \text{ GeV m}^{-1}$ and $b = 3.4 \times 10^{-4} \text{ m}^{-1}$ [110]. Due to the energy losses, small local cascades can be produced along the muon track. These processes can deflect the muon a small amount during its propagation. A muon continues to travel until it has lost its kinetic energy or until it undergoes muon capture at rest.

Tau Neutrino CC Interaction

The outgoing tau lepton from a CC interaction will decay and produce a secondary cascade [110]. The lifetime of the tau is $2.96 \times 10^{-13} \text{ s}$ [110] and so the energy of the

tau lepton dictates what the topology of this interaction looks like. A low energy tau will decay close to the initial interaction point. Consequently the cascade from the tau decay is indistinguishable from the hadronic cascade produced by the neutrino interaction. A higher energy tau will travel a short distance before undergoing decay, producing an event with two distinct cascades. A 1 PeV tau travels approximately 50 m before decaying to produce a secondary cascade [131]. An event of this type, contained within the detector, is called a double-bang event. If one of the two cascades occurs outside of the detector volume the event is called a lollipop event.

2.2.2 Cherenkov Radiation

Cherenkov radiation occurs when any charged particle travels faster than the local speed of light in a dispersive medium [36]. Cherenkov radiation is produced at a distinct angle relative to the path of the particle with the value of the angle dependent on the medium [88]. The Cherenkov radiation from a muon emanates from close to the muon track producing a moving cone of light. The Cherenkov radiation in a cascade event emanates from each charged particle within the cascade. Due to the scattering of the photons a spherical front is observed in the detector. These event topologies are shown in Figure 2.3.

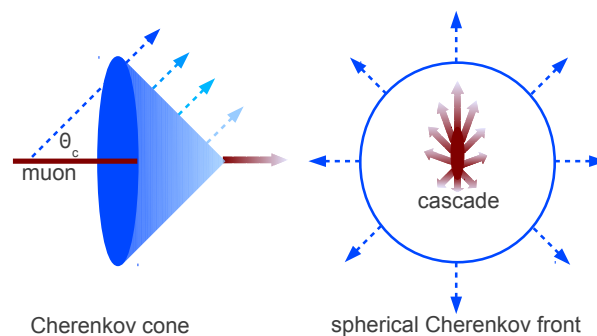


Figure 2.3: Event topology of tracks and cascades from Cherenkov radiation. The particle track produces the Cherenkov cone, the cascade produces a spherical front.

The local speed of light in a medium is

$$c_n = \frac{c}{n(\lambda)} \quad (2.4)$$

where c is the speed of light in vacuum and n is the wavelength dependent refractive index of the medium. The Cherenkov angle θ_c is

$$\theta_c = \frac{1}{n(\lambda)\beta}, \quad (2.5)$$

with $\beta = \frac{v}{c} \approx 1$ for speeds close to the absolute speed of light in vacuum. As the relativistic charged particle speed decreases the number of Cherenkov photons produced declines and they are emitted with a higher momentum [88, Ch.13]. The value of the Cherenkov angle also increases and when $v < c_n$ Cherenkov radiation ceases being emitted.

The energy loss due to Cherenkov radiation is much less than other radiative energy loss processes [66]. However, Cherenkov radiation is important because the photons produced are at visible wavelengths between 300 nm and 610 nm, and so are detectable in transparent media. The Cherenkov radiation emitted per unit distance along the path of the particle is

$$\left(\frac{dE}{dx}\right)_{\text{rad}} = \frac{(ze)^2}{c^2} \int_{\epsilon(\omega) \geq \frac{1}{\beta^2}} \left(1 - \frac{1}{\beta^2 \epsilon(\omega)}\right) \omega d\omega \quad (2.6)$$

where ze is the charge of the particle and $\epsilon(\omega)$ is the dielectric constant of the medium as a function of particles frequency, ω . Cherenkov radiation is emitted in bands where $\epsilon(\omega) \geq \beta^2$. This condition means the speed of the particle must be larger than the phase velocity of the electromagnetic field [88, Ch.13]. For energies between 10 GeV and 50 GeV the number of optical photons expected due to Cherenkov radiation is approximately 500 photons per centimetre [76]. The optical photons from Cherenkov radiation ultimately undergo one of two processes: scattering or optical absorption.

2.3 Origins

This section introduces the sources of neutrinos of interest to the IceCube telescope. The energy threshold of IceCube is from approximately 10^{11} eV and beyond [21], precluding the detection of low energy neutrinos such as solar neutrinos. In this section atmospheric neutrinos originating from cosmic-ray interactions in the atmosphere and the expected sources of astrophysical neutrinos are described.

2.3.1 Cosmic-rays and Atmospheric Neutrinos

Cosmic-ray physics is central to IceCube science. One of the main physics goals of IceCube is the identification of the origin of cosmic-rays. In addition to this cosmic-ray interactions in the Earth's atmosphere produce the majority of the background to all astrophysical neutrino searches in the form of atmospheric muons and atmospheric neutrinos.

Cosmic-Rays

Cosmic-rays are charged particles that travel through the interstellar medium to Earth with velocities close to the speed of light. They consist of approximately 85% protons, 14% helium nuclei, 1% electrons and other elementary particles, and a small fraction of heavier nuclei [58, Ch.1]. Cosmic-rays are observed over a wide energy spectrum up to 3×10^{20} eV [80] as shown in Figure 2.4. The sources of the highest energy cosmic-rays, where particles are able to be accelerated to the energies observed, are unknown [79].

One mechanism that may be used to explain the highest-energy cosmic-rays is Fermi acceleration [54]. This is often referred to as diffusive shock acceleration because charged particles iteratively gain energy through multiple particle collisions over shock fronts or inhomogeneous magnetic fields in plasma clouds throughout the interstellar medium. There are two types of Fermi acceleration: first order and second order. In first order Fermi acceleration the charged particle gains energy as it travels through a shock front and encounters moving charges. The gain in energy per shock crossing in first order Fermi acceleration is proportional to β . In second order Fermi acceleration the charged particle gains energy as it has collisions with moving interstellar magnetised clouds. Since the probability of a head-on collision is higher than a head-tail collision the charged particles are on average accelerated. The gain in energy in second order Fermi acceleration is proportional to β^2 . Every crossing of a shock front by a charged particle results in a relative energy gain which leads to an expected energy spectrum following a power law. The energy spectrum obtained depends on the conditions of the acceleration effects and generically leads to a spectral index of -2.0 .

During particle propagation of charged cosmic rays from the acceleration site an additional energy dependence of approximately $E^{-0.6}$ is gained [58]. The source energy spectrum of $E^{-2.0}$ and the propagation spectrum of $E^{-0.6}$ ultimately leads to a cosmic-ray spectral index of 2.6 which agrees reasonably well with the experimental value of 2.7 that is observed.

The observed cosmic-ray spectrum, shown in Figure 2.4 follows a broken power law with a spectral index of 2.7 up to energies of 1×10^6 GeV. At this energy the spectral index changes to 3.0. This transition is called the spectral knee and arises from the origin of the cosmic-rays changing from galactic to extragalactic sources. At energies above 1×10^9 GeV the spectral index reverts back to 2.7. This second transition is called the spectral ankle and its cause is unknown [80], although it is predicted to arise from either a change in origin or a change in primary particle composition.

Cosmic-rays interact with molecules in the Earth's atmosphere to create particle

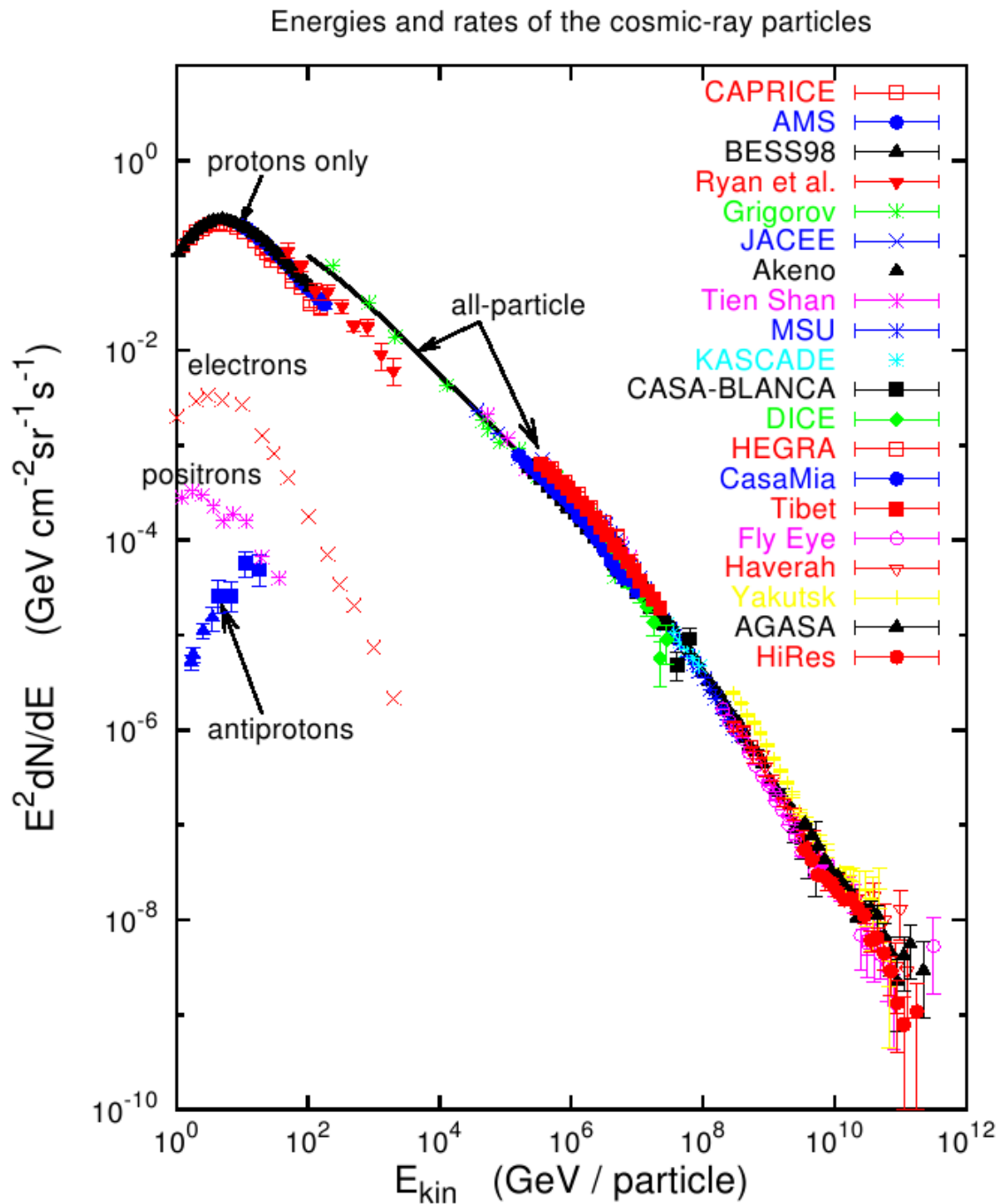


Figure 2.4: Cosmic-ray energy spectrum as observed by different experiments, from [80]. The spectral knee is seen at 10^6 GeV, arising from the origin of cosmic-rays changing from galactic to extragalactic sources. The spectral ankle is seen at 10^9 GeV.

air showers. Of particular interest to neutrino detectors are the muons and neutrinos produced in these particle air showers [58]. IceCube detects over 10^9 cosmic-ray induced atmospheric muons every year [92]. Regardless of the distribution of their sources in the sky cosmic-rays arrive from all directions [80] because they are charged and therefore their directions are randomized by the deflections from the magnetic fields throughout the interstellar medium. Consequently it is not possible to identify cosmic-ray origins from their arrival direction¹.

The sources that produce cosmic-rays must be within approximately 10–100 megaparsecs of the Earth because cosmic-rays at high energies interact with the 2.7 K relic *Cosmic Microwave Background* (CMB) radiation which can lower the energy or absorb the cosmic-ray. This effect means that cosmic-rays originating from astrophysical sources at large distances from Earth should not be observed above energies of 4×10^{19} eV, which is known as the *Greisen-Zatsepin-Kuzmin* (GZK) cut-off [64, 140]. As will be described in section 2.3.2 neutrinos are expected to be produced in regions where cosmic-rays are accelerated. As neutrinos are unaffected by the interstellar medium it is hoped that their detection will enable the identification of the origins of the highest energy cosmic-rays.

Atmospheric Neutrinos

Particle interactions of cosmic rays in the Earth’s atmosphere produce neutrinos. Atmospheric neutrinos can be used to explore a range of physics. For example, through the observation of atmospheric neutrinos, neutrino oscillations and the mixing of neutrino flavours can be studied. In the context of this thesis the atmospheric neutrinos are a background to the search for astrophysical neutrinos. Electron and muon neutrinos arise mainly from the decay of pions, kaons, and muons. For energies less than a few GeV the fraction of muon neutrinos to electron neutrinos from these decay chains is about $\nu_\mu : \nu_e = 2 : 1$ (as is also shown in equations 2.7 and 2.8). However, as the energies increase this ratio increases because the higher-energy parent muons begin to reach the ground before decaying. At energies above $E_\pi = 115$ GeV and $E_K = 850$ GeV for the pions and kaons respectively, the mesons are more likely to interact than decay. As neutrinos only result when the mesons decay, and not when they interact, this results in a steepening of the neutrino spectrum for energies above $E_\pi = 115$ GeV. The ratio of the probability for meson decay to the probability for interaction is approximately proportional to $1/E$ and means that the atmospheric neutrino spectrum is one

¹At the highest energies above 4×10^{19} GeV, near the *Greisen-Zatsepin-Kuzmin* (GZK) cutoff, charged particles may retain some directional information that can be used to locate their sources. The Auger Collaboration has searched for sources using their highest energy cosmic-ray sample [45].

power of E softer than the cosmic-ray energy spectrum and so follows approximately a power law of $E^{-3.7}$. The spectrum of atmospheric neutrinos is also dependent on the zenith angle. This is again due to the competition between interaction and decay for the pions and kaons, with the probability for interaction increasing with the depth of atmosphere traversed.

Neutrinos resulting from pion or kaon decay are usually referred to as conventional atmospheric neutrinos. Mesons containing charm quarks are also produced in cosmic-ray air showers and their decay also produces atmospheric neutrinos. Due to the short lifetime of the “charm mesons” these neutrinos are called prompt neutrinos [87]. As the charm mesons predominantly decay rather than interact, the spectrum of prompt neutrinos follows the cosmic-ray energy spectrum and therefore has a spectrum with a spectral index of ~ -2.7 . For the same reason the prompt flux is isotropic. The contribution of prompt neutrinos, to the overall atmospheric neutrino flux, is small at low energies. This is due to the much suppressed production of charm mesons, compared to that of pions and kaons. However due to the harder spectrum of the prompt neutrinos they should become dominant over the conventional neutrinos at higher energies. The cross-over is predicted to be at approximately 10^6 GeV [49].

Calculations of the conventional neutrino flux have been made by Honda et al. [85] and Barr et al. [27]. The Barr et al model is usually referred to as the Bartol model. Calculations of the prompt neutrino flux have been made by Naumov [111] and Enberg et al. [49] (referred to as the Sarcevic model). All of these models for the atmospheric neutrino spectrum are shown in Figure 2.5. The Sarcevic atmospheric model is the most recent model. The parameters which give the best prediction are denoted by the line labeled Sarcevic std. The theoretical uncertainty band arises from uncertainty in the cross-section for charm production. In the Figure the upper value for cross-section values yields the model labeled Sarcevic max, while the lower limits gives the model Sarcevic min. These maximum and minimum models are expected to be reasonable predictions for the upper and lower limits of the prompt atmospheric neutrino flux.

2.3.2 High Energy Astrophysical Neutrinos

High energy neutrino production is predicted to occur in regions of the universe where cosmic rays are accelerated. Some of the cosmic-ray protons are expected to interact with ambient protons or photons surrounding their acceleration site. These interactions produce neutrinos and gamma rays as detailed below. The observation of high-energy gamma-ray sources motivates these sources as being candidates for high-energy neu-

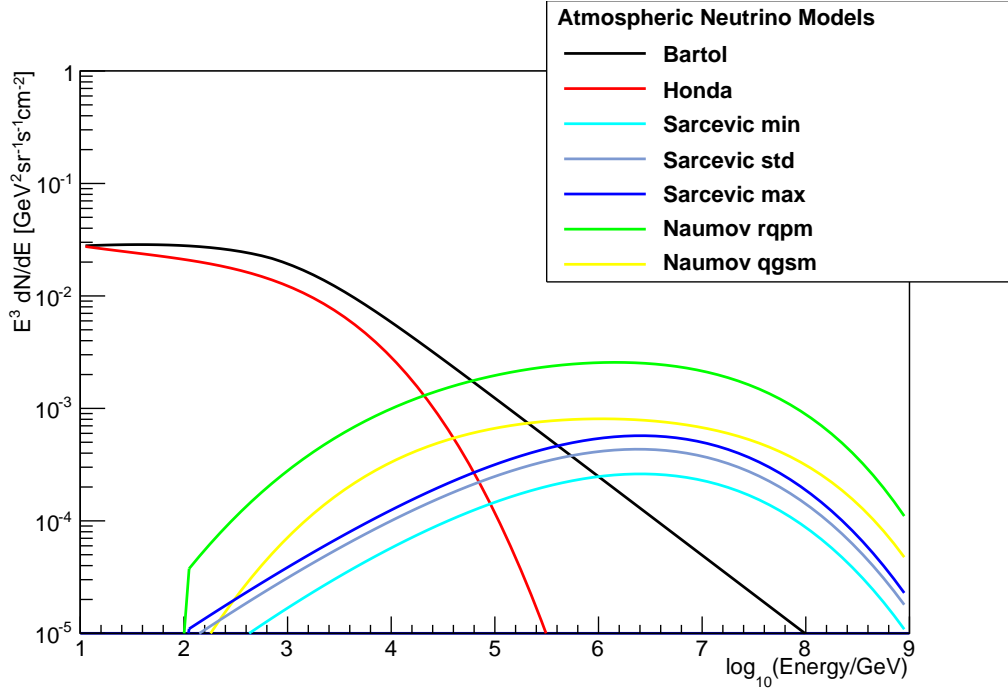


Figure 2.5: Atmospheric neutrino models. The conventional atmospheric models shown are Bartol [27] and Honda [85]. The prompt atmospheric models shown are Naumov [111] and Sarcevic [49].

trino and cosmic-ray production.

There are two types of hadronic interactions that produce neutrinos. The first is the interaction of protons with protons which can produce either neutral pions or charged pions and kaons [110]. The decay products include gamma rays and neutrinos:

$$\begin{aligned}
 p + p &\longrightarrow \pi^0 + X \\
 &\quad \longmapsto 2\gamma \\
 p + p &\longrightarrow \pi^\pm / K^\pm + X \\
 &\quad \longmapsto \mu^\pm + \nu_\mu (\bar{\nu}_\mu) \\
 &\quad \longmapsto e^\pm + \nu_e (\bar{\nu}_e) + \bar{\nu}_\mu (\nu_\mu).
 \end{aligned} \tag{2.7}$$

The second is the interaction of protons with photons which produce charged pions [110]. The decay products include neutrinos:

$$\begin{aligned}
 p + \gamma &\longrightarrow \pi^+ + n \\
 &\quad \longmapsto \mu^+ + \nu_\mu \\
 &\quad \longmapsto e^+ + \nu_e + \bar{\nu}_\mu.
 \end{aligned} \tag{2.8}$$

These interactions predict a large high-energy neutrino flux that is dependent on the optical thickness of the source and the energy transfer to the secondary particles which differs for the two types of interactions. Both of these types of interactions at astrophysical sources produce neutrinos with a flavour ratio of $\nu_\mu : \nu_e = 2 : 1$ independent of energy because no energy is lost due to muon interaction (assuming interaction length in the source medium is much longer than the decay length). Due to neutrino oscillations as they travel through the interstellar medium, neutrinos from high energy astrophysical sources are expected to be observed at the Earth with a flavour ratio of $\nu_\tau : \nu_\mu : \nu_e = 1 : 1 : 1$ [25, 29].

The astrophysical neutrino spectrum is expected to follow the source proton spectrum because the entire energy of a primary proton is transferred to the pions produced in the interactions. The source proton spectrum is assumed to be E^{-2} as motivated by Fermi acceleration. The wide range of TeV gamma ray spectral indices implies that there is likely to be a range of neutrino source spectral indices. Given no particular theoretical prejudice for any other spectral index, E^{-2} is usually used as a benchmark spectra in searches for astrophysical neutrinos and is used in this thesis. Since the neutrino spectrum follows the proton generation spectrum the observed high-energy cosmic-ray spectrum can be used to estimate the diffuse neutrino flux from astrophysical optically thin sources. This gives an upper bound by calculating the flux normalization for the expected E^{-2} neutrino spectrum which generates the same energy density as the charged cosmic-ray flux [133]. Such a conservative model-independent flux limit for muon neutrino production was calculated by Waxman and Bahcall. For sources of size not much larger than the proton photo-meson (or p-p) mean free path this flux limit is $2 \times 10^{-8} \text{ GeVsr}^{-1}\text{s}^{-1}\text{cm}^{-2}$ [136]. The flux limit is corrected for redshift and for all three flavours of neutrinos (through multiplying by $\frac{3}{2}$) to give an upper bound of $6.75 \times 10^{-8} \text{ GeVsr}^{-1}\text{s}^{-1}\text{cm}^{-2}$.

The production of neutrinos during the propagation of ultra-high energy cosmic-rays was calculated by Engel, Seckel, and Stanev. Their high energy model is called ESS Cosmogenic $\nu_\mu + \nu_e$ [51].

Regions where particles are accelerated can be identified through gamma-ray observations. However, gamma-rays can be produced as a result of leptonic acceleration through the inverse Compton mechanism, as well as the decay of mesons as described in equation 2.7. Thus while gamma-ray observations identify possible cosmic-ray accelerator sites it is likely that unambiguous identification of these sites will require coincident neutrino detection. Astrophysical objects which are targeted as possible

sources of the cosmic-rays are now outlined.

SuperNova Remnant (SNR)

A SNR is a compact spinning neutron star or black hole with an expanding shock wave of relativistic electrons, originating from the supernova explosion of a massive star. This is an evolving source and is believed to be the distributor of heavy elements throughout the universe. It is widely believed that SNRs are the source of galactic cosmic-rays up to energies of at least 10^{15} GeV, and possibly beyond, where the knee of the cosmic ray spectrum is located [81].

A shell-type SNR is created when the shockwave from the supernova explosion expands out through space heating and stirring the interstellar material that it encounters which produced a shell of hot material in space. Cosmic-rays are presumed to be generated by diffusive acceleration at the remnants' forward shocks. Estimates on the neutrino flux from these sources predict observable event rates in neutrino telescopes of cubic kilometres in volume [91], such as the IceCube neutrino telescope.

A pulsar is a rotating neutron star with axial radio emission. The rotation periods of pulsars range from $1 \mu\text{s}$ to 10s, depending on its age. A constant flow of particles along the magnetic field lines from the pulsar's surface creates a pulsar wind nebula. High energy gamma-rays from pulsars and nebulae have been detected [18, 69]. The most famous pulsar SNR is the Crab nebula. Using the Crab nebula and other sources the expected neutrino flux from SNRs can be estimated assuming hadronic models for the production of gamma-rays [65].

Active Galactic Nuclei (AGN)

AGN are bright cores of galaxies with a supermassive black hole and an accretion disk at their centre. Relativistic jets of heated matter are ejected perpendicular to the disk as matter spirals into the black hole. In the plane of the accretion disk a toroidal gas cloud feeds additional material to the disk [121]. AGN are extremely compact objects with energy emission similar to that of an entire galaxy. Their luminosity can flare more than an order of magnitude within an hour. The emission spectrum of AGNs ranges over the full electromagnetic spectrum and exhibits a double-humped shape with a high-frequency peak and a low-frequency peak. Simultaneous measurements in the regions of these peaks show correlations between their fluxes which suggest a common electron population as the origin of the radiation. There are however, exceptions to these measurements indicating that hadronic models play some part in AGN spectral energy distributions.

The subclasses of galactic objects that constitute an AGN are: *Narrow Line Radio*

Galaxy (NLRG), *Broad Line Radio Galaxy* (BLRG), *Steep Spectrum Radio Quasar*, *BL-Lac* object, and *Flat Spectrum Radio Quasar* (FSRQ). These objects are distinguishable by their radio flux, observation angle from Earth, and luminosity [12]; they are shown in Figure 2.6.

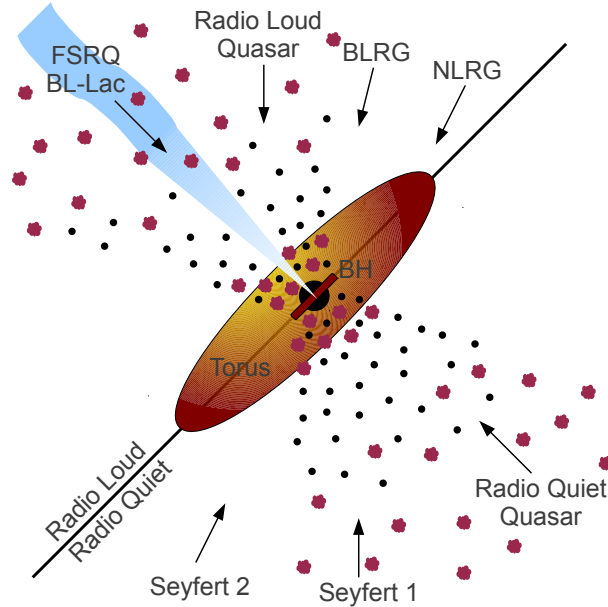


Figure 2.6: *Active Galactic Nuclei* (AGN) made from subclasses of galactic objects: *Narrow Line Radio Galaxies* (NLRGs), *Broad Line Radio Galaxies* (BLRGs), *Steep Spectrum Radio Quasars*, *BL-Lac* objects, and *Flat Spectrum Radio Quasars* (FSRQs).

Many AGN neutrino flux models have been predicted using observations of AGN. A popular example is that of Stecker, Done, Salamon, and Sommers [128] which was later revised by Stecker [127]. They used ultra-violet and x-ray observations to define the photon fields and an accretion-disk shock-acceleration model for producing high-energy particles.

Another AGN model is that of Mücke et al. [109]. This model concerns BL Lac objects which are AGN characterised by their rapid and large variability. The spectral energy distribution of electromagnetic radiation and the spectrum of high energy neutrinos from BL Lac objects in the context of the Synchrotron Proton Blazar Model was calculated. In this model, the high energy part of the spectral energy distribution is due to accelerated protons in large magnetic fields, while most of the low energy part is due to synchrotron radiation by co-accelerated electrons.

Gamma Ray Burst (GRB)

GRBs are the most luminous stellar-sized sources of light in the universe. Their extragalactic origin is indicated by their isotropic distribution throughout the sky. They

are transient sources with most of their energy released from 10^{-3} s to 10 s. The most popular model of GRBs is that they are a relativistically expanding fireballs, produced by the explosion of a supernova, or the merging of two neutron stars. In these models gamma-rays are produced by ultra-relativistic electrons accelerated in the fireballs [104]. If protons are also accelerated along with the electrons then neutrinos will be produced from the interaction of these protons with the radiation field of the burst.

The expected neutrino flux can be calculated as a function of the ratio of protons and electrons in the fireball. A popular such model is the Waxman-Bahcall prompt fireball neutrino model [135]. This model has a flux limit of $0.3 \times 10^{-8} \text{ GeVsr}^{-1}\text{s}^{-1}\text{cm}^{-2}$ for the energy range $10^{14} \text{ eV} < E < 10^{16} \text{ eV}$ which is consistent with the upper bound from Waxman-Bahcall described in section 2.3.2.

High energy neutrinos can serve as probes of the stellar progenitor and jet dynamics of GRBs arising from stellar core collapses. A detailed neutrino spectra from shock accelerated protons in jets just below the outer stellar envelope, before their emergence was calculated by Razzaque, Mészáros, and Waxman giving neutrino flux estimates from pre-burst jets for massive stellar progenitor models [120].

The strongest experimental constraints placed on GRB models come from the recent IceCube-40 + 59 combined analysis [11]. The model-independent search observed two candidate events at low significance which are consistent with muons from cosmic-ray air showers due to coincident events in the IceTop surface air shower array. A model-dependent analysis was also performed on this data which yielded no observed events. The results were scaled to the expected emission for all GRBs, producing the most stringent limit to date on neutrino production in GRBs. These results conclude that either the proton density in GRB fireballs is substantially below the level required to explain the highest-energy cosmic-rays or the physics in GRB shocks is significantly different from that included in current models [11]. In either case our current theories of cosmic-ray and neutrino production in GRBs will need to be revisited.

2.3.3 Low Energy Astrophysical Neutrinos

There are some astrophysical sources that are predicted to produce neutrinos in the MeV to TeV energy range. These include core-collapse supernova and dark matter annihilation.

Core-collapse Supernova

Core-collapse supernova bursts emit MeV neutrinos. A core-collapse supernova burst

occurs when a massive² star undergoes catastrophic core-collapse at the end of its lifetime [35]. During the collapse virtually all of the gravitational energy is emitted as MeV neutrinos [35]. Supernova are a transient source and can last from milliseconds to several minutes. The neutrinos from the collapse reach the Earth before photons and hence can be used as an early warning system for optical telescopes to be orientated in the correct direction to observe the supernova visually.

Neutrinos were first detected from an astrophysical source, SN1987A, on 24th February 1987. These astrophysical neutrinos originated from the supernova of the blue supergiant star Sanduleak. SN1987A is situated in the Tarantula nebula in the Large Magellanic Cloud. This is a small satellite galaxy of the Milky Way, 179000 light years from Earth. A total of 24 neutrinos were detected [96] by the Cherenkov detectors Kamiokande II in Japan [82] and *Irvine Michigan Brookhaven* (IMB) in America [67], and the liquid scintillator detector Baksan in Russia. This was the first observation of astrophysical neutrinos.

It has been estimated that a galactic supernova would result in $0.067\text{--}0.396 \times 10^6$ neutrinos within 380 ms, dependent on supernova collapse model and mass, in the completed IceCube detector volume [95]. Although a single MeV neutrino would not trigger the detector the collective effect from numerous MeV neutrino interactions in a short time would show an increase in the overall rate from all optical sensors above the dark noise rate, the sensitivity is approximately 20 standard deviations at the galactic edge and 6 standard deviations in the Large Magellanic Cloud [95].

Dark Matter Searches

Dark matter models predict massive non-luminous particles which contribute up to 90% of the mass of the universe. The *Weakly Interacting Massive Particle* (WIMP) is a generic class of dark matter candidate. A WIMP is a hypothetical particle with mass in the range of 10 GeV–10 TeV and interaction strength characteristics of the weak interaction. WIMPs may be captured in gravitational potential wells of objects such as the Sun or the Earth, and accumulate at their centres, which increases their annihilation rate. This subsequent self-annihilation produces standard model particles including neutrinos.

The predicted WIMP mass range implies that the neutrinos produced from their annihilation will be lower energy than the neutrino energies of other targeted astrophysical sources. The lightest stable super-symmetric WIMP is called the neutralino. The neutralino's mass is predicted to be below 1 TeV [90].

²The mass criteria for core-collapse supernova is $M \gtrsim 8M_{\odot}$, where M_{\odot} is the solar mass.

2.4 Analyses

One of the principal objectives of the IceCube neutrino telescope is the detection of sources of high energy neutrinos of astrophysical origin as was described in the previous section. Due to oscillations neutrinos from meson decay sources arrive at the Earth with a flavour ratio of $\nu_\tau : \nu_\mu : \nu_e = 1 : 1 : 1$. IceCube is sensitive to all flavours of neutrinos over a wide range of energies. Muons can be detected from approximately 10^{11} eV and above. All flavour hadronic and electron neutrino electromagnetic cascades can be isolated above energies of 10^{13} eV. Tau events can be identified above energies of 10^{15} eV [21]. Although, to date, no astrophysical neutrinos have been identified, analyses searching for them can establish limits, thus enabling astrophysical models to be constrained.

2.4.1 Astrophysical Models and Fluxes

The astrophysical neutrino flux models described in section 2.3.2 are illustrated in Figure 2.7.

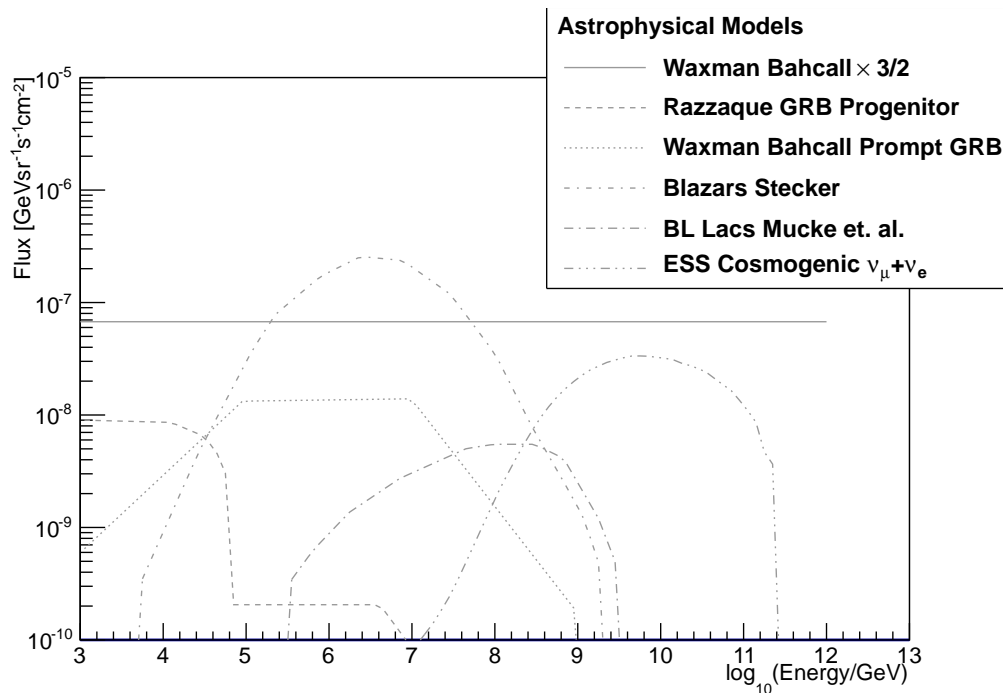


Figure 2.7: Astrophysical model flux predictions including Waxman Bahcall $\times \frac{3}{2}$ [136], Razzaque GRB Progenitor [120], Waxman Bahcall Prompt GRB [135], Blazars Stecker [127], BL Lacs Mücke et. al. [109], and ESS Cosmogenic $\nu_\mu + \nu_e$ [51].

For a given astrophysical neutrino flux the event rates generated in the full IceCube

detector by all three flavours of neutrinos can be calculated. This can be compared with the event rate from atmospheric neutrinos and atmospheric muons. For example Table 2.2 shows the results of a study [21] which was undertaken where the assumed astrophysical flux was $1 \times 10^{-7} \text{ GeVsr}^{-1}\text{s}^{-1}\text{cm}^{-2}$. In this table triggered events refers to the number of events which would be detected by IceCube³, while filtered events refers to the number of events that remain in the data sample after basic event reconstruction cuts have been applied to reject the cosmic-ray background. The astrophysical flux is now constrained to be below $1 \times 10^{-7} \text{ GeVsr}^{-1}\text{s}^{-1}\text{cm}^{-2}$. For an E^{-2} spectrum at a flux level of $1 \times 10^{-8} \text{ GeVsr}^{-1}\text{s}^{-1}\text{cm}^{-2}$ the results in Table 2.2 imply around 100 events per year can be expected at the filter level.

	Triggered	Filtered
Astrophysical neutrinos	3.3×10^3	1.1×10^3
Atmospheric neutrinos	8.2×10^5	9.6×10^4
Atmospheric muons	4.1×10^{10}	1.0×10^5

Table 2.2: Number of events per year in the IceCube telescope from [21].

The event rates in Table 2.2 are normalised for one year of the full detector operating. The full detector is referred to as IceCube-80, this means 80 of the IceCube strings are deployed and operational. However many analyses were carried out during the construction of IceCube with a smaller number of strings. The partially complete configurations of IceCube were named according to the number of strings deployed. The configurations were IceCube-9, IceCube-22, IceCube-40, IceCube-59, IceCube-79, and IceCube-80. For details on the construction of IceCube refer to Chapter 3.

Two all-flavour analyses were performed using the 2007–2008 IceCube-22 data. The first of these was an *Ultra High Energy* (UHE) analysis that set a flux limit of $15.19 \times 10^{-8} \text{ GeVsr}^{-1}\text{s}^{-1}\text{cm}^{-2}$ [10] for the energy range $339 \text{ TeV} < E < 199.5 \text{ PeV}$. The second was a cascade analysis that observed 14 events on a background of 8.3 ± 3.6 events and set an all-flavour flux limit of $3.6 \times 10^{-7} \text{ GeVsr}^{-1}\text{s}^{-1}\text{cm}^{-2}$ [7] for the energy range $24 \text{ TeV} < E < 6.6 \text{ PeV}$. At the time IceCube-40 analyses commenced this was

³The trigger requires a minimum number of *Digital Optical Module* (DOM) signals within one section of a string. In the study presented in [21] the minimum number of DOM signals required was five which is different from the IceCube multiplicity trigger which was operative for the data used in this thesis (eight DOMs hit within 5000 ns).

the best limit for an E^{-2} spectrum diffuse cascade flux.

Several IceCube-40 diffuse analyses were performed using the 2008–2009 IceCube-40 data, including the high energy cascade analysis that is presented in this work. One of the IceCube-40 cascade analyses set a flux limit of $9.5 \times 10^{-8} \text{ GeVsr}^{-1}\text{s}^{-1}\text{cm}^{-2}$ for the energy range $89 \text{ TeV} < E < 28 \text{ PeV}$ [114]. This high-energy analysis acts as a cross-check with others and was designed to quickly reach a result and thus is aimed to accept a higher energy threshold than the cascade analysis presented in this work. It included no containment filters and only observed background events to set its limit. A UHE analysis was performed on IceCube-40 data which aimed at detecting an all-flavour E^{-2} spectrum astrophysical flux with neutrino primary energy greater than 1 PeV. It used detector filters from the muon, cascade and high-energy streams of data and set a flux limit of $2.32 \times 10^{-8} \text{ GeVsr}^{-1}\text{s}^{-1}\text{cm}^{-2}$ [89] for the energy range $290 \text{ TeV} < E < 220 \text{ PeV}$. An *Extremely High Energy* (EHE) analysis was also performed on the IceCube-40 data. This type of analysis targets the energy range $10^7 \text{ GeV} - 10^{10} \text{ GeV}$ where GZK neutrinos are expected. Only two basic variables are used as the filter for the data which select extremely energetic events. This analysis set a flux limit of $3.57 \times 10^{-8} \text{ GeVsr}^{-1}\text{s}^{-1}\text{cm}^{-2}$ for the energy range $2000 \text{ TeV} < E < 6300 \text{ PeV}$ [6].

An IceCube-40 diffuse search was also performed using muons only. This analysis observed no events and set a flux limit of $8.9 \times 10^{-9} \text{ GeVsr}^{-1}\text{s}^{-1}\text{cm}^{-2}$ [5] for the energy range $35 \text{ TeV} < E < 7 \text{ PeV}$. For comparison to other diffuse analyses the limit is multiplied by a factor of 3 to give an all flavour flux limit of $2.53 \times 10^{-8} \text{ GeVsr}^{-1}\text{s}^{-1}\text{cm}^{-2}$.

Three dedicated searches were also performed using IceCube-40 data for lower energy atmospheric neutrinos. One using only the IceCube-40 detector, one using the IceCube-40 detector with the *Antarctic Muon And Neutrino Detector Array* (AMANDA) detector (for a description of AMANDA refer to section 3.2.4), and one using the IceCube-40 detector with the DeepCore detector (for a description of DeepCore refer to section 3.2.4). In this final analysis using the DeepCore detector atmospheric neutrino-induced cascades were observed by IceCube and so no limit was set [8].

The astrophysical models described in section 2.3.2 and the flux limits set by IceCube high energy analyses are shown in Figure 2.8. The model predictions are shown by the grey lines, the analyses flux limits are shown by the coloured lines.

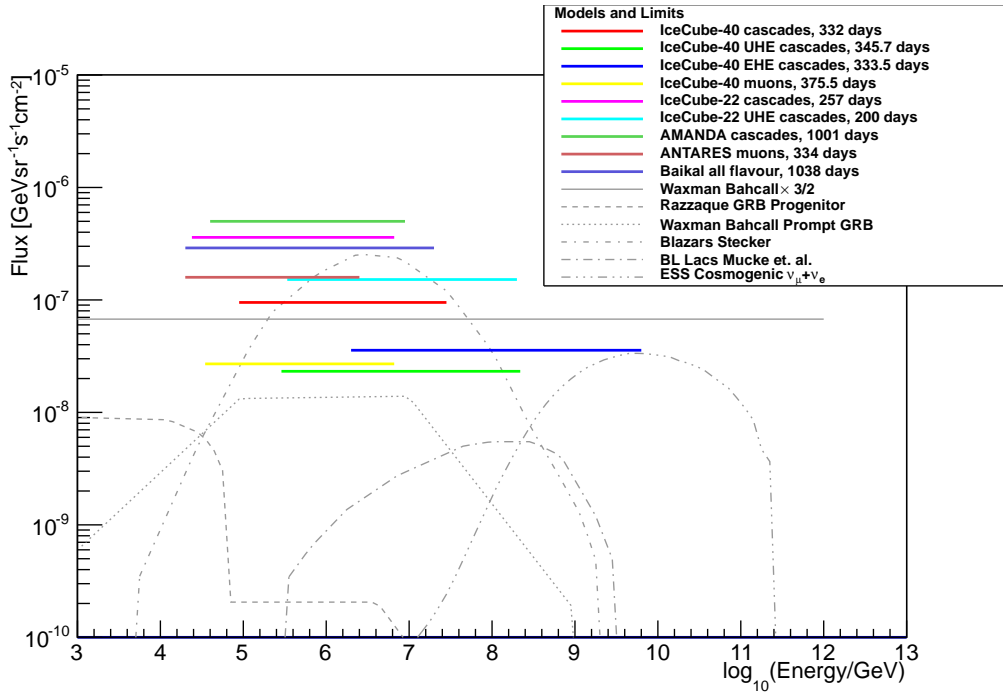


Figure 2.8: IceCube analyses limits and model flux predictions. The analyses are all at the 90% confidence level and are shown by the coloured lines [2, 5–7, 10, 17, 48, 89, 114], The model predictions are shown by the grey lines [51, 109, 120, 127, 135, 136].

2.4.2 High Energy Cascade Analysis

The IceCube-40 analyses are improving flux limits to the E^{-2} spectrum diffuse astrophysical neutrino models as shown in Figure 2.8. The flux limits from analyses using the IceCube-40 data have progressed below the Waxman Bahcall upper bound and continue to approach other flux models. These analyses results and the first observation of atmospheric cascades encourage the continued search for astrophysical neutrino-induced cascades with neutrino telescopes, with the promise of tighter constraints on models or the discovery of an astrophysical flux.

2.5 Detectors

Neutrino detectors require a large effective volume of transparent medium to overcome the small neutrino interaction cross-section with matter. The flux from astrophysical neutrinos is lower than that from atmospheric neutrinos, so the detection of higher energy neutrinos requires an increase in the effective volume of the detector.

Many Cherenkov detectors have been constructed using large underground tanks of

water. The largest of these is Super-Kamiokande[129], the successor of Kamiokande[30], which is 41.4 m tall and 39.3 m in diameter. Underground neutrino detectors investigate neutrino properties using neutrinos that originate from the sun, the atmosphere, or nuclear reactors.

To detect high energy neutrinos originating from astrophysical sources it has been established that cubic kilometre detectors are required [68]. To meet this size requirement Cherenkov detectors have been constructed deep in naturally occurring bodies of water such as oceans and lakes.

The first detector proposed to be constructed in the ocean was the *Deep Underwater Muon And Neutrino Detection* (DUMAND) telescope in 1976 [1]. The DUMAND telescope was intended to be located at a depth of 4760 m in the Pacific Ocean at Keahole Point, 30 km off the coast of the Big Island of Hawaii, occupying a cubic kilometre of the ocean. The project was canceled in 1995, DUMAND did however demonstrate the technology for deep underwater neutrino detection and carried out the first analysis of ocean optics measurement of the cosmic-ray muon flux in the deep ocean. The DUMAND project set the then best limits on PeV neutrinos from AGN.

Following DUMAND, the Baikal collaboration constructed a neutrino telescope in 1993 [47], which was later upgraded in 1998 [138]. This detector is located 1370 m deep in the southern part of the freshwater Lake Baikal, 3.6 km off the shore of Siberia. Lake Baikal is the world's deepest lake and has a water transparency almost of the quality of deep ocean water. Background light in Lake Baikal is mostly due to bioluminescence from animal life and is comparable to the level of light due to radioactive decay seen in the deep ocean. Lake Baikal has the advantage of thick ice on its surface during the winter, which provides a stable platform for maintenance on the detector during this season.

Neutrino Extended Submarine Telescope with Oceanographic Research (NESTOR) was the next deep underwater telescope to be constructed at a depth of 3800 m [16]. NESTOR is located in the Mediterranean Sea, 15 km south-east off the coast of Peleponnisios, Greece.

In the same location of the Mediterranean Sea is *Astronomy with a Neutrino Telescope and Abyss environmental RESearch* (ANTARES). The prototype of the ANTARES experiment was developed in 1999 [23]. It has a surface area of 0.1 km² and a height of 350 m. ANTARES is situated at a declination of +43° North and is sensitive to upward going neutrinos originating from negative declinations. This complements the IceCube telescope, described in Chapter 3.

Also located in the Mediterranean Sea, near the Sicilian coast, is *NEutrino Mediteranean Observatory* (NEMO). This telescope is in the development stages and is progressing towards a kilometre-scale neutrino telescope [130].

These three groups (NESTOR, ANTARES, and NEMO), joined together to form a collaboration called *Cubic Kilometre Neutrino Telescope* (KM3NeT) [93]. This detector will also be located in the Mediterranean Sea and will be on the multi-kilometre scale and together, with the IceCube neutrino detector (described in Chapter 3), will view the full sky and form a global neutrino observatory.

Chapter 3

IceCube

The naturally occurring, transparent ice at the South Pole offers a large, pure, and homogeneous volume that is suitable for the detector medium. The prototype ice Cherenkov telescope was AMANDA. This chapter describes AMANDA and its successor IceCube, which is the largest ice Cherenkov telescope.

3.1 Ice Cherenkov Detectors

The low flux levels predicted for astrophysical neutrinos necessitates a telescope with an effective area on the order of square kilometres [99]. Although underground tanks and deep underwater Cherenkov detectors were operational by the 1990s, these detectors did not have the effective volume to allow them to be sensitive to astrophysical neutrino sources [99]. The large volumes required means that neutrino telescopes are constructed in naturally occurring, transparent mediums. The deep Antarctic ice fits this criteria well and its suitability as a Cherenkov neutrino detector has been proven by the AMANDA and IceCube projects [99].

3.1.1 Ice Properties

In order to reconstruct the characteristics of the initial neutrino-nucleon interaction from the light distribution detected in the ice an understanding of the ice properties and the photon propagation throughout the medium is required. Mie scattering is assumed as the dominant scattering. The optical properties of the ice at the South Pole vary with depth. Within a fixed wavelength range the ice properties can be described, using Mie scattering, with two parameters; the effective scattering length

and the absorption length.

Effective scattering length, $\lambda_{\text{effective}}$

The scattering length $\lambda_{\text{scattering}}$ is the mean free path between scatters in ice. In the shallow ice, scattering is caused by air bubbles. In the deeper ice, below 1300 m, the bubbles have converted to air hydrate crystals (clathrates) because of the increased pressure. The air hydrate crystals are non-scattering because they have the same refractive index as ice [132]. The dominant source of scattering in this region is due to dust. The dust has four main components: mineral grains, sea salt crystals, liquid acid droplets, and soot [14]. The scattering is mostly caused by the mineral grains, which are the most abundant component [72].

The scattering phase function is the scattering angle probability and is approximated using the Henyey-Greenstein function [75]. The average scattering angle probability $\langle \cos(\theta) \rangle$ is estimated for the dust-component in the South Pole ice to be

$$\langle \cos(\theta) \rangle = 0.94 \quad (3.1)$$

at 400 nm, meaning that optical photons from Cherenkov radiation are strongly peaked in the forward direction. It is not possible to measure $\lambda_{\text{scattering}}$ and $\langle \cos(\theta) \rangle$ independently and the combination, the effective scattering length $\lambda_{\text{effective}}$, is determined instead. $\lambda_{\text{effective}}$ can be interpreted as the distance after which the photon scattering distance becomes isotropic and is

$$\lambda_{\text{effective}} \simeq \frac{\lambda_{\text{scattering}}}{1 - \langle \cos(\theta) \rangle}. \quad (3.2)$$

In most cases the effective scattering coefficient b_e , which is the reciprocal of the effective scattering length

$$b_e = \frac{1}{\lambda_{\text{effective}}}, \quad (3.3)$$

is quoted. The scattering coefficient for the Antarctic ice is shown in Figure 3.1. The four peaks labeled A through D correspond to stadials during the last glacial period. The wavelength dependence of the scattering coefficient is highly dependent on the cause of the scattering. Below 1300 m where scattering is due to dust the wavelength dependence can be described by the power law

$$b_e(\lambda) \propto \lambda^{-0.9} \quad (3.4)$$

for the wavelength range between 300 nm and 600 nm. The scattering coefficient is wavelength independent when scattering is due to air bubbles in the ice within this optical wavelength range.

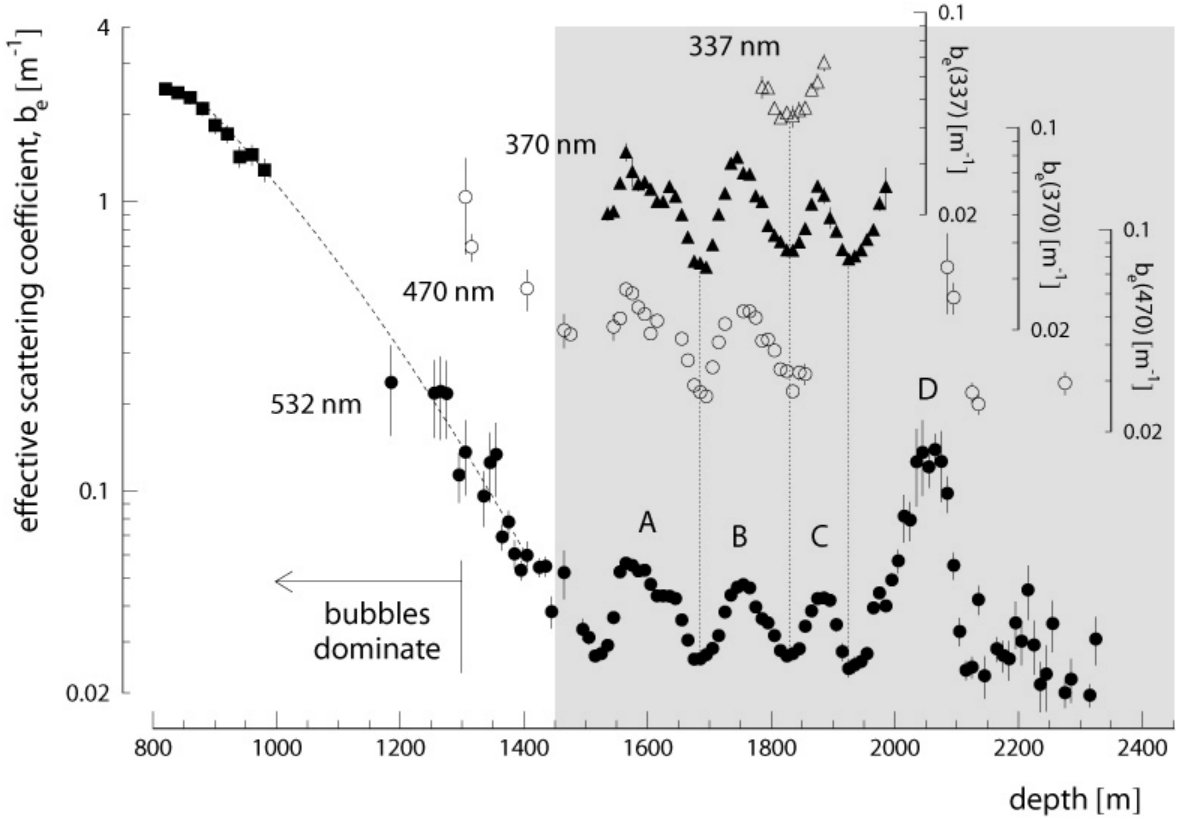


Figure 3.1: Depth dependence of the effective scattering coefficient b_e measured with pulsed sources at four wavelengths, from [14]. Bubbles in the ice are the dominate cause of scattering above 1300 m, below dust is the dominate cause. The four peaks labeled A through D correspond to stadials in the last glacial period, the grey area corresponds to the IceCube detector depth.

Absorption length, $\lambda_{\text{absorption}}$

The absorption length $\lambda_{\text{absorption}}$ is defined as the distance at which the survival probability of a photon drops to $1/e$. The absorption coefficient is the reciprocal of the ice absorption length [24]

$$a = \frac{1}{\lambda_{\text{absorption}}}. \quad (3.5)$$

The absorption coefficient is shown in Figure 3.2 where the four peaks corresponding to the stadials during the last glacial period are also seen here.

The absorption in ice follows the same trend as the scattering coefficient at depths below 1300 m. Above 1300 m, as described previously, scattering is dominated by air bubbles characterised through the large values of b_e . By comparison, absorption is only affected by dust, mainly the mineral grain and soot components [14], and is not affected by bubbles. For this reason the absorption coefficient does not climb in the way the effective scattering coefficient does above 1300 m.

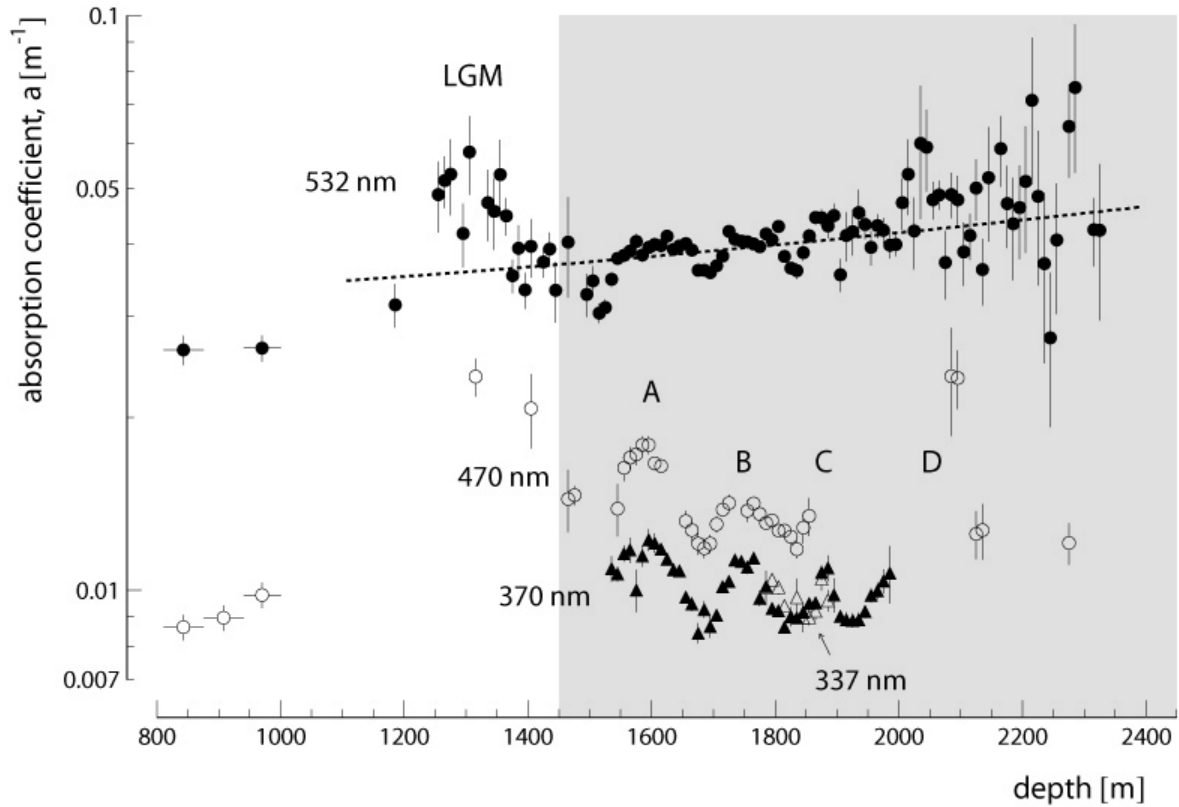


Figure 3.2: Depth dependence of the absorption coefficient a measured with pulsed sources at four wavelengths, from [14]. The four peaks labeled A through D correspond to stadials in the last glacial period, the grey area corresponds to the IceCube detector depth.

Absorption in the ice has a strong wavelength dependence [118]. Below 200 nm, in the Urbach tail, absorption increases exponentially because of the electronic band structure of the ice crystals. Between 200 nm and 500 nm ice is an almost perfectly transparent medium with no absorption. The absorption which does arise is due to dust impurities. Above 500 nm absorption increases exponentially because of H_2O molecules. The highly transparent region coincides well with the optical wavelengths of Cherenkov radiation [88, Ch.13]. The absorption in the Antarctic ice is significantly lower than in water and is one of the advantages ice has over water for neutrino detection.

3.1.2 AMANDA

The first ice Cherenkov neutrino telescope was the AMANDA [28]. The initial detector, AMANDA-A, was constructed between depths of 800 m and 1000 m in the ice cap at the South Pole. Here the contamination from air bubbles was so large that no events could be reconstructed. The observation that the air bubbles disappear below depths

of 1300 m, as discussed in section 3.1.1, led to the construction of the subsequent AMANDA optical modules being deployed between depths of 1550 m and 1950 m. The subsequent telescopes were called AMANDA-B [32] and AMANDA-II [139]. AMANDA detected the first neutrinos using ice as the interaction medium and paved the way for the larger IceCube detector to be constructed [22].

3.2 Construction of IceCube

IceCube is a kilometre-scale Cherenkov telescope. IceCube consists of optical sensors designed to detect Cherenkov photons produced by secondary particles from neutrino-nucleon interactions in the ice. These detecting sensor for IceCube is the *Digital Optical Module* (DOM). The DOMs form a lattice spanning 1 km^3 . The DOMs are deployed on 80 strings, lowered into the ice through water columns that have been melted by a hot water drill. Each string has 60 DOMs attached. After the water column refreezes the DOMs are optically coupled to the surrounding ice. The vertical spacing of the DOMs on each string is approximately 17 m and the horizontal spacing between the strings is approximately 125 m. The DOMs connect to each other, and to the surface, by copper twisted-pair wires bundled together to form cables that can carry event data to the *IceCube Laboratory* (ICL) situated on the surface above the detector. This section will describe the DOM components, their deployment, and the subdetectors associated with IceCube.

3.2.1 Digital Optical Modules

The DOM is the fundamental element in IceCube for photon detection and data acquisition. It contains a 25 cm diameter *PhotoMultiplier Tube* (PMT) supported by coupling gel, a PMT high voltage generator and divider circuits, a *Light Emitting Diode* (LED) flasher board, and the DOM mainboard which contains the analog and digital signal processing electronics [3]. A mu-metal grid surrounds the PMT to shield it from the terrestrial magnetic field and improve PMT performance. All systems are housed within a pressure sphere made of 13 mm thick borosilicate glass with low potassium content. The DOMs are capable of withstanding the pressures from its deep deployment which are up to 70 MPa [3]. The borosilicate glass has good mechanical properties, a broad transparency window up to 350 nm and low background radioactivity from ^{40}K . The DOM is filled with dry nitrogen to a pressure of approximately half an atmosphere. A photograph of a DOM is shown in Figure 3.3(a) and a schematic diagram of a DOM

with its components is shown in Figure 3.3(b). Each of the DOM components will be described in this subsection.

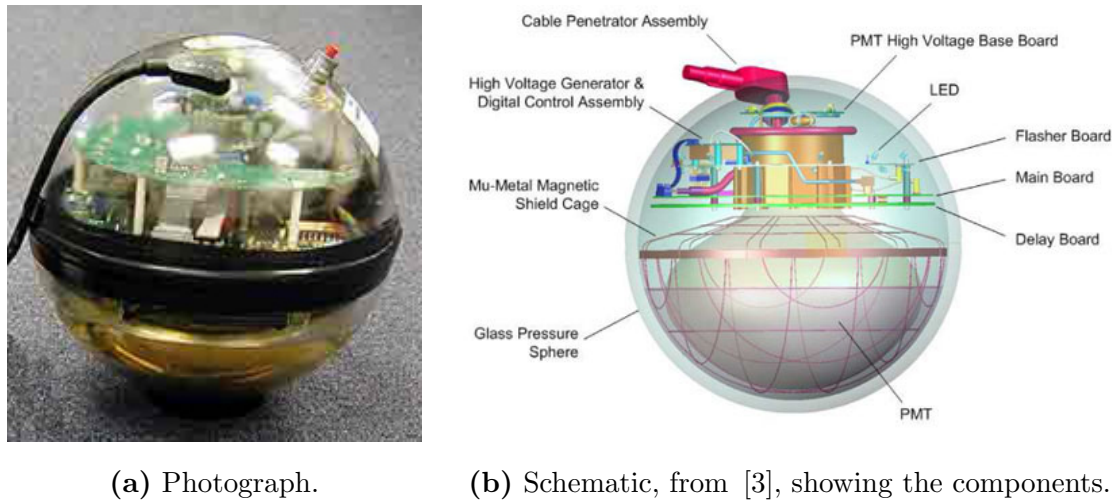


Figure 3.3: The IceCube *Digital Optical Module* (DOM).

On board each DOM is a 25 cm diameter R7081-02 PMT made by Hamamatsu Photonics [4]. The PMTs produce time-stamped digitized signal waveforms which are transmitted to the surface for analysis. The PMT is capable of detecting both single photons, and pulses of up to thousands of photons, which allows the PMT to be sensitive to events over a range of energies and distances from the DOM.

Spectral response	300 nm to 650 nm
Quantum efficiency at 390 nm	25%
Supply voltage for gain of 10^7	1500 V
Dark noise rate at -40°C	500 Hz
Transit time speed	3.2 ns
Peak to valley ratio for single photons	2.5
Pulse linearity at 2% deviation	70 mA

Table 3.1: Hamamatsu specifications for the R7081-02 *PhotoMultiplier Tube* (PMT), from [4].

The PMT's dynamic range is 200 photoelectrons per 15 ns and it is designed to accurately record the amplitudes and widths of the pulses with a timing resolution of 5 ns. To produce clean event information R7081-02 PMTs were manufactured with a

custom low-radioactivity glass. This was to ensure that there would be a low dark noise count rate, of less than 500 Hz, at the cold temperatures in which the PMTs are operating. The spectral response is 300 nm to 650 nm which encompasses the range over which the optical Cherenkov photons are produced. The quantum efficiency is 25%. The PMT specifications are shown in Table 3.1.

The DOM mainboard is the central processor that receives signals from the PMT. It is 274 mm in diameter and sits above the PMT at the centre of the DOM [3]. After digitization, the DOM mainboard formats the data to create a “hit”. High-bandwidth waveform capture is accomplished by an *Application Specific Integrated Circuit* (ASIC) including an *Analog-to-digital Transient Waveform Digitizer* (ATWD) and a *flash Analog-to-Digital Converter* (fADC). The ATWDs provide a sampling rate of 300 MHz over a time window of 450 ns. They have four channels, each storing 128 samples with 10 bit resolution. One of these channels is used for flasher runs and calibration, while the other three channels have different gains ($\times 0.25$, $\times 2$, $\times 16$) which are used to digitize the PMT output. The fADC has a coarser sampling of 40 MHz and records data over a longer time period of up to 6.4 μ s. The data is buffered until the DOM mainboard receives a request to transfer the data to the surface. The DOM mainboard also has a light emitting diode which flashes precisely timed signals for calibration of single photoelectron pulses and PMT transit times.

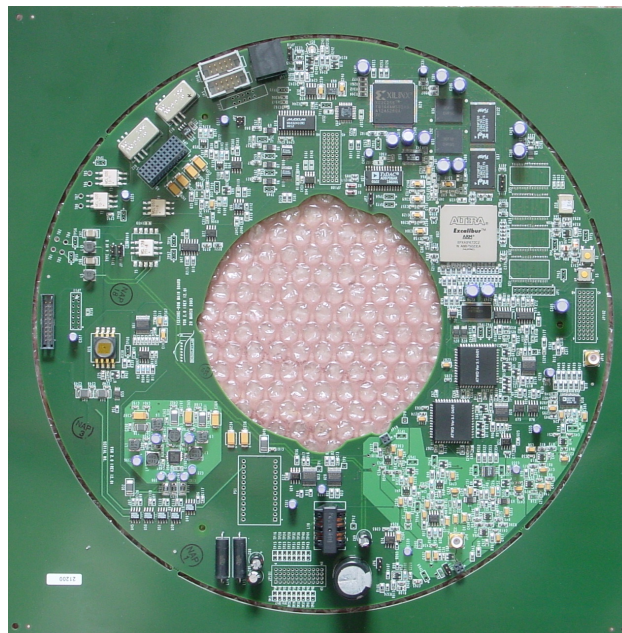


Figure 3.4: Photograph of a DOM mainboard and its components from [3]. This is the central processor which communicates with the surface, provides power, and drives the PMT and other DOM components.

The DOM includes a flasher board which sits above the DOM mainboard. This flasher board holds 12 LEDs, six pointing horizontally and six pointing upwards at 45° [3]. The upward facing LEDs sit at this angle to simulate the angle at which Cherenkov photons are radiated with respect to a vertical upgoing particle track. The LEDs produce bright ultraviolet optical pulses which are detected by other DOMs deployed in the ice. Individual LEDs can each be pulsed separately or in combinations at programmable output levels and pulse lengths. The flashers are used for calibration of the DOMs and to investigate optical properties of the ice [3].

3.2.2 Deployment

The deployment of the IceCube detector spanned seven years, with completion in December 2010. The bore holes that the strings were lowered into could only be drilled during the Antarctic summer months so the DOMs were deployed in stages over several years. The layout of IceCube is shown in Figure 3.6; the year of deployment of the strings is illustrated by the colour, as described in Table 3.2. The detector configuration used in the analysis described in this thesis incorporates the yellow, green, red, and pink coloured strings.

The bore holes were drilled into the ice using a *Enhanced Hot Water Drill* (EHWD) which is a high-velocity stream of hot water, directed by gravity. The bore holes were drilled approximately 1 m in diameter. Shortly after drilling a string was deployed into each water-filled bore hole. Once the water refroze the DOMs became optically well coupled¹ to the surrounding ice and permanently inaccessible. Heat flow from the Earth's core introduces a vertical thermal gradient in the ice. This in turn leads to a variation in the internal operating temperature of the DOMs from -9°C at the lowest elevation DOM, to -32°C at the highest elevation DOM [3]. Figure 3.5 shows a drilled hole with a string of DOMs being lowered into the ice.

3.2.3 Data Acquisition

The purpose of the *Data Acquisition* (DAQ) system is to capture and timestamp, with high accuracy, the optical signals received from the PMTs [3]. It is located in the ICL on the surface above the detector as shown in Figure 3.6.

The DAQ architecture is decentralized and the digitization is done individually

¹The refractive index of the glass of the *Digital Optical Module* (DOM) matches closely to that of the glacial ice.

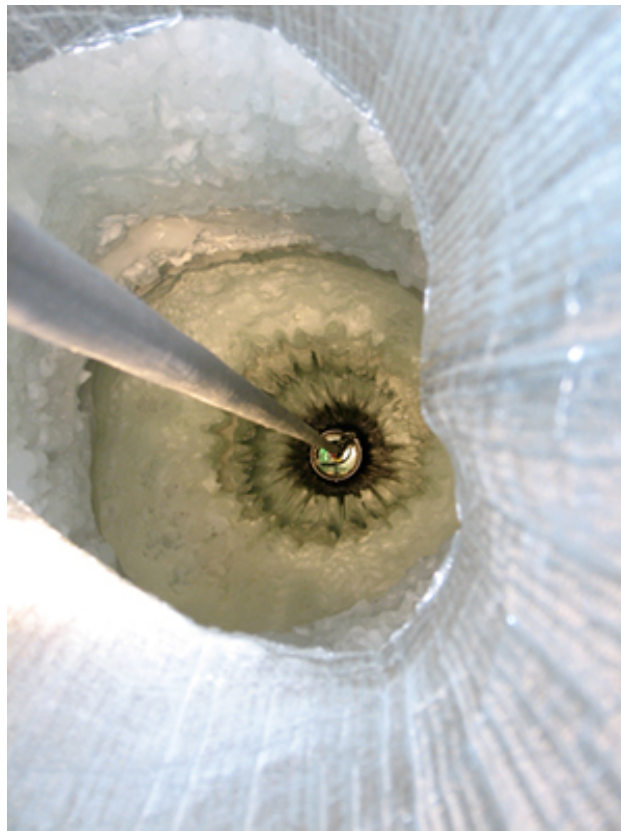


Figure 3.5: Deployment of an IceCube string of DOMs down a hot water drilled hole into the ice. The hole is filled with water which freezes the DOMs into their permanent positions.

String colour	Deployment year	Detector configuration
Yellow	2004–2005	IceCube-1
Green	2005–2006	IceCube-9
Red	2006–2007	IceCube-22
Pink	2007–2008	IceCube-40
Purple	2008–2009	IceCube-59
Blue	2009–2010	IceCube-77
Orange	2010–2011	IceCube-80

Table 3.2: Year of IceCube string deployment and detector configuration. The colours correspond to those shown in Figure 3.6.

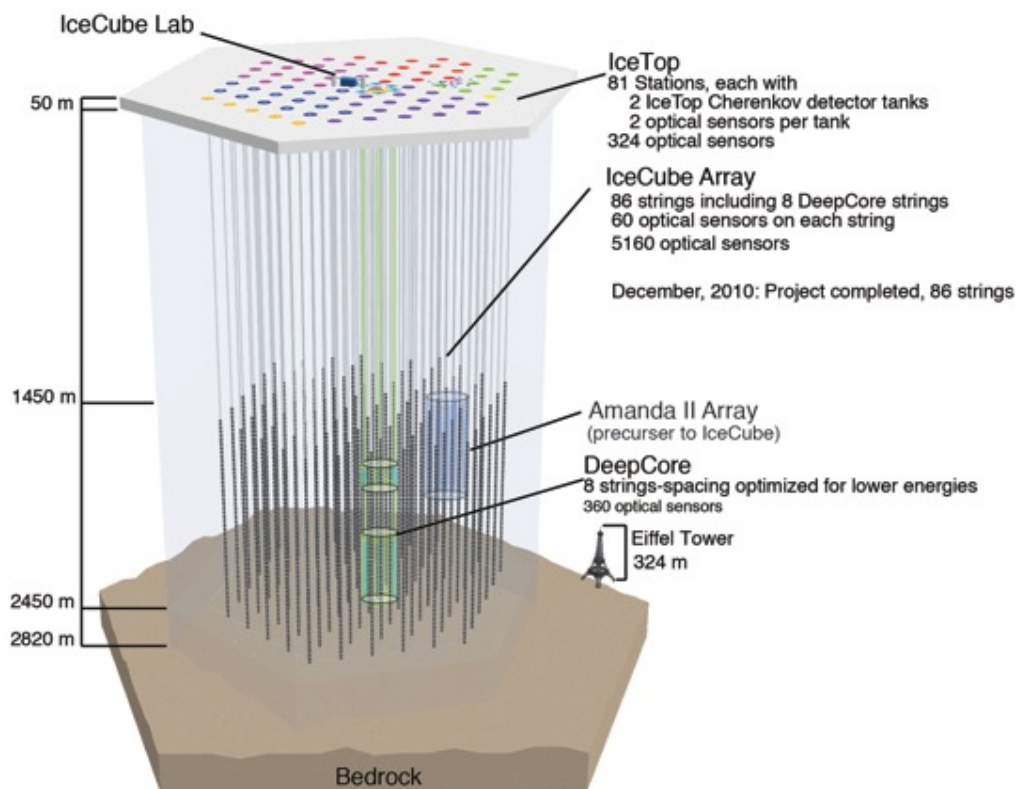


Figure 3.6: The IceCube detector instrumented between 1450 m and 2450 m in the ice at the South Pole, with the Eiffel Tower shown for size perspective. The IceTop array is shown on the surface, the tanks and strings are colour coded by deployment year, shown in Table 3.2. The prototype detector AMANDA-II is shown by the shaded dark blue region inside IceCube. The extension detector *DeepCore* (DC) is shown by the light yellow shaded region.

inside each DOM. When event information is requested it is sent from the DOMs to the ICL along the twisted copper-pair wires. In the ICL the data collection process is centrally managed and power is distributed over the network. This architecture obtains very high information quality with minimal on-site monitoring during operation. At the ICL event data is initially analysed by computers. Data to be used in analyses is sent north via satellite for further processing and analysis.

3.2.4 Subdetectors

The IceCube neutrino detector is complemented by a surface air shower array called IceTop [59] and by a low energy extension called *DeepCore* (DC) [123].

The IceTop subdetector consists of stations situated above each IceCube string. These stations contain two 1 m^2 tanks of ice separated by 10 m. The tanks are instrumented with two DOMs frozen in each tank. One DOM operates at low gain and the other DOM at high gain to achieve a wide dynamic range [59]. IceTop uses DOMs that are identical to those deployed in the ice and detect Cherenkov light from charged particles passing through the tanks. The signals that IceTop detects arise from muons, electrons, and gamma rays in cosmic-ray air showers. These particles deposit energy in the IceTop tanks, resulting in light pulses up to hundreds of nanoseconds in duration. The arrival times and amplitudes are then used to reconstruct the shower core position, direction, and energy [59]. An overall timing resolution of 10 ns provides a pointing accuracy of about one degree [4]. Combining neutrino signals from the IceTop and IceCube detectors covers a wide energy range. The IceTop array is shown with the IceCube detector in Figure 3.6.

The DC extension consists of six additional strings located at the centre of the IceCube detector [123]. DC is more a densely instrumented array than the rest of IceCube. The interstring spacing is 72 m and each DC string has 60 DOMs approximately 7 m apart in depth. The DC DOMs house PMTs that are almost identical to those deployed in IceCube but with a higher quantum efficiency photocathode [4]. DC is located at the bottom region of the IceCube array where the ice is clearest. DC lowers IceCube's energy threshold for muon neutrinos down to energies of 10 GeV–20 GeV and uses IceCube to provide a veto against atmospheric muons that allows a solid angle of 4π steradian detection for low energy neutrinos. DC enhances IceCube's sensitivity to solar WIMP dark matter, GRBs, galactic point sources, and neutrino particle properties [123]. The DC extension to IceCube is also shown in Figure 3.6.

Chapter 4

Cascade Analysis

The work presented in this thesis is a high-energy, diffuse, cascade analysis of one year of IceCube data taken between 6th April 2008 and 20th May 2009. Diffuse analyses search for an all-sky neutrino flux in contrast to point-source searches which target specific sources. If there are numerous astrophysical sources with unobservably low fluxes the aggregate flux may still be observable as a diffuse flux and detected by IceCube. A cascade analysis searches for the signature of an astrophysical neutrino-induced particle shower within the IceCube detector. Cascade analyses are motivated by the fact that cascades arise from the interaction of all three active flavours of neutrinos; the CC electron-neutrino interaction and the NC electron-, muon-, and tau-neutrino interactions produce detectable cascades, as discussed in section 2.2.1. A further advantage of a cascade search over a muon search is that cascade events typically have superior energy resolution. This is particularly important for diffuse searches which use a change in the spectral shape to recognise the presence of an astrophysical neutrino flux on top of the atmospheric neutrino background.

The superior energy resolution for cascade events is due to the fact that cascades deposit their energy within a small spatial region while muons deposit energy over their entire track length. Thus a component of the muon's energy may be deposited outside the instrumented volume rather than being wholly contained within the detector. With constraints placed on the containment of an event the energy resolution of a cascade event is therefore much better than that of a muon event. For the IceCube-40 detector the energy resolution in a muon analysis is 0.27 in $\log(E)$ estimated from a Gaussian fit [5] using energy reconstruction routines on simulated events. The resolution in this cascade analysis is 0.08 in $\log(E)$ estimated from a Gaussian fit. The value of this resolution is dependent on the reconstruction algorithms used in the analysis and is

shown for simulated IceCube-40 cascades in Figure 4.1.

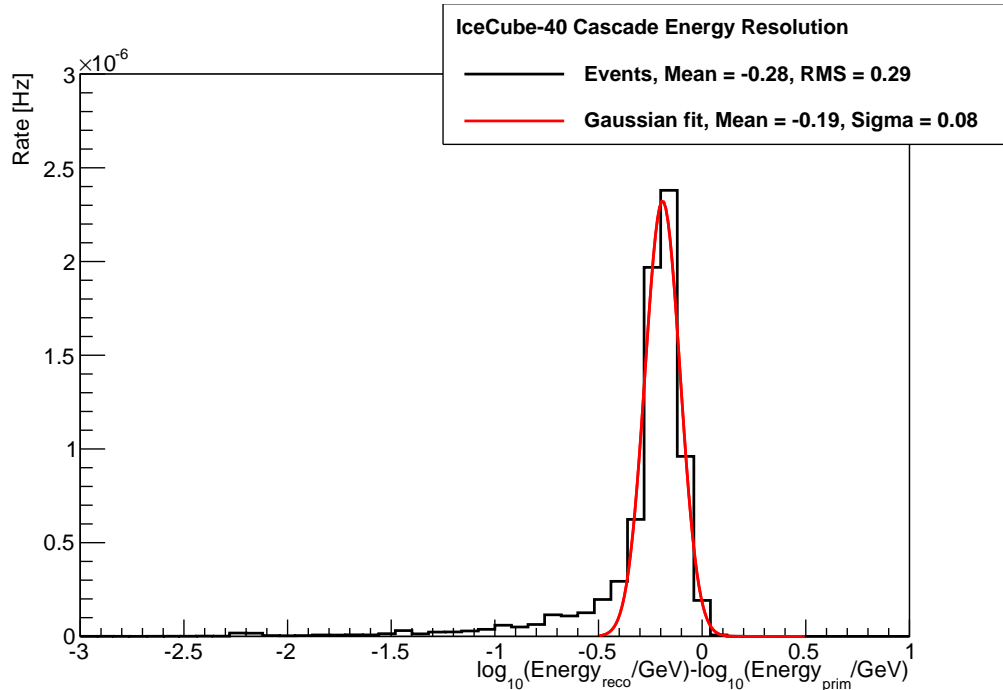


Figure 4.1: Energy resolution from Credo reconstruction. The red line is a Gaussian fit to the data which gives a resolution value of 0.08 in $\log(\text{Energy})$.

There have been two prior diffuse cascade searches using IceCube when 22 strings were deployed. These searches set a limit of $3.6 \times 10^{-7} \text{ GeVsr}^{-1}\text{s}^{-1}\text{cm}^{-2}$ on an E^{-2} spectrum of astrophysical neutrinos [7], assuming a flavour ratio of 1: 1: 1. This limit is over the energy range of 24 TeV to 6.6 PeV and was the best all-flavour limit on an E^{-2} spectrum diffuse flux at the time of the analysis presented in this work.

4.1 Method

All of the neutrino events detected so far by IceCube are consistent with being atmospheric muon neutrinos. Atmospheric cascades are also expected and recent evidence for these events has strengthened using the IceCube and DC combined detectors. Atmospheric muon neutrino events and atmospheric cascade events make up the background in a high energy diffuse cascade analysis. The analysis consists of cuts, done at different filter levels, on reconstructed event variables designed to distinguish between the background events and signal events.

The atmospheric background arising from muons is easier to reject in a cascade analysis compared with muon neutrino analysis. This is because muon events have

distinct track-like distributions of light detected compared to that of the cascade events which are more spherical. Atmospheric muon events can be rejected using cuts based on the shape of the event as well as the speed and direction of the track reconstruction.

The atmospheric neutrino background is harder to reject in a high energy cascade analysis because there is no distinction in the topology of the two types of events. However, the astrophysical neutrino flux energy spectrum is most likely harder than the energy spectrum from atmospheric neutrinos. The superior energy resolution expected for cascades means that the break in the energy spectrum due to the transition from atmospheric neutrinos to astrophysical spectrum neutrinos should be easier to observe compared to a muon analysis.

The backgrounds arising from atmospheric muons and atmospheric neutrinos contained within the experimental data are many orders of magnitude above the rate of cascades arising from astrophysical sources. These backgrounds are simulated in order to develop filter cuts to reject them from the analysis dataset and to estimate the remaining background on which a signal will be observed.

To meet the simulation requirements many events are needed over a large energy range. To fulfil this requirement weighted simulations are performed as well as unweighted. For unweighted simulation the weight for each event is equal to one and the time for event generation is

$$T_j = \frac{N^{\text{gen}}}{A^{\text{sum}} F^{\text{sum}}}, \quad (4.1)$$

where N^{gen} is the number of generated events, A^{sum} is the simulation area integrated over solid angle, and F^{sum} is the energy integrated flux

$$F^{\text{sum}} = \int_{E_{\text{min}}}^{E_{\text{max}}} dE \Phi(E), \quad (4.2)$$

with flux $\Phi(E)$. To improve statistics for interesting events weighted simulation datasets are under- or over-sampled at different energies using a varying power law constant δ . A modified flux $\Phi'(E)$ is generated which is biased by a factor of E^δ

$$\Phi'(E) \propto \Phi(E) E^\delta. \quad (4.3)$$

An energy independent event weight w_i is then assigned to each event to cancel the extra factor of E^δ

$$w_i(E) \propto E^{-\delta}. \quad (4.4)$$

The power law constant can be defined such that the weight of each event is dimensionless

$$w_i(E) = \left(\frac{E_0}{E} \right)^\delta \quad (4.5)$$

where E_0 is some reference energy. This allows background events over all energy ranges to be simulated at the necessary rates across a wide range of energies.

After event generation, the propagation of particles and the detector response are simulated. The simulation is then treated identically to the experimental data. Using the background simulation, the all flavour neutrino simulation, and a portion of the data, a full set of analysis cuts are developed. The analysis cuts at the final level aim to reject the remaining background events to isolate high energy astrophysical cascade events within the IceCube-40 experimental data.

4.2 Data

The experimental data used in this analysis is from the IceCube detector when 40 IceCube strings were deployed and operational. The detector configuration of IceCube-40 is shown in Figure 4.2. The IceCube-40 data is split into runs of eight hours or less. Each run is classified as a “physics” run if the purpose for data collection was not for calibration or verification. Each run is classified as “good” if it fulfils a basic set of criteria dependent on the length and human monitoring of the run. Runs are removed if they are shorter than 10 minutes in duration, or have been flagged as having problems from their monitoring. The first IceCube-40 good physics run was taken on 6th April 2008 and the final on 20th May 2009. This dataset has 1472 runs and a duration of 373.6 days of livetime. The AMANDA detector was also running during this period. The data received from the AMANDA *Optical Module* (OM) require special treatment because their information is in analog format rather than digital. The AMANDA data is not used in this cascade analysis. However, a combined cascade analysis of the IceCube-40 and AMANDA data was performed in a search for an atmospheric neutrino flux [122].

When conducting an analysis on such a large quantity of data there is always a risk of finding false positives. To reduce this risk numerous signal and background simulations were run. Cuts were developed using the simulation and a sample of 10% of the data. The remaining 90% of the data was “blinded” until all cuts were finalised. The 10% of the data used to develop the cuts is referred to as the burn sample. In this analysis the burn sample is defined by run numbers ending in a zero and consists of 144 runs with a total duration of 36.36 days livetime.

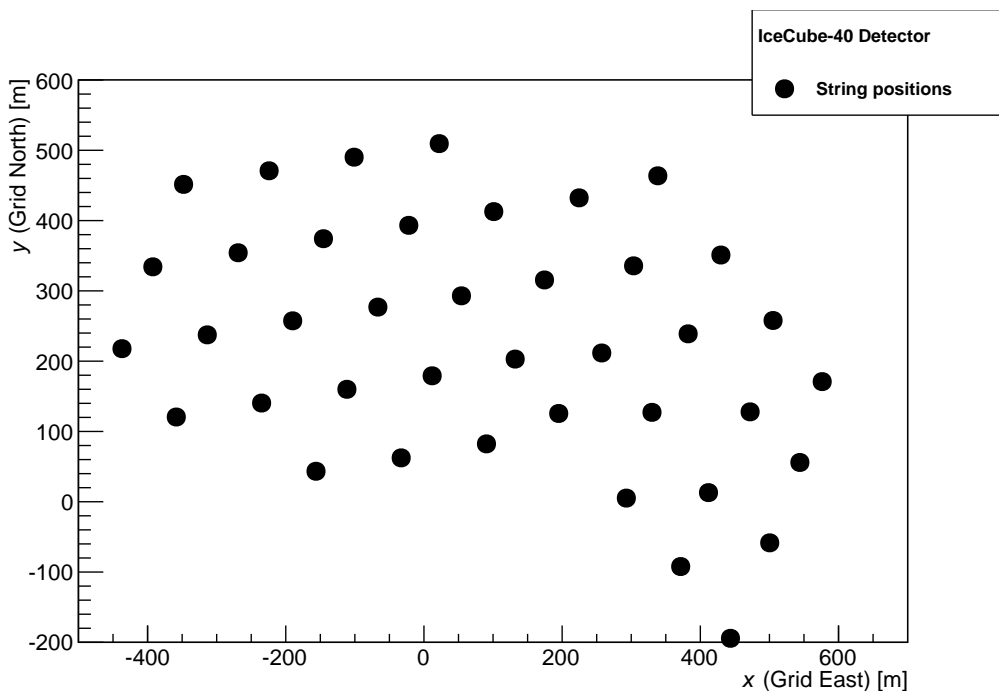


Figure 4.2: IceCube-40 detector configuration. The xy -coordinates of the string locations are shown where they are deployed in the ice.

4.3 Simulation

Monte Carlo data is used throughout analyses for both signal and background estimates. Neutrino and muon events are simulated. Neutrino events are generated from all-flavour neutrino interactions and muon events are generated from atmospheric cosmic-ray simulations. The particles are propagated through the detector and their interactions simulated. The Cherenkov light yield from the charged particles is calculated and properties of the ice are used to estimate the amount of light arriving at each DOM. The record of the event includes this information and the detector response.

The software framework used for IceCube event generation, detector simulation, and event reconstruction is called IceTray [46]. The following sections describe neutrino simulation, cosmic-ray background simulation, light propagation, and the detector response.

4.3.1 Neutrino simulation

Interactions, both CC and NC, of all flavours of neutrinos are simulated to model signal and backgrounds. Examples of the CC event topologies, as described in section 2.2.1 are shown in Figure 4.3.

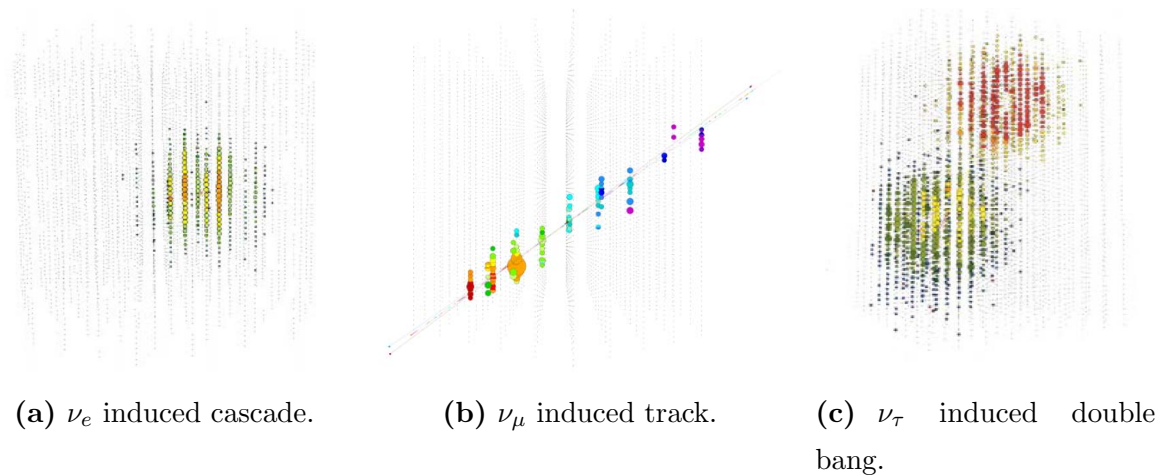


Figure 4.3: Neutrino event topologies in IceCube, taken from [20]. The simulated *Charged-Current* (CC) neutrino interactions are: a 375 TeV electron neutrino, a 10 TeV muon neutrino, and a 1 PeV tau neutrino. The grey dots are DOMs on the IceCube strings, the coloured dots are the hit DOMs. The sizes represent the amount of charge deposited and the colours represent the timing.

The neutrino event generator use Monte Carlo techniques. The simulation program used is called Neutrino Generator and is based on the program *All Neutrino Interaction Simulation* (ANIS) [61] which was originally developed for AMANDA simulations. The neutrinos are produced isotropically over the Earth’s surface and then propagate to interact in or near the detector volume. The *Coordinated Theoretical-Experimental project on QCD* (CTEQ) 5 [97] model is used for the neutrino cross-sections.

The cascade simulation inside the detector is handled by the *Cascade Monte Carlo* (CMC) program [133]. For electromagnetic cascades the total length from all particles in the cascade is proportional to the energy of the cascade. The treatment of hadronic cascades is more difficult than that of electromagnetic cascades. The slow neutral particles such as neutrons and the dissipation of energy into hadronic processes means that the track length does not scale linearly with energy as for electromagnetic cascades. The total light output in a hadronic cascade is lower compared to an electromagnetic cascade. However the light output can be parameterised by the difference in the total track lengths $F = T_{\text{hadronic}}/T_{\text{electromagnetic}}$ as a function of the energy of the incident particle [133]. The energy of an hadronic cascade is scaled to that of an electromagnetic cascade in simulation algorithms so that both types of events can be handled using the same simulation tools.

For low-energy cascades, of less than 1 TeV, the event is treated as an anisotropic point source. For high-energy cascades, of greater than 1 TeV, the event is split into

several smaller cascades along the longitudinal directional of the cascade. The energy distribution is calculated using a parameterisation [137]. Above energies of 1 PeV the *Landau-Pomeranchuk-Midgal* (LPM) effect [98] is taken into account by reducing bremsstrahlung and pair production interaction cross-sections.

Table 4.1 gives a summary of the neutrino simulation used in this analysis.

Spectrum	Approximate number of generated events	Energy range (GeV)
Electron neutrino	4.0×10^6	10^1 – 10^{10}
Muon neutrino	6.0×10^6	10^1 – 10^{10}
Tau neutrino	1.5×10^7	10^1 – 10^{10}

Table 4.1: Simulation of neutrino events.

In this analysis the signal arises from the combined flux from many astrophysical neutrino sources. The spectrum for these sources is assumed to have an E^{-2} dependency. The neutrino background for this search is from atmospheric neutrinos. Fundamentally the neutrino events for signal and atmospheric background are not simulated differently, the only difference arising from their energy distributions which are drawn from the appropriate model spectrum. The conventional atmospheric neutrino spectrum can be drawn from either the Bartol [27] or Honda [85] models and prompt atmospheric neutrino spectrum from either the Naumov [111] or Sarcevic [49] models. The atmospheric neutrino background in this analysis are assumed to arise from the Bartol model [27] for conventional atmospheric neutrinos and the Sarcevic model [49] for prompt atmospheric neutrinos.

4.3.2 Background muon simulation

The dominant background in this analysis comes from atmospheric muons that are created in air showers due to cosmic-ray interactions in the Earth’s atmosphere. These air showers are simulated using Monte Carlo techniques with a modified version [39, 40] of *COsmic Ray Simulations for KAscade* (CORSIKA) [73]. The interaction models used are Gheisha and QGSJET-II [112], and primary energy spectra are simulated from the polygonato model [84]. The polygonato model uses different energy spectra according to the primary element of the cosmic-ray. The elements are grouped by

atomic mass and six different energy spectra are simulated. These spectra are for the mass groups: protons ($A = 1$), helium ($A = 2$), lithium to fluorine ($A = 3-9$), neon to chromium ($A = 10-24$), manganese to cobalt ($A = 25-27$), and nickel to uranium ($A = 28-92$). This model is shown in Figure 4.4. Air showers resulting from cosmic rays up to a primary energy of 10^{20} eV are simulated in CORSIKA. The model used for hadronic interactions is SIBYLL [50, 55].

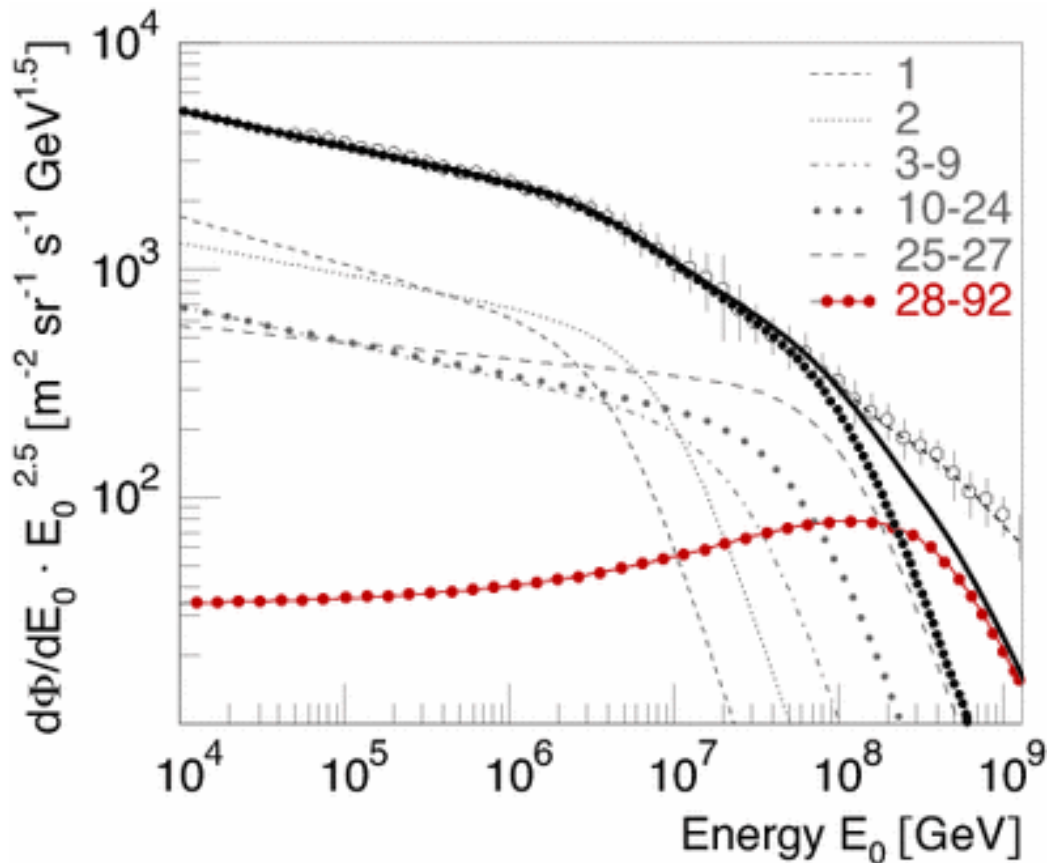


Figure 4.4: Polygonato model, from [84], used to describe the cosmic ray composition for background simulation in CORSIKA. The different energy spectra arise from groupings based on the elemental masses. The six groups are: protons ($A = 1$), helium ($A = 2$), lithium to fluorine ($A = 3-9$), neon to chromium ($A = 10-24$), manganese to cobalt ($A = 25-27$), and nickel to uranium ($A = 28-92$).

After the generation of muons from showers using CORSIKA, the muons are propagated through the ice to the detector volume. The energy losses the muons undergo as they travel through the ice are bremsstrahlung, pair production, multiple scattering, and ionization [110] as described in section 2.2.1. The propagation of muons (and taus) through the detector and their energy losses are simulated using a program called *Muon Monte Carlo* (MMC) [38].

Coincident muon events, those with two or three muons travelling through the detector simultaneously, need to be simulated because the IceCube-40 detector is large enough that simultaneous background events have a significant probability of occurring. To simulate coincident events two or three single muon events, in which at least one DOM was hit, are combined. The events are combined using a Poisson probability

$$P(n, f\tau) = \frac{(f\tau)^n e^{-f\tau}}{n!} \quad (4.6)$$

where f is the rate of n events in a time window τ . This probability is the coincident weight W^C . For the IceCube-40 detector the ratio of coincident weights for single, double, and triple muons is approximately

$$W_{\mu_{\text{single}}}^C : W_{\mu_{\text{double}}}^C : W_{\mu_{\text{triple}}}^C = 0.9325 : 0.1298 : 0.0075. \quad (4.7)$$

A limited amount of CORSIKA air showers can be produced because their production is constrained by available computing facilities and data storage. For the IceCube-40 detector approximately 7 days of single unweighted muon background from CORSIKA simulations were produced. At high filter levels in the analysis only the most “signal-like” background events survive. If these events only occur once in tens or hundreds of days the simulation, constraints mean they are difficult to produce for the background estimation. Due to the large amount of simulation that is required for this analysis, unweighted and weighted datasets are produced using the weighting method described in section 4.1.

In addition to the unweighted and weighted polygonato datasets, further two-component datasets are produced using the Glasstetter model [63]. The polygonato model assumes cosmic-rays to be composed of all elements up to uranium, however CORSIKA only simulates cosmic-ray primaries up to iron. Elements beyond iron start to contribute to the cosmic-ray spectrum above primary energies of approximately 50 PeV and this fraction of the cosmic-ray flux is ignored in polygonato CORSIKA simulations. The most difficult background to simulate in a high-energy cascade analysis is the highest energy muons arising from high-energy cosmic-rays. In order to circumvent this problem the two-component model is used which assumes the cosmic-ray flux is composed of only proton and iron elements. The energy spectra of these elements was fitted to data taken from the *KArlsruhe Shower Core and Array Detector* (KASCADE) array and is called the Glasstetter model. The Glasstetter model is shown in Figure 4.5.

Initially a two-component dataset of approximately 1.2×10^9 proton events and 1.2×10^9 iron events was used in this analysis. After the analysis was complete a further

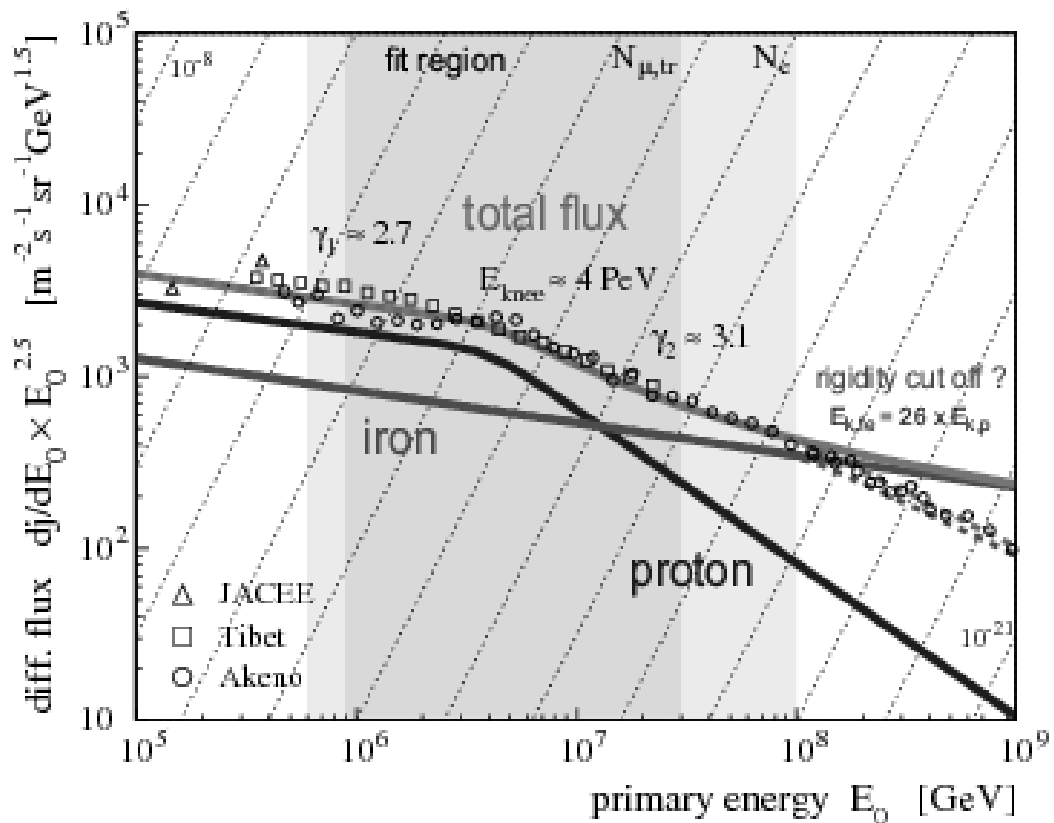


Figure 4.5: Two-component Glasstetter model from [63]. The energy spectra arise from proton and iron primary particles.

dataset of proton only events with the Glasstetter energy spectrum was used to give a more robust estimation of the background. Protons were used as the primary particle for this additional muon background simulation because the background contribution from them was found to be the deficient component in the simulations. The requirement and effect of the additional proton only CORSIKA is described in section 6.2.

Table 4.2 gives a summary of the muon background simulation used throughout this analysis. The livetime of the weighted muon background datasets is dependent on the analysis cut values and the remaining event weighting. The effective livetime of the weighted muon background datasets therefore can not be calculated until the analysis is complete. This calculation is shown in section 5.7.3.

4.3.3 Light Propagation

Photon propagation is simulated using PHOTONICS, a photon tracking Monte Carlo package [108]. PHOTONICS assumes a planar ice structure and uses five free parameters in simulation. These free parameters are

Spectrum	Approximate number of generated events	Livetime
Unweighted single muons	2.3×10^{10}	6.7 days
Unweighted double muons	7.9×10^9	16.5 days
Unweighted triple muons	1.2×10^9	43.4 days
Weighted single muons	8.4×10^9	-
Weighted double muons	5.7×10^8	-
Two-component iron	1.2×10^9	-
Two-component proton	1.2×10^9	-
Two-component additional proton	2.9×10^{11}	-

Table 4.2: CORSIKA simulation of muon background events.

- z -position of the source
- z -position of the DOM
- distance from the source to the DOM
- angle between the source and the DOM
- zenith direction of the source

PHOTONICS then calculates the photon flux and time distributions in the ice surrounding the light source [101] for both muon and cascade events. It produces tables that describe the distribution of photons for the light source at each location in the detector. Scattering and absorption are taken into account during the photon propagation through the ice.

For a moving background or signal event the photon flux distributions are integrated over for many point-like Cherenkov emitters. Both Cherenkov showers and Cherenkov cone emitters are simulated for the varying event topologies of cascades and tracks observed in the detector.

4.3.4 Detector Simulation

Once photons have been propagated using PHOTONICS the DOM electronic response is simulated accounting for DOM-to-DOM variations such as their orientation and detection efficiency. The probability of photon detection is calculated given each DOM efficiency. DOM mainboard electronics are simulated including the PMT saturation, input discriminator, *flash Analog-to-Digital Converter* (fADC), *Analog-to-digital Transient Waveform Digitizer* (ATWD), and local coincidence logic.

For each event hits are created in DOMs by the HitMaker module within the IceTray software. This program loops over all DOMs and creates the hit pattern for the event. The trigger logic is simulated and events that do not fulfil the trigger conditions are rejected.

4.4 Reconstruction

The term reconstruction is used to describe a range of analysis algorithms. Some of these seek to reconstruct the physical quantities related to the neutrino which is assumed to have initiated the event. For example the algorithms attempt to determine the vertex location, the time of the neutrino interaction, and the energy and direction of the incoming neutrino. Other algorithms within the reconstruction framework calculate quantities describing the detected light distribution. These quantities can be used to determine the topological parameters of the event to distinguish between signal and background.

In this section the preliminary algorithms that are applied to all events in a cascade analysis are described. More advanced algorithms will be described in the next chapter when the reconstructed cut variables are used in the analysis filter levels.

The photon hits from each event are sent to the surface of the detector in the form of digitized waveforms as described in section 3.2.1. The first step in the reconstruction phase is feature extraction of the photon hits from the waveforms. The feature extractor and DOM calibrator combines the information from each ATWD channel and calibrates them against each other obtaining the timing, charge, and width of each pulse from an event. The voltage arising from the photon hits in each event is then calculated from the PMT pulses.

The preliminary reconstruction which is performed on each event is called CFirst. The initial step in CFirst is to calculate the *Centre Of Gravity* (COG). This is a

quantity that indicates centre of the light distributions and is calculated analogous to the classical mechanical COG with the pulse amplitudes recovered from the DOMs acting as the “masses”. The location of each DOM \mathbf{r}_i gives the position for the “mass”. The COG quantity is then calculated using the summation over all hit DOMs

$$\mathbf{COG} = \sum_{i=1}^N A_i^w \mathbf{r}_i \quad (4.8)$$

where A_i is the amplitude from the i^{th} PMT and w is an amplitude weight power which can be used to give the light hits a “mass”. In the case of the CFirst algorithm $w = 0$ so the amplitudes of the hits are not taken into account in this preliminary calculation for the COG. The result is used as a seed for more accurate reconstruction algorithms.

Once the COG has been calculated the CFirst algorithm calculates a number of parameters related to the timing of the hits recovered by the DOMs and estimates the time of the neutrino interaction. The time residual τ_i of each DOM as a function of the vertex time t_v is

$$\tau_i(t_v) = t_i - \left(t_v + \frac{d_i}{c_n} \right) \quad (4.9)$$

where $d_i = |\mathbf{COG} - \mathbf{r}_i|$, t_i is the DOM hit time, and c_n is the speed of light in ice. A direct hit is defined as one in which the time residual satisfies $0 < \tau_i < 200$ ns. The CFirst algorithm uses only DOMs located in a sphere of 100 m around the COG to find a trial vertex time

$$t_v = t_i - \left(\frac{d_i}{c_n} \right). \quad (4.10)$$

For each DOM the number of direct hits from other DOMs is also calculated. The vertex time is chosen to be the earliest time such that the number of direct hits is greater than the number of triggered hits, which is 8 DOMs hit for the IceCube-40 trigger.

A quantity t_{max} is also calculated, this is the vertex time that would result in the most direct hits. t_{max} is not uniquely defined; different times could yield this same maximum number of direct hits. The IceTray implementation of CFirst chooses t_{max} to be the earliest such time.

The number of early hits is calculated by CFirst. An early hit is defined as a hit that falls within a time window earlier than would be possible for light travelling from the COG. If the trigger condition (described in section 5.1) is not met for any vertex time a fallback algorithm is used. The fallback algorithm takes the vertex time to be equal to the earliest hit time for hits within a sphere centered around the COG. Two radii are used; first a smaller radius and then, if there are no hits within the smaller

sphere, a larger radius. The results from the CFirst module are used as seeds for all subsequent algorithms that calculate the event parameters.

The cascade reconstruction algorithm which is used most in this analysis is called Credo [106] which is a PHOTONICS based reconstruction. It is a 7-dimensional algorithm that uses a minimiser from within the IceTray framework [106]. An iterative approach is used where the expended computational time of high-iteration calculations results in better cascade variable reconstruction resolutions, especially in the calculation of the direction and energy of the neutrino compared to previous cascade reconstruction methods.

Credo uses light distributions determined by the PHOTONICS package which was described in section 4.3.3. It incorporates the ice model using the PHOTONICS tables and uses the full timing information by considering each individual pulse. Credo was developed specifically for cascade event reconstruction and calculates variables from neutrino-induced cascades including the direction and energy of the incident neutrino. The one-iteration and four-iteration Credo reconstruction resolutions of the cascade variables used in this analysis will be shown in section 6.4.

Chapter 5

Event Selection Criteria

In this chapter the filter levels of the analysis are presented. The data collected by the IceCube detector is dominated by atmospheric muons and is processed in stages to progressively remove this background. At each stage cuts are made based on event characteristics chosen for their ability to discriminate between background and signal. An ideal characteristic would have different values for background and signal. There are no such ideal characteristics and, for any given quantity, its value serves as an indication of whether the event is more likely to be signal than background. This means that cuts will remove both background and a portion of the signal. In the first stages of the filter levels the guiding principle is to reduce the experimental data to a rate for which it is feasible to run more computationally expensive reconstructions. These reconstructions have improved cut variable resolutions and return cut variables with higher discriminating power used at subsequent filter levels.

The data analysed in cascade analyses start with the trigger conditions and pole filter, which are carried out on site at the detector. This is followed by event selection cuts performed after the data has been transferred via satellite to the Northern hemisphere. These cuts are called level 3 cuts and are global to all cascade analyses. Beyond level 3, analyses separate to focus on specific energy regions. For an overview of the other IceCube-40 cascade analyses see References [89, 107, 114, 122]. The high-energy analysis described in this thesis consists of three additional cut levels; level 4 which reduces background to a manageable level necessary to run iterative reconstruction algorithms, level 5 in which containment cuts are performed and machine learning algorithms are run, and level 6 which is the final level of cuts optimised on the machine learning responses and event energy.

In the final section of this chapter the expected number of events in experimental

data, signal, and background after unblinding are presented. A comparison of the number of atmospheric neutrino events expected from different atmospheric neutrino models is shown.

The histograms displayed throughout this chapter show the distributions for the cut variables at each level. The burn sample of the experimental data is shown by the black line. Single, double, and triple muon events are shown by the blue lines. The combined muon background is shown by the red line. The single, double, and triple coincident events are combined using the coincident weighting scheme as is described in section 4.3.2. At early filter levels neutrino events are shown for only electron neutrino interactions. The atmospheric electron neutrino background is shown by the yellow line, and the E^{-2} spectrum electron neutrino signal events is shown by the magenta line. At filter level 6 the simulated muon neutrino and tau neutrino events are introduced. For an E^{-2} spectrum muon and tau neutrino signal events are shown by the green lines. At this filter level the atmospheric muon background also changes. This background is still simulated using CORSIKA, however the cosmic-ray spectrum and composition model used changes from polygonato to two-component as described in section 4.3.2. The muon background distributions are still shown by the blue lines and the combined muon background by the red line.

5.1 Trigger Level

There are several trigger conditions, some of which must be satisfied for the event information to be captured and sent to the detector surface for further processing. The trigger requirement for the IceCube-40 cascade physics stream is called the *Simple Multiplicity Trigger* (SMT). This trigger requires that eight DOMs are “hit” within a 5000 ns time window. A DOM is “hit” if it detects light above its threshold. A waveform is produced, of photons versus time, for the event. The hit is sent to the surface of the detector if it meets the local coincidence criteria. Local coincidence requires that a neighbouring DOM on the same string, either one DOM above or one DOM below, also detected light within the local coincidence time window of ± 1000 ns for IceCube-40. DOMs that detect light but have no local coincidence with their neighbouring DOMs are considered to be noise hits and the hit is not stored or sent to the surface as part of the event. The data rate for IceCube-40 from the trigger level is approximately 1500 Hz. This rate largely arises from background atmospheric muons.

Once at the surface of the detector the data is converted from the *Processing and*

Filtering (PnF) format, to the online IceCube (i3) format used in the analysis. This format of data has “frames” which contain event information. Geometry, calibration, and detector status information are also added to frames in the i3 data:

- Geometry

The detector geometry frame contains information on the position and azimuthal orientation of every DOM involved in the run.
- Calibration

The detector calibration frame contains information on the settings of each DOM, such as baselines and saturation levels.
- Detector Status

The detector status frame contains information on the settings of the detector during the run, including the trigger mode, local coincidence window, and internal DOM threshold settings.

5.2 Pole Filter

The pole filter is run on the experimental data at the detector at the South Pole. It is designed to cut a large part of the background while keeping the majority of the signal from the trigger level for more sophisticated processing. Each run is scanned and non-operational DOMs are removed from the event information, followed by calibration of the event waveforms. The calibration involves aligning the timing of waveforms, correcting for saturation in large hits, correcting the baseline, and correcting pedestal droop¹ in the waveform. Hits are then created using the feature extraction algorithm. This algorithm extracts the arrival times of the photons from the recorded waveforms in the PMTs and writes them into a pulse series which is used throughout the rest of the analysis. Hit cleaning is also undertaken which removes early or late hits that are unlikely to belong to the events. Early and late hits are defined as hits that are not within a 6 μ s time window of the calibrated event.

Using the calibrated, extracted, and cleaned data, reconstructions algorithms are run on each event to obtain parameters which are used for the pole filter cuts. The

¹Pedestal droop occurs when waveform shapes are distorted by transformer droop between the PMT and the *High Voltage* (HV) board in the DOM. This occurs because the toroid coupling effectively acts as a high-pass filter on the PMT output, which makes the tails of the waveforms “droop” and even undershoot. The effect is temperature dependent, growing worse at lower temperatures, and is corrected for during calibration.

pole filter consists of two cuts placed on variables, the line-fit velocity and the tensor of inertia eigenvalue ratio. These variables are described in sections 5.2.1 and 5.2.2. The pole filter reduces the data rate by approximately two orders of magnitude to 16 Hz. This reduction makes it possible, given the bandwidth limitations, for the data to be transferred from the South Pole for further analysis.

5.2.1 Line-fit Velocity

The line-fit velocity variable is a quantity which aims to characterise the speed at which the light from an event passes through the detector. It seeks to exploit a basic difference between cascade events and muon events, that is, the Cherenkov light from a cascade is produced in a small region whereas a muon travels a long distance through the detector at speeds close to c . The Cherenkov light produced in a cascade originates from a small region since the total length of the cascade is not significant when compared with the distance between the IceCube strings. Although originally the light distribution is a Cherenkov cone, determined by the direction of the cascade, scattering causes it to disperse throughout the medium and evolves to have a more spherical shape. In this way the effects of the cascade development is diminished and the light distribution is similar to that from a stationary source. In contrast, for muon events where the light source is moving through the detector at a speed close to c , the Cherenkov light front propagates through the detector, also at a speed close to c .

The line-fit velocity reconstruction fits a straight line for the light source based on the DOM hit times. Using this fit an average speed, as a fraction of c , for the event is calculated. This is the speed that the Cherenkov light has appeared to travel through the detector along the direction of the fit. Cascade events are expected to have a line-fit velocity close to zero and muon events are expected to have larger values of line-fit velocity.

For a given event the line-fit velocity algorithm ignores the geometry of the Cherenkov cone and the optical properties of the ice, and assumes photons are travelling on a wave-front perpendicular to a track with velocity V along a one-dimensional path. Using the DOM locations \mathbf{r}_i and hit times t_i the free parameters velocity \mathbf{v} and vertex location \mathbf{r} are calculated so that

$$\mathbf{r}_i = \mathbf{r} + \mathbf{v}t_i \tag{5.1}$$

is minimised. By differentiation with respect to the free parameters the vertex location

and average velocity of the event as a fraction of the speed of light are calculated:

$$\mathbf{r} = \langle \mathbf{r}_i \rangle - V \langle t_i \rangle \quad (5.2)$$

$$V = \frac{\langle \mathbf{r}_i t_i \rangle - \langle \mathbf{r}_i \rangle \langle t_i \rangle}{\langle t_i^2 \rangle - \langle t_i \rangle^2} \quad (5.3)$$

where $\langle \mathbf{r}_i \rangle$ is the amplitude weighted average on \mathbf{r} and $\langle t_i \rangle$ is the amplitude weighted average on t . The direction of travel e is obtained from

$$e = \frac{\mathbf{v}}{|\mathbf{v}|}. \quad (5.4)$$

The zenith θ and azimuth ϕ directions of the track can then be calculated with

$$\theta = \arccos \left(-\frac{v_z}{|\mathbf{v}|} \right), \quad \phi = \arctan \left(\frac{v_y}{v_x} \right). \quad (5.5)$$

The line-fit distributions for simulated background and signal events are shown in Figure 5.1. The line-fit velocities for neutrino events are peaked closer to zero than those of background muon events. The line-fit velocity cut for the IceCube-40 cascade stream requires the event velocity to be less than $0.13c$ which can also be seen in Figure 5.1 where all the distributions cut off.

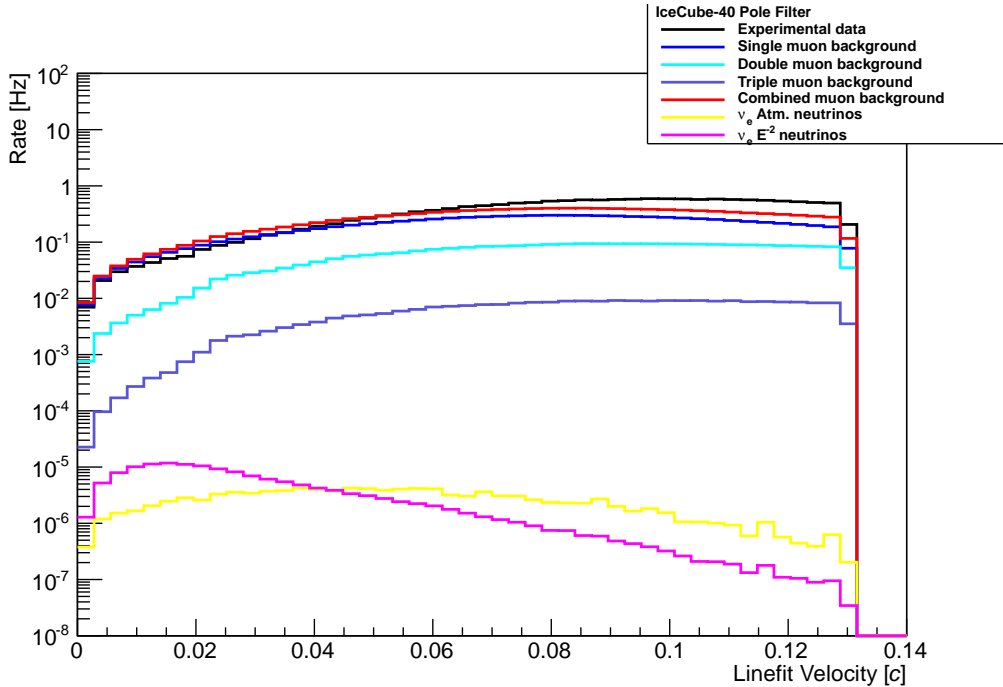


Figure 5.1: Reconstructed velocities, in units of c , from a line-fit to the timing of the hit DOMs. The effect of the pole filter cut is seen where the experimental data, muon background, and neutrino signal cut off at $0.13c$.

5.2.2 Tensor of Inertia Eigenvalue Ratio

In IceCube, tensor of inertia quantity is a reconstruction algorithm *analogous* to the classical mechanics tensor of inertia. In this analogy the distribution of light detected by the DOMs plays the role of the “mass” distribution. As described above the defining characteristic of cascade events is that the Cherenkov light is emitted over a small region compared to the IceCube string spacing. After scattering this means that the light distribution is approximately spherical while the light distributions from muon events is elongated. The eigenvalues of the tensor associated with the light distribution corresponds to finding values for the lengths of the distributions along the three principal axes. The eigenvalue ratio is the ratio of the lowest eigenvalue to the sum of all three eigenvalues. This quantity is a measure of how spherical the light distribution is. A perfectly spherical event would have all three eigenvalues equal and the eigenvalue ratio would be $\frac{1}{3}$. Track-like events are elongated and so have an eigenvalue ratio approaching zero. The smallest eigenvalue of the tensor of inertia corresponds to the longest axis, which approximates the background muon track length if the smallest eigenvalue is much smaller than the other two eigenvalues.

The centre of gravity is calculated using equation (4.8) in section 4.4. For the tensor of inertia algorithm the amplitude weight power in this equation is set to $w = 1$ so the pulse amplitudes of the PMTs are treated as equal virtual “masses”. The tensor of inertia matrix $I^{k,l}$ has indices k and l which each run over the three orthogonal directions x , y , and z . The index i runs over all DOMs hit in the event and the 3×3 tensor of inertia matrix is given by

$$I^{k,l} = \sum_{i=1}^N A_i^w (\delta^{k,l} \mathbf{r}_i^2 - r_i^k r_i^l) \quad (5.6)$$

where N is the number of hit DOMs in the event, A_i is the pulse amplitude of the i^{th} DOM, and \mathbf{r}_i is the distance of the i^{th} DOM from the COG. The eigenvalues of an event I_1 , I_2 , and I_3 can be found by diagonalizing this tensor and are ordered so that $I_1 \leq I_2 \leq I_3$. An event’s eigenvalue ratio q is the ratio of the smallest eigenvalue to the sum of all three eigenvalues

$$q = \frac{I_1}{I_1 + I_2 + I_3}. \quad (5.7)$$

The tensor of inertia eigenvalue ratio distributions for simulated background and signal events are shown in Figure 5.2. It can be seen that the eigenvalue ratios for neutrino events are peaked at approximately $\frac{1}{3}$, whereas ratios for the background muon events increase towards smaller values. The eigenvalue ratio cut requires that

the event have an eigenvalue ratio of greater than 0.12 to exclude track-like events. This cut can also be seen in Figure 5.2.

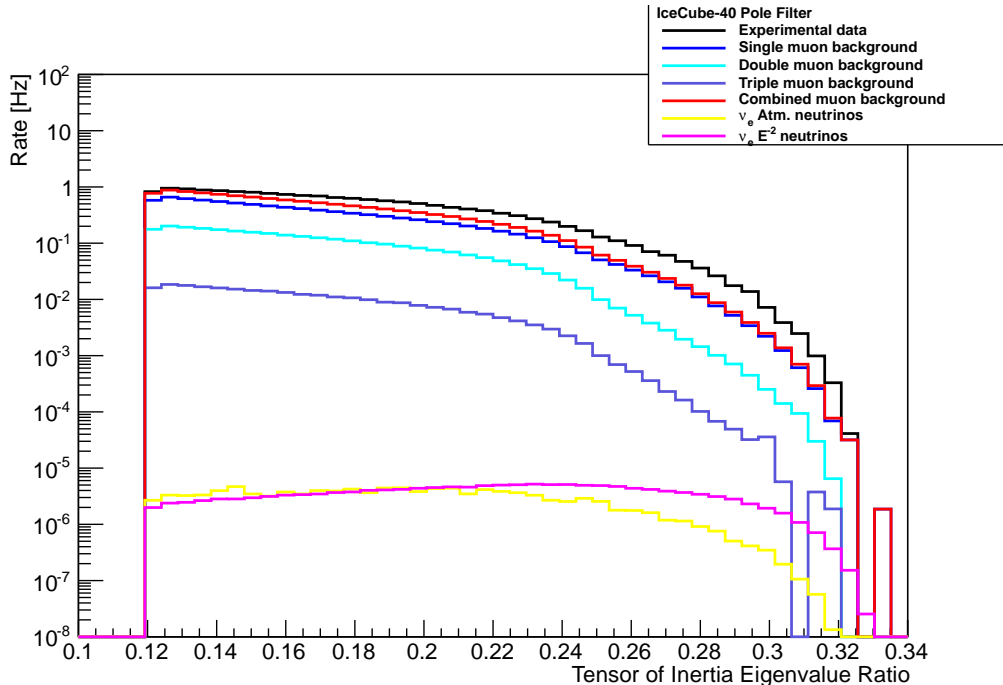


Figure 5.2: Reconstructed eigenvalue ratio from tensor of inertia. The effect of the pole filter cut is seen where the experimental data, muon background, and neutrino signal cut off at 0.12.

5.3 Level 3

This filter aims to further reduce the background rate to a level at which it is possible, within computing time and storage constraints, to run more advanced algorithms. An experimental data rate below approximately 2 Hz is necessary to meet these requirements. The level 3 algorithms calculate variables which will be used in subsequent filtering levels. At level 3 the background is most dominant at lower energies; consequently, to effectively reduce the data while keeping as much of the signal as possible, the filter is only run on events with a reconstructed energy of less than 10 TeV. There are two cuts performed below this energy: a cut on the reconstructed zenith direction variable and a cut on the reduced log-likelihood variable. These cuts reduce the data rate by an order of magnitude to approximately 1.8 Hz.

5.3.1 Zenith

The reconstructed zenith angle is calculated assuming that the event has a track topology. Using this assumption the best fit to the event is found and the zenith direction of the track calculated. The zenith direction is defined so that:

$$\begin{aligned} 0^\circ \leq \text{Zenith} \leq 90^\circ & \quad \} \text{ above the horizon} \\ 90^\circ \leq \text{Zenith} \leq 180^\circ & \quad \} \text{ below the horizon,} \end{aligned} \quad (5.8)$$

For events with reconstructed energies of less than 10 TeV, the zenith cut is placed at 80° removing most track-like events that originate from above the horizon. This value was chosen as it met the requirement to reduce the rate to 2 Hz and is seen in Figure 5.3 which has four panels showing the experimental data, combined muon background, atmospheric spectrum neutrinos, and E^{-2} spectrum neutrinos. The combined muon background includes single, double, and triple atmospheric muon events summed together with coincident weighting as described in section 4.3.2. The energy and zenith cut values are shown by the black lines, where the lower left quadrant in each of the panels corresponds to the region of the parameter space where events are removed.

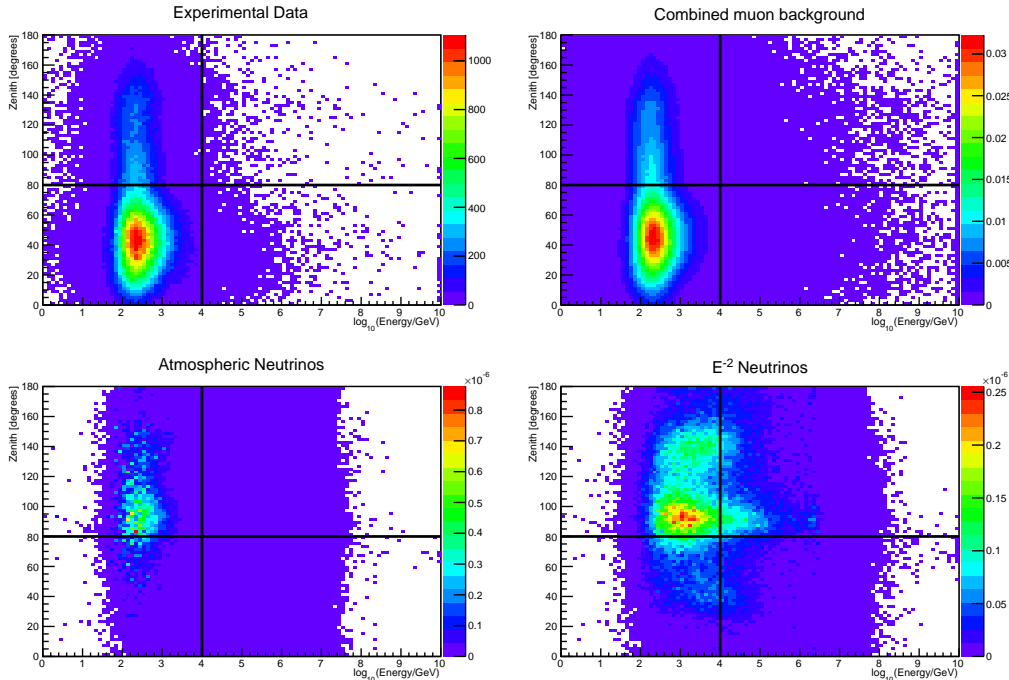


Figure 5.3: Reconstructed zenith direction versus reconstructed energy. The four panels show experimental data, muon background, atmospheric neutrinos, and E^{-2} spectrum neutrinos. The level 3 cuts are shown by the black lines at Zenith = 80° and $\log_{10}(\text{Energy}) = 4.0$. Events in the lower left quadrant of each of the panels are removed.

5.3.2 Reduced log-likelihood

The energy and zenith cuts at level 3 do not reduce the rate of the experimental data by the amount required to run advanced reconstructions. An additional cut is required and a reduced log-likelihood reconstruction is performed and cut on at this filter level after the energy and zenith cuts.

The cascade log-likelihood module calculates a variable which gives the probability of observing the event hit pattern in the detector, assuming the hypothesis of a cascade event. A *probability density function* (pdf) is specified which describes the probability $p(t_i, \mathbf{r}_i; \mathbf{a})$ that a DOM with hit time t_i and position $\mathbf{r}_i = (x, y, z)$ would result from a cascade characterized by a set of parameters \mathbf{a} where the index i runs over the DOMs hit in the event. The cascade parameters used by the minimizer are $(t, x, y, z, \theta, \phi, E)$, where t, x, y, z are the vertex time and position, θ, ϕ are the polar and azimuthal angles of the incident neutrino, and E is its energy. For each event the cascade log-likelihood algorithm passes a list of DOM hits to a minimizer which finds the parameters \mathbf{a} such that the log-likelihood \mathcal{L} gives the maximum probability:

$$\mathcal{L} = \prod_i p_i(t_i, \mathbf{r}_i; \mathbf{a}) \quad (5.9)$$

or equivalently, the minimum negative log-likelihood:

$$-\ln(\mathcal{L}) = -\sum_i \ln(p_i(t_i, \mathbf{r}_i; \mathbf{a})). \quad (5.10)$$

A small value for the log-likelihood indicates consistency with the cascade hypothesis. This variable becomes a reduced log-likelihood \mathcal{L}_r by normalising the log-likelihood [134, Pg.122].

$$\mathcal{L}_r = -\frac{\ln(\mathcal{L})}{N_{\text{DOF}}}, \quad (5.11)$$

where the number of degrees of freedom N_{DOF} is defined as the number of hit DOMs N_{DOM} , minus the number of fitted parameters N_{param}

$$N_{\text{DOF}} = N_{\text{DOM}} - N_{\text{param}}. \quad (5.12)$$

For events with a reconstructed energy of less than 10 TeV and reconstructed zenith direction less than 80° , the cut on the cascade reduced log-likelihood is placed at 10, as shown in Figure 5.4. The neutrino event distributions in this Figure peak at low reduced log-likelihood values around seven and then fall away rapidly, whereas the distribution for muon background events are slower to rise before peaking around reduced log-likelihood values of nine and falling away. The black line vertical line in this Figure

shows the cut at the reduced log-likelihood value of 10. These level 3 cuts all together reduce the experimental data by enough so that advanced reconstruction algorithms can be run for the next filter level.

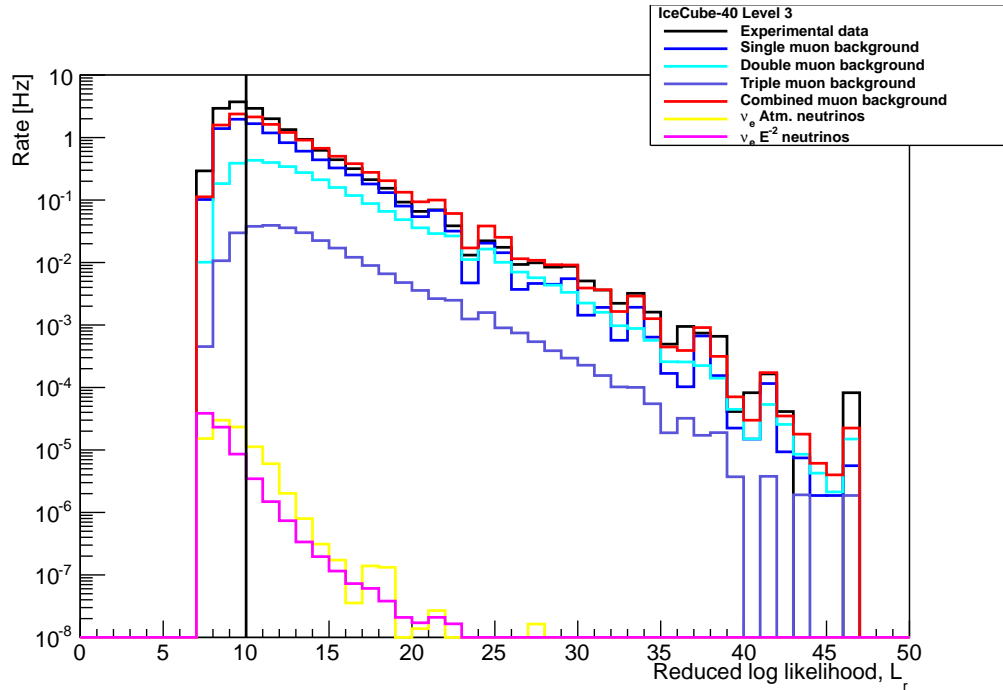


Figure 5.4: Reduced log-likelihood. The level 3 cut is shown by the black line at 10. Events with a reduced log-likelihood value greater than 10 are removed.

5.4 Level 4

The cascade analyses performed on IceCube-40 data diverge after the common level 3 filter in order to focus on specific energy regions. The analysis described in this thesis aims to find evidence for high energy neutrino events. The first cut at this level is therefore an energy cut on the one iteration energy reconstruction calculated at level 3. This is followed by two further cut variables, called spatial distance and fill ratio, whose values were also calculated at level 3. The level 4 cuts reduce the experimental data rate by a further two orders of magnitude to 2.5×10^{-2} Hz.

The reconstructed energy distributions for simulated background and signal events are shown in Figure 5.5. It can be seen that there is an absence of E^{-2} spectrum neutrino events at low energies which is the region that the muon background is most dominant. The level 4 energy cut requires that the event be reconstructed at greater than 2.5 TeV, as shown by the black vertical line in Figure 5.5.

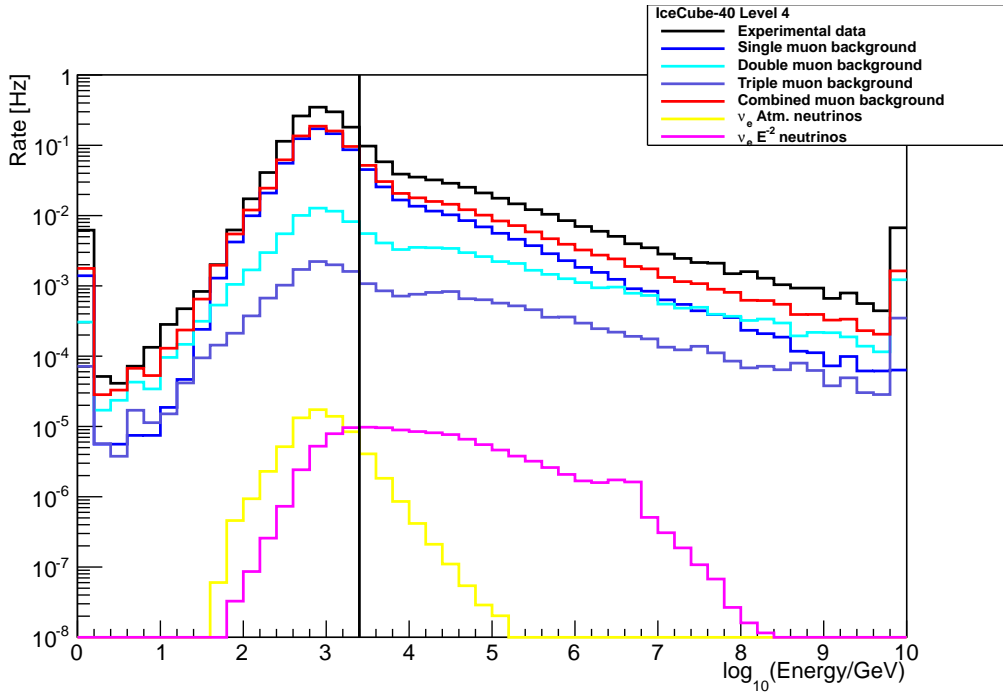


Figure 5.5: One iteration energy reconstruction. The level 4 cut is shown by the black line at 2.5 TeV. Events with a reconstructed energy of less than 2.5 TeV are removed.

5.4.1 Spatial Distance

The next cut performed at level 4 after the energy cut is the spatial distance cut. The spatial distance variable is formed from a split reconstruction run at level 3. In a split reconstruction an event is divided into two parts based on the times of the hits. The first part of the event is then reconstructed using only the first half of the hits and the second part using only the second half of the hits.

Reconstructed quantities using the first part of the hits in the event are denoted by the subscript 1 and reconstructed quantities from the second part of the hits in the event are denoted by the subscript 2. The spatial distance variable SD is formed from the vertex position reconstruction of the two parts of the event and is calculated by

$$SD = \sqrt{(X_2 - X_1)^2 + (Y_2 - Y_1)^2 + (Z_2 - Z_1)^2}. \quad (5.13)$$

If the event is a cascade event, and hence has a spherical hit topology, the vertex positions from each part of the event should reconstruct to the same location in the detector. If the event is a background muon event and hence has a track-like topology, the vertex positions from each part of the event are expected to reconstruct to different locations in the detector. The schematic in Figure 5.6 illustrates how the spatial distance variable is calculated for typical cascade and muon events.

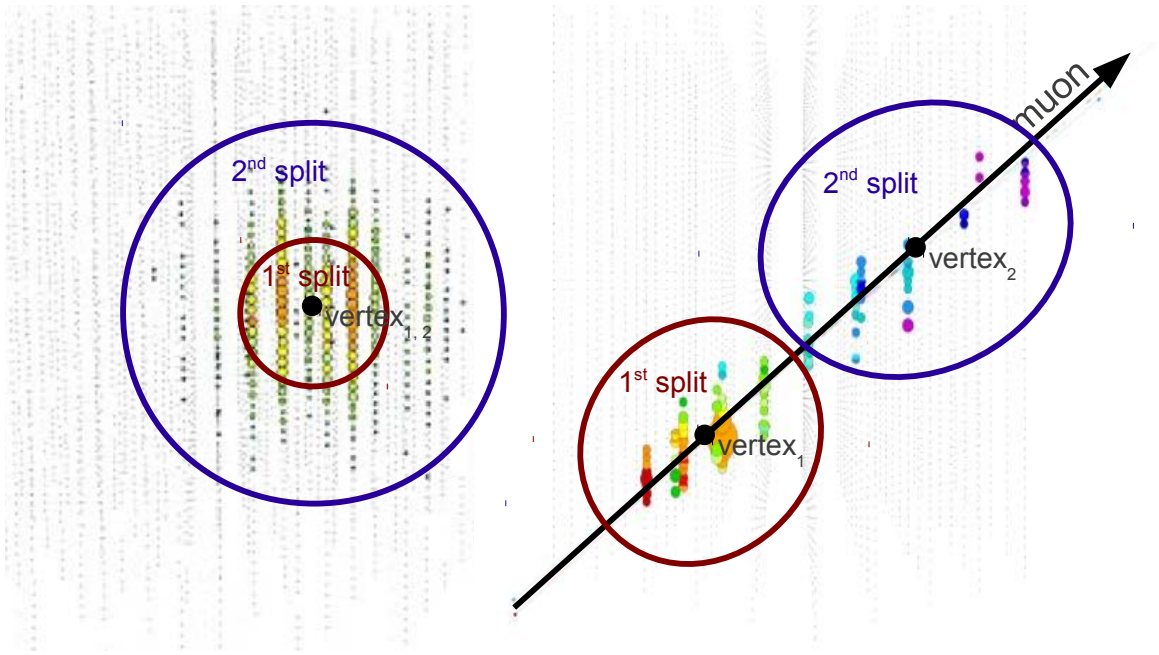


Figure 5.6: Illustration of the spatial distance reconstruction for cascade and muon events. The grey dots are DOMs, forming the IceCube strings. The coloured dots are hits, with size proportional to the amount of charge and colour representing the timing.

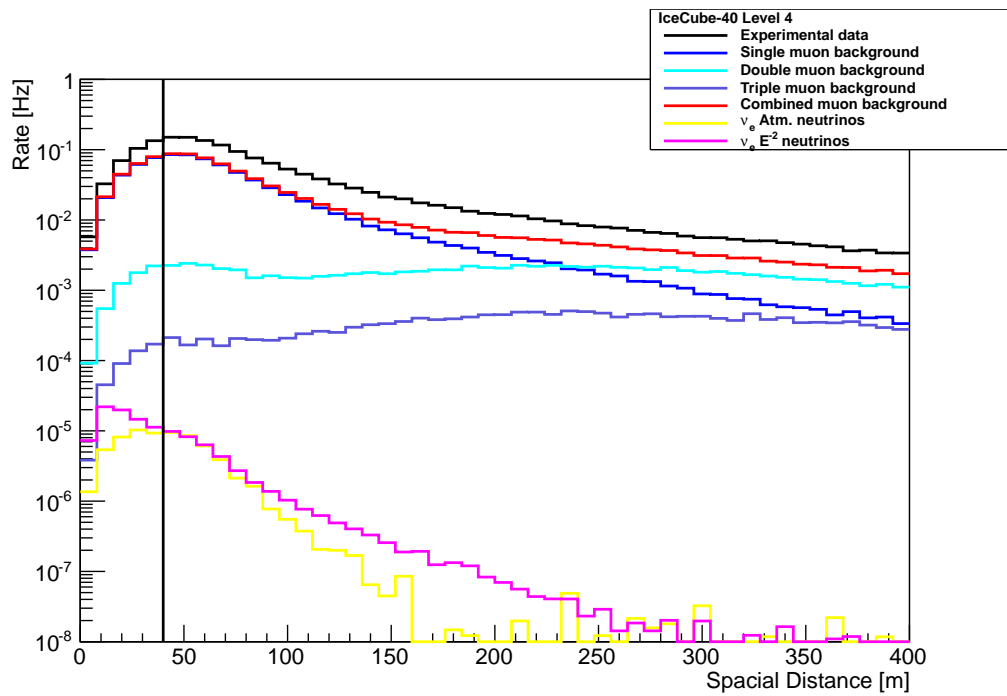


Figure 5.7: Spatial distance reconstruction. The level 4 cut is shown by the black line at 40 m, events with their two split vertices reconstructed more than 40 m apart are removed.

The spatial distance distributions for simulated background and signal events are shown in Figure 5.7. It can be seen that neutrino events peak at low values where the two vertices have been reconstructed approximately 20 m apart from each other. The background muon events peak with their vertices reconstructed approximately 50 m apart from each other. The cut on the spatial distance variable is placed at 40 m, events with their two vertices reconstructed more than 40 m apart are removed. The cut value is shown by the black vertical line in Figure 5.7.

5.4.2 Fill Ratio

The second cut performed at level 4 after the spatial distance cut is on the fill ratio variable. This variable is calculated at level 3. A sphere of radius R centered on the reconstructed vertex r is defined by the mean position of each hit DOM in the event

$$R = \langle d(\mathbf{r}, \mathbf{r}_i) \rangle \quad (5.14)$$

where i runs over the DOMs in the event and $d(\mathbf{r}, \mathbf{r}_i)$ gives the distance between each DOM hit and the reconstructed event vertex. The fill ratio variable is the ratio of the number of hit DOMs within this sphere to the total number of DOMs within the sphere.

If the event is a cascade event, and hence has spherical topology, the fill ratio should be close to one. If the event is track-like the fill ratio will be much less than one. The schematic in Figure 5.8 illustrates how the fill ratio variable is calculated for typical cascade and muon events.

The fill ratio distributions for simulated background and signal events are shown in Figure 5.9. The fill ratio value for neutrino events peaks at approximately 0.6. The background muon events fill ratio distribution has the majority of events with low fill ratio values. The cut on fill ratio variable is placed at 0.4, as shown by the black vertical line in Figure 5.9.

After the level 4 cuts are performed another energy reconstruction is run. This algorithm is the same as the one used in level 3, however, the reconstruction is run with four iterations, using the one-iteration reconstructed value as its seed. This means the reconstructed variables such as energy, vertex position, and direction of events have an improved resolution, as described in section 6.4. The rest of the analysis from this level uses the higher iteration reconstruction variables.

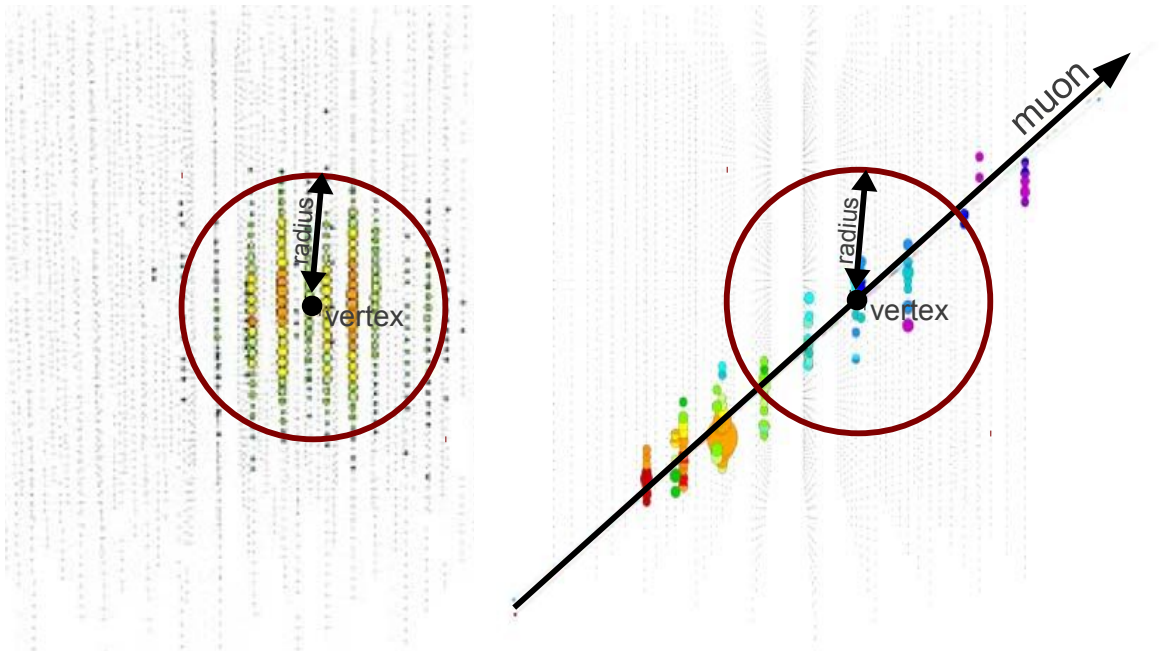


Figure 5.8: Illustration of the fill ratio reconstruction for cascade and muon events. The grey dots are DOMs, forming the IceCube strings. The coloured dots are hits, with size proportional to the amount of charge and colour representing the timing.

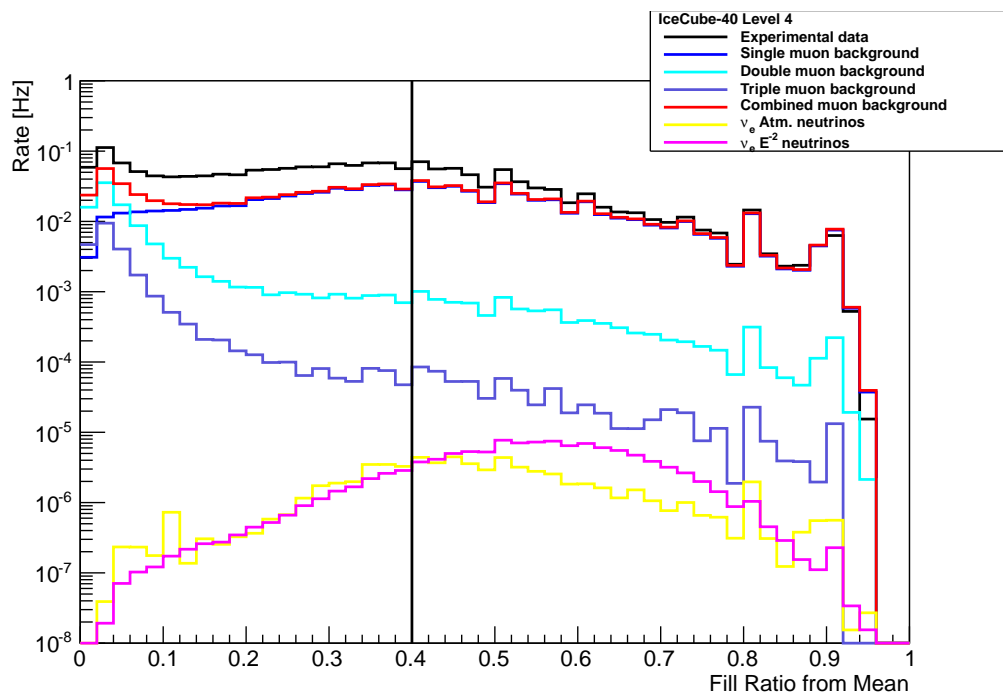


Figure 5.9: Fill Ratio. The level 4 cut is shown by the black line at 0.4, events with a fill ratio of less than 0.4 are removed.

5.5 Level 5

At level 5 a machine learning algorithm [83] is run to produce a *Boosted Decision Tree* (BDT) [71, Ch.10] response score that is used as a cut variable in the final level.

Prior to this containment cuts are performed. Containment cuts are necessary because the background events which survive to this filter level are cascade-like and are mostly at the edges of the detector. The containment cuts reduce the experimental data rate by another order of magnitude to 2.1×10^{-3} Hz.

5.5.1 z -Containment

The first containment cut is a cut on the reconstructed z -vertex position. The cut is placed at -450 m and at 450 m, shown in Figure 5.10. This removes events that lie within 50 m of the top and bottom boundaries of the detector. These events are muons that have survived to this filter level because they pass by the edges of the detector, depositing only a portion of the light from their track inside the detector volume. This can be seen by the background muon distributions which peak near the top and bottom of the detector. The effect of the non-uniform ice properties can be seen throughout the detector depth in this distribution. The neutrino event distributions are also affected by the ice properties, but are relatively flat across the entire depth and do not peak near the edges of the detector.

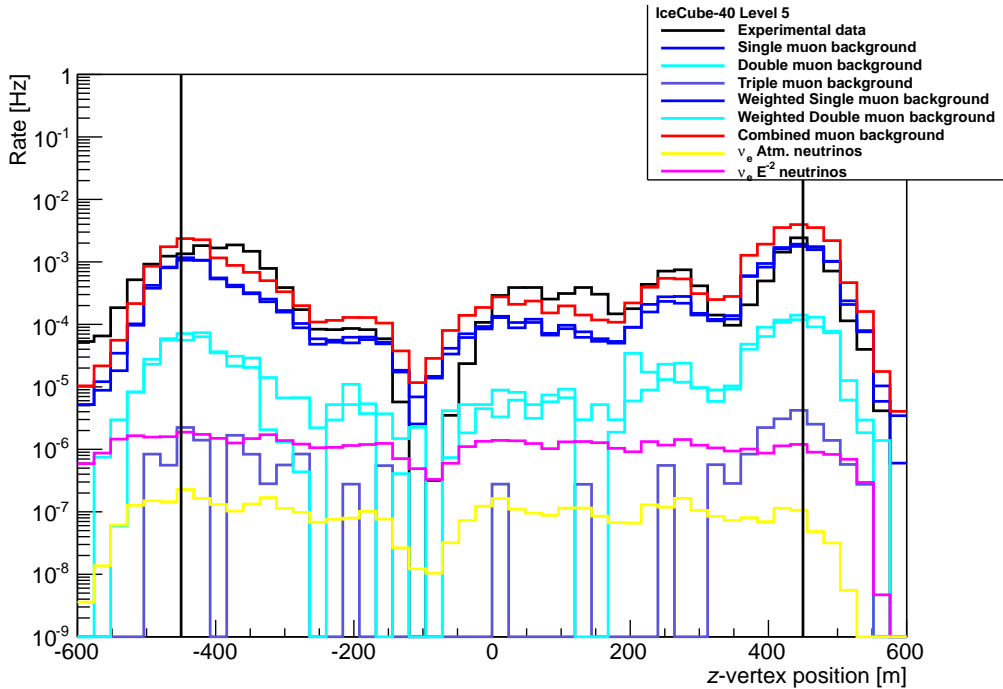


Figure 5.10: Reconstructed z -vertex position. The level 5 cuts are shown by the black lines at -450 m and 450 m, events with a reconstructed z -vertex position outside of these limits are removed.

5.5.2 xy -Containment

There are two containment cuts on the xy -event position. The first, called string containment, is on the event's reconstructed xy -vertex. This cut requires the vertex location to be reconstructed inside the outer ring of strings. This requirement excludes string 21 because it forms a sharp point in the detector layout in which a lot of background is reconstructed due to muons passing nearby without depositing light in other parts of the detector. The second xy -containment cut is called DOM charge containment and is concerned with the DOM that measures the largest deposited charge. This cut requires that the DOM with the largest deposited charge be located on an inner string.

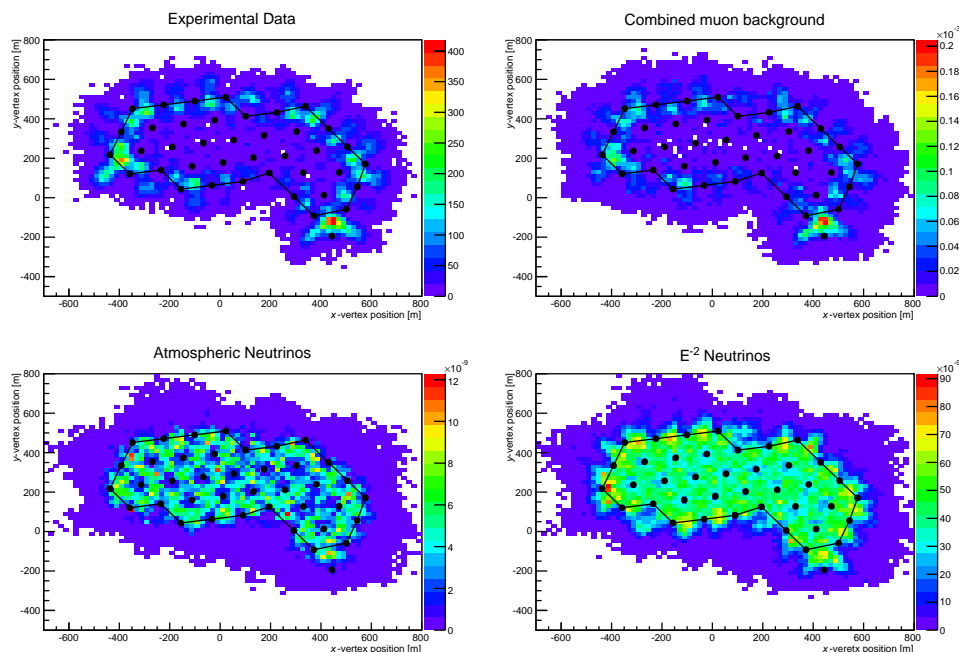


Figure 5.11: Reconstructed xy -vertex positions before any xy -containment cuts have been performed. The four panels show experimental data, muon background, atmospheric neutrinos, and E^{-2} spectrum neutrinos.

The boundary of the string containment cut and the effect of these containment cuts are shown in Figures 5.11–5.13. These plots show experimental data, combined muon background, atmospheric neutrinos, and E^{-2} spectrum neutrinos. The effect of each containment cut is shown by the distribution of the reconstructed vertex positions. Figure 5.11 shows the distribution of the reconstructed vertex positions before either xy -containment cut, Figure 5.12 shows the distribution of the reconstructed vertex positions after the string containment cut and Figure 5.13 shows the distribution of the reconstructed vertex positions after the string containment cut and the DOM charge

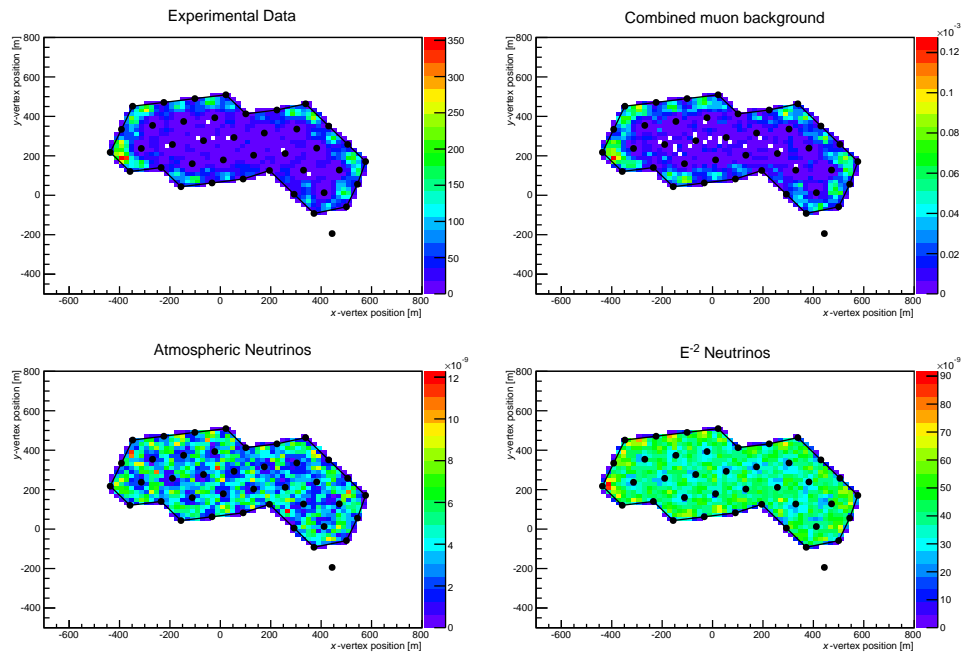


Figure 5.12: Reconstructed xy -vertex positions after events that do not satisfy the string containment cut have been removed. The four panels show experimental data, muon background, atmospheric neutrinos, and E^{-2} spectrum neutrinos.

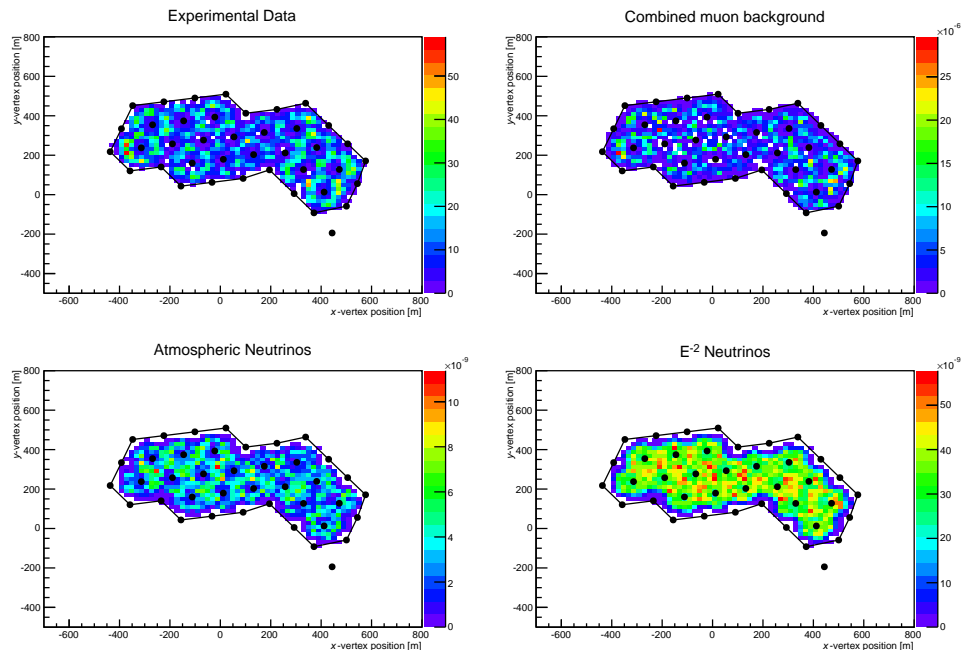


Figure 5.13: Reconstructed xy -vertex positions after events that do not satisfy either the string containment cut or the DOM charge containment cut have been removed. The four panels show experimental data, muon background, atmospheric neutrinos, and E^{-2} spectrum neutrinos.

containment cut. These plots show that the DOM charge containment cut is a harder cut than the string containment cut, as it restricts the reconstructed vertex positions further inside the outer ring of strings.

5.5.3 Multivariate Analysis

After the level 5 containment cuts have been performed background and signal are fed into a machine learning algorithm. The package used in this analysis is *Toolkit for MultiVariate Analysis* (TMVA) [83] which operates within the ROOT [34] framework. Eight variables, from muon background simulation and neutrino signal simulation, were chosen for the TMVA algorithm. A training phase was performed, using half of the simulation as input, where the algorithm learns the different characteristics of the eight variables for background and signal. A testing phase is then performed using the other half of the simulation where it checks, based on the learning from the training phase, whether it can indeed correctly characterise an event as background or signal.

The final output from TMVA is a variable called the BDT response score [83] where the boosting algorithm used is AdaBoost [56]. This variable is the score that each event is assigned depending on how background-like or signal-like TMVA has determined the event to be. For an event, \mathbf{x} , the BDT response score is

$$BDT(\mathbf{x}) = \frac{1}{N} \sum_i^N \ln(\alpha_i) h_i(\mathbf{x}) \quad (5.15)$$

where N is the number of variables, α is the boost weight, and $h(\mathbf{x})$ is the individual classifier encoded for signal and background as $+1$ and -1 respectively. Large values of BDT response score indicate the event is signal-like and small values indicate the event is background-like.

The final phase of TMVA is the evaluation phase. This is run on the experimental data, and the background and signal simulation that were not used in the training or testing phases. The BDT response score is used as a cut variable at the final level of cuts.

The signal simulation used for TMVA training and testing is approximately $\frac{1}{4}$ of the electron neutrino signal available. The remaining $\frac{3}{4}$ of the electron neutrino signal is used in the TMVA evaluation and throughout the rest of the analysis. All atmospheric muon background from unweighted and weighted simulation using the polygonato cosmic-ray spectrum is used in the training and testing. The muon background simulated using the two-component cosmic-ray spectrum are used in TMVA

evaluation and throughout the rest of the analysis. For a summary of these simulations see Tables 4.1 and 4.2 in section 4.3. Using separate simulation for the evaluation is necessary so as to avoid bias from the training and testing phases. No experimental data is used in the training or testing of TMVA.

The BDT response score is formed from the eight variables given to the TMVA. The BDT response score has a strong separation power between background and signal, and gives a better separation than could be achieved using the variables individually. The eight variables fed into TMVA are as follows:

- ***z*-vertex position**

The reconstructed *z*-vertex position. Cascade events are distributed more evenly throughout the depth of the detector than track events. This is because the majority background events are muons that travel across the top or bottom boundaries of the detector. This cut variable was used as a straight containment cut in filter level 5 described in section 5.5.1.

- **Track zenith direction**

The reconstructed zenith direction assuming a track hypothesis. Cascade events are distributed uniformly in zenith direction than track events which originate mainly from the horizon. This variable was reconstructed, with a lower number of iterations, as an energy dependent straight cut in filter level 3 described in section 5.3.1.

- **Track reduced log-likelihood**

The likelihood that the hit pattern in the detector arises from a muon track. Cascade events should score low values for this variable. The cascade version of this variable was an energy dependent cut in filter level 3 described in section 5.3.2.

- **Line-fit velocity**

The line-fit velocity of the event. This is a fit to the timing of the hit pattern in the detector. Cascade events appear stationary and therefore have lower line-fit velocities than track events which travel close to the speed of light through the detector. This variable was used as a straight cut in the pole filter described in section 5.2.1.

- **Tensor of inertia eigenvalue ratio**

The ratio of the smallest eigenvalue to the sum of the three eigenvalues. This

comes from the tensor of inertia and is a measure of the sphericity of the event. Cascade events have an eigenvalue ratio close to 0.3, because they are more spherical than track events. This variable was used as a straight cut in the pole filter described in section 5.2.2.

- **Fill ratio from mean+RMS**

The fill ratio is the ratio of the number of hit DOMs to the total number of DOMs within a sphere. The sphere has radius R obtained from the mean location of the hit DOMs and the width of their distribution around the reconstructed event vertex. Cascade events have a fill ratio close to 1.0, because they have a more spherical event topology than track events. The version of this variable using a sphere of radius R arising from only the mean of the location of the hit DOMs was used in filter level 4 described in section 5.4.2.

- **Split time vertex**

The difference in the reconstructed vertex time based on splitting the event due to the hit times. The event is divided into two parts based on the timing of each of the hits at the DOM locations. The split reconstruction algorithm was used in filter level 4 and was described in section 5.4.1. Cascade events have similar reconstructed vertex position and timing from the first and second parts of the event because they are spherical, track events have widely varying vertex position and timing because their two vertices are far apart along their track length.

- **Split containment**

The distance of the reconstructed vertex of the event from the centre of the detector. This is calculated using only the first part of the hits in the event. The split reconstruction algorithm was used in filter level 4 and was described in section 5.4.1. Cascade events are reconstructed closer to the centre of the detector. This is because background muon events survive to high levels when they travel close to the edges of the detector without depositing all the light from their track inside the detector volume.

These eight input variables are shown in Figure 5.14 as assessed by TMVA. These events are from the training sample only, which consists of half the background and half the signal simulation. In these Figures the background is shown in red and the signal in blue. The background and signal are scaled so that they are normalised to each other, although at this level the rate of the signal is still far below that of the background.

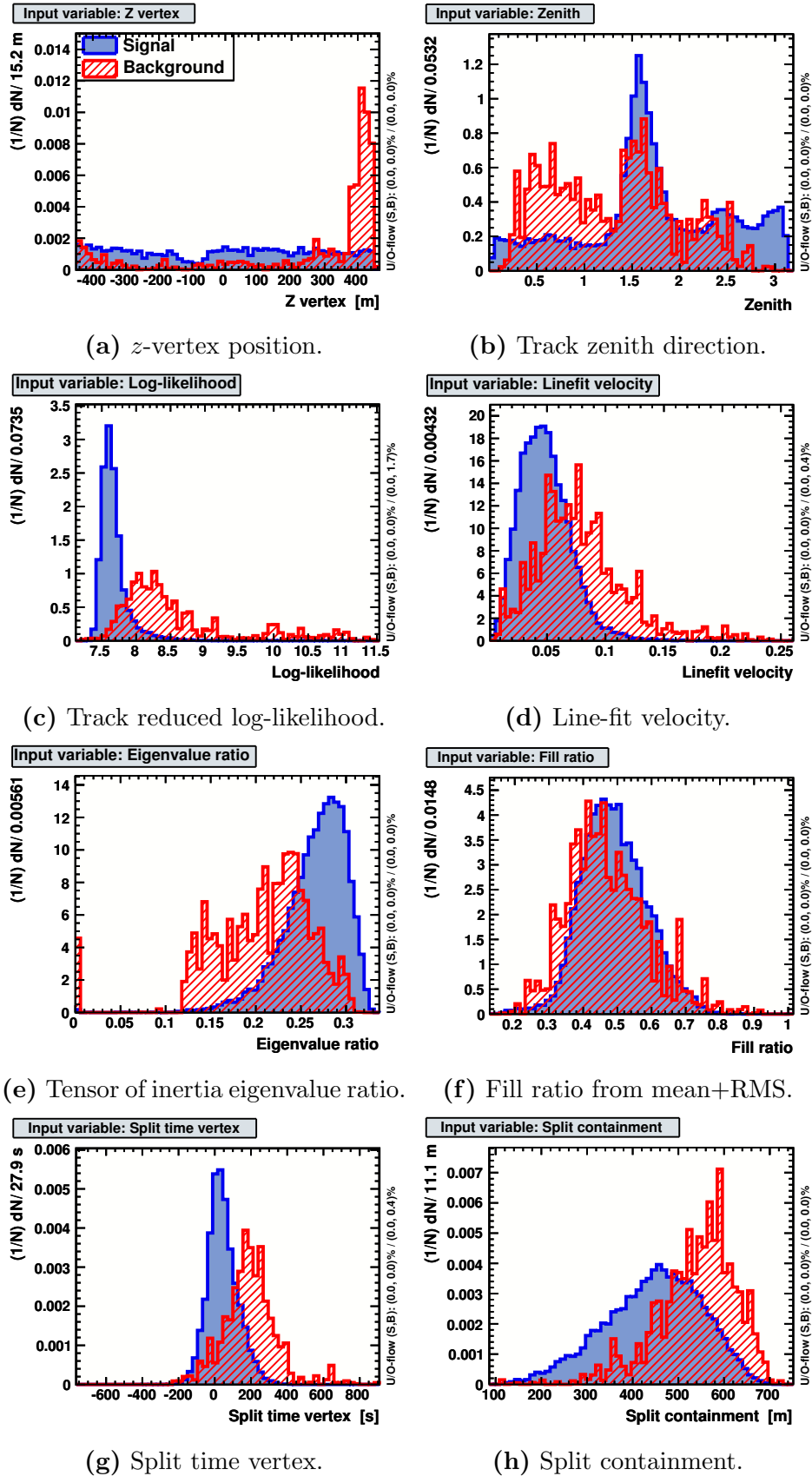
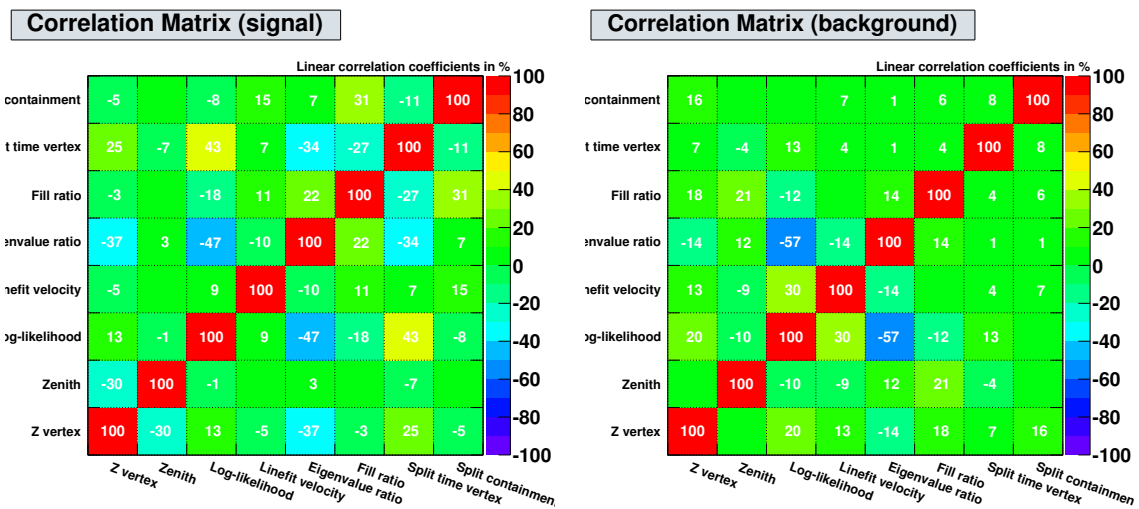


Figure 5.14: The eight input variables that are fed into the TMVA algorithm to produce a BDT response score. The BDT response score has much greater separation power of background and signal than these variables do individually.

TMVA also provides correlation matrices of all the input variables for signal and background. These show the correlation between each set of variables used in the TMVA training. Ideally the correlation between each variable is low, so that every variable contributes to making the BDT response score decision without redundancy. The correlation matrices are shown in Figure 5.15. These show that the correlation in both signal and background reconstruction variables is low and flat over all pairings of the input variables.



(a) Signal.

(b) Background.

Figure 5.15: The correlation matrices for the eight variables fed into TMVA. For both background and signal the correlation between each variable is low, meaning that every variable is useful for TMVA to make a BDT response score decision.

A risk in using machine learning is that there may be overtraining [71, Ch.10], where the BDT response score output is ineffective. To ensure that this does not happen the TMVA uses half the simulation for training and the other half for testing. With no overtraining the BDT response score curve will be exactly the same for both samples. TMVA produces an overtraining check plot using the Kolmogorov-Smirnov test [126], which uses the training and testing probability distributions to check the consistency of the data samples. This plot is shown in Figure 5.16. Here the background is shown in red and the signal in blue. The training samples are square points and the testing samples are the shaded regions. The training and testing samples do have the same BDT response curve for both background and signal, although it is clear that statistical uncertainties are the limiting factor. It is for this reason that none of the simulation used for training or testing in TMVA is used for evaluation, or subsequent analysis levels.

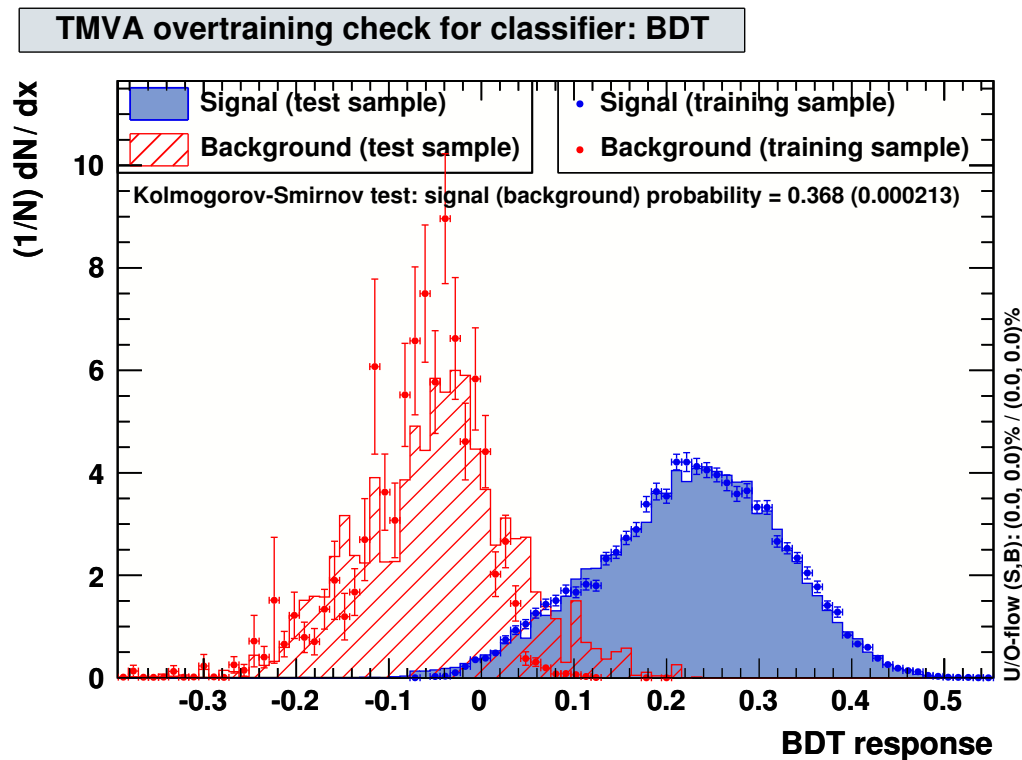


Figure 5.16: Overtraining check of training and testing samples from TMVA. The background is shown in red and the signal in blue. The training samples are shown by the square points, the testing samples by the shaded regions. Evidence of overtraining is suggested if the distributions of the training and testing samples differ.

5.6 Level 6

Level 6 is the final analysis filter level. It consists a cut on the BDT response score and a cut on the energy. These cuts are optimised based on the sensitivity and discovery potential using the Feldman-Cousins method [52]. The level 6 cuts reduce the experimental data by a further four orders of magnitude to 6.4×10^{-7} Hz. The background rate at this level is below that estimated for the signal and the experimental data can be unblinded.

5.6.1 Optimisation

To optimise the final level of cuts the experimental data is used rather than the remaining muon background from simulation. This is because the available muon background simulation was limited by this stage of the analysis, and so will not provide a robust estimation for the best values to place the final cuts. This can be seen in Figure 5.17, which shows experimental data, combined muon background, atmospheric neutrinos,

and E^{-2} spectrum neutrinos in each of the panels. In the muon background panel there is no simulation left in the signal region of the parameter space.

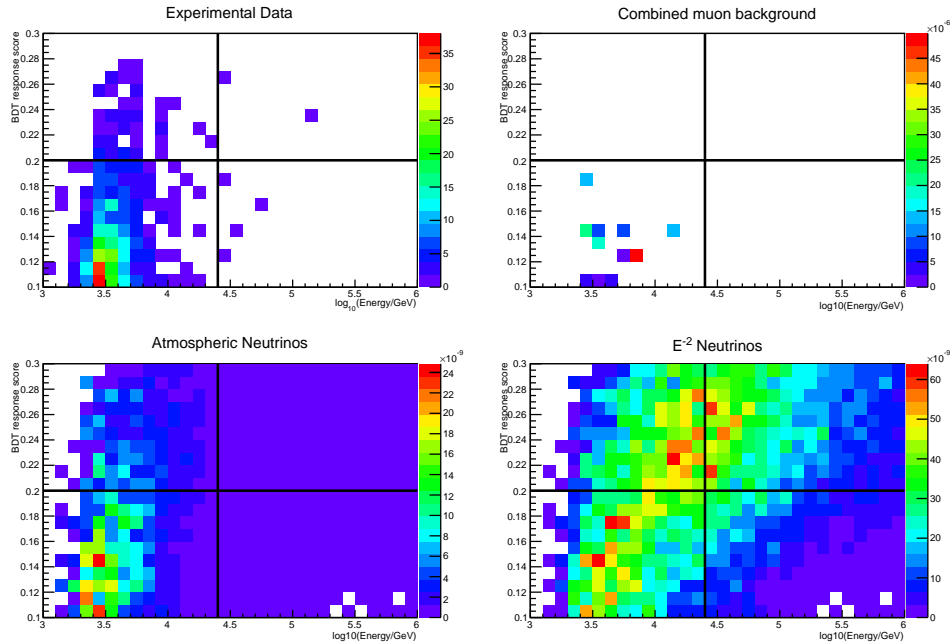


Figure 5.17: BDT response score versus $\log_{10}(\text{Energy})$. These are the final two cut variables. The four panels show experimental data, muon background, atmospheric neutrinos, and E^{-2} neutrinos. The experimental data is used to optimise the final cuts, the eventual cuts are shown by the black lines in each panel.

The experimental data can be used for the optimisation because most events are still expected to be from muon background events, even at this high filter level. However, there may be some real signal events within the remaining experimental data sample, so these must be treated carefully. Consequently, events lying far into the signal region of the parameter space are excluded from the optimisation. In the 10% burn sample of the experimental data there are two events that lie in this signal region. These can be seen in Figure 5.17 in the upper right quadrant of the experimental data panel. These two signal events are excluded from the optimisation of the final level cut values.

The final level analysis cuts are optimised based on the sensitivity and discovery potential of the final sample [77]. These methods assume either no neutrino signal or small neutrino signal.

No signal

In the case of no detectable signal the best limit is set. To optimise for this scenario the expected upper limit is calculated using the Feldman-Cousins method [52]. This gives the *Model Rejection Factor* (MRF) from the number signal events μ_s , the number of

background events μ_b , and the number of observed events n_{obs} using Poisson statistics

$$\text{MRF} = \frac{\mu(n_{\text{obs}}, \mu_b)}{\mu_s}, \quad (5.16)$$

and when multiplied by the flux, the best average upper limit $\bar{\Phi}_{\text{limit}}$ as

$$\bar{\Phi}_{\text{limit}} = \Phi_{\text{assumed}} \times \text{MRF} \quad (5.17)$$

where Φ_{assumed} is the best current all-flavour E^{-2} flux limit.

Small signal

In the case where a small signal is detected the significance of the detection will be calculated. To optimise for this scenario the number of critical events n_{crit} is calculated assuming a 5σ discovery. The least detectable signal μ_{lds}^{90} is calculated with a 90% confidence level. This gives the *Model Discovery Factor* (MDF)

$$\text{MDF} = \frac{\mu_{\text{lds}}^{90}}{\mu_s}, \quad (5.18)$$

and when multiplied by the flux, the discovery potential Φ_{detected} is

$$\Phi_{\text{detected}} = \Phi_{\text{assumed}} \times \text{MDF}. \quad (5.19)$$

To optimise for either the case of no observed signal, or a small observed signal, the MRF and MDF both have to be minimised [77]. It turns out that for this analysis both of these minimise to the same final cut values, meaning the best sensitivity and the best discovery potential are at the same region of parameter space for the final level of cuts [78]. This is shown in Figure 5.18, where the MRF and MDF are both at a minimum at final cut values of $\text{BDT} = 0.2$ and $\log_{10}(\text{Energy}) = 4.4$.

5.6.2 Final cuts

The BDT response score distributions for simulated background and signal events are shown in Figure 5.19. It can be seen that neutrino events peak at high BDT response scores, approximately 0.3, as opposed to the background muon events which peak at low BDT response scores, approximately -0.1 . As described in section 5.6.1 the optimum cut for the BDT response score, based on minimising the MRF and MDF, is 0.2. This cut is illustrated by the black vertical line in Figure 5.19, where events with a BDT response score below this cut value are removed from the final event selection.

The reconstructed energy distributions for simulated background and signal events are shown in Figure 5.20. It can be seen that neutrino events have a relatively flat energy spectrum between $\log_{10}(E) = 3.0$ and $\log_{10}(E) = 5.0$ before gradually dropping at

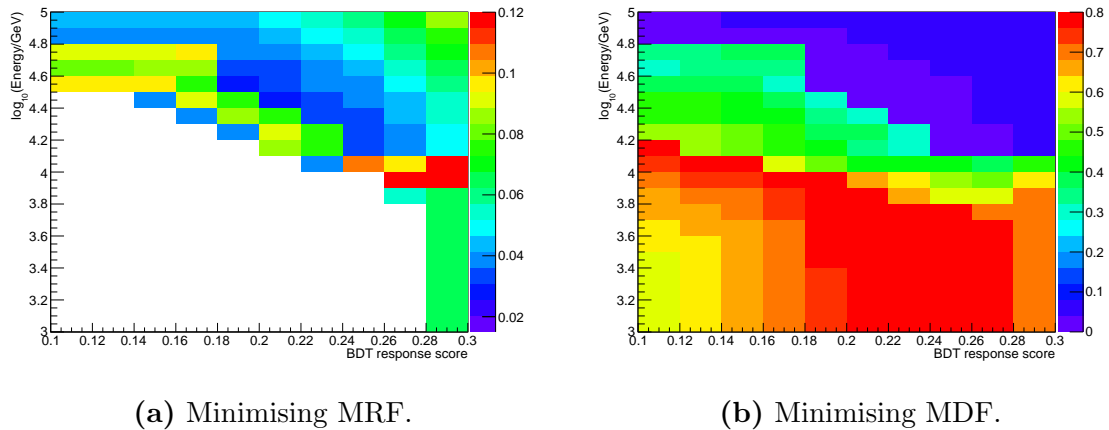


Figure 5.18: Optimisation of final level cuts for best sensitivity and discovery potential. The plots are $\log_{10}(\text{Energy})$ versus BDT response score, where the colour represents the values for the MRF and MDF.

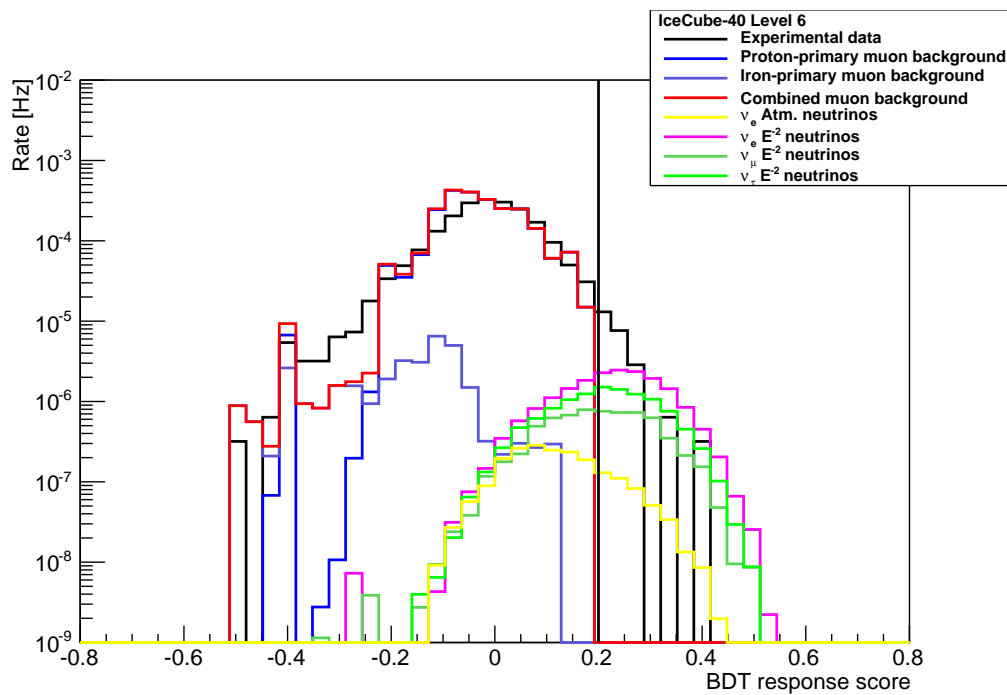


Figure 5.19: BDT response score. The level 6 cut is shown by the black line at 0.2, events with a BDT response score of less than 0.2 are removed.

higher energies. The muon background energy spectra however peak at approximately $\log_{10}(E) = 3.4$ and then rapidly decline. As described in section 5.6.2 the optimum cut for the energy, based on minimising the MRF and MDF, is 25 TeV. This is illustrated by the black vertical line in Figure 5.20, where events with a reconstructed energy less than 25 TeV are removed from the final event selection.

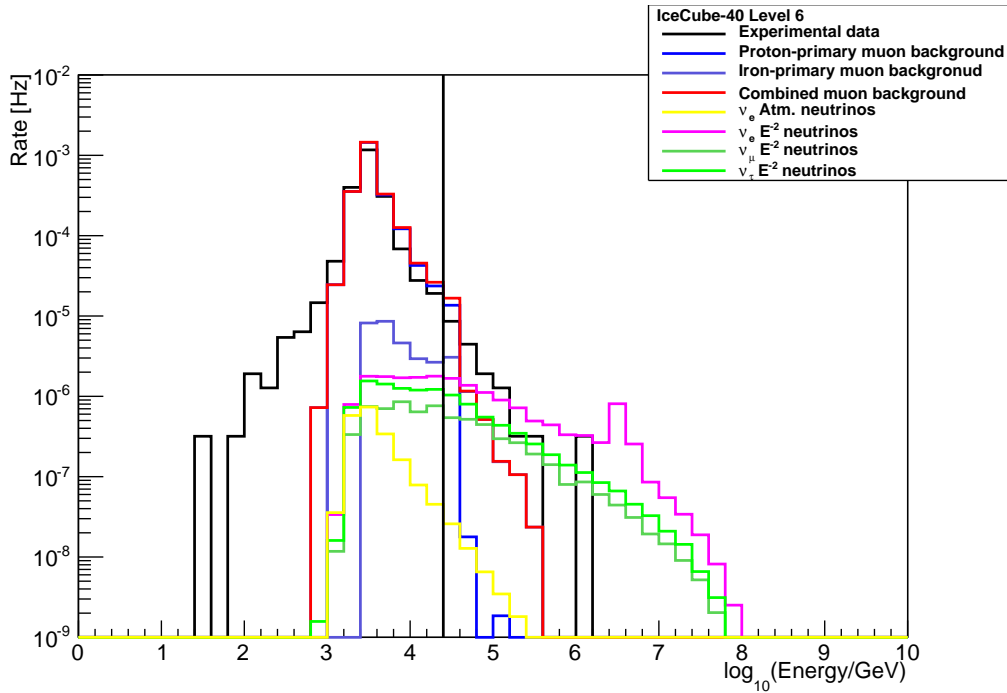


Figure 5.20: Four iteration reconstruction of event energy. The level 6 cut is shown by the black line at 25 TeV, events with a reconstructed energy of less than 25 TeV are removed.

5.6.3 Final Rates

After all filtering cuts have been performed the background rate from atmospheric muons, estimated using the available simulation, has been reduced to 0 Hz. The experimental data rate has been reduced ten orders of magnitude to 6.4×10^{-7} Hz, at a level where the remaining events are cascade-like. By comparison, the rate for the simulated neutrino signal has only been reduced by two orders of magnitude throughout all filtering levels.

The experimental data rate is now below that of the simulated neutrino signal, and the experimental data can be unblinded. The rate after each analysis filter level for experimental data, muon background, and neutrino signal is summarised in Table 5.1. The rates shown in this Table for the neutrino signal have an E^{-2} weighting and an assumed all-flavour flux of $1 \times 10^{-6} \text{ GeVsr}^{-1}\text{s}^{-1}\text{cm}^{-2}$.

Recall, as explained in section 4.3.2, that the muon background simulations were obtained using two different cosmic-ray spectra. The first type of muon background used the polygonato cosmic-ray spectrum model and the second type used the two-component cosmic-ray spectrum model. There is more muon background simulation using the two-component model and so this simulation has a longer livetime and pro-

	Trigger	Pole filter	Level 3	Level 4	Level 5	Level 6
Data	1500	16	1.7	2.5×10^{-2}	2.1×10^{-3}	6.4×10^{-7}
Atm. muons	1300	12	0.9	3.3×10^{-2}	2.5×10^{-3}	0
Signal (E^{-2})	2.5×10^{-4}	1.5×10^{-4}	1.2×10^{-4}	5.6×10^{-5}	1.8×10^{-5}	7.4×10^{-6}

Table 5.1: Rates in Hz of data, atmospheric muon background, and neutrino signal at each filter level.

vides a more robust estimation of the background levels at the end of the analysis. Up to and including level 4 and BDT training, muon background from the polygonato cosmic-ray spectrum is used. Beyond level 4 the muon background from the two-component proton and iron cosmic-ray spectra is used. The background simulation from both types of simulation should track the experimental data throughout the filter levels until the final level when the data could contain a significant fraction of signal events. Table 5.2 show the ratio of experimental data to the simulated muon background at each filter level. At low filter levels there is an excess of data over background simulation. At higher filter levels, as the data samples become more pure because they contain a larger proportion of signal events, this discrepancy diminishes and the rate of simulated background becomes larger than that remaining in the experimental data.

	Trigger	Pole filter	Level 3	Level 4	Level 5	Level 6
Data/Muon background	1.2	1.3	1.9	0.8	0.8	undefined

Table 5.2: Excess of experimental data over simulated atmospheric muon background at each filter level.

The available muon background simulation after the final level of analysis cuts has diminished and has limited event statistics. This could be due to lack of simulation or because the analysis successfully removes all the background events. The more muon background produced in simulation the more confident that all the background has been removed from the analysis. At this point of the analysis it was decided to proceed to unblinding to see what events, if any, are present in the entire IceCube-40 dataset. However, the discrepancy between the data and the muon background simulation became more pronounced after unblinding when the full experimental dataset was used.

This resulted in the need for further background simulation which will be described in section 6.2.

A comparison of the rates from the different filter levels is made with the equivalent IceCube-22 high energy cascade analysis [7]. Improvement is expected in this analysis over the 22-string detector analysis because the IceCube-40 detector is almost twice the size and has a much larger effective area. In addition to this the IceCube-40 detector had a longer livetime and the analysis uses more advanced reconstruction algorithms and machine learning algorithms to develop cut variables.

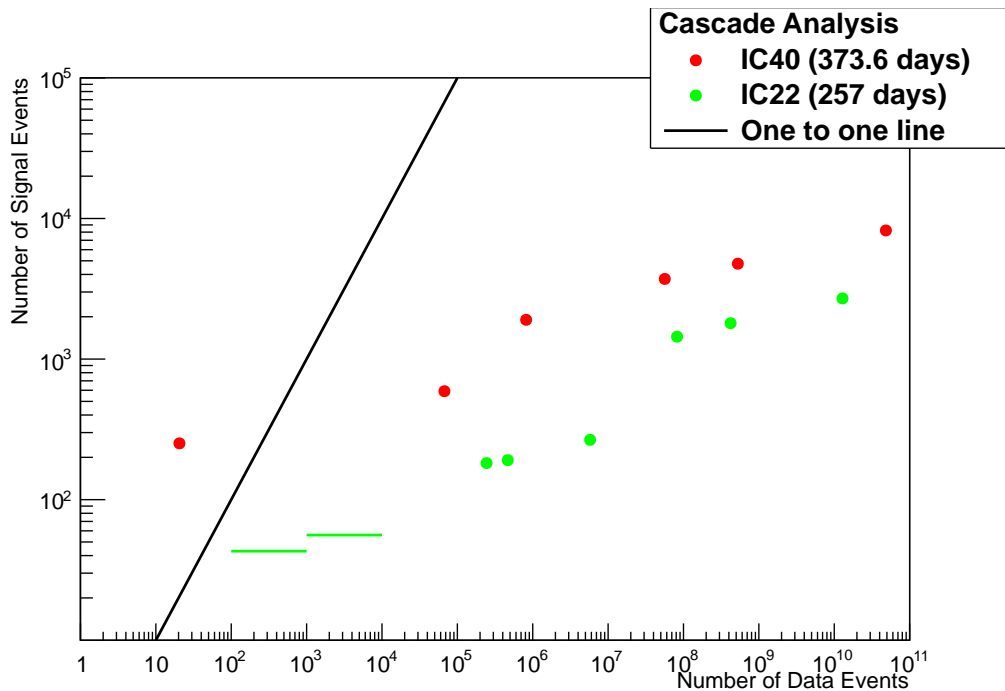


Figure 5.21: Comparison of number of signal events and number of background events from IceCube-40 and IceCube-22 filter levels. The number of events in IceCube-40 after each filter levels are given by the red points, the number of events in IceCube-22 after each filter level are given by the green points. The one-to-one line is shown in black.

Figure 5.21 shows this comparison, where the expected number of signal events are plotted against the number of experimental data events derived from the 10% burn sample for each filter level before unblinding. An all-flavour flux of $1 \times 10^{-6} \text{ GeVsr}^{-1}\text{s}^{-1}\text{cm}^{-2}$ is assumed for comparison between both analyses. In the IceCube-22 analysis the burn sample of the experimental data ran out of statistics before the final two filter levels, so these points are depicted as limits. The one-to-one line is also shown in this Figure. Reducing the experimental data rate below this line, while keeping the signal expectation above it represents the discovery region given the assumed astrophysical flux. In this IceCube-40 analysis the final filter level crosses the one-to-one line.

5.7 Expectation Of Events

The expected number of events N_{events} for experimental data, atmospheric muon background, atmospheric neutrino background, and E^{-2} neutrino signal is calculated by multiplying the event rates in Hz by the IceCube-40 livetime:

$$N_{\text{events}} = \text{Rate} \times L \quad (5.20)$$

where the total livetime for this IceCube-40 analysis is $L = 373.6$ days (32279040 seconds).

5.7.1 Experimental Data

Using the rate from the 10% burn sample of the experimental data an estimate of the number of events that will be observed after unblinding is calculated. This is shown in Table 5.3.

	Rate (Hz)	Number of Events
Experimental data	6.4×10^{-7}	20.6

Table 5.3: Expected events to be observed in unblinded experimental data.

5.7.2 Signal

The expected signal from each flavour of neutrino can be calculated from the rate. The rate can be estimated after all analysis cuts have been performed on the E^{-2} spectrum simulation. The efficiency of the detector can be represented by the effective area of the detector. The neutrino effective area $A_{\text{eff}}^{\nu}(E_{\nu}, \theta)$ is a function of primary energy and zenith angle. It is the surface corresponding to 100% detection efficiency for neutrino detection. This includes contributions from event interaction probability, absorption in the Earth, propagation, neutrino cross-section, detection probability, and cut efficiencies. The effective area is

$$A_{\text{eff}}^{\nu}(E_{\nu}, \theta) = A_{\text{gen}} \frac{N_{\text{selected}}(E_{\nu}, \theta)}{N_{\text{gen}}(E_{\nu}, \theta)} \quad (5.21)$$

where A_{gen} is the generation area, N_{gen} is the number of generated events, and N_{selected} are the events that have survived all filtering cuts. The neutrino effective area is

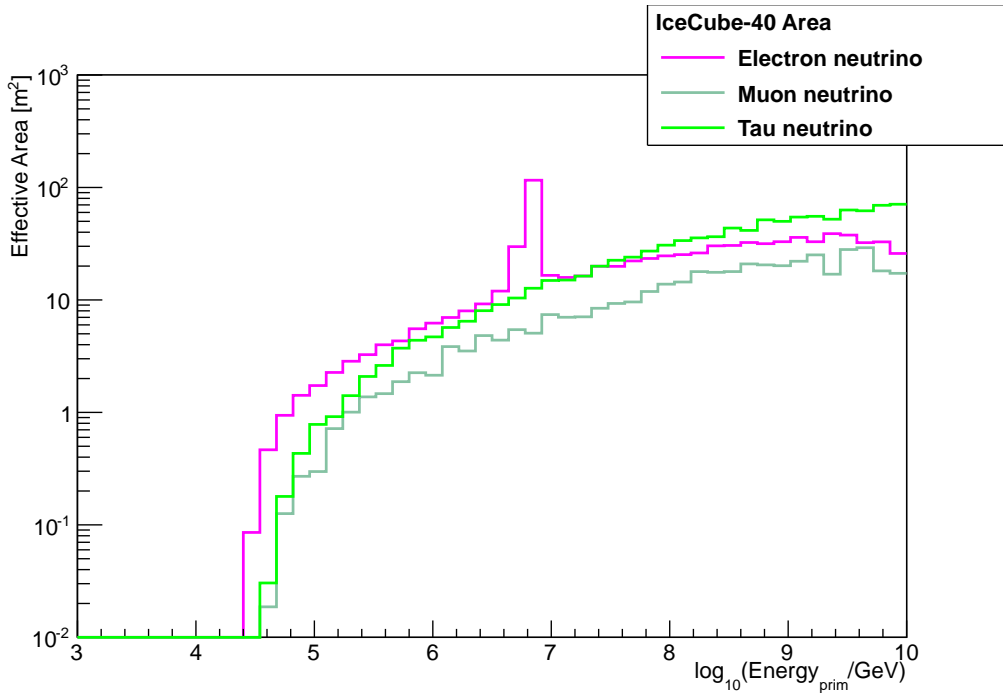


Figure 5.22: IceCube-40 neutrino effective area as a function of primary neutrino energy. The three curves show electron, muon, and tau neutrino simulated signals. The peak in the electron neutrino curve corresponds to the Glashow resonance. The colour of the muon neutrino signal line has been changed in this histogram (compared to previous one throughout the chapter) for clarity.

calculated for this analysis for all flavours of signal simulation as a function of primary energy and integrated over a 4π solid angle.

The neutrino effective area is shown in Figure 5.22 where it can be seen the analysis is equally sensitive to electron and tau neutrino events. The sensitivity to muon neutrino events is slightly lower because of the steps necessary to remove the atmospheric muon background. The effect of the Glashow resonance [62] ($\bar{\nu}_e + e^- \rightarrow W^-$) can also be seen in the electron neutrino curve at $\log_{10}(E/\text{GeV}) = 6.3$.

Given a signal spectrum and flux, the effective area can be used to estimate the rate. In this case the rate is calculated for an E^{-2} spectrum and for two different fluxes. The first flux is an all-flavour astrophysical flux of $3.6 \times 10^{-7} \text{ GeVsr}^{-1}\text{s}^{-1}\text{cm}^{-2}$. This flux is the best limit set by previous cascade analyses [7]. The second flux is that calculated assuming a muon neutrino flux of $8.9 \times 10^{-9} \text{ GeVsr}^{-1}\text{s}^{-1}\text{cm}^{-2}$. This is the limit calculated in the IceCube-40 muon analysis [5]. Assuming the ratio of neutrino flavours is 1 : 1 : 1 this muon limit corresponds to an all-flavour limit of $2.7 \times 10^{-8} \text{ GeVsr}^{-1}\text{s}^{-1}\text{cm}^{-2}$. The expected number of signal events assuming these two fluxes is shown in Table 5.4.

	Rate (Hz)		Number of Events	
	assuming flux from [7]	assuming flux from [5]	assuming flux from [7]	assuming flux from [5]
Electron neutrinos	8.9×10^{-7}	6.7×10^{-8}	28.7	2.2
Muon neutrinos	2.3×10^{-7}	1.7×10^{-8}	7.5	0.6
Tau neutrinos	4.1×10^{-7}	3.1×10^{-8}	13.2	1.0
Total	$(\nu_e + \nu_\mu + \nu_\tau)$		49.4	3.8

Table 5.4: Expected neutrino signal events.

5.7.3 Background

The analysis removed all the simulated muon background events from the initial simulation datasets. As will be described in section 6.2 this muon background estimate is revised using additional background simulation. The values given here are only those calculated from the original muon background simulation.

There is a background contribution from atmospheric neutrinos arising from both electron and muon atmospheric neutrinos. This is shown in Table 5.5, where the contributions from conventional and prompt atmospheric neutrinos are combined. After unblinding the total number of background events expected from atmospheric muons was zero, and the number from atmospheric neutrino sources was approximately two.

	Rate (Hz)	Number of Events
Muon background	0	0
Atmospheric electron neutrinos	4.1×10^{-8}	1.3
Atmospheric muon neutrinos	5.4×10^{-8}	1.7
Total	Muon background + Atm ν_e + Atm ν_μ	3.0

Table 5.5: Expected background events.

A comparison of the predicted number of events from atmospheric neutrino models is shown in Table 5.6, where the conventional atmospheric models shown are Bartol [27]

and Honda [85], and the prompt atmospheric models shown are Sarcevic [49] and Naumov [111]. From previous IceCube analyses the Naumov models have been ruled out [5] so the models used for the background prediction in this analysis, given in Table 5.5, are Bartol and Sarcevic standard.

	ν_e Events	ν_μ Events	ν_τ Events	Total Events
Bartol	0.54	1.58	–	2.12
Honda	0.08	0.74	–	0.82
Sarcevic standard	0.78	0.15	0.02	0.95
Sarcevic minimum	0.46	0.09	0.02	0.57
Sarcevic maximum	0.99	0.20	0.02	1.21
Naumov RQPM	6.56	1.22	–	7.78
Naumov QGSM	1.80	0.34	–	2.14

Table 5.6: Comparison of number of events expected assuming various atmospheric neutrino models.

The effective livetime T_{eff} is the amount time the weighted simulation of the atmospheric muon background corresponds to at a given energy, that is, the equivalent amount of unweighted simulation required to obtain the same relative error bars as the weighted simulation [102]. It is calculated from

$$T_{\text{eff}} = \frac{\sum_{i=0}^N w_i}{\sum_{i=0}^N w_i^2} \quad (5.22)$$

where N is the number of events and w_i is the weight of the i^{th} event. The effective livetime gives the number of days of muon background simulation remaining in the analysis and is an indication of how effectively the muon background is simulated. This is an important quantity in an analysis because it is an indication of the reliability of the background prediction which has an effect on the outcome of the results when observing the full dataset and placing any limits on the astrophysical neutrino flux.

Figures 5.23 and 5.24 show the effective livetime in days of the muon background simulation from the polygonato and two-component cosmic-ray spectra, as a function of the simulated primary energy. Figures 5.25 and 5.26 show the same, as a function of the four iteration reconstructed energy calculated in the analysis. The points on these

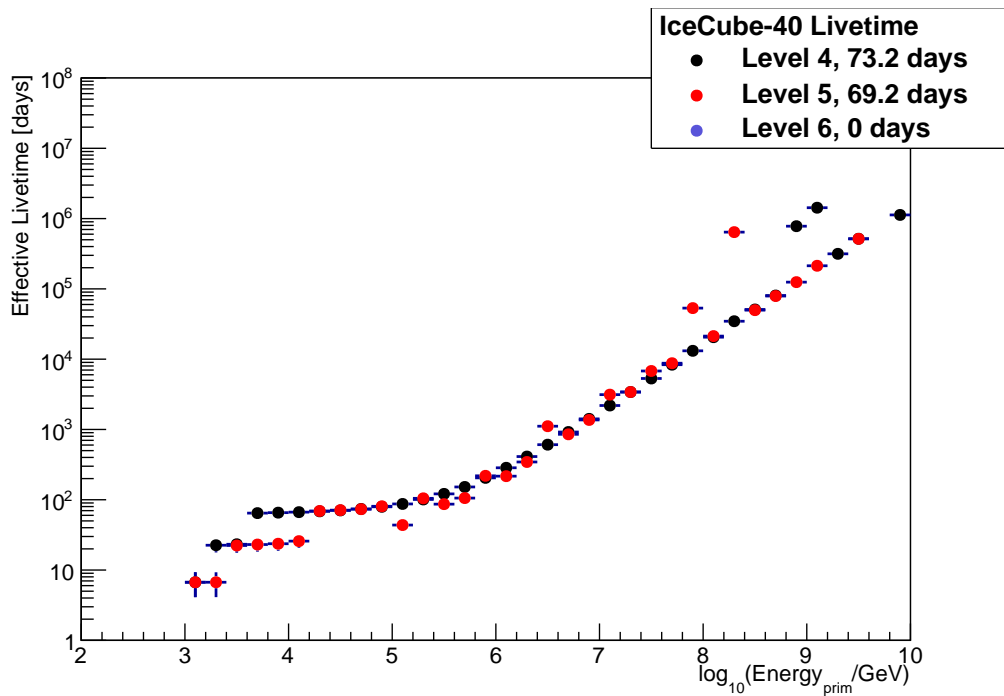


Figure 5.23: IceCube-40 effective livetime of the muon background simulation, using the polygonato cosmic-ray spectrum, as a function of primary energy.

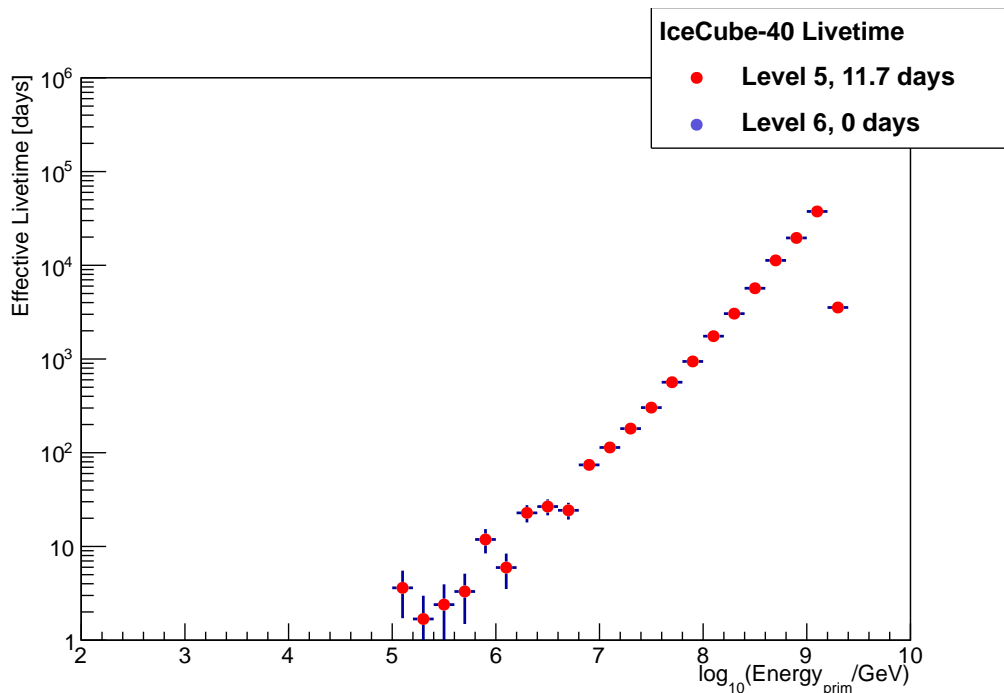


Figure 5.24: IceCube-40 effective livetime of the muon background simulation, using the two-component cosmic-ray spectrum, as a function of primary energy.

plots give the effective livetime for the given energy bin. The total effective livetime is the weighted average over the non-zero energy bins.

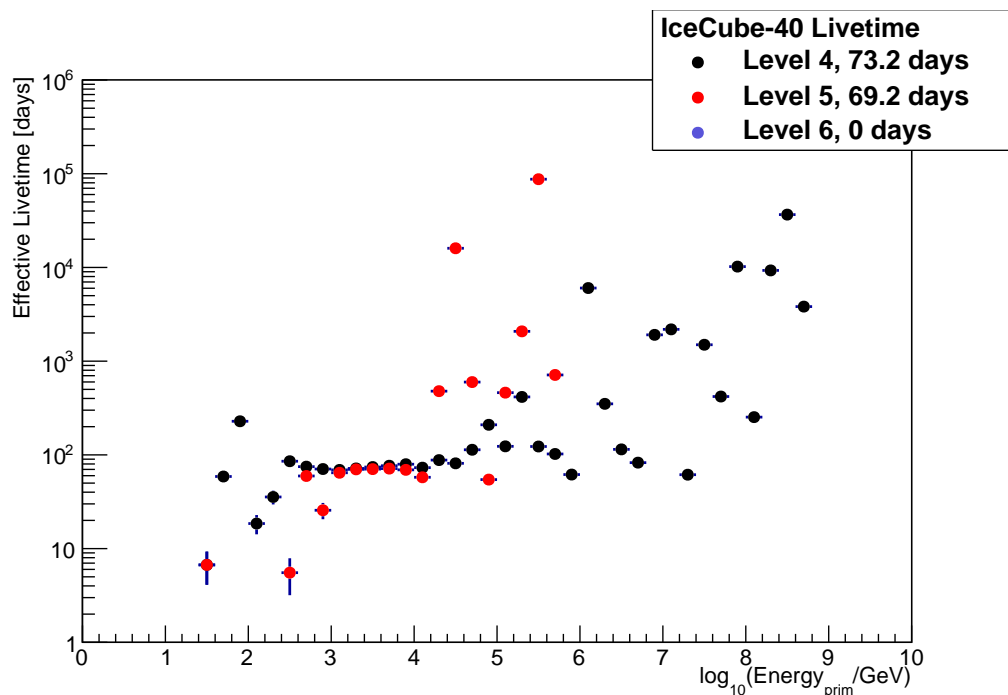


Figure 5.25: IceCube-40 effective livetime of the muon background simulation, using the polygonato cosmic-ray spectrum, as a function of reconstructed energy.

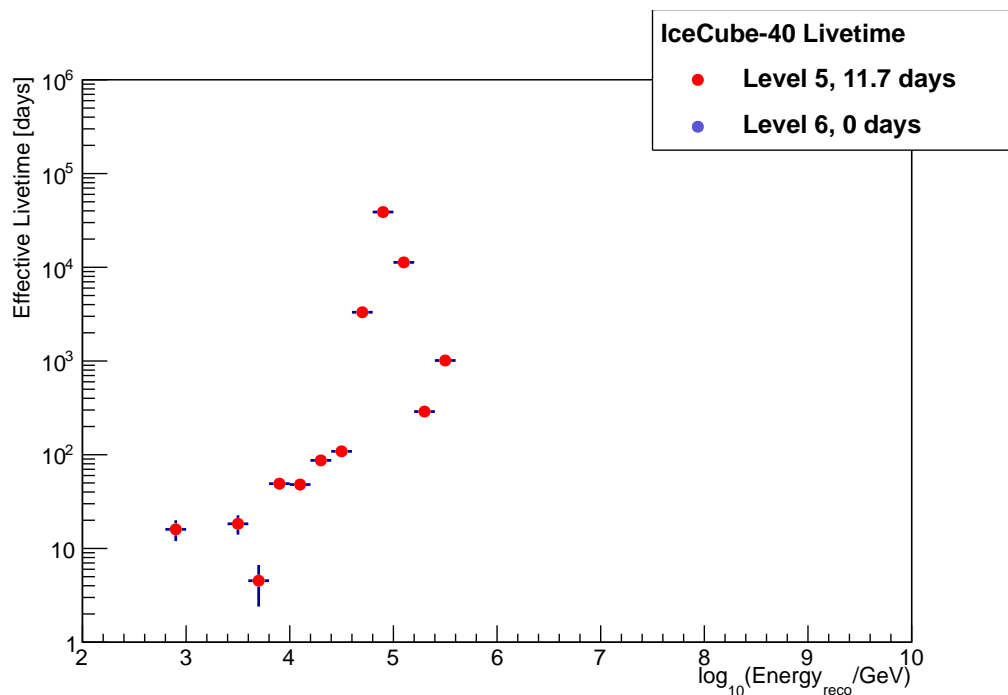


Figure 5.26: IceCube-40 effective livetime of the muon background simulation, using the two-component cosmic-ray spectrum, as a function of reconstructed energy.

For the original polygonato spectrum simulation and two-component spectrum simulation the total livetime is the same for primary energy and reconstructed energy. No

muon background events remain after all filtering cuts were performed in these original muon background datasets. Using the livetime of the muon background from the two-component cosmic-ray simulation after filter level 5, as a function of the four iteration reconstructed energy (Figure 5.26), the livetime can be estimated after the final level energy cut of Energy > 25 TeV. This estimation of the livetime does not include the BDT response score cut (see section 5.6) and gives an effective livetime of 121.9 days. However, this can not be extrapolated to estimate the livetime after the final cuts.

Chapter 6

Results

This chapter contains a summary of the results of the high-energy cascade analysis. Fourteen events remained after all filtering cuts were applied to the full IceCube-40 experimental dataset. However, as mentioned in the previous chapter, once the full dataset was examined discrepancies between the simulated muon background distributions and the data became apparent. For this reason additional background simulation was generated after the data was unblinded. This additional muon background is discussed in section 6.2. The new simulation showed that the remaining background at the final cut level is 7.7 events which means that the number of events observed is consistent with the background expectation.

This chapter begins by examining the characteristics of the fourteen data events which were identified by the filtering stages. This is followed by a description of the new background simulation and its implications. The resolutions of the reconstructed variables and the systematic uncertainties of the analysis are also presented.

6.1 Final Events

After all analysis filter levels have been performed the experimental data was unblinded. In addition to the two events in the 10% burn sample, another 12 events are observed.

A summary of the events is shown in Table 6.1, where the date, time, run number, event ID, and number of DOMs hit in each event is listed. The 14 events are distributed throughout the IceCube-40 livetime and are shown in Table 6.1 ordered by date of occurrence. The number of DOMs hit in each event is loosely correlated to the energy.

Event	Date	Time	Run Number	Event ID	DOMs hit
1	18 th Apr 08	09:56:42	110860	10601974	88
2	19 th Apr 08	04:48:26	110862	24088349	139
3	23 rd Apr 08	01:23:14	110884	19256253	194
4	10 th May 08	03:21:05	110964	20513518	76
5	28 th May 08	23:54:42	111076	13154654	103
6	5 th Jun 08	17:20:05	111113	31099997	264
7	6 th Jul 08	21:54:24	111281	8301037	81
8	30 th Aug 08	09:47:41	111558	25342134	123
9	16 th Oct 08	23:32:47	111780	29420816	359
10	8 th Nov 08	02:25:22	111917	729171	121
11	14 th Jan 09	20:43:29	112406	9187097	82
12	6 th Feb 09	21:20:07	112782	26904925	109
13	12 th May 09	13:03:25	113693	4218819	98
14	17 th May 09	21:54:19	113802	17797579	67

Table 6.1: Summary of events: date, time, run number, event ID, and DOMs hit.

Figure 6.1 is an IceCube event viewer display of Event 3. Here the DOMs are depicted by the white dots making up the IceCube-40 detector strings. The coloured circles represent the hits, where their size shows the size of the charge received by the DOM and their colours show the relative hit times. Red hits are early hits in the event and blue hits are later hits in the event. The charge and timing of the event is also depicted along the right side of the event viewer display. Event 3 is the highest energy event observed in this analysis with the highest BDT response score and is well centred within the detector. The energy of this event is 175.28 TeV and the BDT response score is 0.416. All 14 observed events are shown in Appendix A.

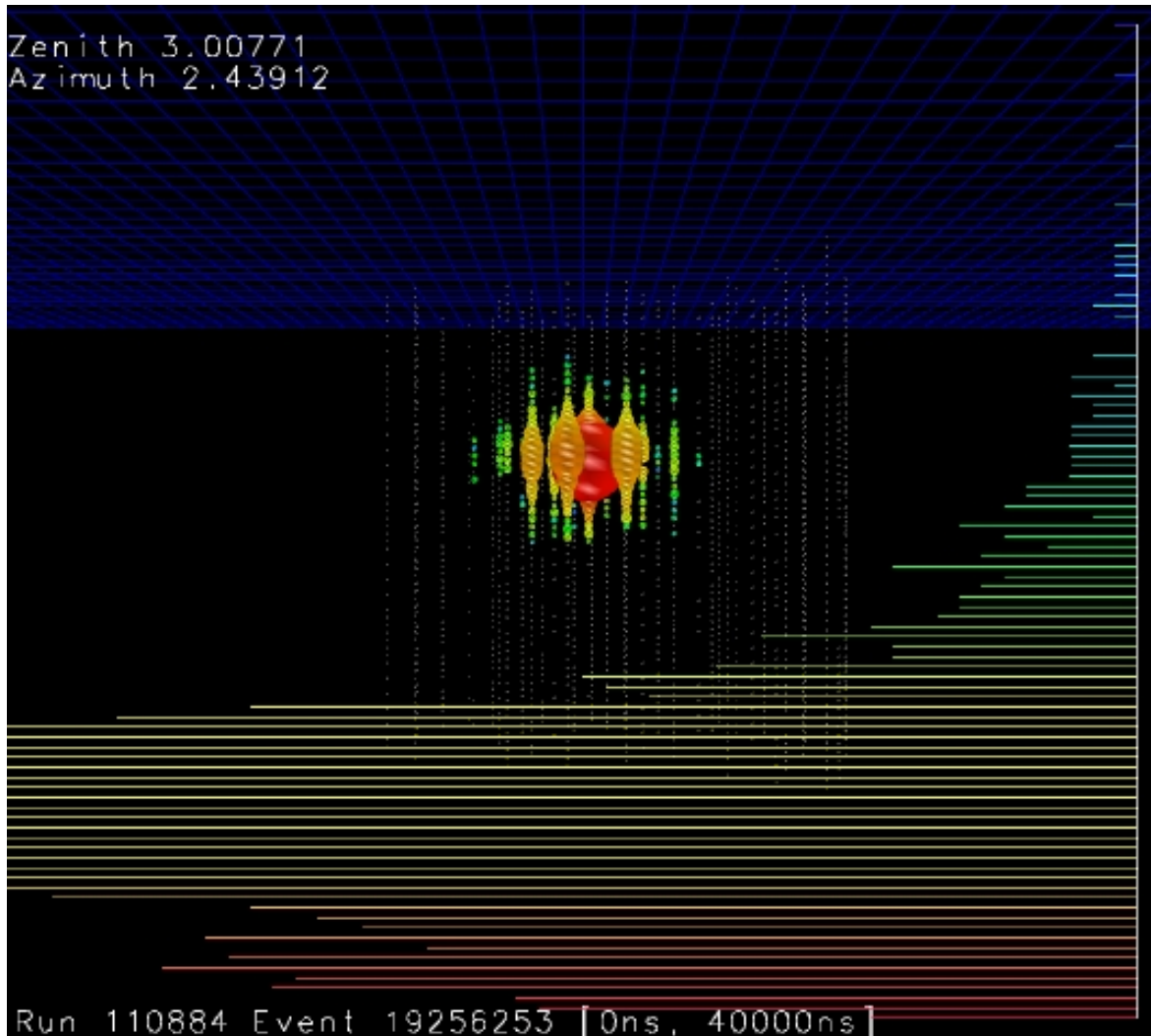


Figure 6.1: Event 3 viewer display. DOMs are depicted by the white dots making up the IceCube strings. Hits are represented by the coloured circles where their size depicts the amount of charge received by the DOM and their colour depicts the timing of the hit (red circles are early hits in the event and blue circles are later). The charge and timing is also depicted along the right hand side of the event viewer display. This is the event with the highest reconstructed energy of 175.28 TeV and the highest BDT response score of 0.416.

In the next few sections the parameters and cut variables of the observed events will be examined with a view to determining whether the events have any characteristics which could allow them to be identified as background. These characteristics can also be used to improve future cascade analyses.

The fourteen events have properties of the high-energy cascade signal that was the target of this analysis. However, additional muon background simulations showed that background muon events can have very similar properties to signal events. It appears that these muon background events form an irreducible background to an astrophysical cascade search. Future IceCube cascade analyses, however will have two main advantages. The first concerns the size of the detector. As the detector is deployed it has a larger effective volume. This means that muon events are more likely to produce track-like topologies in the detector volume that are distinguishable from cascade events. The larger volume of the detector also allows analyses to have stricter containment cuts so that background events can be more easily removed. The second is the upgrade of the hardware of the detector. For analyses later than 2010 the local coincidence criteria was relaxed. This means that some information from DOMs is kept even if the local coincidence is not met. Although this relaxed local coincidence encumbers the experimental dataset with larger datasets to filter, the extra hit information is particularly useful in cascade analyses because it may be used to identify muons entering the detector before catastrophically losing energy in a “cascade-like” event.

In the next sections the location, direction, line-fit velocity, eigenvalue ratio, spatial distance, fill ratio, BDT response score, and energy characteristics of the fourteen remaining events are examined.

6.1.1 Location

Containment cuts restrict the event vertex locations to be within the detector volume. Table 6.2 shows the reconstructed location of the events. The vertex positions (x, y, z) are in metres in the detector coordinates where $(0, 0, 0)$ is the detector centre.

Event	x -position (m)	y -position (m)	z -position (m)
1	-79.58	322.01	201.82
2	442.29	167.46	-427.36
3	5.57	147.82	110.94
4	-310.92	177.57	24.49
5	-226.14	355.98	300.18
6	-159.49	301.21	-230.91
7	326.92	59.76	23.90
8	303.03	210.05	167.72
9	378.63	225.91	-303.59
10	352.15	-17.81	-200.99
11	469.60	56.77	254.13
12	-318.58	169.02	-201.75
13	-225.53	385.72	166.87
14	164.71	138.55	300.26

Table 6.2: Location of events.

Figure 6.2 shows the distribution of event vertex depths in the detector. The 14 events are shown by the black points along with an E^{-2} spectrum neutrino signal shown in green assuming an astrophysical flux of $3.6 \times 10^{-7} \text{ GeVsr}^{-1}\text{s}^{-1}\text{cm}^{-2}$, which is the best current cascade limit [7]. The atmospheric neutrino background is shown by the blue lines, where it is separated into conventional and prompt contributions.

Figure 6.3 shows the xy -coordinates of the vertex locations. The strings of the detector are shown by the black circles, and the 14 event locations by red squares.

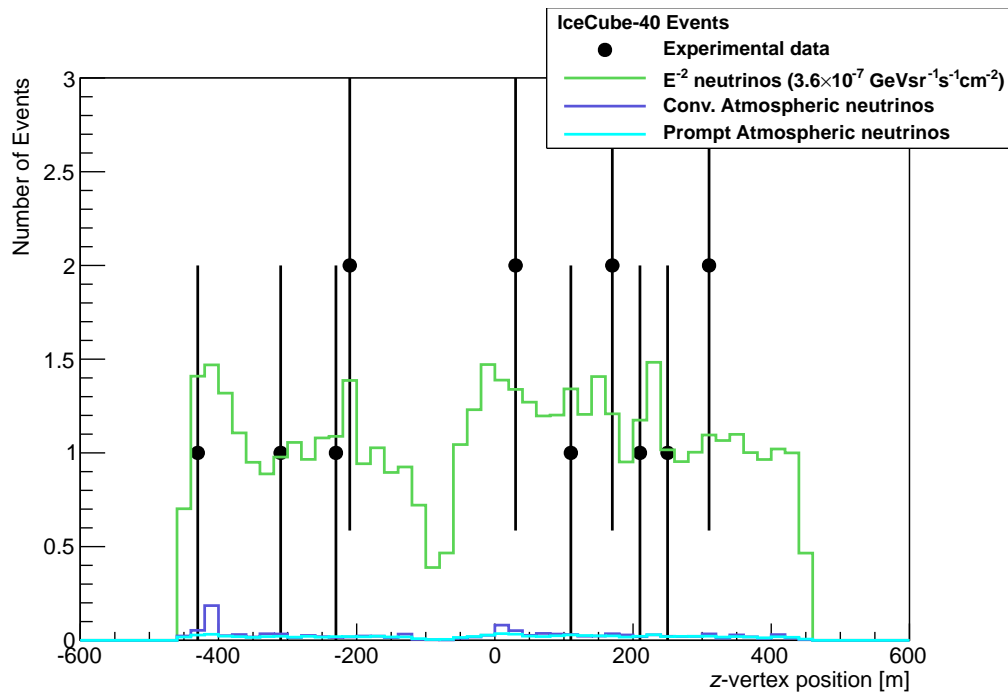


Figure 6.2: Event vertex depth. The predicted all-flavour signal is shown by the green line, the atmospheric neutrino background is shown by the blue lines.

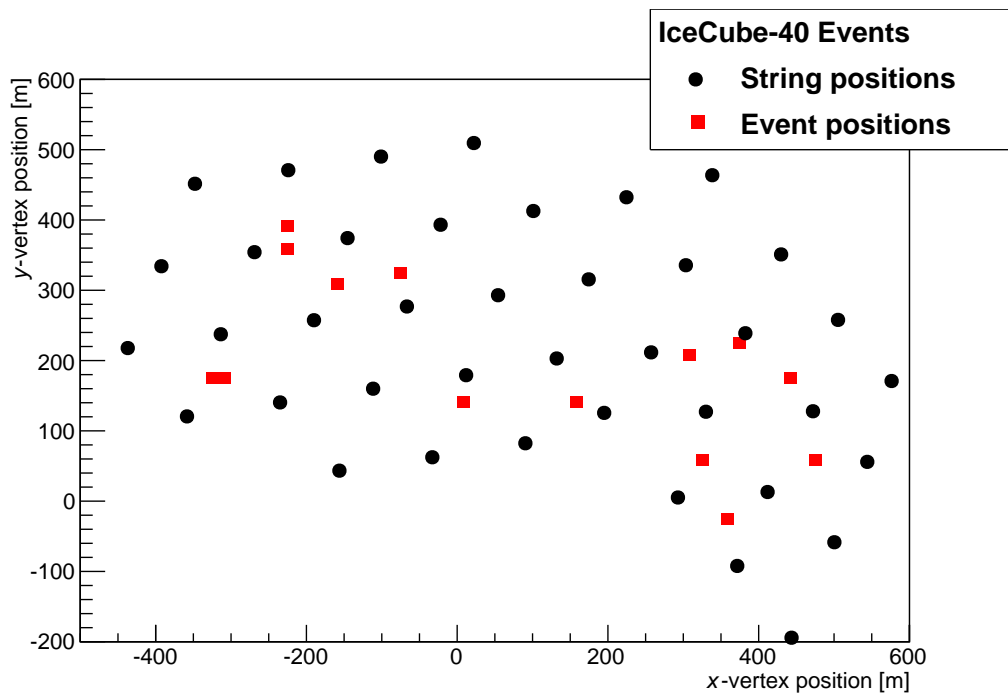


Figure 6.3: Event vertex location in xy -coordinates. The IceCube-40 string positions are shown by the black dots and the event positions are shown by the red squares. All 14 events are contained within the detector area.

6.1.2 Direction

Table 6.3 shows the reconstructed zenith and azimuth directions of the events as calculated by the reconstruction program called Credo [107]. A neutrino originating from directly above the detector has a zenith value of 0° and from directly below has a zenith value of 180° . A neutrino originating from the horizon in the Eastern direction has a zenith value of 90° and an azimuth value of 0° . The events are evenly distributed in azimuth and zenith directions. The uncertainties quoted are from the reconstructed resolution as discussed in section 6.4.2.

Event	Zenith ($^\circ$) $\pm 25.45^\circ$	Azimuth ($^\circ$) $\pm 54.14^\circ$
1	70.58	79.14
2	81.58	305.85
3	172.33	139.75
4	113.87	283.36
5	37.10	161.12
6	129.74	249.59
7	112.33	267.31
8	142.91	53.72
9	72.63	148.70
10	104.65	203.01
11	149.19	210.48
12	107.81	290.94
13	28.06	120.51
14	77.28	284.67

Table 6.3: Direction of events.

Figure 6.4 shows the azimuth direction. The strings of the detector are shown by the black circles and each of the 14 incoming neutrino event azimuth directions by a red arrow, where the point of the arrow is the event vertex. The angular resolution in azimuth is one of the worst resolution for cascades, as shown in section 6.4.2, where it can be seen that the RMS is 54.14° in the azimuth reconstruction. However even with

a large RMS of over 50° the containment of events with a vertex reconstructed near to the edge of the detector can be loosely seen from the general direction. For example, events 4, 7, 10, 12, and 14 have azimuth directions originating from the “inside”, or “other side” of the detector, despite their reconstructed vertex location near the edge of the detector. Such events should arise rarely from atmospheric muons as such a muon would have travelled across the entire detector without leaving any trace of light deposited until the cascade-like event.

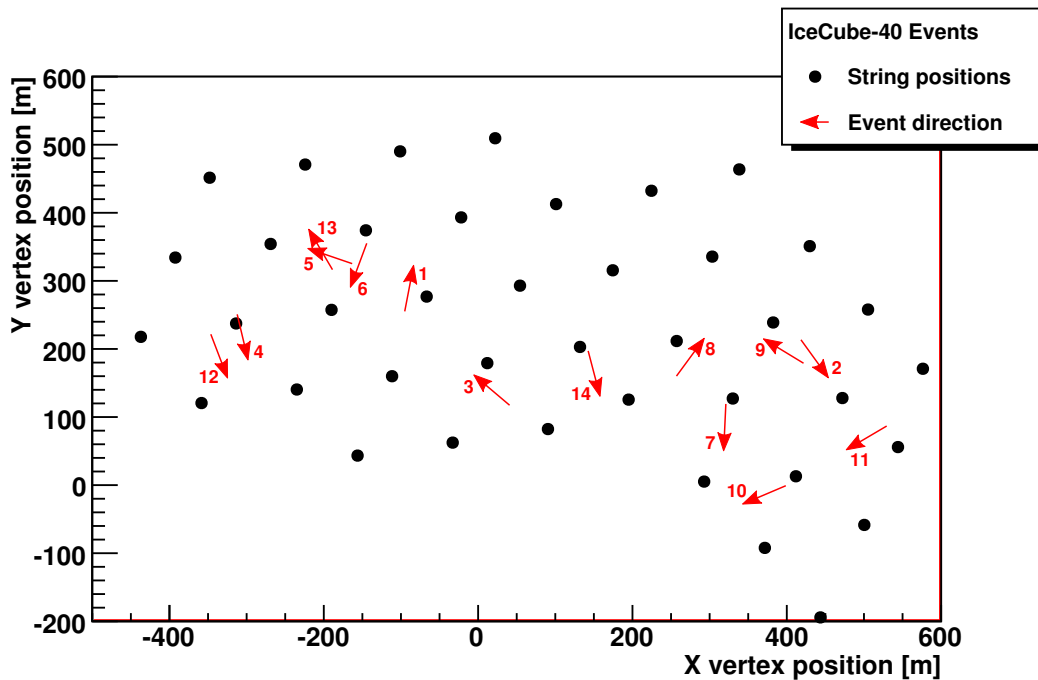


Figure 6.4: Event azimuth directions. The IceCube-40 string positions are shown by the black dots, the arrows show the incoming azimuth direction of the neutrino where the point of the arrow is the event vertex. Each event is labeled with its event number.

Table 6.4 shows the reconstructed values of other low level cut variables. The line-fit velocity and tensor of inertia eigenvalue ratio are determined from the pole filter, the spatial distance and fill ratio from mean are shown from the level 4 filter:

- Line-fit velocity < 0.13
- Tensor of Inertia eigenvalue ratio > 0.12
- Spatial distance < 40 m
- Tensor of Inertia eigenvalue ratio > 0.4

The values of these low level cut variables indicate that the 14 observed events lie far into the cascade signal parameter space.

Event	Line-fit velocity	Eigenvalue ratio	Spatial distance (m)	Fill ratio
	< 0.13	> 0.12	< 40 m	> 0.4
1	0.013	0.283	38.78	0.500
2	0.029	0.260	5.43	0.662
3	0.014	0.286	21.53	0.564
4	0.037	0.269	23.27	0.524
5	0.016	0.261	8.53	0.451
6	0.045	0.304	7.17	0.492
7	0.023	0.246	11.62	0.441
8	0.009	0.249	10.13	0.494
9	0.019	0.291	9.93	0.697
10	0.030	0.293	31.86	0.525
11	0.008	0.268	14.37	0.529
12	0.024	0.263	16.09	0.543
13	0.006	0.260	18.02	0.533
14	0.030	0.219	12.37	0.485

Table 6.4: Other reconstructed cut variables.

6.1.3 BDT and Energy Spectra

The BDT response score and reconstructed energy cuts have the following values:

- BDT response score > 0.2
- Reconstructed energy > 25 TeV,

and are shown for each event in Table 6.5.

The BDT response score and reconstructed energy of the 14 observed events are shown in Figures 6.5 and 6.6. The experimental data is shown by the black points and the all-flavour E^{-2} spectrum neutrino signal is shown by the green line, assuming an astrophysical flux of $3.6 \times 10^{-7} \text{ GeVsr}^{-1}\text{s}^{-1}\text{cm}^{-2}$ [7]. The background from conventional and prompt atmospheric neutrinos is shown by the blue lines. The red vertical line on

Event	BDT response score	Reconstructed energy (TeV)
	> 0.2	> 25 TeV
1	0.268	29.13
2	0.375	30.81
3	0.416	175.28
4	0.230	27.14
5	0.225	41.36
6	0.380	174.09
7	0.293	31.20
8	0.232	45.33
9	0.236	144.20
10	0.279	32.06
11	0.203	46.83
12	0.219	57.19
13	0.295	39.88
14	0.281	27.15

Table 6.5: BDT response score and reconstructed energy of events.

each plot shows the cut value from the final level of analysis cuts.

The BDT response and energy spectra are shown again in Figures 6.7 and 6.8, where the experimental data from below the cuts is shown. In these plots the remaining muon background is also shown below the cut values. However, there are very few background events left at this cut level. If the simulation was reproducing the muon background the red line should follow the experimental data below the cut. This is because the experimental data is assumed to still be dominated by muon background events in this region of the parameter space. Here the mis-match between the background simulation and the experimental data can be seen in the parameter space close to the boundary of the cuts. This deficit of simulated background data led to the generation of additional muon background described in section 6.2.

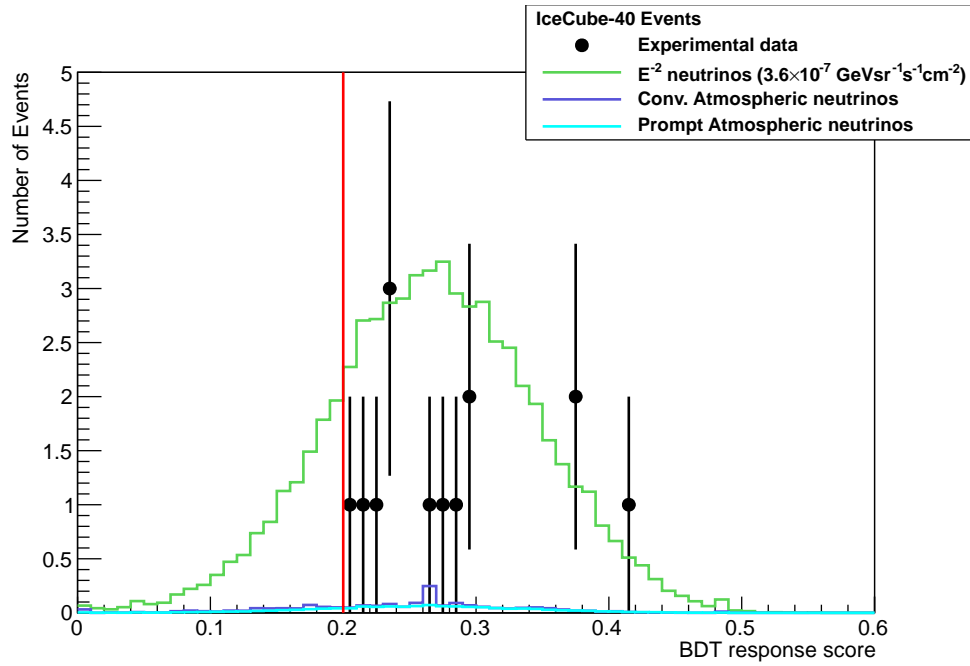


Figure 6.5: BDT response score of the final 14 events. The predicted all-flavour signal is shown by the green line, the atmospheric neutrino background is shown by the blue lines. The cut value is shown in red at BDT response score > 0.2 .

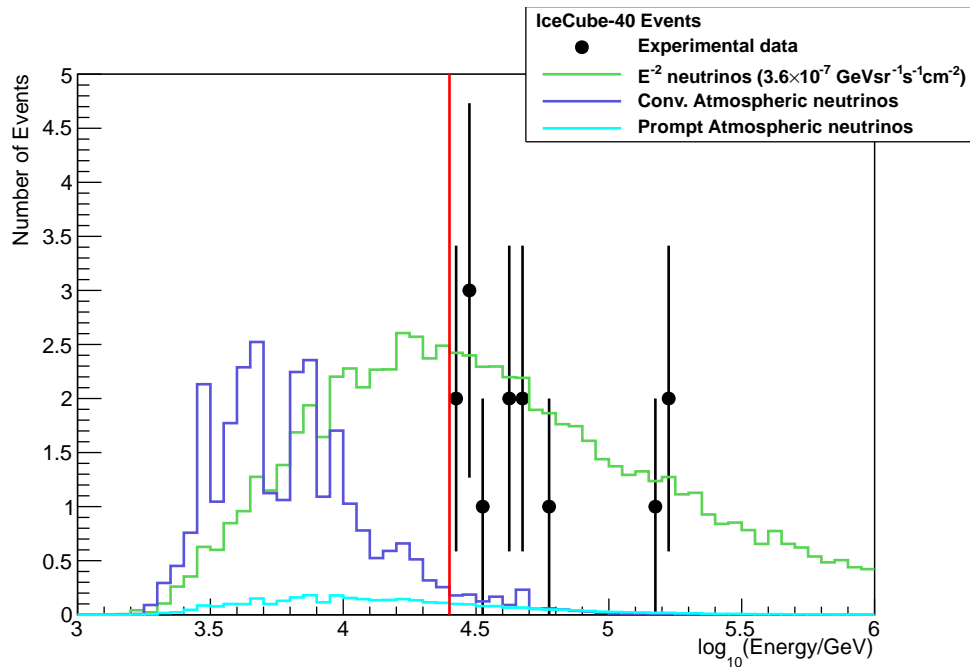


Figure 6.6: Reconstructed energy of the final 14 events. The predicted all-flavour signal is shown by the green line, the atmospheric neutrino background is shown by the blue lines. The cut value is shown in red at Energy > 25 TeV.

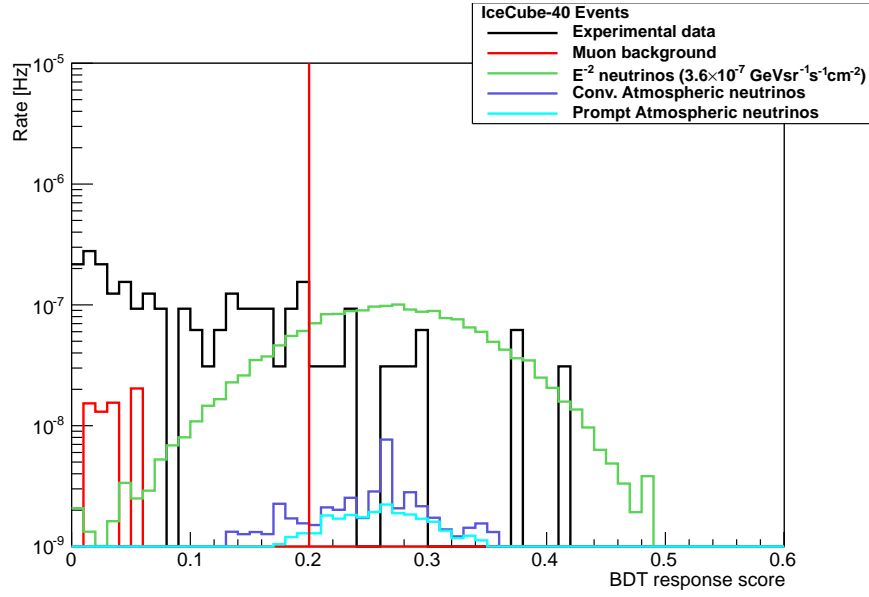


Figure 6.7: BDT response score of the final 14 events and the data below the final BDT response score cut. The predicted all-flavour signal is shown by the green line, the atmospheric neutrino background is shown by the blue lines, and the atmospheric muon background is shown by the red line. The cut value is shown in red at BDT response score > 0.2 .

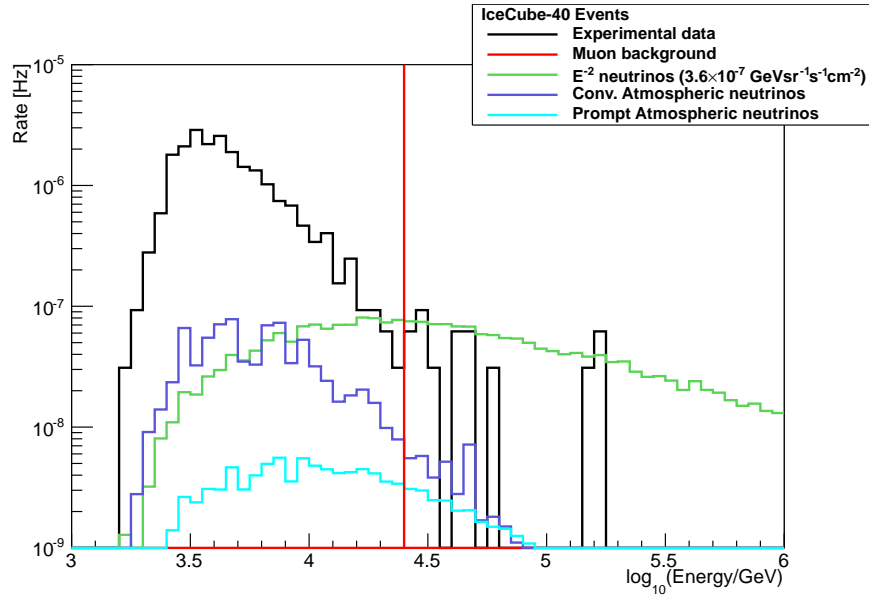


Figure 6.8: Reconstructed energy of the final 14 events and the data below the final energy cut. The predicted all-flavour signal is shown by the green line, the atmospheric neutrino background is shown by the blue lines, and the atmospheric muon background is shown by the red line. The cut value is shown in red at Energy > 25 TeV.

6.1.4 Classification

The 14 observed events can be classified into three categories dependent on their characteristics. The events are classified qualitatively by inspection of their waveforms and event parameters.

Good cascade events

(Events 1, 3, 6, 8, and 9).

Events in this category have reconstructed parameters that are highly consistent with cascade events. These events are also situated close to the centre of the detector. With the vertex far from the edges of the detector it is unlikely that the light pattern could originate from a track-like particle such as a muon leaving no evidence of its track on the outside strings. This category also contains the three highest energy events (> 100 TeV). Event 3 has the highest reconstructed energy and the highest BDT response score, this is the best cascade event candidate detected by IceCube-40.

Likely cascade events

(Events 5, 7, 11, 12, and 13).

Events in this category are also good cascade candidates, although their reconstructed location in the detector is more varied. They are also lower in reconstructed energy.

Evidence of a muon

(Events 2, 4, 10, and 14).

Events in this category have evidence of a muon in the topology. This is indicated from inspection of the timing of the hits. These events contain one early hit, meaning an outer DOM detected light before the DOMs at the vertex of the event. This could mean a muon traveled through the detector leaving little evidence of its track other than an early hit and then produced a cascade-like pattern as it catastrophically lost energy in a bremsstrahlung interaction.

It is technically possible that the last category of events could be cascade events. Given the additional simulation, described in the next section, does predict some atmospheric muon background events it is likely that these events are muon background. The early hits may come from other light in the detector, or from a muon produced in the cascade. Such muons can be produced in a hadronic cascade of high enough energy. The possibility of these types of hybrid muon-cascade events arising from high energy muons being produced within a hadronic cascade is described in Chapter 7.

6.2 Additional Background Simulation

After unblinding there was a large mis-match between the background muon simulation and the experimental data at the highest filter levels observed. Additional muon background was generated to gain a more robust estimate of the background for the analysis. For this additional muon background the two-component Glasstetter spectrum model [63] was used (described in section 4.3.2 and Figure 4.5), although only proton primaries were generated. The original muon background consisted of approximately 1.2×10^9 generated events from proton primaries and the additional simulation consisted of approximately 2.9×10^{11} generated events from proton primaries. This additional simulation was produced over the primary energy range $2500 \text{ GeV} < E_{\text{prim}} < 1 \text{ EeV}$ (rather than $600 \text{ GeV} < E_{\text{prim}} < 100 \text{ EeV}$) because at high-energies there were enough statistics and simulation at low-energies was unnecessary for the analysis and too time consuming. Although these background were simulated over slightly different energy ranges, the increase in the number of generated events provides much more atmospheric muon background simulation for the analysis in the region where it was required.

After all filtering cuts were performed the additional muon background from this simulation has a rate of $2.4 \times 10^{-7} \text{ Hz}$ which corresponds to 7.7 background muon events over the IceCube-40 livetime. This is shown in Table 6.6.

	Rate (Hz)	Number of Events
Additional muon background	2.4×10^{-7}	7.7

Table 6.6: Expected background events from additional simulation.

The livetime plots previously shown in Figures 5.24 and 5.26 can now be re-made including the additional muon background. This is shown in Figures 6.9 and 6.10 for the primary energy and reconstructed energy respectively.

Before the additional muon background simulations were added to the analysis the livetime after filter level 5 cuts was 11.7 days and had completely run out after filter level 6 so was 0 days. When the additional simulation is added to the analysis the livetime after filter level 5 is 18.2 days and after filter level 6 is 52.5 days. This increase in effective livetime is because there are high-energy events remaining which contribute a large weighting in the average effective livetime calculation. This increase in the effective livetime leads to a more reliable estimation of the expected simulated

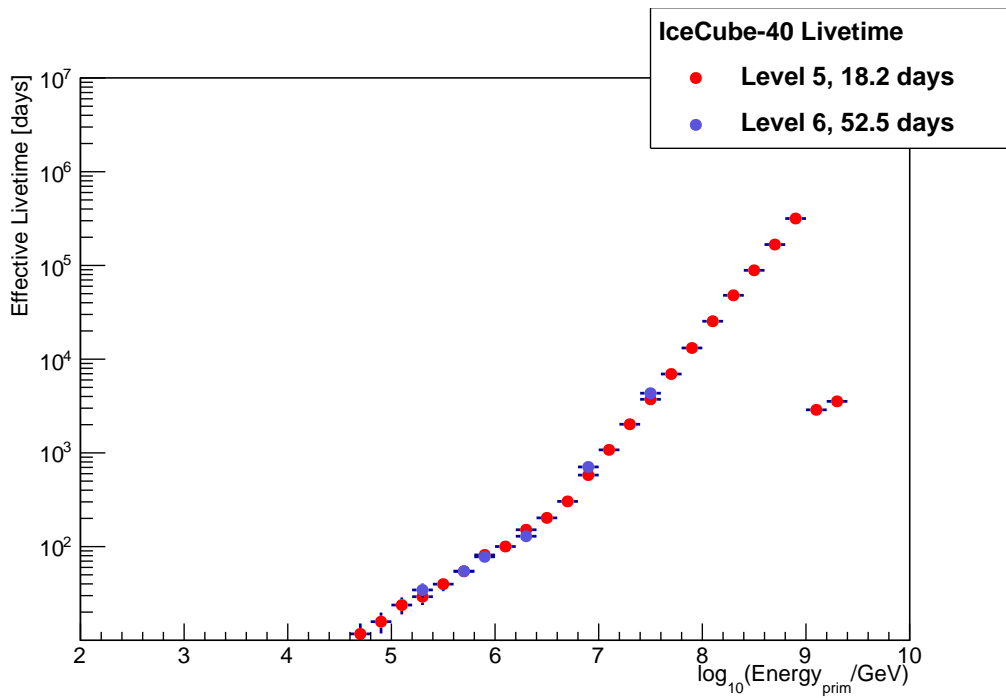


Figure 6.9: IceCube-40 effective livetime of the muon background simulation, using the two-component spectrum, as a function of primary energy.

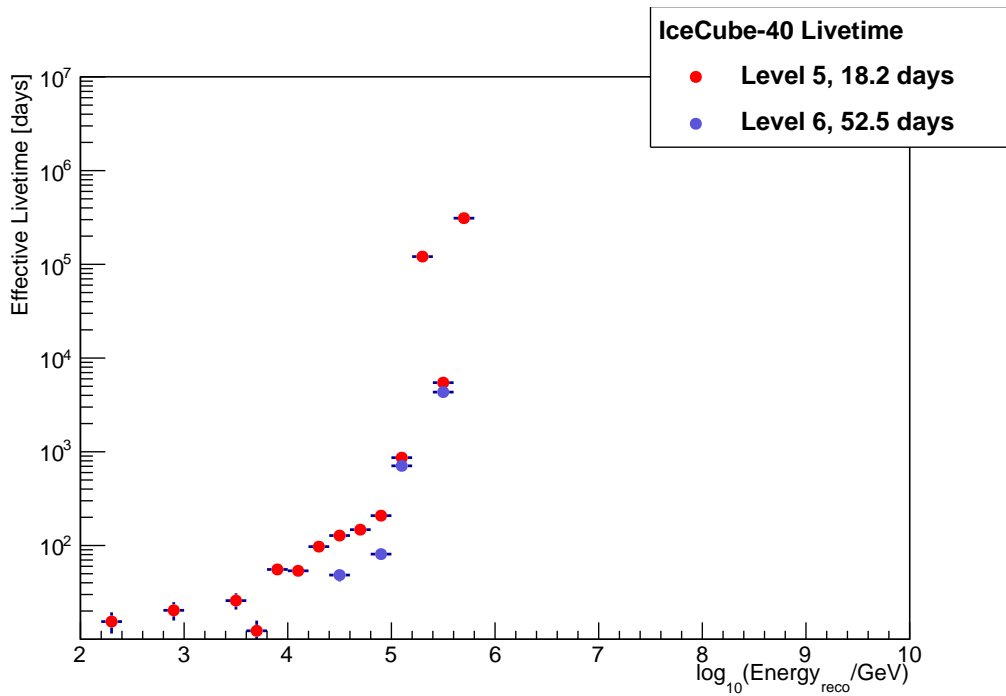


Figure 6.10: IceCube-40 effective livetime of the additional muon background simulation, using the two-component spectrum, as a function of reconstructed energy.

atmospheric muon background and calculation of the astrophysical neutrino flux limit.

Table 6.7 gives a summary of the seven background muon events remaining from the additional simulation after all filter levels. The event viewer displays and event parameters of the remaining seven background muon events are displayed in Appendix B.

Event	Event ID	DOMs hit	BDT response score	Reconstructed energy (TeV)
1	17158	64	0.244	25.40
2	50002	131	0.217	37.28
3	25707	304	0.230	291.67
4	13967	128	0.248	136.38
5	37632	92	0.219	32.73
6	1193	102	0.304	72.46
7	7886	70	0.202	26.78

Table 6.7: Summary of muon background events: event ID, DOMs hit, BDT response score, and reconstructed energy.

The BDT response score and energy spectra are shown again in Figures 6.11 and 6.12. These plots include the additional muon background simulation. Below the final cut values it can be seen that the additional muon background simulation does a much better job of simulating the muon background present within the experimental data. The additional events from this simulation can be used to give a more robust estimation of the muon background to this analysis.

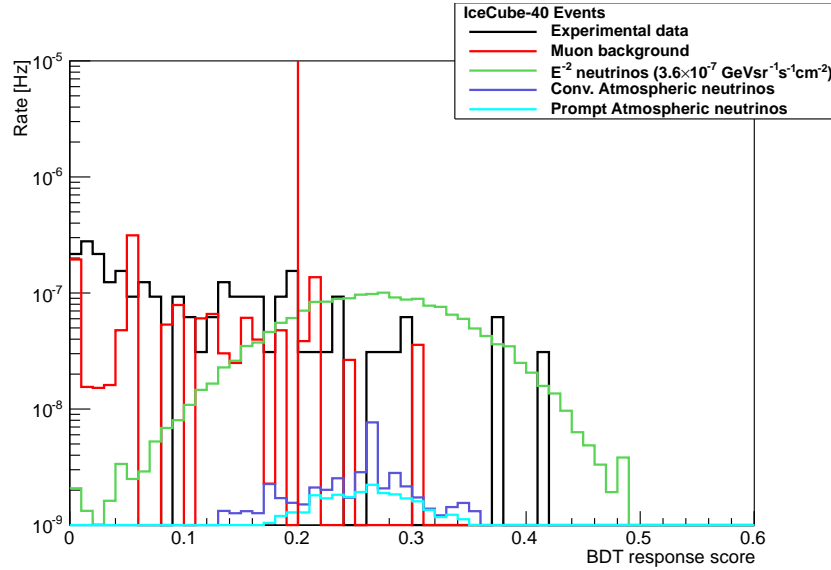


Figure 6.11: BDT response score of the final 14 events and the data below the final BDT response score cut of 0.2 with additional muon background. The predicted all-flavour signal is shown by the green line, the atmospheric neutrino background is shown by the blue lines, and the atmospheric muon background is shown by the red line. The cut value is shown in red at BDT response score > 0.2 .

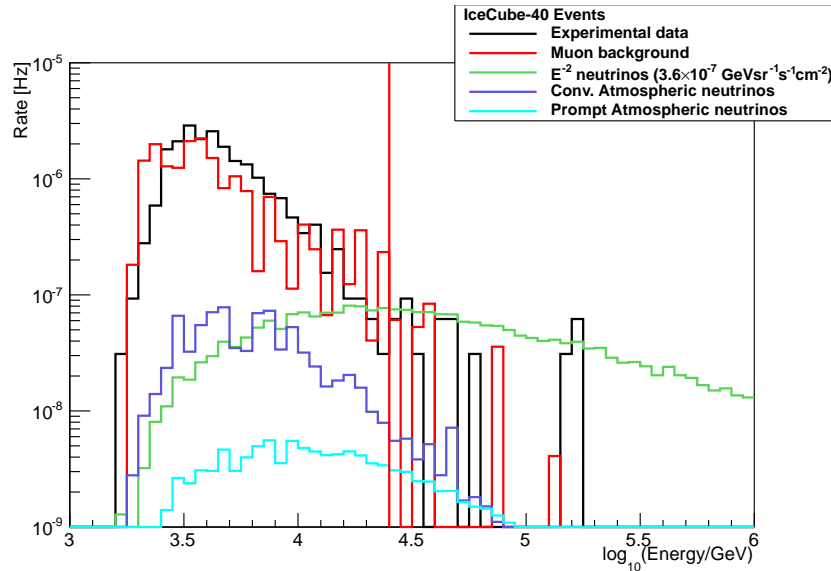


Figure 6.12: Reconstructed energy of the final 14 events and the data below the final energy cut of 25 TeV with additional muon background. The predicted all-flavour signal is shown by the green line, the atmospheric neutrino background is shown by the blue lines, and the atmospheric muon background is shown by the red line. The cut value is shown in red at Energy > 25 TeV.

6.3 Flux Limit

Using the 14 observed high energy cascade candidate events and a background of 2.2 events from atmospheric neutrinos and 7.7 events from atmospheric muons, a flux limit is calculated [77]. In this limit calculation the method of TRolke is used [100]. This approach was taken instead of Feldman-Cousins which was used for the optimisation of the final filter level of cuts, described in section 5.6.1. This is because the TRolke method is more capable of taking into account large uncertainties in the signal and background estimates. The uncertainty on the signal estimates is 28% and on the background estimate is 38% which arise from the systematic uncertainties in the analysis. These are described in section 6.5. For an E^{-2} astrophysical spectrum and assuming a 1: 1: 1 flavour ratio at the detector, the flux limit at a 90% confidence level is

$$\Phi_{\text{lim}} E^2 \leq 7.46 \times 10^{-8} \text{GeVsr}^{-1} \text{s}^{-1} \text{cm}^{-2}. \quad (6.1)$$

Figure 6.13 shows the flux limits from various IceCube analyses, and model predictions. The analyses limits are shown by the coloured lines, with the limit from this work by the black line. The model predictions are shown by the grey lines.

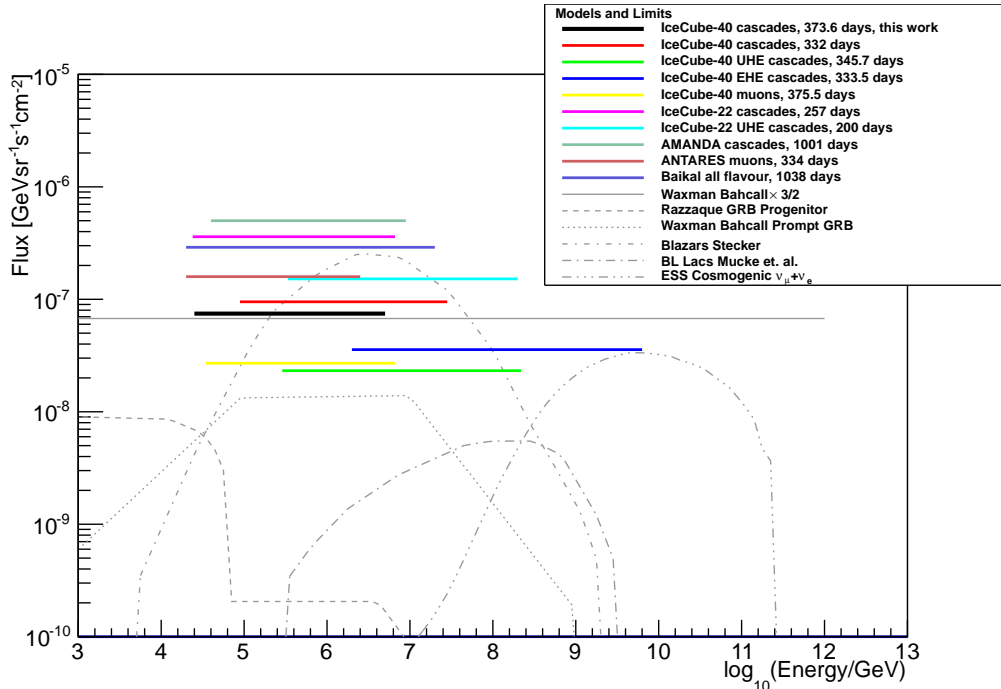


Figure 6.13: IceCube analyses limits and model flux predictions. The analyses are all at the 90% confidence level and are shown by the coloured lines [2, 5–7, 10, 17, 48, 89, 114], with this analysis in black. The model predictions are shown by the grey lines [51, 109, 120, 127, 135, 136].

The energy range for this calculation containing 90% of the signal is from 25.12 TeV to 5011.87 TeV. This limit is higher than some others calculated from IceCube-40 analyses because of the large number of events observed (on a comparatively small background) for the first time. The observation of these events does not rule out the limits set by previous IceCube analyses.

6.4 Reconstruction Resolutions

The accuracy of the reconstruction algorithms can be seen in resolution plots of the simulated neutrino signal. These plots show the difference between the reconstructed value and the true simulated value of the reconstruction quantities.

The main reconstruction algorithm used throughout the high filter levels of this analysis is called Credo [107]. The one iteration Credo reconstruction was run at filter level 3. In filter level 4 the data rate had been reduced enough to rerun Credo with four iterations, using the one iteration reconstruction as its seed and improving the resolution of the reconstructed variables. This section shows the resolution of the energy, direction, and vertex position.

6.4.1 Energy

Figure 6.14 shows the reconstructed energy resolution. The one iteration reconstruction resolution has a mean of -0.26 and an RMS of 0.30 . The four iteration reconstruction resolution has a mean of -0.28 and an RMS of 0.29 . This plot shows that the four iteration reconstruction does not over-estimate the reconstructed energy to the large extent that the one iteration reconstruction does. This is particularly important in a high-energy cascade analysis because the filter level cuts rely on the energy reconstruction.

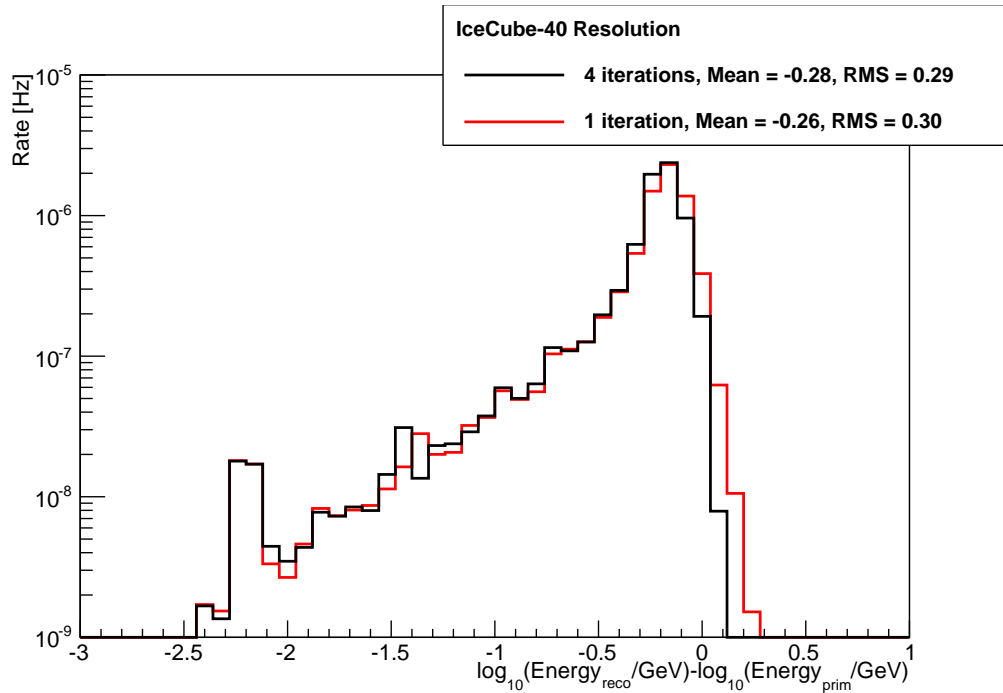


Figure 6.14: Energy resolution. The red line shows the one iteration resolution from filter level 3, the black line shows the four iteration resolution from filter level 4.

6.4.2 Direction

Cascade reconstructions have poor directional resolution compared to the reconstructions for track-like events because of their spherical light pattern in the detector. Despite this, some directional information is still obtained from cascade events.

Figure 6.15 shows the reconstructed zenith angle resolution. The one iteration reconstruction resolution has a mean of 26.26° and an RMS of 44.94° . The four iteration reconstruction resolution has a mean of 14.93° and an RMS of 25.29° . The zenith angle reconstruction shows the greatest improvement in resolution when running the four iteration reconstruction.

Figure 6.16 shows the reconstructed azimuth angle resolution. The one iteration reconstruction resolution has a mean of 2.40° and an RMS of 68.38° . The four iteration reconstruction resolution has a mean of 0.23° and an RMS of 53.55° . The azimuth angle reconstruction is the weakest reconstruction because of the wider string spacing in the xy -plane compared to the xz -plane and the yz -plane. The four iteration reconstruction provides some improvement in the azimuth resolution.

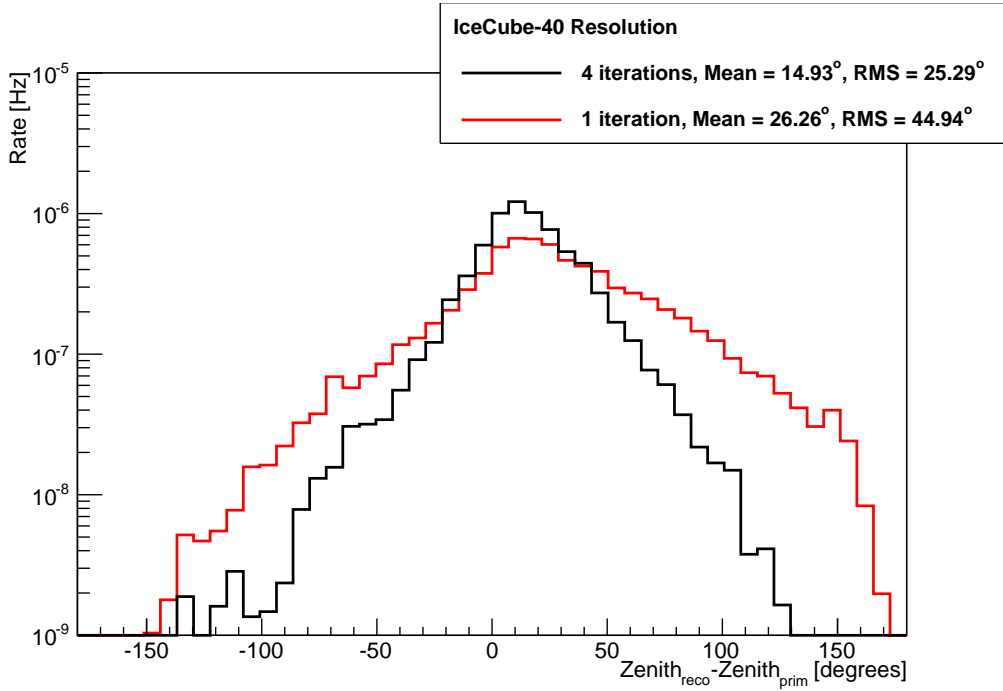


Figure 6.15: Zenith resolution. The red line shows the one iteration resolution from filter level 3, the black line shows the four iteration resolution from filter level 4.

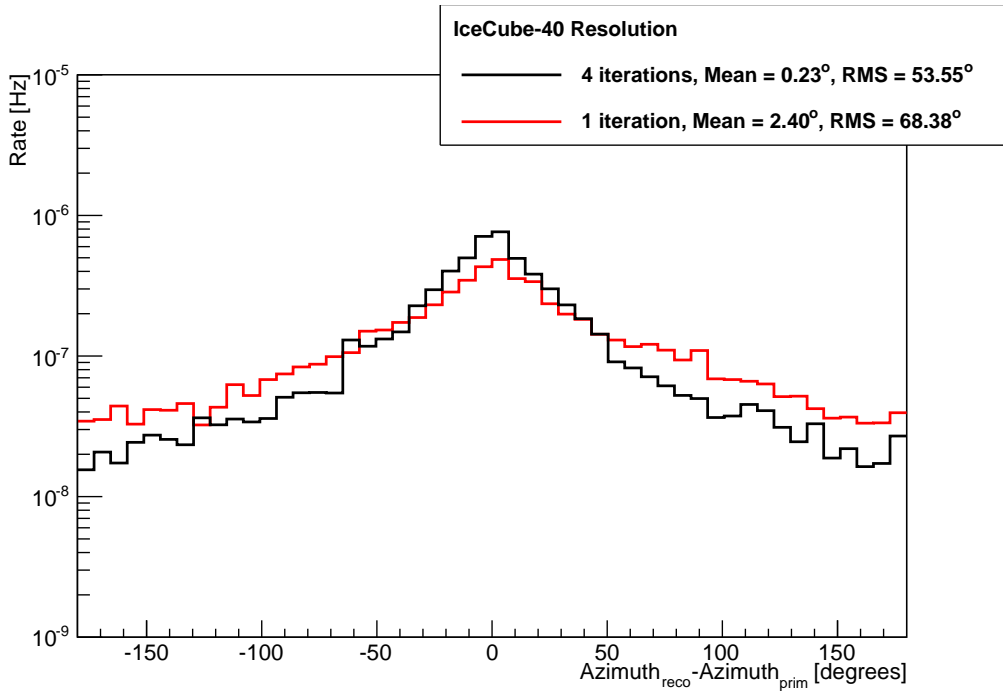


Figure 6.16: Azimuth resolution. The red line shows the one iteration resolution from filter level 3, the black line shows the four iteration resolution from filter level 4.

6.4.3 Position

The accuracy of the vertex position reconstruction is important in a cascade analysis because of the containment cuts used throughout the filter levels. The event vertex

position influences other reconstructed variables, especially the energy reconstruction.

Figure 6.17 shows the reconstructed x -vertex position resolution. The one iteration reconstruction resolution has a mean of 0.41 m and an RMS of 11.88 m. The four iteration reconstruction resolution has a mean of 0.12 m and an RMS of 8.17 m. Running the four iteration reconstruction greatly improves the x -vertex position resolution.

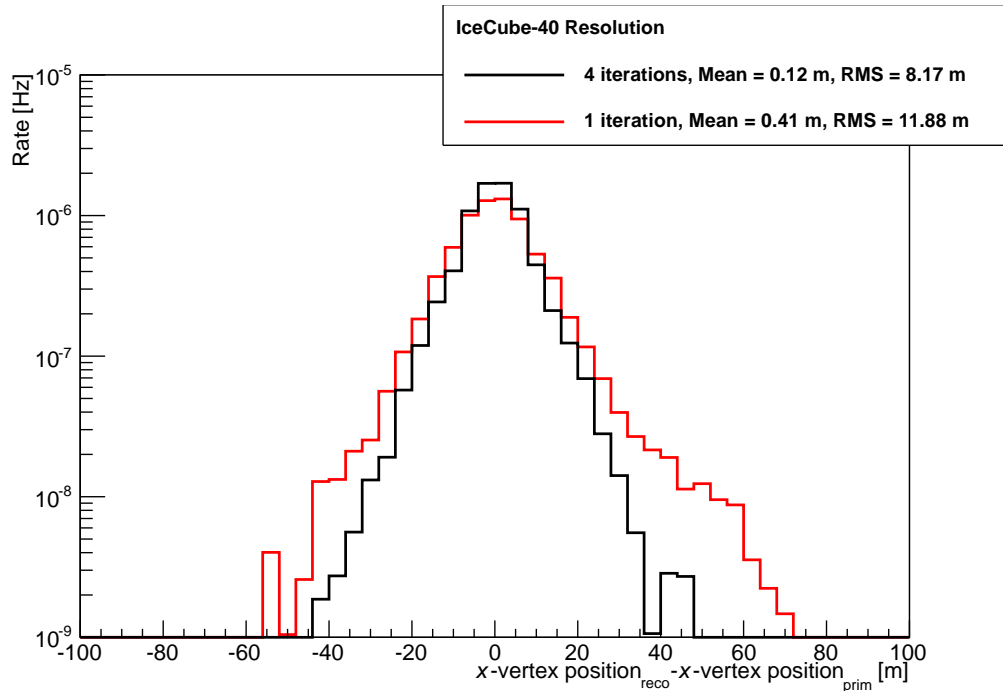


Figure 6.17: x -vertex resolution. The red line shows the one iteration resolution from filter level 3, the black line shows the four iteration resolution from filter level 4.

Figure 6.18 shows the reconstructed y -vertex position resolution. The one iteration reconstruction resolution has a mean of 0.27 m and an RMS of 11.24 m. The four iteration reconstruction resolution has a mean of 0.16 m and an RMS of 8.07 m. The y -axis of the IceCube-40 detector is shorter than the x -axis, so the mean and RMS of the resolution is similar but slightly improved over the x -vertex position resolution.

Figure 6.19 shows the reconstructed z -vertex position resolution. The one iteration reconstruction resolution has a mean of -2.83 m and an RMS of 7.37 m. The four iteration reconstruction resolution has a mean of -1.08 m and an RMS of 4.59 m. The resolution of the vertex depth in the detector is the best of the position reconstructions because the uncertainty in the vertical depth is the smallest due to the smaller spacing between the DOMs along the strings in the z -direction.

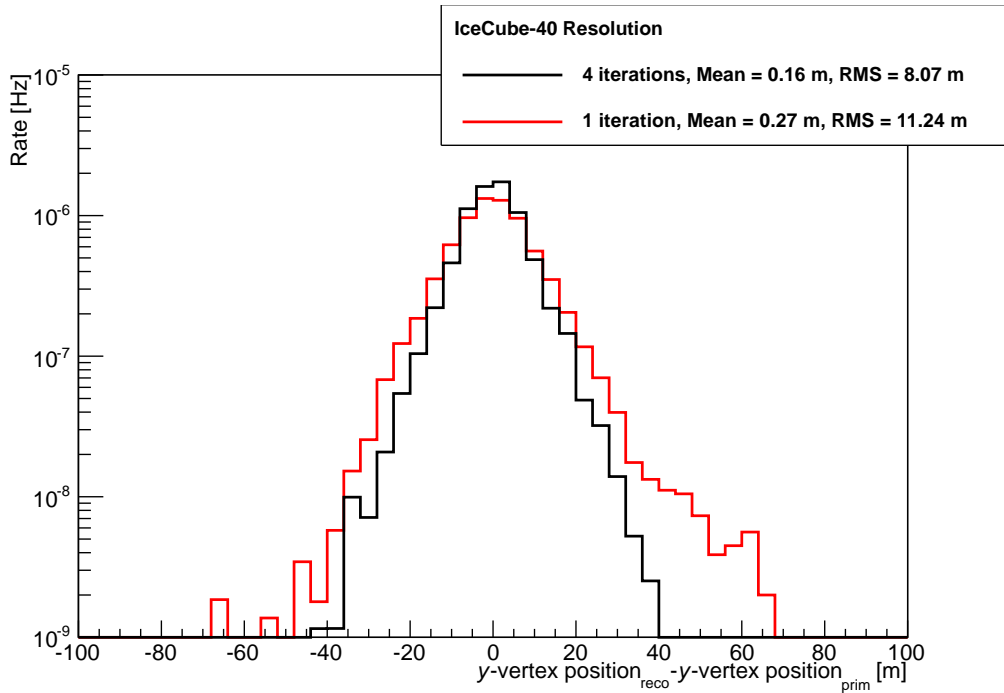


Figure 6.18: y -vertex resolution. The red line shows the one iteration resolution from filter level 3, the black line shows the four iteration resolution from filter level 4.

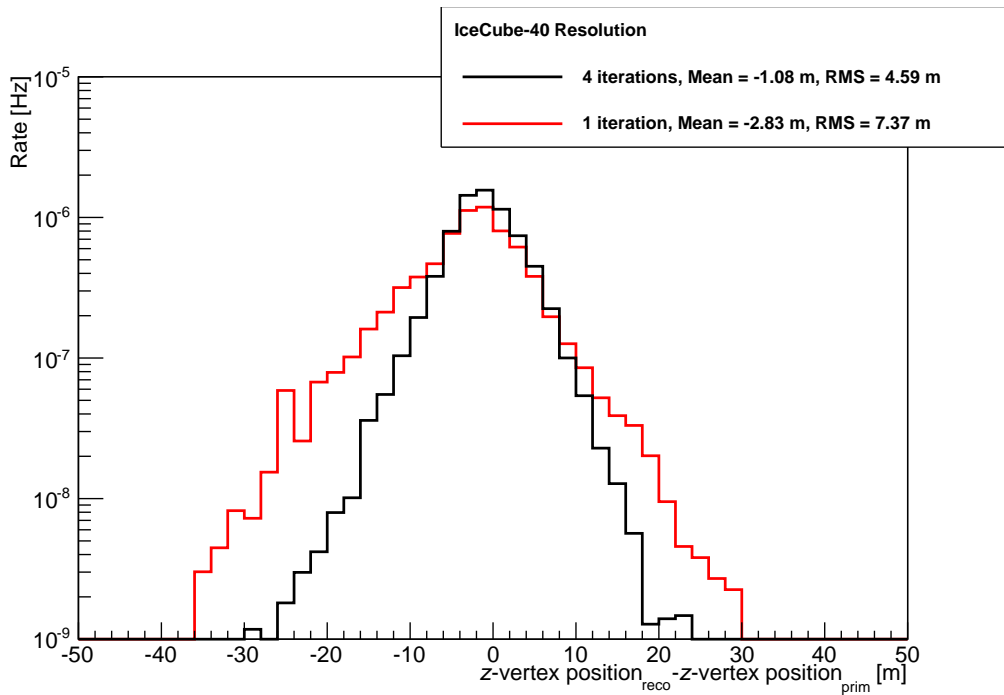


Figure 6.19: z -vertex resolution. The red line shows the one iteration resolution from filter level 3, the black line shows the four iteration resolution from filter level 4.

6.5 Systematic Uncertainties

The simulation of ice properties throughout the detector volume contributes large uncertainty to the simulated E^{-2} spectrum neutrino signal, atmospheric neutrino back-

ground, and atmospheric muon background. The simulation of DOM efficiency contributes uncertainty to the simulated E^{-2} spectrum neutrino signal and the simulated atmospheric neutrino background. These simulations are also affected by the neutrino-nucleon cross-section model used. A small contribution of systematic uncertainty to the simulated atmospheric muon background also arises from the atmospheric model used in the simulations. These systematic errors are described in this section.

The E^{-2} spectrum is chosen as a standard spectrum to search for evidence of astrophysical neutrinos. In the future it would be useful to investigate the limit that could be placed on alternate spectral indices or, if an excess of events is seen over the expected background, the spectral index of these events could be fitted.

6.5.1 Ice properties

The largest systematic uncertainty originates from the simulation of the ice properties at the South Pole. Flasher data from calibration runs, described in section 3.2.1, is used to develop ice models by measuring absorption and scattering at different points throughout the ice with the known light source [14]. An ice model contains the depth, wavelength, and temperature dependent information throughout the detector and surrounding ice and bedrock. In simulation this information is passed into the PHOTONICS [101] photon propagation algorithms.

The model used in all simulations for this analysis is the *Additionally Heterogeneous Absorption* (AHA) model [14]. This model, developed in 2007, superseded the MILLENNIUM [14] ice model. To carry out a study of the uncertainties arising from the ice model, simulated datasets were produced using an updated ice model. This model, called *South Pole ICE* (SPICE) [9], was developed after this analysis was complete. The version of SPICE used for systematic studies was released in 2009, improvements have since followed. Approximately 5.12×10^8 events of single weighted muon background simulation and approximately 3.96×10^6 events of electron neutrino simulation were generated using the SPICE model for systematic studies.

- **Muon background**

No background events passed filter levels 5 or 6 from the SPICE simulation, so the systematic uncertainty is estimated after filter level 4 is performed. The rate of the SPICE muon background after filter level 4 is 1.6×10^{-2} Hz, compared to a rate of 1.4×10^{-2} Hz using the AHA ice model. This gives an ice property systematic uncertainty for atmospheric muon background of $\pm 12.4\%$.

- **Atmospheric neutrino background**

The atmospheric neutrino background rate using the SPICE model is 3.3×10^{-8} Hz after all filtering cuts are performed. The rate using the AHA ice model is 3.9×10^{-8} Hz. This gives an ice property systematic uncertainty for atmospheric neutrino background of $\pm 16.3\%$.

- **E^{-2} spectrum neutrino signal**

The E^{-2} spectrum neutrino signal rate using the SPICE model is 5.9×10^{-6} Hz after all filtering cuts are performed. The rate using the AHA ice model is 7.8×10^{-6} Hz. This gives an ice property systematic uncertainty for E^{-2} spectrum neutrino signal of $\pm 24.9\%$.

6.5.2 DOM efficiencies

A DOM's efficiency is the ratio of the light collected by a DOM to the total light incident upon the DOM. The DOM efficiency includes the quantum efficiency of the PMT and the transmissivity of the optical gel and glass of each sphere. All DOMs in the IceCube-40 detector operate at $\pm 10\%$ efficiency [4]. Approximately 1.2×10^7 events of muon neutrino simulation were generated with 90% DOM efficiency and approximately 1.2×10^7 events of muon neutrino simulation were generated with 110% DOM efficiency for systematic studies.

- **Atmospheric neutrino background**

The atmospheric neutrino background rate using 90% DOM efficiency is 2.0×10^{-8} Hz and using 110% DOM efficiency is 3.2×10^{-8} Hz, after all filtering cuts are performed. The rate using the standard 100% DOM efficiency is 2.8×10^{-8} Hz. This gives a DOM efficiency systematic uncertainty for atmospheric neutrino background of -30.0% and $+15.2\%$.

- **E^{-2} neutrino signal**

The E^{-2} spectrum neutrino signal rate using 90% DOM efficiency is 1.7×10^{-6} Hz and using 110% DOM efficiency is 1.9×10^{-6} Hz, after all filtering cuts are performed. The rate using the standard 100% DOM efficiency is 1.9×10^{-6} Hz. This gives a DOM efficiency systematic uncertainty for E^{-2} spectrum neutrino signal of -10.3% and $+2.4\%$.

6.5.3 Neutrino Cross-sections

This analysis uses neutrino-nucleon cross-sections from HTEQ [60]. An alternative cross-section model is CSS [41]. Approximately 2.5×10^6 electron neutrino events were generated with CSS cross-sections for systematic studies.

- **Atmospheric neutrino background**

The atmospheric neutrino background rate using the CSS cross-section model is 3.6×10^{-8} Hz after all filtering cuts are performed. The rate using the HTEQ cross-section model is 3.9×10^{-8} Hz. This gives a neutrino cross-section systematic uncertainty for atmospheric neutrino background of $\pm 9.0\%$.

- **E^{-2} spectrum neutrino signal**

The E^{-2} spectrum neutrino signal rate using the CSS cross-section model is 7.1×10^{-6} Hz after all filtering cuts are performed. The rate using the HTEQ cross-section model is 7.8×10^{-6} Hz. This gives a neutrino cross-section systematic uncertainty for E^{-2} spectrum neutrino signal of $\pm 8.7\%$.

6.5.4 Seasonal variation

The atmosphere above the IceCube detector varies throughout the year. This is because of temperature and pressure variations in the layers of the Antarctic atmosphere [13]. The muon background simulation is generated assuming an October atmosphere because this is close to the average for the whole year. The systematic uncertainty from seasonal variation is small but still contributes to the overall uncertainty of the background simulation. The E^{-2} spectrum neutrino signal and the atmospheric neutrino background simulations both use an average atmosphere so seasonal variation does not contribute to their systematic uncertainties.

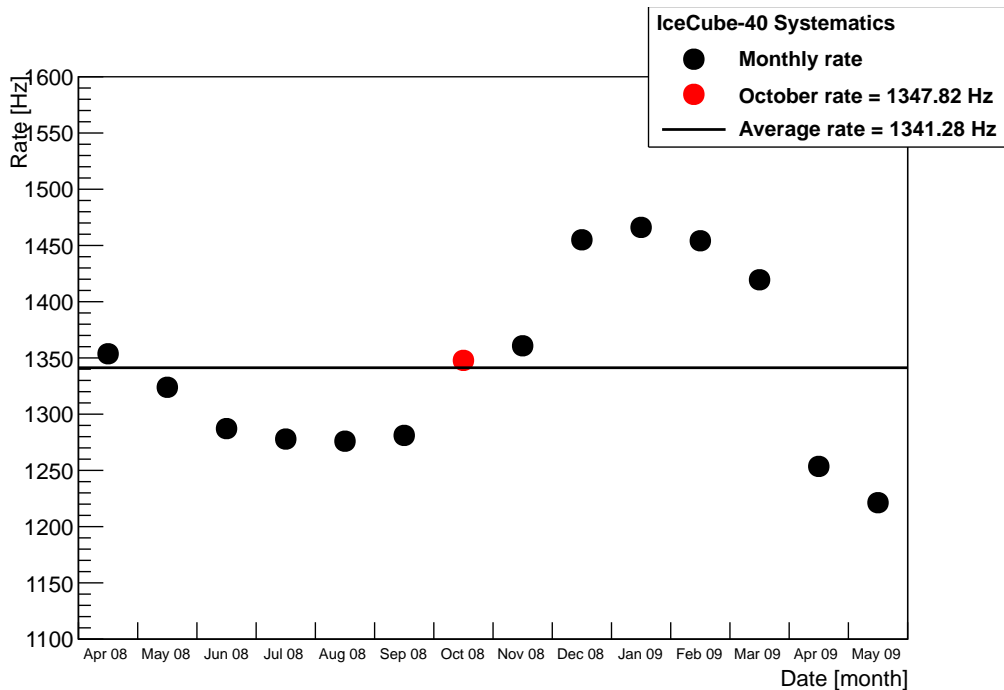


Figure 6.20: Seasonal variation in rate at trigger level for IceCube-40. Average values for each month in the IceCube-40 experimental data are shown. October, the atmosphere used for simulation, is highlighted in red. The average over the entire IceCube-40 livetime is shown by the black line.

Figure 6.20 shows the seasonal variation for IceCube-40. Using the 10% burn sample of experimental data, the rate for each month is plotted. The average rate over the entire IceCube-40 livetime is 1341 Hz, shown by the black line. This compares to an average October rate of 1348 Hz which is the value used in the generation of the muon background simulation. This gives a seasonal variation systematic uncertainty on atmospheric muon background of $\pm 0.5\%$.

6.5.5 Total systematics

Table 6.8 shows a summary of the systematic uncertainties in this analysis described in this section. The total systematic uncertainty for each type of simulation is obtained by the square-root of the sum of the squares from each independent systematic source.

	E^{-2} neutrino signal	Atmospheric background	Muon background
Ice properties	$\pm 24.9\%$	$\pm 16.3\%$	$\pm 12.4\%$
DOM efficiencies	$-10.1\% + 2.4\%$	$-30.0\% + 15.2\%$	-
Cross-sections	$\pm 8.7\%$	$\pm 9.0\%$	-
Seasonal variation	-	-	$\pm 0.5\%$
Total	$-28.2\% + 26.5\%$	$-35.3\% + 24.0\%$	$\pm 12.4\%$

Table 6.8: Systematic uncertainties.

Chapter 7

Muons In Hadronic Cascades

High energy hadronic cascades contain muons. If a muon is energetic enough it will traverse a significant distance through the detector, changing the topology of the cascade. This has implications for the development of high energy cascade analyses and for the interpretation of results. This chapter introduces these hybrid muon-cascade events and presents the simulations performed to parameterise the muon flux in high energy hadronic cascades. This work is independent of the cascade analysis presented in earlier chapters, however, the results may be used to improve future cascade analyses.

7.1 Hadronic Cascades

As described in Chapters 2 and 3 a hadronic cascade arises in the IceCube detector when a neutrino interacts with a nucleon in the ice. In this interaction the energy of the collision splits the nucleus to produce quark singlets and hadrons are produced by jet fragmentation [124]. The energy transferred to the cascade is typically about 20% of the incoming neutrinos energy [60]. However, there are large fluctuations in the neutrino-nucleon interaction and in some cases almost all of the neutrino's energy can be transferred into the hadronic cascade [60].

Hadronic cascade events can be differentiated from electromagnetic cascades by their event topology. Hadronic cascades begin with quark singlets from nuclei which interact via hadronic processes to produce further hadrons. This is in contrast to an electromagnetic cascade whose particles only interact via electromagnetic interactions. The spread of a hadronic cascade is broader than that of an electromagnetic cascade as the individual particle tracks within the cascade spread further apart from each other.

The Cherenkov photons produced from charged particles in both hadronic and electromagnetic cascades are scattered while propagating through the detector medium so that the light distribution becomes spherical. However in hadronic cascades the light distribution is less isotropic because not all particle tracks point back towards the centre of the cascade. The Cherenkov light from a hadronic cascade is somewhat dimmer than that from an electromagnetic cascade because of the presence of neutral particles in the hadronic cascade [137].

Another unique occurrence in hadronic cascades is the production of long range particles such as muons. A muon, if produced with high enough energy, can travel through the detector. If the distance travelled is significant, greater than the DOM and string spacing, then the track-like properties change the topology of the event. This can greatly affect the reconstructed variables of the event and consequently the cut values in an analysis. A representation of a long range muon produced in a hadronic cascade is shown in Figure 7.1, where it can be seen that the topology of the event can be dramatically altered due to the light from the muon.

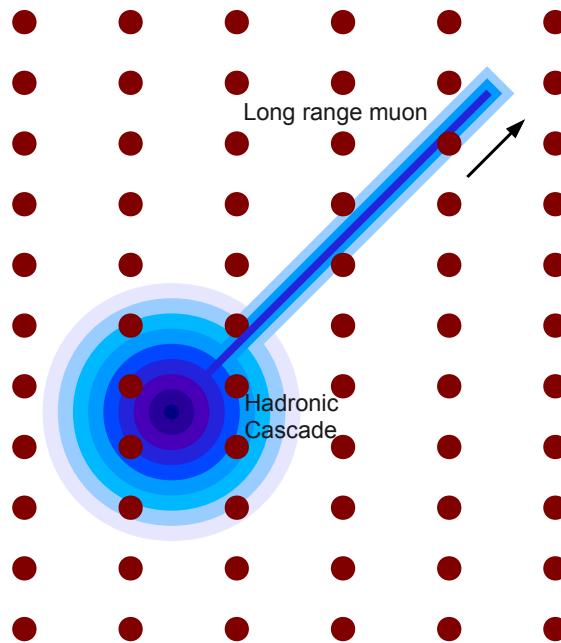


Figure 7.1: A high energy muon produced in a hadronic cascade. DOMs are depicted by red circles, the muon travelling across the detector significantly changes the topology of the cascade event.

Accurate simulation of the signal and the background is required for neutrino searches, as discussed in previous Chapters. The simulation of high energy muons originating from hadronic cascades is important for the interpretation of these events.

Such an event may reconstruct as background when it is signal and may be wrongly removed from an analysis. Simulation of muon production in high energy cascades provides the expected muon flux in a cascade analysis and leads to refined reconstruction variables that may be used in future analyses.

7.2 Theory

An analytical model exists for the development of electromagnetic cascades called the Heitler model [74]. The development of hadronic cascades is more complex because of the variety of particles produced. However, the Heitler model can be extended [103] to describe the production of muons within a hadronic cascade.

7.2.1 Electromagnetic Cascades

An electromagnetic cascade contains photons, electrons, and positrons. Photons create electron-positron pairs via pair production. The electron and positron then radiate photons via bremsstrahlung. In the Heitler model of electromagnetic cascades [74] these interactions are forced to occur after each interaction length and the primary energy is distributed evenly to the particles at each interaction so that throughout the progression of an electromagnetic cascade the energies of the particles is reduced.

The total charged track length of the electromagnetic cascade is the sum of the length of the tracks from all the particles in the cascade, calculated from the total amount of Cherenkov light detected [76]. All the electrons and positrons produce their own Cherenkov cone, so the light produced from an electromagnetic cascade appears as a diffuse ring of light. The total track length is proportional to the energy of the electromagnetic cascade [131].

7.2.2 Hadronic Cascades

A hadronic cascade contains many more types of particles than an electromagnetic cascade. These particles undergo more interactions so the hadronic cascade needs a more complex model to describe its development. This is done in the extended Heitler model [103]. This model assumes that ten hadrons are produced in each interaction. One third of the hadrons produced will be neutral particles such as the π^0 . These will then produce an electromagnetic sub-cascade by decaying to two gamma particles.

The reaction channels for different hadrons is neglected and a constant branching ratio is assumed independent of the incident particle.

Muons are mainly produced from the decay of pions and kaons so these are the hadrons that are important in this parameterisation. The muon flux is a function of particle energy and is given by the hadron flux multiplied by the decay probability.

7.2.3 Decay

The pions and kaons produced in a hadronic cascade will lose energy, through processes such as ionization, until they undergo decay.

The probable decay modes and corresponding branching ratios for pions are shown in Table 7.1. The charged pion has a branching ratio of 99.99% for decay to a muon, so it can be assumed that every charged pion in the hadronic cascade will produce a muon.

Decay mode	Branching ratio
$\pi^\pm \rightarrow \mu^\pm + \nu_\mu$	99.99%
$\pi^0 \rightarrow \gamma + \gamma$	98.80%
$\pi^0 \rightarrow e^+ + e^- + \gamma$	1.20%

Table 7.1: Branching ratios for pion decay modes, from [66].

The probable decay modes and corresponding branching ratios for kaons are shown in Table 7.2. A charged kaon in a hadronic cascade will not always produce a muon, however, kaon decay often results in a charged pion which will subsequently decay, producing a muon.

The pions and kaons in the hadronic cascade may either decay in flight, or slow down to a stop. Those that decay in flight will produce high energy muons. Of those that slow to a stop, the negatively charged particles may get captured by the Coulomb field of a nearby atom in the surrounding medium. This occurs because of the central positive charge of the atom and is called a pionic or kaonic atom [26] because the pion or kaon has taken the place of an electron. This particle is now analogous to a nucleon in an excited state and loses energy by evaporation of low energetic particles leaving the nucleus.

Decay mode	Branching ratio
$K^\pm \rightarrow \mu^\pm + \nu_\mu$	63.43%
$K^\pm \rightarrow \pi^0 + e^\pm + \nu_e$	4.87%
$K^\pm \rightarrow \pi^0 + \mu^\pm + \nu_\mu$	3.27%
$K^\pm \rightarrow \pi^\pm + \pi^0$	21.13%
$K^\pm \rightarrow \pi^\pm + \pi^0 + \pi_0$	1.73%
$K^\pm \rightarrow \pi^\pm + \pi^\pm + \pi_\mp$	5.58%
$K_S^0 \rightarrow \pi^+ + \pi^-$	68.60%
$K_S^0 \rightarrow \pi^0 + \pi^0$	31.40%
$K_L^0 \rightarrow \pi^\pm + e^\mp + \nu_e$	38.79%
$K_L^0 \rightarrow \pi^\pm + \mu^\mp + \nu_\mu$	27.18%
$K_L^0 \rightarrow \pi^0 + \pi^0 + \pi_0$	21.08%
$K_L^0 \rightarrow \pi^+ + \pi^- + \pi_0$	12.58%

Table 7.2: Branching ratios for kaon decay modes, from [66].

Because of this process there will be fewer muons produced from the decay of negative pions and kaons at rest, than from positive pions and kaons at rest. A peak is expected in the muon flux corresponding to positive pion and kaon decay at rest. A pion decaying from rest produces a muon at approximately 110 MeV and a kaon decaying from rest produces a muon at approximately 258 MeV. These are low energetic muons that will not travel a significant distance through the IceCube detector. Muons produced from pion and kaon decay in flight can potentially have much higher energies.

7.3 Simulations

Simulations were performed to parameterise the muon flux in hadronic cascades. Using these simulations a greater understanding of the production of high energy muons can be used to develop better analysis cut variables and to characterise events. Two methods are used to run simulation of the production of muons in hadronic cascades. The first was previously performed by Sebastian Panknin [114,115] using CORSIKA [73] the program used for IceCube's background simulation. The work performed for this

thesis uses the programs Pythia [125] and *GEometry ANd Tracking* (GEANT) [33,44]. These simulation programs provide a more accurate model of the IceCube detector and the events observed. The simulation programs CORSIKA, Pythia and GEANT are described in this section.

7.3.1 CORSIKA

This simulation, performed previously by Sebastian Panknin [114,115], uses a modified version of CORSIKA [73], based on the official version 6.2040. This modified version allows the event to take place in a medium of salt water rather than in the Earth's atmosphere [31]. The interaction models used in CORSIKA simulation are Gheisha for low energy interactions and QGSJet 01 for high energy interactions [73].

The simulation set up is shown in Figure 7.2, where an incoming proton interacts with a proton in a salt water medium. The muons produced in the cascade are recorded as they pass through the observation level, 9 m from the interaction point in the forward direction. A distance of 9 m was chosen for the observation level as the cascade is expected to be fully developed [115] and only the lowest energy muons will undergo decay before reaching the observation level.

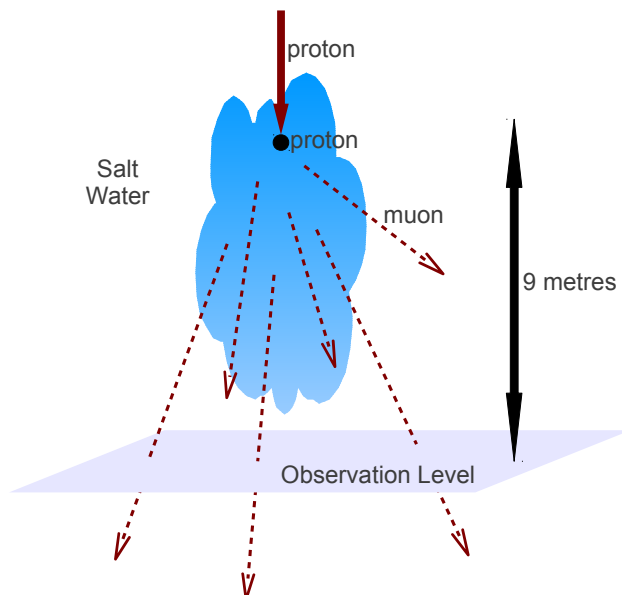


Figure 7.2: CORSIKA simulation. An incoming proton interacts with a proton in salt water to produce hadrons. High energy muons are recorded as they pass through the observation level 9 m below the interaction point.

7.3.2 Pythia

Pythia is an event generator for high energy physics [125]. Simulation of an interaction is divided into components, each handled separately with a high level of accuracy. The simulation uses Monte Carlo techniques so the output is non-deterministic and contains fluctuations. The version of Pythia used in this work is version 6.2 and is written in FORTRAN 77 [105].

The Pythia event generator simulates *Charged-Current* CC interactions in media and includes initial and final state radiation, multiple interaction among beam jets, and fragmentation in the generation. The code includes a *High Energy Physics* (HEP) subroutine that produces the event record in a Monte Carlo independent format. These components are enabled in the simulations.

Initial and final state radiation

In the language of Feynman diagram perturbation theory initial and final state radiation are higher order loop corrections. These interactions are enabled in the simulation. Initial state radiation occurs when an initial particle emits a photon that is then absorbed by a final particle. Final state radiation is the timelike version of this; a final particle emits a photon that is then absorbed by an initial particle.

Multiple interaction among beam jets

Every particle in the simulation may leave a beam remnant, which has properties of flavour and colour, dependent on the particle. The beam remnant can undergo multiple interactions, enabled in the simulation.

Fragmentation

Fragmentation is modeled by the Lund string scheme [124]. This model is an iterative approach where an initial quark may create a new quark pair, forming a meson and one remaining quark. The remaining quark may also create a new quark pair with another quark remaining and so on. This model uses the relative probabilities for quark-antiquark formation and the relative probabilities that a given quark pair forms a specific meson. In the Lund string scheme the concept of quantum tunneling is used to form quark-antiquark pairs which lead to string break ups.

HEP subroutine

The HEP subroutine produces output from Pythia in a format that may be read by the GEANT interface. GEANT is the next simulation program in the chain and the GEANT interface requires specific information about each particle for the continued simulation of the propagation of the cascade event through the detector.

7.3.3 GEANT

GEANT is a program used to simulate the passage of particles through matter [33,44]. The version of GEANT used in this work is 4.8 and is written in C++. It is able to simulate the interactions of particles with matter over a large energy range.

Hadronic processes and Cherenkov radiation are accurately simulated in GEANT. Realistic models of particle detectors can be programmed into the simulation such as the IceCube neutrino detector. These components are modeled as follows.

Hadronic processes

Hadronic processes are modeled using the *Quark-Gluon String Precompound* (QGSP) model, which is an educated guess physics list of hadronic interactions contained within GEANT [33,44]. This uses theory driven modeling for reactions of pions, kaons, and nucleons.

Cherenkov radiation

The production of optical photons via Cherenkov radiation was enabled in the GEANT simulations. This is done using the additional physics constructor in GEANT and includes absorption, Rayleigh scattering, and boundary processes undergone by optical photons.

Detector construction

GEANT provides code for generating specific detector constructions. The code does not include simulation of neutrino detectors by default, so the properties of the Antarctic ice that the IceCube detector is constructed in are added to the detector construction. The kilometre cubed block of ice was defined by creating a three dimensional volume of H₂O with the correct properties of refractive index and absorption for each wavelength of light that propagates through the ice in a neutrino interaction. Values for the refractive index depend only on the phase velocity of the medium [108], and are taken from the tables in PHOTONICS [119].

The simulation set up of Pythia and GEANT is shown in Figure 7.3, where an incoming neutrino interacts with a proton in the Antarctic ice medium. The particles and all their interactions are recorded as they travel through the ice.

The simulation of high energy muon production in hadronic cascades using Pythia and GEANT (Figure 7.3) has three major advantages over the simulation using CORSIKA (Figure 7.2):

- **Interaction particles**

The CORSIKA simulation uses a proton+proton interaction to approximate the

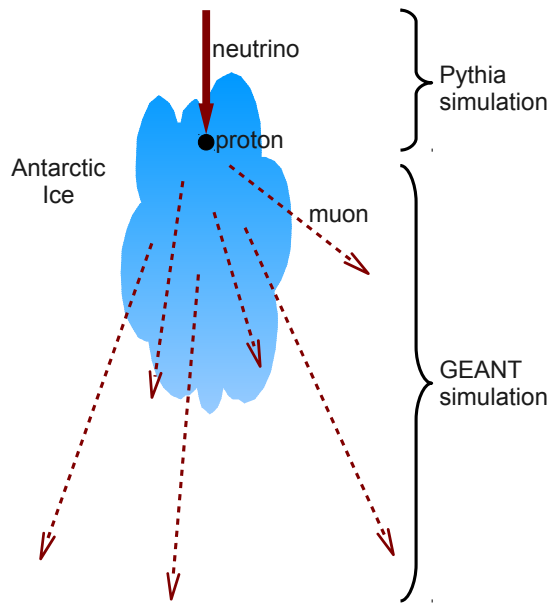


Figure 7.3: Pythia and GEANT simulation. An incoming neutrino interacts with a proton in the Antarctic ice to produce hadrons. All high energy particles are recorded as they travel through the medium.

neutrino+nucleon interaction that occurs in the ice. The Pythia event generator simulates a neutrino+proton interaction. It is expected that the CORSIKA simulation will over-estimate the number of hadrons produced by more than an order of magnitude because of the increased number of quarks in the proton+proton interaction compared to the neutrino+nucleon interaction.

- **Detector medium**

The CORSIKA simulation uses salt water as the interaction medium. This is because the CORSIKA was initially developed for use in the Earth's atmosphere and then modified for other neutrino detectors located in oceans. GEANT allows specific detector construction, which includes the Antarctic ice properties that IceCube is constructed in. It is expected that the ice properties will contribute approximately 10% uncertainty to the simulation.

- **Observation of muons**

The CORSIKA simulation only records muons at the observation level, defined as being 9 m in the forward direction from the interaction point. GEANT tracks the muons, as well as all other particles, throughout their entire track length in all directions.

7.4 Muon Flux

This section contains the results from the previous CORSIKA simulations performed by Sebastian Panknin [114,115] and the results from the GEANT simulations performed in this work. Histograms are shown presenting the number of muons produced as a function of the muon energy. These simulations are performed over a range of incoming particle energies and are compared using power law fits to the muon flux.

7.4.1 Results

The CORSIKA simulation was performed for incoming proton energies of 1 TeV, 10 TeV, 100 TeV, and 1 PeV. These simulations were run with 1000, 1000, 100, and 10 events respectively by [114, 115].

Figure 7.4 shows the number of muons produced as a function of the muon energy for each of these simulations. The straight lines are the power law fits for each incoming proton energy simulation.

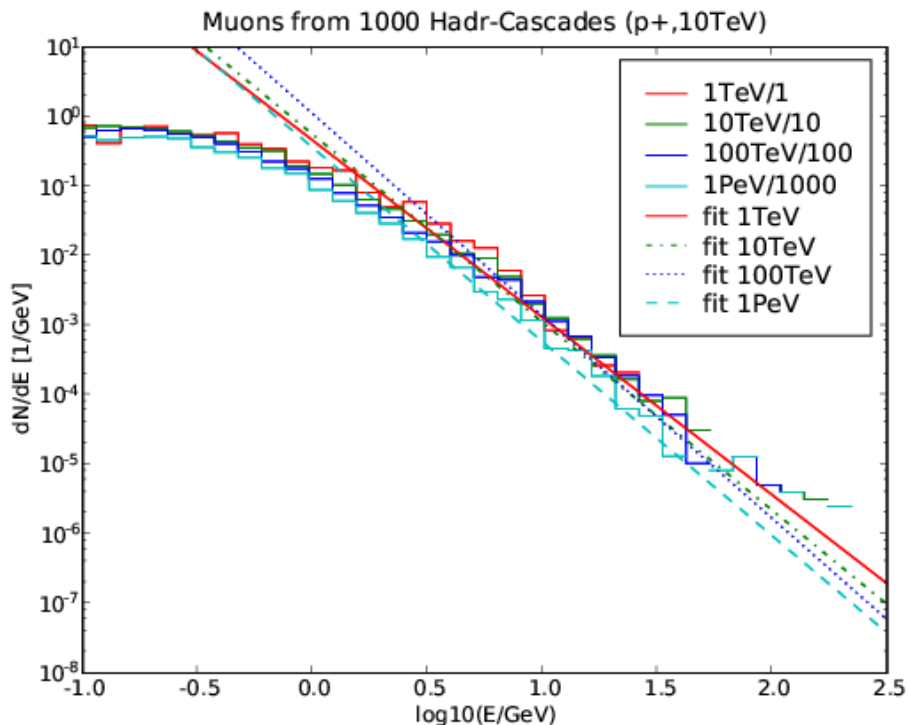


Figure 7.4: Number of muons produced in a hadronic cascade as a function of the muon energy, from the CORSIKA simulations in [114, 115]. The straight lines show the power law fits.

The CMC simulations in the IceCube software incorporates muons in its simulation based on the results from the CORSIKA simulation shown above. Hadronic cascades above an energy threshold (usually set to 1 GeV by default) generate muons above this same threshold. There is only a maximum number of muons taken into account in the a hadronic cascade (usually set to 10 by default) and the cascade energy is reduced by the energy of the muon produced.

The Pythia and GEANT simulation was performed for incoming neutrino energies of 10 TeV, 100 TeV, 500 TeV, and 1 PeV. These simulations were run with 1000, 100, 20, and 10 events respectively in order to generate the events in an acceptable time frame. Figure 7.5 shows the number of muons produced from pion decay, as a function of muon energy for each simulation. The y -axis shows the number of muons produced in the simulation scaled by the neutrino energy and the number of simulated events. The peaks from pion and kaon decay at rest can be seen at approximately $\log(E) = -0.96$ (110 MeV) and $\log(E) = -0.59$ (258 MeV) as discussed in section 7.2.3.

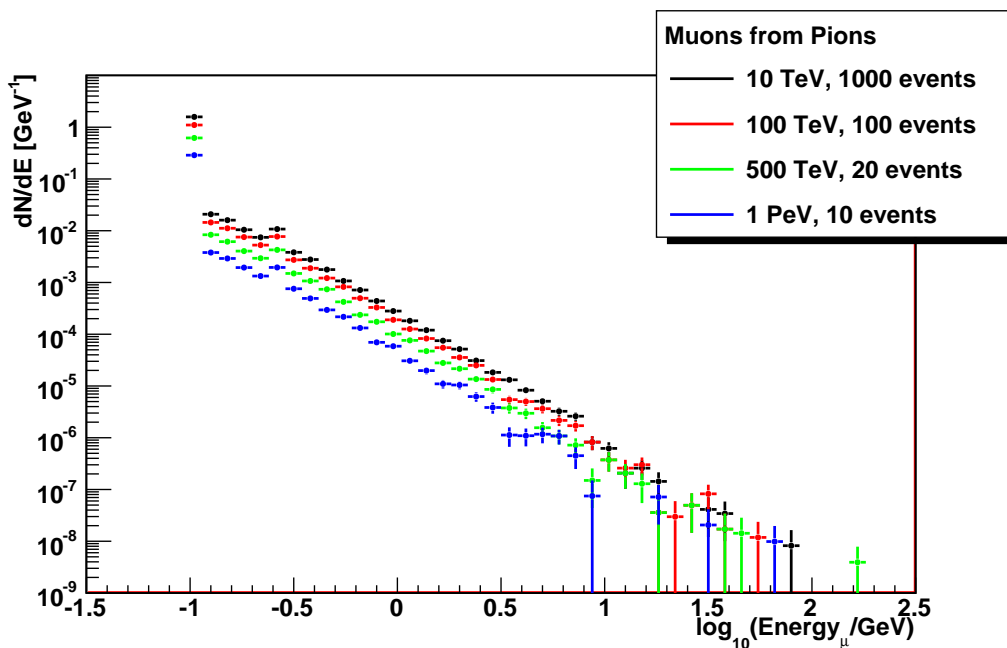


Figure 7.5: Number of muons produced from pion decay as a function of the muon energy.

Figure 7.6 shows the number of muons produced from kaon decay, as a function of muon energy for each simulation. The peaks from pion and kaon decay at rest can also both be seen in this histogram, because kaons decay to pions in flight creating both peaks.

Figure 7.7 shows the number of muons produced from pion and kaon decay, as a

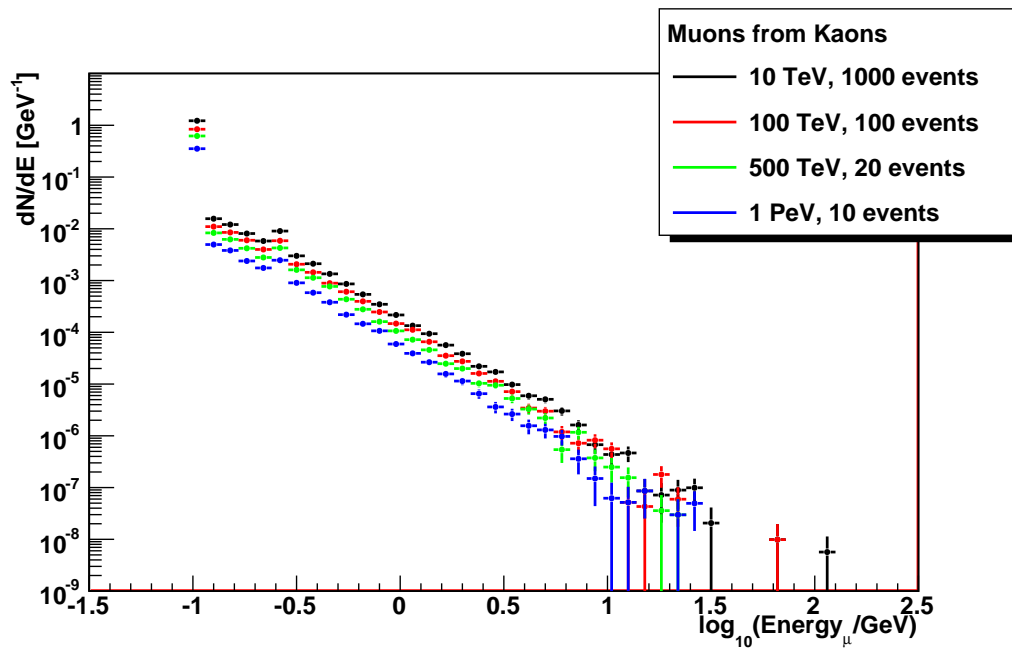


Figure 7.6: Number of muons produced from kaon decay as a function of the muon energy.

function of muon energy for each simulation. This histogram is Figures 7.5 and 7.6 combined and enlarged to the higher energy region of muon production.

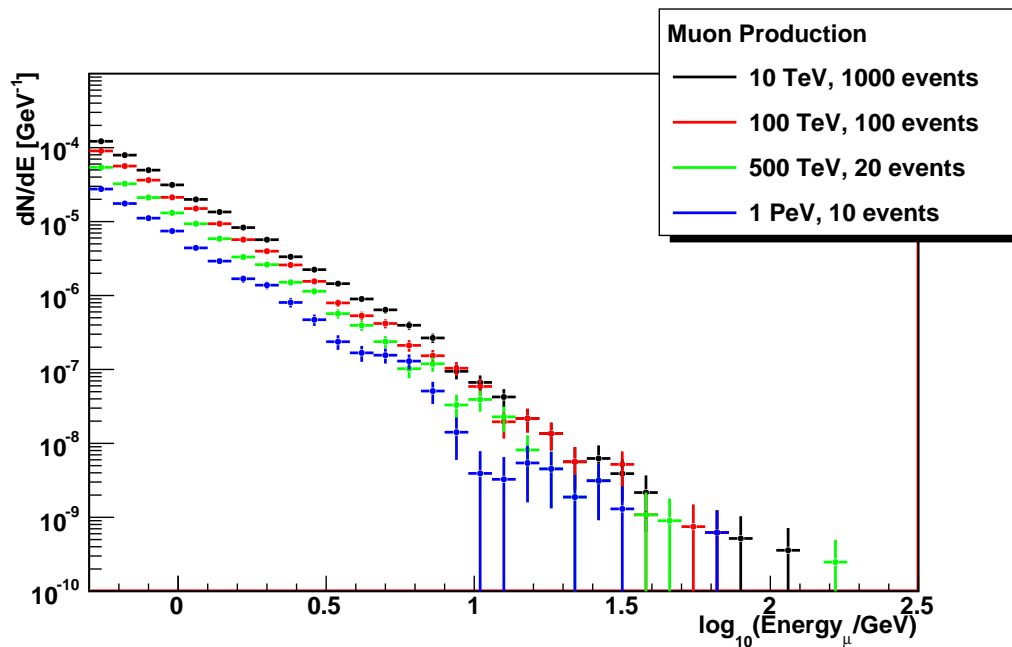


Figure 7.7: Number of muons produced in a hadronic cascade as a function of the muon energy.

Figure 7.8 shows the same, with the power law fits to the muon flux at each energy

displayed by the straight lines. The fit uses a power law

$$\frac{dN}{dE} = A(E/\text{GeV})^\gamma, \quad (7.1)$$

where A and γ are the power law parameters. The fit is calculated between the limits of $-0.3 < \log_{10}(\text{Energy}_\mu/\text{GeV}) < 0.7$, where muons are produced in the hadronic cascade with high statistics.

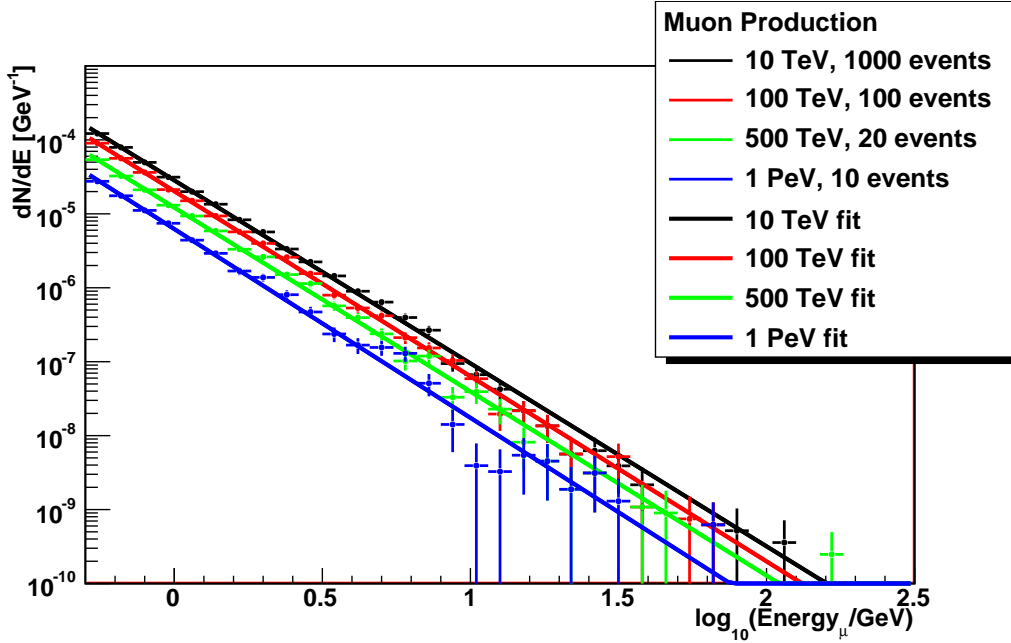


Figure 7.8: Number of muons produced in a hadronic cascade as a function of the muon energy. The straight lines show the power law fits.

The numerical values for the parameters in the power law fit are shown in Table 7.3. This table shows a comparison of the fits from the CORSIKA simulation (Figure 7.4) to the GEANT simulation (Figure 7.8).

The value of the parameter A is expected to differ largely between the CORSIKA and GEANT simulation because of their differences discussed in section 7.3 and normalisation differences. However, the slope γ is expected to have the same value for both simulations. The numerical value of γ is $-2.74 \pm 0.48 \text{ GeV}^{-1}$ from the CORSIKA simulation and $-2.50 \pm 0.03 \text{ GeV}^{-1}$ from the GEANT simulation. These values are the same to within the uncertainties of the fits. The GEANT simulation has much smaller uncertainties in the power law fit than the CORSIKA simulation.

By integrating equation 7.1 the number of muons produced can be calculated using the fits from Table 7.3. The average value of $\gamma = -2.5$ and the values for A at each incoming neutrino energy are used. The number of muons produced per cascade event

Energy	$\gamma_{\text{CORSIKA}} (\text{GeV}^{-1})$	A_{GEANT}	$\gamma_{\text{GEANT}} (\text{GeV}^{-1})$
1 TeV	-2.91 ± 0.65	-	-
10 TeV	-2.55 ± 0.40	2.84×10^{-5}	-2.48 ± 0.02
100 TeV	-2.71 ± 0.40	2.03×10^{-5}	-2.50 ± 0.02
500 TeV	-	1.22×10^{-5}	-2.49 ± 0.03
1 PeV	-2.79 ± 0.47	0.62×10^{-5}	-2.55 ± 0.04
Average	-2.74 ± 0.48	-	-2.50 ± 0.03

Table 7.3: Values of parameter γ in the power law fits to the CORSIKA from [113] and GEANT simulations of muon production in hadronic cascades.

above an energy of 10 GeV is 5.99×10^{-3} , 4.28×10^{-2} , 1.29×10^{-1} , and 1.31×10^{-1} for incoming neutrino energies of 10 TeV, 100 TeV, 500 TeV, and 1 PeV respectively. The number of muons produced per cascade event above an energy of 100 GeV is 1.89×10^{-4} , 1.35×10^{-3} , 4.07×10^{-3} , and 4.13×10^{-3} respectively for cascades of the same energies as listed above. These values of the muon production in hadronic cascades are shown in Table 7.4.

Neutrino energy	10 TeV	100 TeV	500 TeV	1 PeV
Muons above 10 GeV	5.99×10^{-3}	4.28×10^{-2}	1.29×10^{-1}	1.31×10^{-1}
Muons above 100 GeV	1.89×10^{-4}	1.35×10^{-3}	4.07×10^{-3}	4.13×10^{-3}

Table 7.4: Number of muons produced, per cascade event, with energy greater than 10 GeV and 100 GeV in hadronic cascades.

The production of muons above approximately 5 GeV is detectable by IceCube as they travel further than the DOM spacing on a string. Muons of much higher energies can traverse across the detector and significantly change the topology of the cascade event. The simulations of hadronic cascades performed with CORSIKA and GEANT show that muons with these energies are produced from the decay of pions and kaons. The muon production will effect analysis by changing the values of cut variables. A hadronic cascade with a high energy muon created will have differing event topology and will be observed as a more elongated shape rather than a spherical diffuse ball of

light.

7.4.2 Long Range Muon

Figure 7.9 is an illustration of the effect of a high energy muon in a hadronic cascade from the lowest energy GEANT simulation. The position of each particle is plotted in metres as the simulation steps through time. Pions are shown by the red points, negative muons by the green points, and positive muons by the blue points. As the simulation progresses the particles trajectories can be seen by the developing path of the particles.

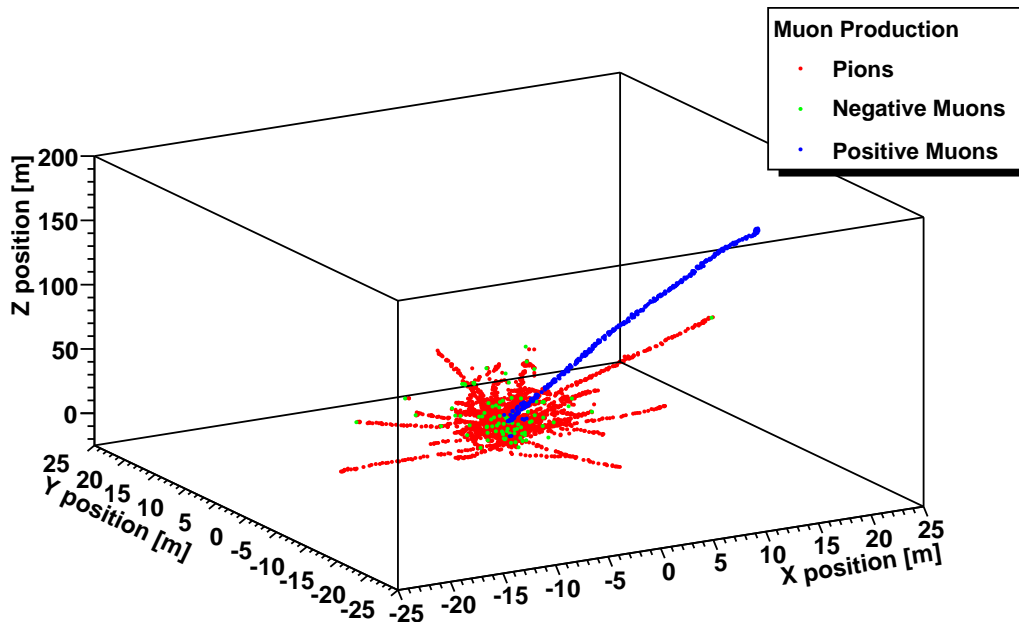


Figure 7.9: Simulation of a 10 TeV hadronic cascade. The points show the positions of each pion and muon particle in the cascade as the simulation steps through in time.

The pions make up the majority of the cascade, largely situated close to the centre forming a roughly spherical topology. The negative muons usually form at the end of a pion track in the detector. This is because the pion has decayed to create a muon at the end of its lifetime. In this simulation one pion decays to a high energy positive muon which subsequently traverses a much greater distance than the cascade size. This is seen by the blue points which form the muon track through the medium. This muon travels approximately 200 m through the detector, originating from a 10 TeV electron neutrino interaction.

7.4.3 Cut Variables

The topology of hadronic cascades with high energy muons present is complex. Consequently traditional analysis cut variables, such as log-likelihood algorithms, will not be as effective in isolating the signal from the background. An analysis dedicated to searching for these hybrid muon-cascade events has not been performed on the data. Once high energy cascades are detected isolation of these types of events within the signal is crucial to the identification of signal from background as seen by the results described from the high energy cascade analysis in Chapter 6. The isolation of these hybrid muon-cascade events also has potential as a method of flavour identification of the initial neutrino interaction. This could be an advantage for studies on neutrino oscillation and flavour ratios.

An analysis that aims to isolate these hybrid muon-cascade events would have to make use of cut variables based on the shape of the event. Three possible cuts for such an analysis are described below.

- **Cascade split cut**

Hits in an event are split into three groups defined by their timing. Each third of hits is reconstructed separately, obtaining a vertex position for each. The first two vertices are required to be located at the same position in the detector, while the third vertex is required to be located in the upward direction. This cut is analogous to the split cuts used in the IceCube-40 cascade analysis where the event was split into two parts dependent on the hit timing.

- **Containment cut**

Hits in an event are split into two groups based on the hit locations. The group of hits reconstructed around the event vertex are removed. The remaining hits are required to reconstruct with a track topology pointing back in the direction of the cascade vertex.

- **Number of DOMs hit/Number of strings hit**

Hits in an event are split into two groups based on their z -position in the detector. The hits located in the bottom half of the event are required to have a high fill ratio corresponding to cascade-like event topology, while the hits located in the top half of the event are required to have a lower fill ratio corresponding to a track-like topology.

Chapter 8

Conclusion

The work presented in this thesis is a high energy cascade analysis on the IceCube-40 experimental data. This dataset, taken from 6th April 2008 to 20th May 2009, was data collected by the first 40 deployed and operational IceCube strings. The analysis aimed to search for high energy neutrino-induced cascades with an E^{-2} spectrum. The cascade signal arises from the interaction of all flavours of neutrinos from astrophysical sources and has the topology of a diffuse ball of light contained within the detector. The background arises from atmospheric muons which present as tracks traversing through the detector and from low energy atmospheric neutrino-induced cascades.

Analysis filter levels isolate the cascade signal from the background by performing sequential cuts on the experimental data. The cut variables came from reconstruction algorithms run on the experimental data using the event information. The values of the cuts were obtained by maximising the signal to background ratio. Machine learning algorithms were also used to further isolate the signal from the background.

This analysis observed 14 high energy cascade events on an expected background of $2.2_{-0.8}^{+0.6}$ atmospheric neutrino events and 7.7 ± 1.0 atmospheric muon events. This gives a limit of

$$\Phi_{\text{lim}} E^2 \leq 7.46 \times 10^{-8} \text{ GeVsr}^{-1} \text{ s}^{-1} \text{ cm}^{-2} \quad (8.1)$$

with a 90% confidence level, assuming a 1: 1: 1 flavour ratio and an E^{-2} astrophysical spectrum. The energy range containing 90% of the signal is from 25 TeV to 5012 TeV. This improves the best previous limit from other neutrino telescopes and IceCube-22 analyses to below the Waxman-Bahcall upper bound. Three other IceCube-40 analyses (EHE, muon, and UHE analyses) subsequently further improved the astrophysical neutrino flux limit after this work.

The production of high energy muons within hadronic cascades is a complication in high energy cascade analyses. Muons are produced from the decay of hadrons, mainly pion and kaon decay. If the muons produced are energetic enough they traverse a significant distance through the detector and change the topology of the cascade event. This has an effect on the reconstructions of the cascade event variables and the cut values in an analysis. Simulations were performed to parameterise the muon flux in hadronic cascades. The average slope of the muon production in hadronic cascades from the GEANT simulations was fitted with a power law with index

$$\gamma_{\text{GEANT}} = 2.50 \pm 0.03 \text{ GeV}^{-1}. \quad (8.2)$$

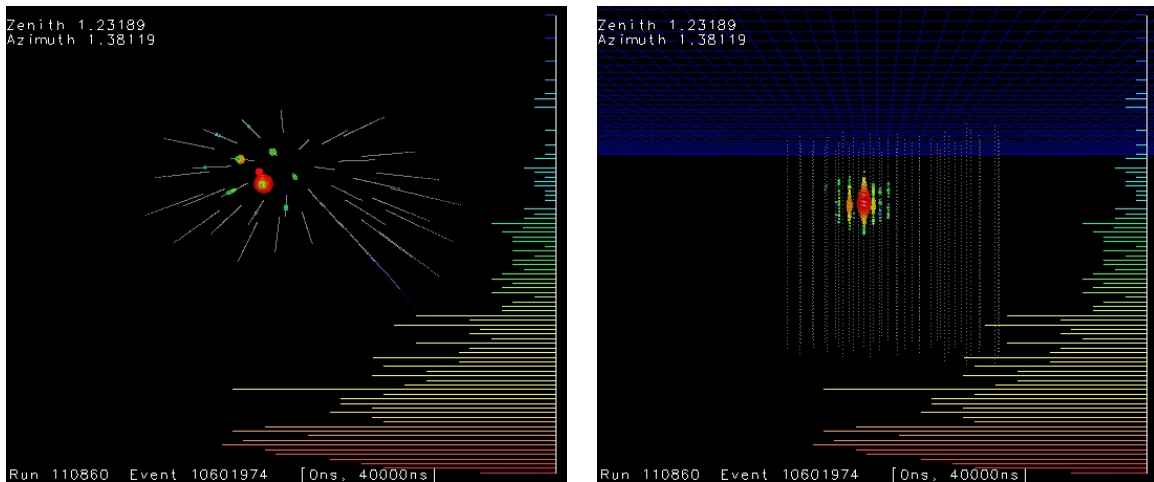
This parameterises the slope of the production of high energy muons in hadronic cascades and shows the effect on the topology and reconstruction variables of a cascade event. The production of these hybrid muon-cascade events may be considered in future high energy cascade analyses and in the classification of neutrino events.

The observation of the 14 high energy events is one of the first detections of cascade candidate events by any neutrino detector. As IceCube grows, further cascade analyses will be performed on the experimental data. These analyses will continue to set limits or make observations of high energy cascade events. High energy cascade analyses are underway using data from the IceCube-59 and IceCube-79 detectors. These future analyses may detect more cascade candidate events arising from neutrinos with astrophysical origins.

Appendix A

Event Displays

This appendix contains the event viewer displays of the 14 observed events. Each event is shown from above (xy -plane) and from the side (xz -plane). The DOMs are depicted as white dots forming the deployed IceCube strings. Every hit in the event is recorded as a coloured dot. The size of the coloured dots depicts the amount of charge received by that DOM, and the colour depicts the timing where red is earlier hits and blue is later hits. The charge and timing of the hits is also depicted along the right hand side of each viewer display.



(a) Top view (xy -plane)

(b) Side view (xz -plane)

Figure A.1: Event 1 viewer display: 29.13 TeV event at $(-79.58, 322.01, 201.82)$.

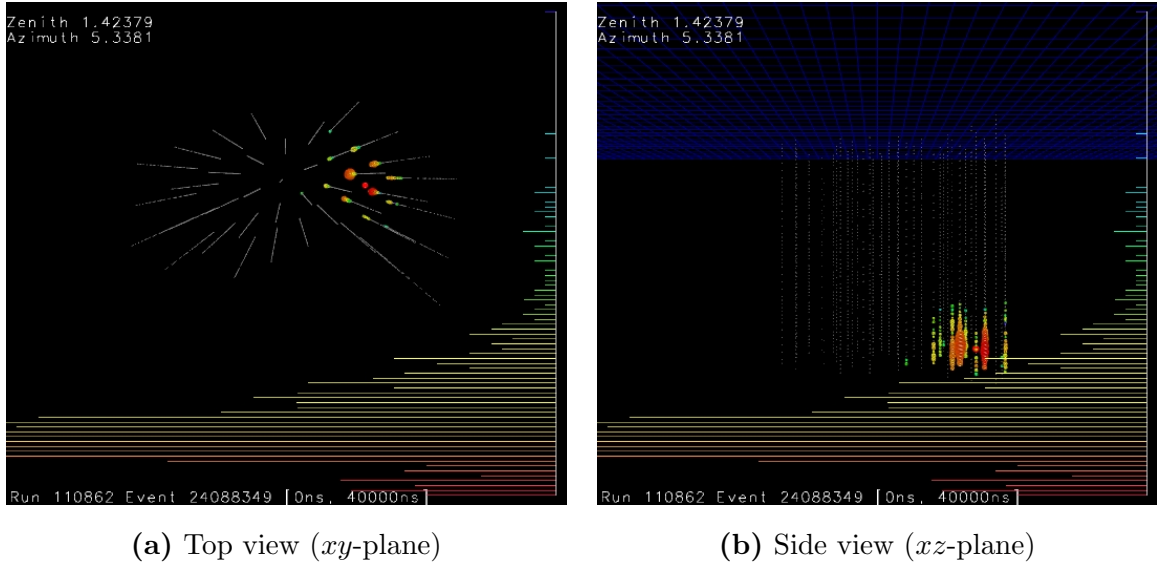


Figure A.2: Event 2 viewer display: 30.81 TeV event at (442.29, 167.46, -427.36).

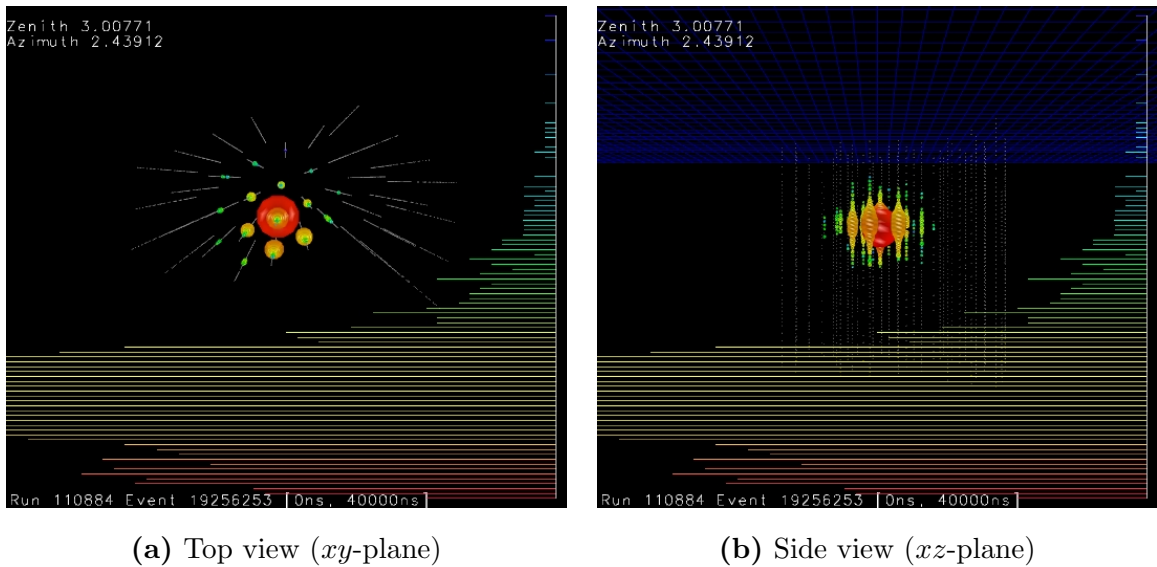
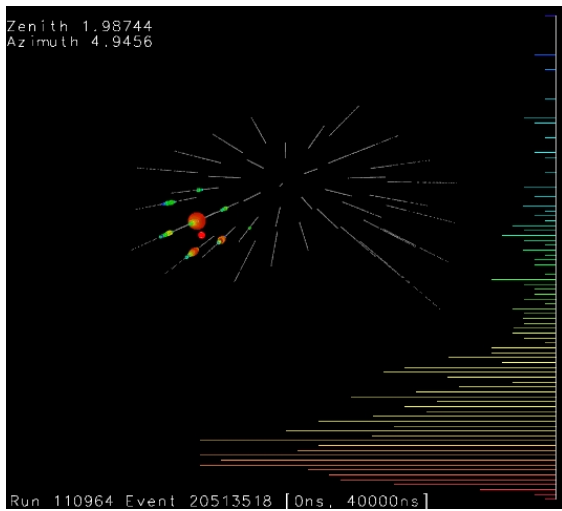
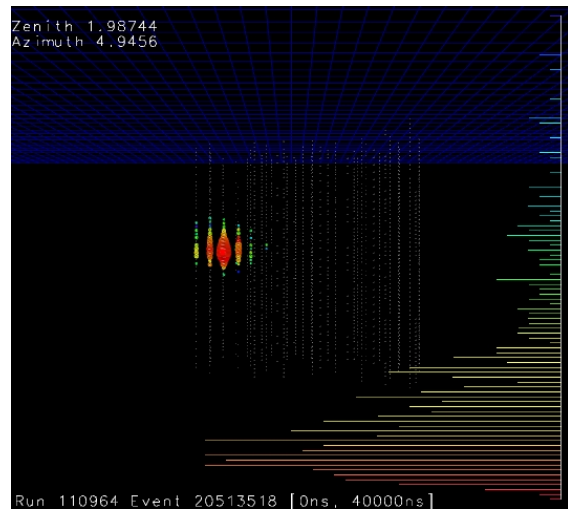
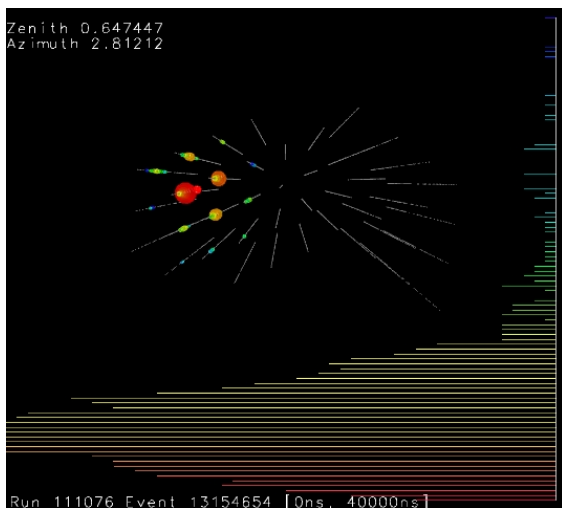
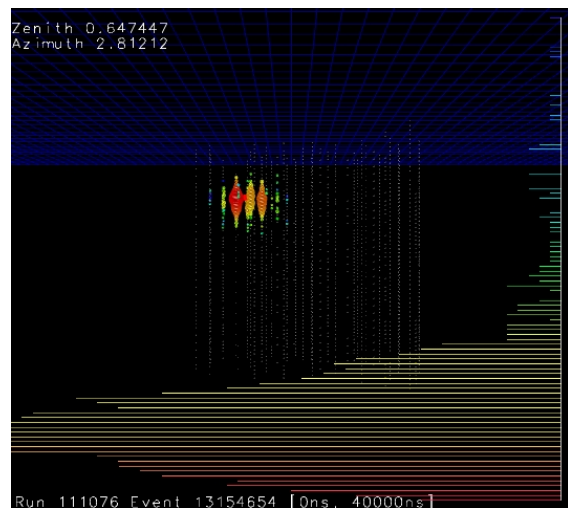


Figure A.3: Event 3 viewer display: 175.28 TeV event at (5.57, 147.82, 110.94).

(a) Top view (xy -plane)(b) Side view (xz -plane)**Figure A.4:** Event 4 viewer display: 27.14 TeV event at $(-310.92, 177.57, 24.49)$.(a) Top view (xy -plane)(b) Side view (xz -plane)**Figure A.5:** Event 5 viewer display: 41.36 TeV event at $(-226.14, 355.98, 300.18)$.

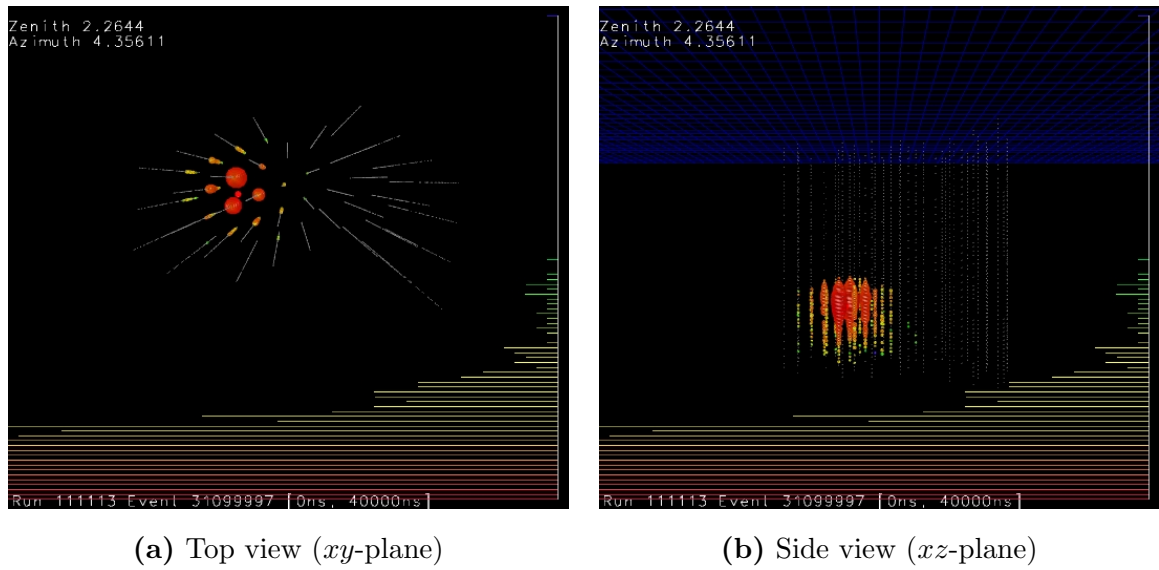


Figure A.6: Event 6 viewer display: 174.09 TeV event at $(-159.49, 301.21, -230.91)$.

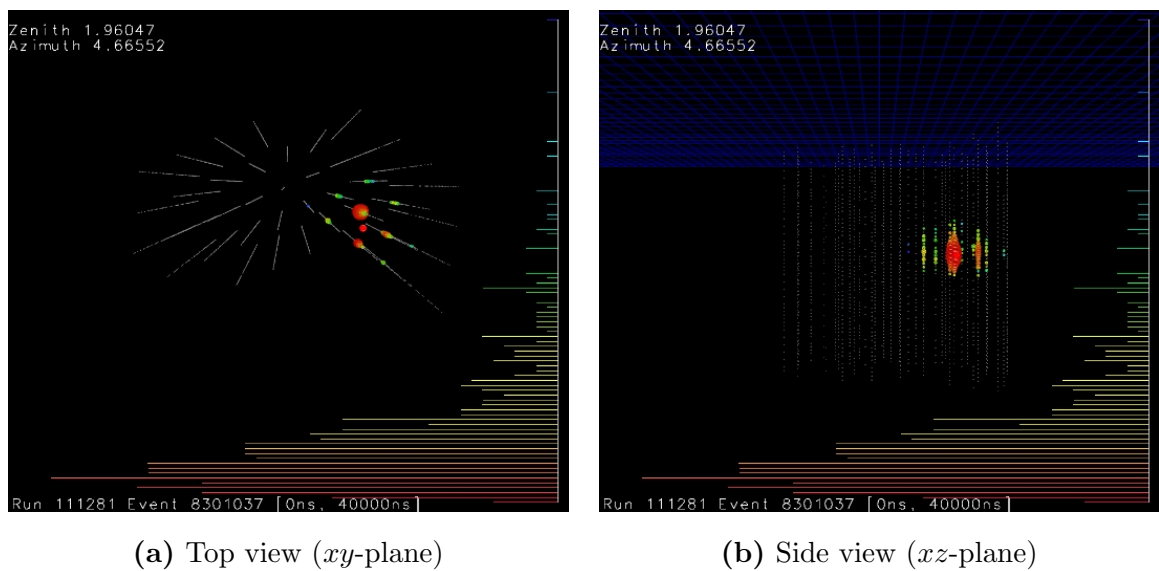
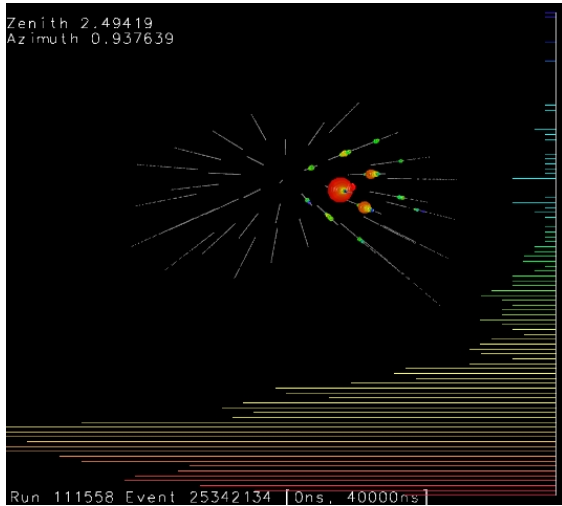
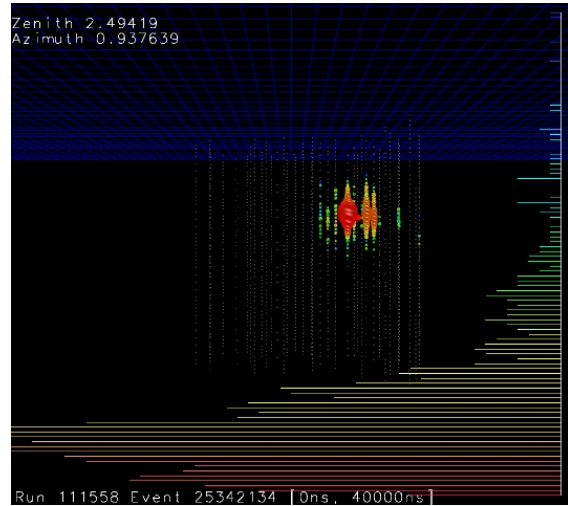
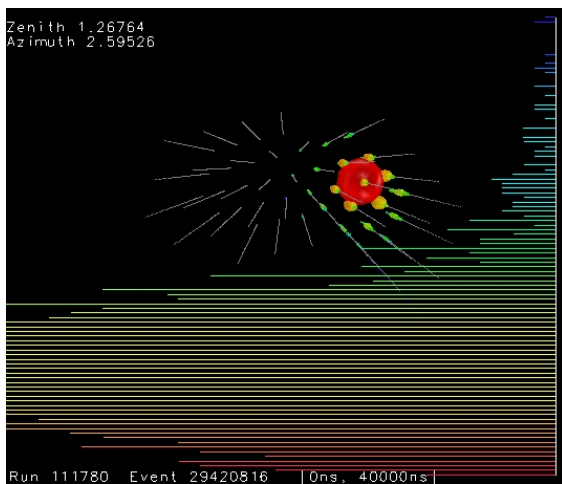
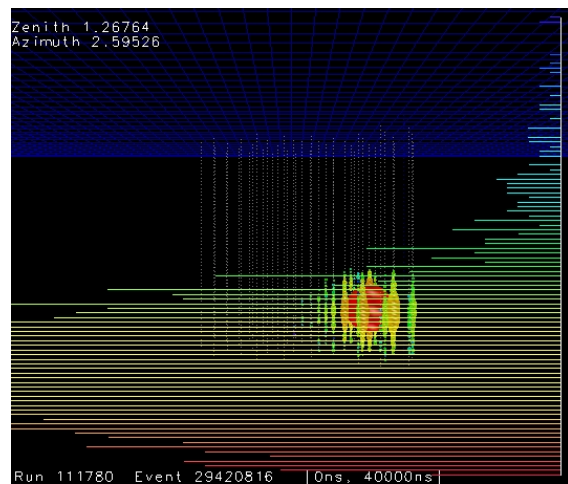


Figure A.7: Event 7 viewer display: 31.20 TeV event at $(326.92, 59.76, 23.90)$.

(a) Top view (xy -plane)(b) Side view (xz -plane)**Figure A.8:** Event 8 viewer display: 45.33 TeV event at (303.03, 210.05, 167.72).(a) Top view (xy -plane)(b) Side view (xz -plane)**Figure A.9:** Event 9 viewer display: 144.20 TeV event at (378.63, 225.91, -303.59).

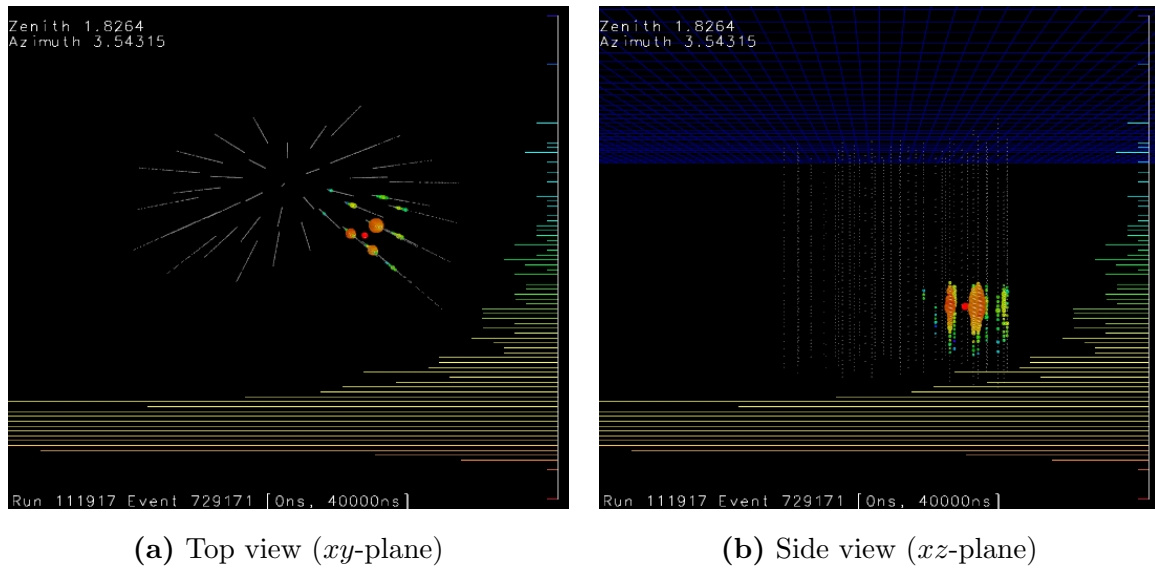


Figure A.10: Event 10 viewer display: 32.06 TeV event at (352.15, -17.81 , -200.99).

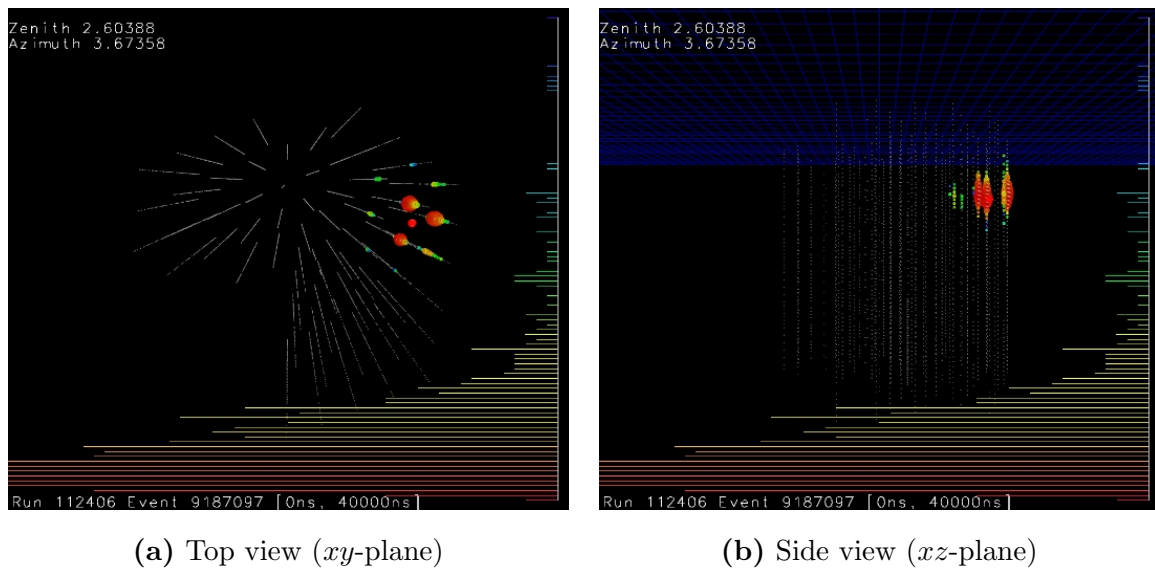
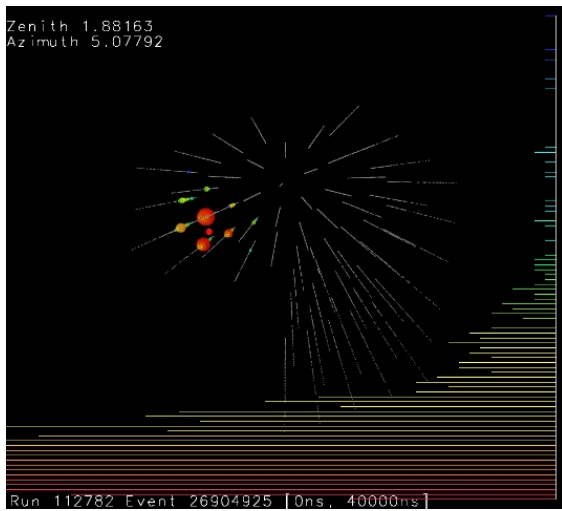
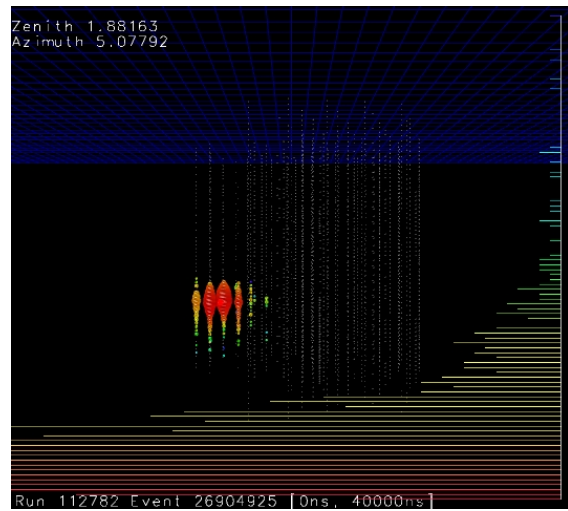
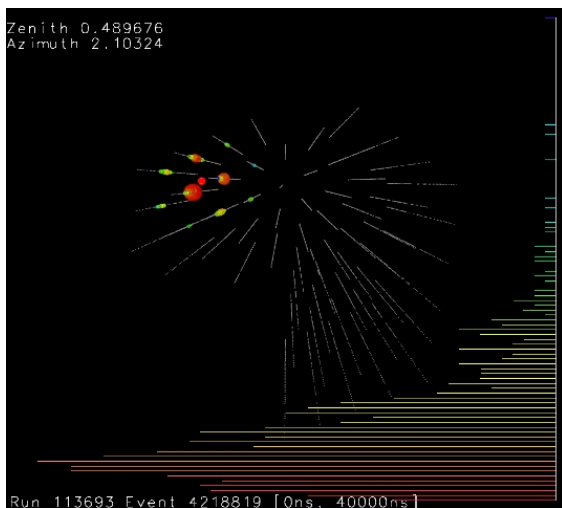
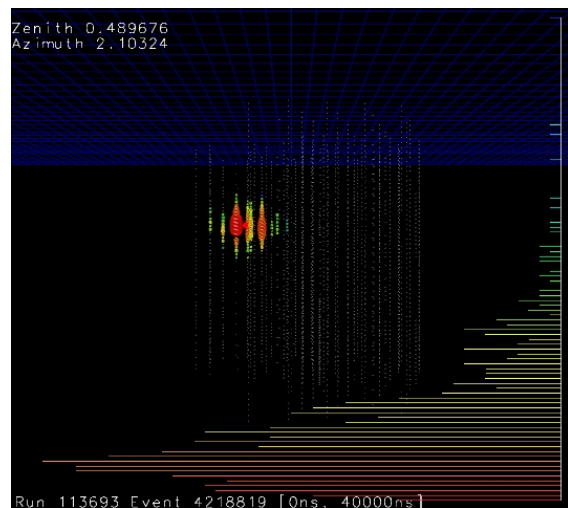


Figure A.11: Event 11 viewer display: 46.83 TeV event at (469.60, 56.77, 254.13).

(a) Top view (xy -plane)(b) Side view (xz -plane)**Figure A.12:** Event 12 viewer display: 57.19 TeV event at $(-318.58, 169.02, -201.75)$.(a) Top view (xy -plane)(b) Side view (xz -plane)**Figure A.13:** Event 13 viewer display: 39.88 TeV event at $(-225.53, 385.72, 166.87)$.

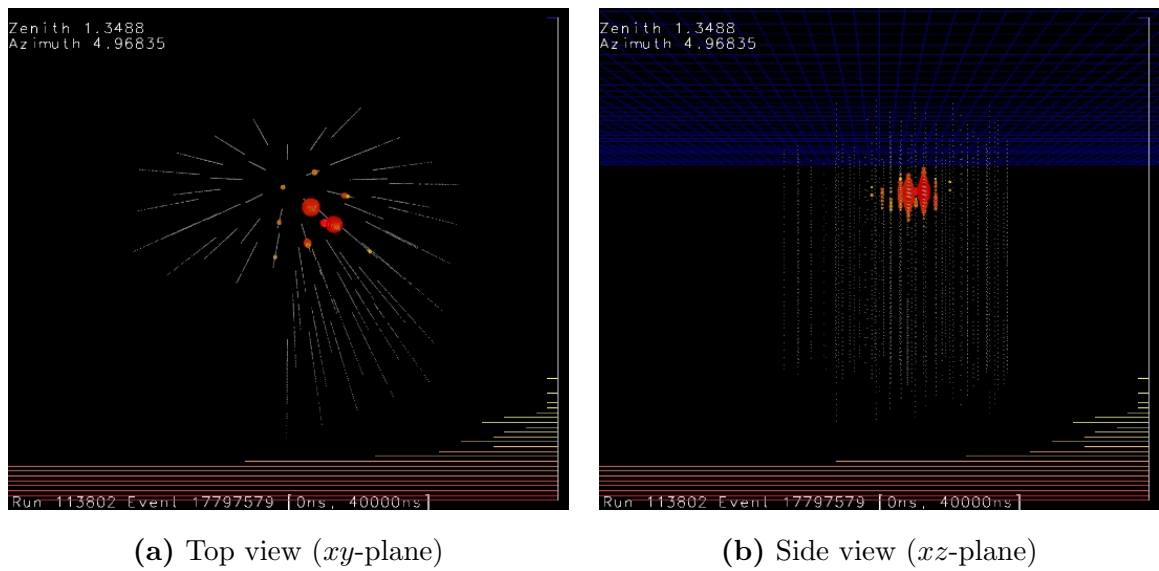
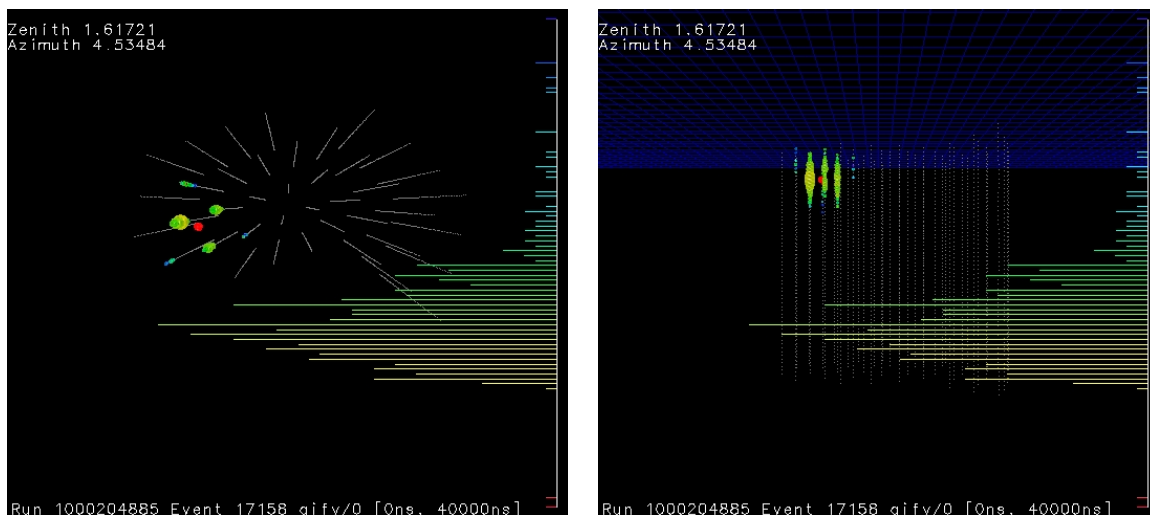


Figure A.14: Event 14 viewer display: 27.15 TeV event at (164.71, 138.55, 300.26).

Appendix B

Background Event Displays

This appendix contains the event viewer displays of the 7 remaining background muon events from the additional muon background simulations described in section 6.2. Each event is shown from above (xy -plane) and from the side (xz -plane). The DOMs are depicted as white dots forming the deployed IceCube strings. Every hit in the event is recorded as a coloured dot. The size of the coloured dots depicts the amount of charge received by that DOM, and the colour depicts the timing where red is earlier hits and blue is later hits. The charge and timing of the hits is also depicted along the right hand side of each viewer display.



(a) Top view (xy -plane)

(b) Side view (xz -plane)

Figure B.1: Simulated background muon event 1 viewer display: 25.40 TeV event at $(-260.21, 213.53, 378.8)$.

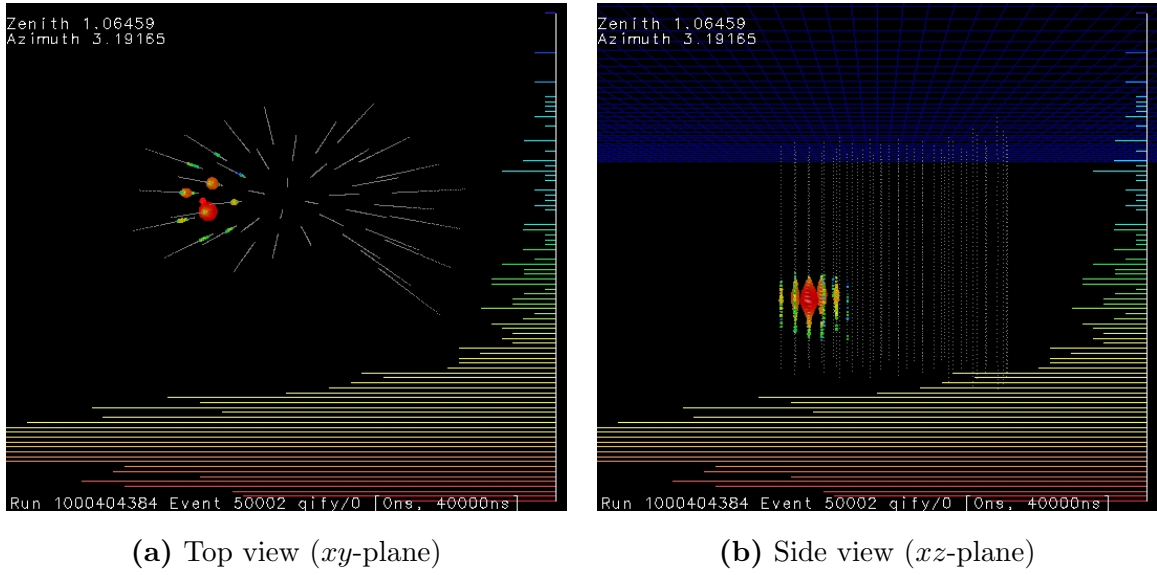


Figure B.2: Simulated background muon event 2 viewer display: 37.28 TeV event at $(-325.52, 286.56, -184.91)$.

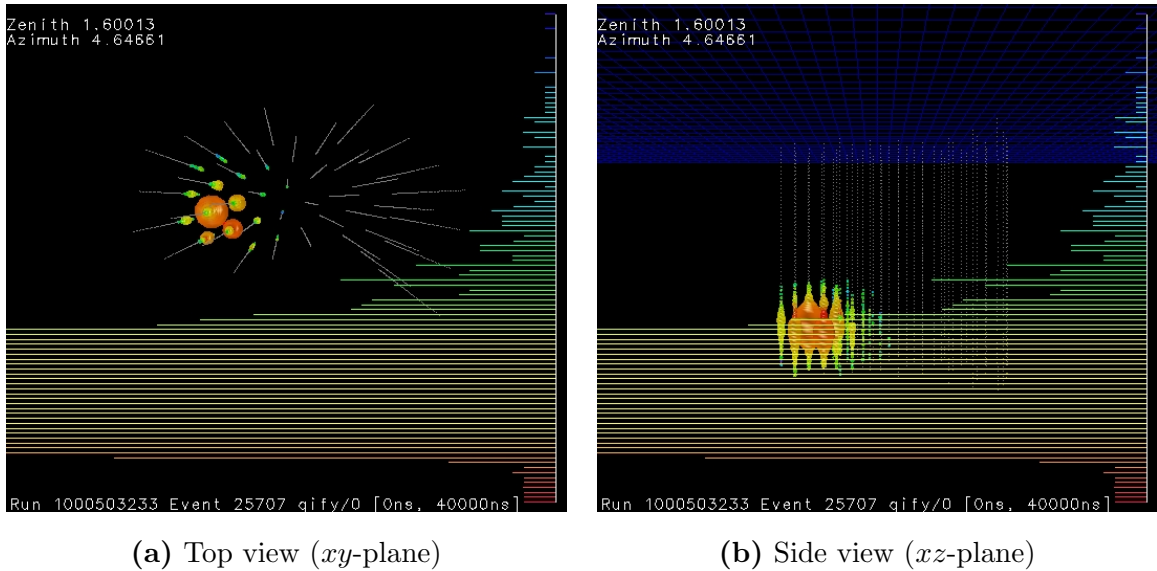


Figure B.3: Simulated background muon event 3 viewer display: 291.67 TeV event at $(-275.07, 180.27, -311.96)$.

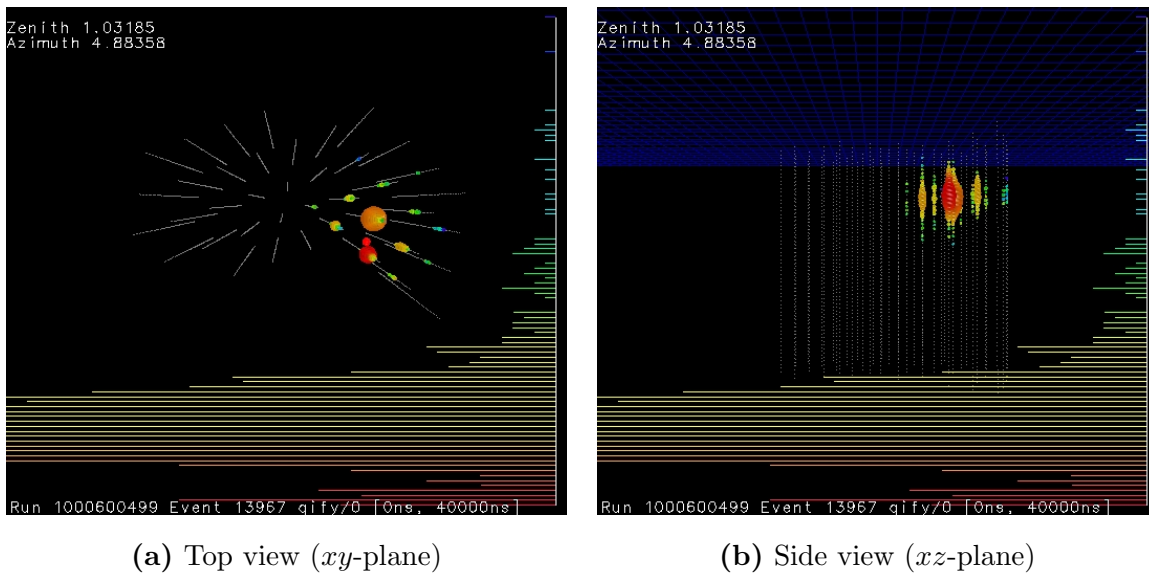


Figure B.4: Simulated background muon event 4 viewer display: 136.38 TeV event at (292.60, 53.14, 280.99).

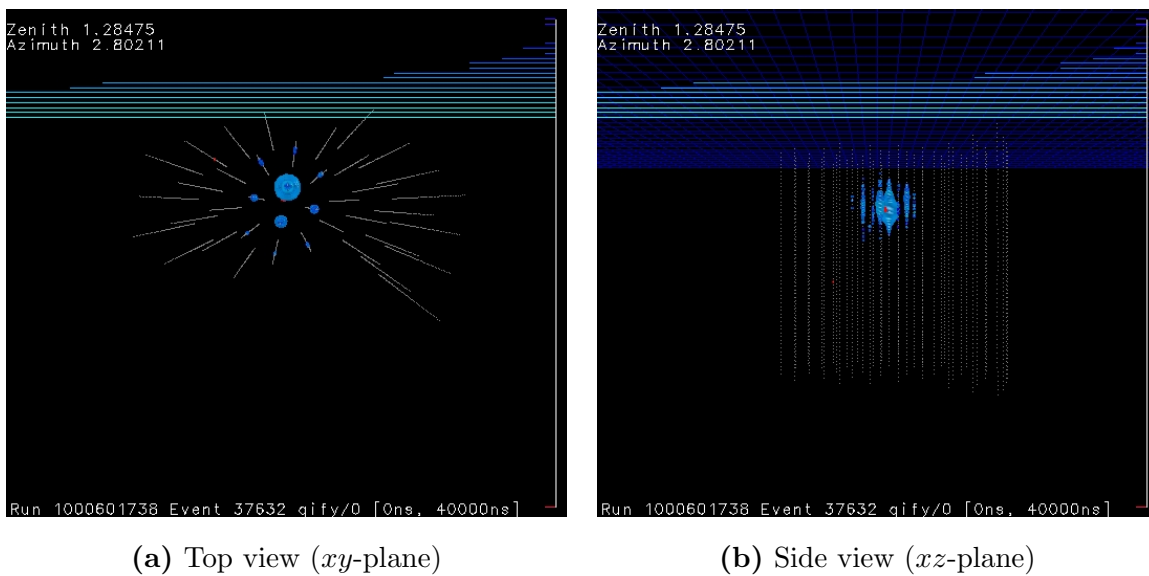


Figure B.5: Simulated background muon event 5 viewer display: 32.73 TeV event at (36.96, 259.93, 245.72).

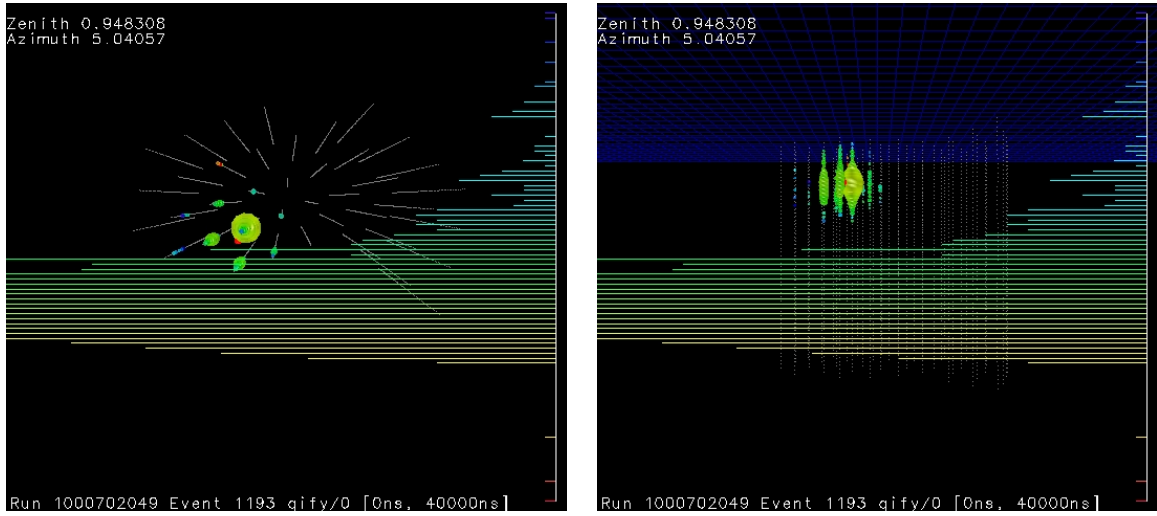
(a) Top view (xy -plane)(b) Side view (xz -plane)

Figure B.6: Simulated background muon event 6 viewer display: 72.46 TeV event at $(-145.00, 124.07, 326.52)$.

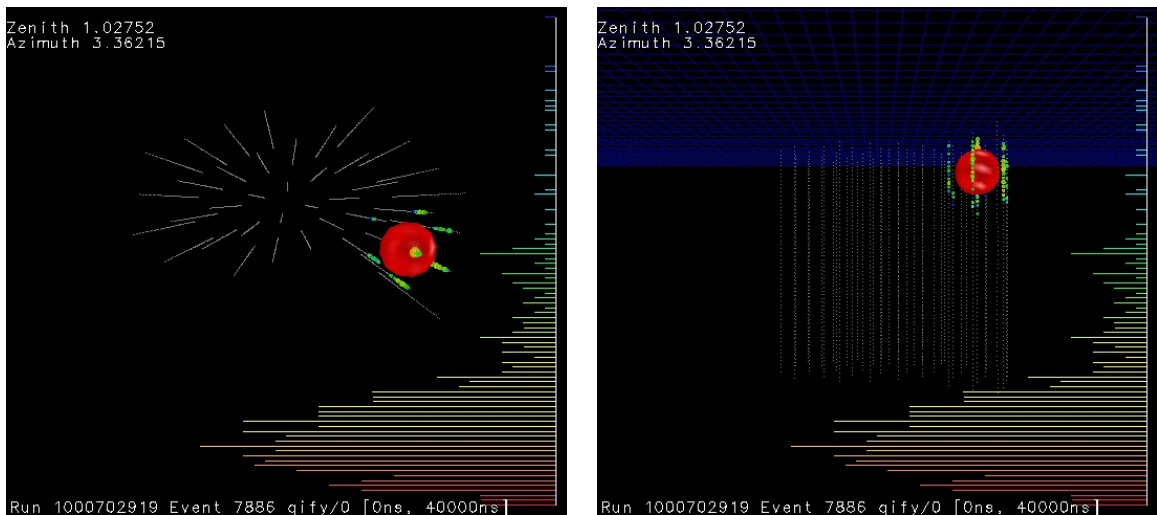
(a) Top view (xy -plane)(b) Side view (xz -plane)

Figure B.7: Simulated background muon event 7 viewer display: 26.78 TeV event at $(415.18, 3.06, 373.32)$.

Bibliography

- [1] DUMAND: Proposal to Construct a Deep Ocean Laboratory for the study of High-energy Neutrino Astrophysics, Cosmic rays, and Neutrino Interactions. Technical report, 1982.
- [2] R. Abbasi, Y. Abdou, T. Abu-Zayyad, O. Actis, J. Adams, et al. Search for neutrino-induced cascades with five years of AMANDA data. *Astropart.Phys.*, 34:420–430, 2011.
- [3] R. Abbasi et al. The IceCube Data Acquisition System: Signal Capture, Digitization, and Timestamping. *Nucl.Instrum.Meth.*, A601:294–316, 2009.
- [4] R. Abbasi et al. Calibration and Characterization of the IceCube Photomultiplier Tube. *Nucl.Instrum.Meth.*, A618:139–152, 2010.
- [5] R. Abbasi et al. A Search for a Diffuse Flux of Astrophysical Muon Neutrinos with the IceCube 40-String Detector. *Phys.Rev.*, D84:082001, 2011.
- [6] R. Abbasi et al. Constraints on the Extremely-high Energy Cosmic Neutrino Flux with the IceCube 2008-2009 Data. *Phys.Rev.*, D83:092003, 2011.
- [7] R. Abbasi et al. First search for atmospheric and extraterrestrial neutrino-induced cascades with the IceCube detector. *Phys.Rev.*, D84:072001, 2011.
- [8] R. Abbasi et al. Observation of Atmospheric Neutrino-induced Cascades in IceCube with DeepCore. *ICRC 2011 Conf. Proc.*, 2011. Papers submitted by the IceCube Collaboration to the 32nd International Cosmic Ray Conference, Beijing 2011/ part II.
- [9] R. Abbasi et al. Study of South Pole ice transparency with IceCube flashers. *ICRC 2011 Conf. Proc.*, 2011. Papers submitted by the IceCube Collaboration to the 32nd International Cosmic Ray Conference, Beijing 2011/ part VI.

- [10] R. Abbasi et al. A Search for UHE Tau Neutrinos with IceCube. *Phys.Rev.*, D86:022005, 2012.
- [11] R. Abbasi et al. An absence of neutrinos associated with cosmic-ray acceleration in γ -ray bursts. *Nature*, 484:351–353, 2012.
- [12] A. Achterberg et al. On the selection of AGN neutrino source candidates for a source stacking analysis with neutrino telescopes. *Astropart.Phys.*, 26:282–300, 2006.
- [13] M. Ackermann and Elisa Bernardini. An investigation of seasonal variations in the atmospheric neutrino rate with the AMANDA-II neutrino telescope. *ICRC 2005 Conf. Proc.*, 2005.
- [14] M. Ackermann et al. Optical properties of deep glacial ice at the South Pole. *Geophys.Res.*, 111(D13203):282–300, 2006.
- [15] B. Adeva et al. A Direct determination of the number of light neutrino families from $e^+ e^- \rightarrow$ neutrino anti-neutrino gamma at LEP. *Phys.Lett.*, B275:209–221, 1992.
- [16] G. Aggouras et al. Recent results from NESTOR. *Nucl.Instrum.Meth.*, A567:452–456, 2006.
- [17] J.A. Aguilar et al. Search for a diffuse flux of high-energy ν_μ with the ANTARES neutrino telescope. *Phys.Lett.*, B696:16–22, 2011.
- [18] F. Aharonian et al. A New population of very high energy gamma-ray sources in the Milky Way. *Science*, 307:1938–1942, 2005.
- [19] Q.R. Ahmad et al. Direct evidence for neutrino flavor transformation from neutral current interactions in the Sudbury Neutrino Observatory. *Phys.Rev.Lett.*, 89:011301, 2002.
- [20] J. Ahrens et al. *IceCube Preliminary Design Document*, 2001.
- [21] J. Ahrens et al. Icecube - the next generation neutrino telescope at the south pole. *Nucl.Phys.Proc.Suppl.*, 118:388–395, 2003.
- [22] E. Andres, P. Askebjør, X. Bai, G. Barouch, S.W. Barwick, et al. Observation of high-energy neutrinos using Cherenkov detectors embedded deep in Antarctic ice. *Nature*, 410:441–443, 2001.

- [23] C. Arpesella. The ANTARES project. *Nucl.Instrum.Meth.*, A409:454–457, 1998.
- [24] Per Askebjerg, Steven W. Barwick, Lars Bergstrom, Adam Bouchta, Staffan Carrius, et al. Optical properties of deep ice at the South Pole: Absorption. *Appl.Opt.*, 36:4168–4180, 1997.
- [25] H. Athar, M. Jezabek, and O. Yasuda. Effects of neutrino mixing on high-energy cosmic neutrino flux. *Phys.Rev.*, D62:103007, 2000.
- [26] G. Backenstoss. Pionic atoms. *Ann.Rev.Nucl.Part.Sci.*, 20:467–508, 1970.
- [27] G.D. Barr, T.K. Gaisser, P. Lipari, Simon Robbins, and T. Stanev. A Three - dimensional calculation of atmospheric neutrinos. *Phys.Rev.*, D70:023006, 2004.
- [28] S. Barwick, D. Lowder, T. Miller, P.B. Price, A. Westphal, et al. AMANDA: (Antartic Muon and Neutrino Detector Array): Observation of muons using ice as a particle detector. *ICCR Symp. on Astrophysical Aspects of the Most Energetic Cosmic Rays Conf. Proc.*, 1991.
- [29] John F. Beacom, Nicole F. Bell, Dan Hooper, Sandip Pakvasa, and Thomas J. Weiler. Measuring flavor ratios of high-energy astrophysical neutrinos. *Phys.Rev.*, D68:093005, 2003.
- [30] Eugene W. Beier. The Kamiokande-II Detector. *ICOBAN 86 Conf. Proc.*, 1986.
- [31] S Bevan., S Danaher., J Perkin., S Ralph., C Rhodes., et al. Simulation of Ultra High Energy Neutrino Interactions in Ice and Water. *Astropart.Phys.*, 28:366–379, 2007.
- [32] Adam Bouchta. A Preliminary position calibration of the AMANDA-B detector. Technical report, Stockholm University, 1996.
- [33] R. Brun, R. Hagelberg, M. Hansroul, and J.C. Lassalle. *GEANT: Simulation Program for Particle Physics Experiments. User Guide and Reference Manual*, 1978. Revised Version.
- [34] R. Brun and F. Rademakers. ROOT: An object oriented data analysis framework. *Nucl.Instrum.Meth.*, A389:81–86, 1997.
- [35] Christian Y. Cardall. Supernova Modeling: Progress and Challenges. In *Proc. of XXIV International Conference on Neutrino Physics and Astrophysics*, Athens, Greece, 2010.

- [36] P.A. Cerenkov. Visible radiation produced by electrons moving in a medium with velocities exceeding that of light. *Phys.Rev.*, 52:378–379, 1937.
- [37] J. Chadwick. Possible Existence of a Neutron. *Nature*, 129:312, 1932.
- [38] D. Chirkin and W. Rhode. Muon Monte Carlo: A new high precision tool for muon propagation through matter. *2nd Workshop on Methodical Aspects of Underwater/Ice Neutrino Telescopes Conf. Proc.*, pages 15–22, 2002.
- [39] Dmitry Chirkin. Fluxes of atmospheric leptons at 600-GeV - 60-TeV. 2004. arXiv:hep-ph/0407078.
- [40] Dmitry Aleksandrovich Chirkin. *Cosmic ray energy spectrum measurement with the Antarctic Muon and Neutrino Detector Array (AMANDA)*. PhD thesis, 2003.
- [41] Amanda Cooper-Sarkar and Subir Sarkar. Predictions for high energy neutrino cross-sections from the ZEUS global PDF fits. *JHEP*, 0801:075, 2008.
- [42] C.L. Cowan, F. Reines, F.B. Harrison, H.W. Kruse, and A.D. McGuire. Detection of the free neutrino: A Confirmation. *Science*, 124:103–104, 1956.
- [43] G. Danby, J.M. Gaillard, Konstantin A. Goulianos, L.M. Lederman, Nari B. Mistry, et al. Observation of High-Energy Neutrino Reactions and the Existence of Two Kinds of Neutrinos. *Phys.Rev.Lett.*, 9:36–44, 1962.
- [44] A. Dellacqua, G. Parrou, S. Giani, P. Kent, A. Osborne, et al. *GEANT-4: An Object oriented toolkit for simulation in HEP*, 1994.
- [45] Charles D. Dermer. On Gamma Ray Burst and Blazar AGN Origins of the Ultra-High Energy Cosmic Rays in Light of First Results from Auger. *ICRC07 Conf. Proc.*, 2007.
- [46] T. DeYoung. IceTray: A software framework for IceCube. *CHEP '04 Conf. Proc.*, pages 463–466, 2005.
- [47] G.V. Domogatsky et al. The Lake Baikal deep underwater detector. *Nucl.Phys.Proc.Suppl.*, 19:388–395, 1991.
- [48] Zh.A. Dzhilkibaev. Search for a diffuse flux of high-energy neutrinos with the Baikal neutrino telescope NT200. *ICRC 2009 Conf. Proc.*, 2009.
- [49] Rikard Enberg, Mary Hall Reno, and Ina Sarcevic. Prompt neutrino fluxes from atmospheric charm. *Phys.Rev.*, D78:043005, 2008.

- [50] R. Engel, T.K. Gaisser, T. Stanev, and P. Lipari. Air shower calculations with the new version of SIBYLL. *ICRC 1999 Conf. Proc.*, 1999.
- [51] Ralph Engel, David Seckel, and Todor Stanev. Neutrinos from propagation of ultrahigh-energy protons. *Phys.Rev.*, D64:093010, 2001.
- [52] Gary J. Feldman and Robert D. Cousins. A Unified approach to the classical statistical analysis of small signals. *Phys.Rev.*, D57:3873–3889, 1998.
- [53] E. Fermi. An attempt of a theory of beta radiation. 1. *Z.Phys.*, 88:161–177, 1934.
- [54] Enrico Fermi. On the Origin of the Cosmic Radiation. *Phys.Rev.*, 75:1169–1174, 1949.
- [55] R.S. Fletcher, T.K. Gaisser, Paolo Lipari, and Todor Stanev. SIBYLL: An Event generator for simulation of high-energy cosmic ray cascades. *Phys.Rev.*, D50:5710–5731, 1994.
- [56] Y. Freund and R.E. Schapire. A decision-theoretic generalization of on-line learning and an application to boosting. *Journal of Computer and System Sciences*, 55:119–139, 1997.
- [57] Y. Fukuda et al. Evidence for oscillation of atmospheric neutrinos. *Phys.Rev.Lett.*, 81:1562–1567, 1998.
- [58] T.K. Gaisser. *Cosmic rays and particle physics*. Cambridge, UK: Univ. Pr., 1990.
- [59] T.K. Gaisser. IceTop: The surface component of IceCube. *ICRC 2003 Conf. Proc.*, pages 1117–1120, 2003.
- [60] Raj Gandhi, Chris Quigg, Mary Hall Reno, and Ina Sarcevic. Ultrahigh-energy neutrino interactions. *Astropart.Phys.*, 5:81–110, 1996.
- [61] Askhat Gazizov and Marek P. Kowalski. ANIS: High energy neutrino generator for neutrino telescopes. *Comput.Phys.Commun.*, 172:203–213, 2005.
- [62] Sheldon L. Glashow. Resonant Scattering of Antineutrinos. *Phys.Rev.*, 118:316–317, 1960.
- [63] R. Glasstetter et al. Analysis of electron and muon size spectra of EAS. *ICRC 1999 Conf. Proc.*, 1999.

- [64] Kenneth Greisen. End to the cosmic ray spectrum? *Phys.Rev.Lett.*, 16:748–750, 1966.
- [65] Dafne Guetta and Elena Amato. Neutrino flux predictions for galactic plerions. *Astropart.Phys.*, 19:403–407, 2003.
- [66] Kaoru Hagiwara et al. Review of particle physics. Particle Data Group. *Phys.Rev.*, D66:010001, 2002.
- [67] T.J. Haines et al. Observation of a Neutrino Burst from SN1987A in IMB. *IN *LES ARCS 87 Conf. Proc.*, 1987.
- [68] Francis Halzen and Todor Stanev. Neutrino Astronomy. *Workshop on astrophysics in Antarctica Proc.*, 1989.
- [69] R.C. Hartman et al. The Third EGRET catalog of high-energy gamma-ray sources. *Astrophys.J.Suppl.*, 123:79, 1999.
- [70] F.J. Hasert et al. Observation of Neutrino Like Interactions without Muon or Electron in the Gargamelle Neutrino Experiment. *Nucl.Phys.*, B73:1–22, 1974.
- [71] T. Hastie, R. Tibshirani, and J Friedman. *The Elements of Statistical Learning: Data Mining, Inference, and Prediction, Second Edition*. Springer Science+Business Media, LLC, 2009.
- [72] Y. He and P. Price. Remote sensing of dust in deep ice at the South Pole. *Geophys.Res.*, 103(D14):1704117056, 1998.
- [73] D. Heck, G. Schatz, T. Thouw, J. Knapp, and J.N. Capdevielle. *CORSIKA: A Monte Carlo code to simulate extensive air showers*, 1998.
- [74] W. Heitler. *The Quantum Theory of Radiation, third edition*. Oxford University Press, London, 1954.
- [75] L.G. Henyey and J.L. Greenstein. Diffuse radiation in the Galaxy. *Astrophysical Journal*, 93:70–83, Jan 1941.
- [76] S.V. Hickford. Simulation of Cascades for the IceCube Neutrino Telescope. Master’s thesis, 2007.
- [77] Gary C. Hill and Katherine Rawlins. Unbiased cut selection for optimal upper limits in neutrino detectors: The Model rejection potential technique. *Astropart.Phys.*, 19:393–402, 2003.

- [78] G.C. Hill, J. Hodges, B. Hughey, A. Karle, and M. Stamatikos. Examining the balance between optimising an analysis for best limit setting and best discovery potential. *PHYSTAT 05 Conf. Proc.*, pages 108–111, 2005.
- [79] A.M. Hillas. The Origin of Ultrahigh-Energy Cosmic Rays. *Ann.Rev.Astron.Astrophys.*, 22:425–444, 1984.
- [80] Anthony M. Hillas. Cosmic Rays: Recent Progress and some Current Questions. *Cosmology, Galaxy Formation and Astroparticle Physics on the pathway to the SKA Conf. Proc.*, 2006.
- [81] J.A. Hinton and W. Hofmann. Teraelectronvolt astronomy. *Ann.Rev.Astron.Astrophys.*, 47:523–565, 2009.
- [82] K. Hirata et al. Observation of a Neutrino Burst from the Supernova SN1987a. *Phys.Rev.Lett.*, 58:1490–1493, 1987.
- [83] Andreas Hocker, Peter Speckmayer, Jorg Stelzer, Fredrik Tegenfeldt, and Helge Voss. TMVA, toolkit for multivariate data analysis with ROOT. *PHYSTAT LHC Conf. Proc.*, pages 184–187, 2007.
- [84] Joerg R. Hoerandel. On the knee in the energy spectrum of cosmic rays. *Astropart.Phys.*, 19:193–220, 2003.
- [85] Morihiko Honda, T. Kajita, K. Kasahara, and S. Midorikawa. A New calculation of the atmospheric neutrino flux in a 3-dimensional scheme. *Phys.Rev.*, D70:043008, 2004.
- [86] K. Hoshino. Result from DONUT: First direct evidence for tau-neutrino. *APPC2000 Conf. Proc.*, pages 58–63, 2000.
- [87] Hiroshi Inazawa and Keizo Kobayakawa. The Production of Prompt Cosmic Ray Muons and Neutrinos. *Prog.Theor.Phys.*, 69:1195, 1983.
- [88] J.D. Jackson. *Classical electrodynamics*. Wiley, 1999.
- [89] H. Johansson. *Searching for an Ultra High-Energy Diffuse Flux of Extraterrestrial Neutrinos with IceCube 40*. PhD thesis, 2012.
- [90] Gerard Jungman, Marc Kamionkowski, and Kim Griest. Supersymmetric dark matter. *Phys.Rept.*, 267:195–373, 1996.

- [91] Alexander Kappes, Jim Hinton, Christian Stegmann, and Felix A. Aharonian. Potential Neutrino Signals from Galactic Gamma-Ray Sources. *Astrophys.J.*, 656:870–896, 2007.
- [92] T. Karg. The IceCube neutrino observatory: Status and initial results. *Astrophys.Space Sci.Trans.*, 7:157–162, 2011.
- [93] Ulrich F. Katz. KM3NeT: Towards a km³ Mediterranean Neutrino Telescope. *Nucl.Instrum.Meth.*, A567:457–461, 2006.
- [94] E. Komatsu et al. Seven-Year Wilkinson Microwave Anisotropy Probe (WMAP) Observations: Cosmological Interpretation. *Astrophys.J.Suppl.*, 192:18, 2011.
- [95] Lutz Kopke. Supernova Neutrino Detection with IceCube. *J.Phys.Conf.Ser.*, 309:012029, 2011.
- [96] I.V. Krivosheina. SN 1987A: Historical view about registration of the neutrino signal with Baksan, KAMIOKANDE II and IMB detectors. *Int.J.Mod.Phys.*, D13:2085–2105, 2004.
- [97] H.L. Lai et al. Global QCD analysis of parton structure of the nucleon: CTEQ5 parton distributions. *Eur.Phys.J.*, C12:375–392, 2000.
- [98] L.D. Landau and I. Pomeranchuk. Electron cascade process at very high-energies. *Dokl.Akad.Nauk Ser.Fiz.*, 92:735–738, 1953.
- [99] D.M. Lowder, T. Miller, P.B. Price, A. Westphal, S.W. Barwick, et al. Observation of muons using the polar ice cap as a Cherenkov detector. *Nature*, 353:331–333, 1991.
- [100] J. Lundberg, J. Conrad, W. Rolke, and A. Lopez. Limits, discovery and cut optimization for a Poisson process with uncertainty in background and signal efficiency: TRolke 2.0. *Comput.Phys.Commun.*, 181:683–686, 2010.
- [101] Johan Lundberg, P. Miocinovic, T. Burgess, J. Adams, S. Hundertmark, et al. Light tracking for glaciers and oceans: Scattering and absorption in heterogeneous media with Photonics. *Nucl.Instrum.Meth.*, A581:619–631, 2007.
- [102] L. Lyons. *Statistics for Nuclear and Particle Physicists*. Cambridge, Uk: Univ. Pr., 1986.

- [103] J. Matthews. A Heitler model of extensive air showers. *Astropart.Phys.*, 22:387–397, 2005.
- [104] P Meszaros and M.J. Rees. Relativistic fireballs and their impact on external matter - Models for cosmological gamma-ray bursts. *Astrophys.J.*, 405:278, 1993.
- [105] Mike Metcalf. *An Introduction to FORTRAN-77*, 1982. Lectures given at CERN in June 1981 and June 1982.
- [106] E. Middell. Reconstruction of Cascade-Like Events in IceCube. Master’s thesis, 2008.
- [107] E. Middell. *Search for atmospheric neutrino induced particle showers with IceCube 40*. PhD thesis, 2012.
- [108] Predrag Miocinovic. *Muon energy reconstruction in the Antarctic Muon and Neutrino Detector Array (AMANDA)*. PhD thesis, 2001.
- [109] A. Muecke, R.J. Protheroe, R. Engel, J.P. Rachen, and T. Stanev. BL Lac Objects in the synchrotron proton blazar model. *Astropart.Phys.*, 18:593–613, 2003.
- [110] K. Nakamura et al. Review of particle physics. *J.Phys.G*, G37:075021, 2010.
- [111] Vadim A. Naumov. Atmospheric muons and neutrinos. *2nd Workshop on Methodical Aspects of Underwater/Ice Neutrino Telescopes Conf. Proc.*, pages 31–46, 2002.
- [112] S. Ostapchenko. QGSJET-II: Towards reliable description of very high energy hadronic interactions. *Nucl.Phys.Proc.Suppl.*, 151:143–146, 2006.
- [113] S. Panknin. CMC with muons. Private communication.
- [114] S. Panknin. *Search for Neutrino-Induced Cascades with the IceCube Neutrino Detector*. PhD thesis, 2011.
- [115] S. Panknin, J. Bolmont, M. Kowalski, and S. Zimmer. Muon Production of Hadronic Particle Showers in Ice and Water. *ICRC 2009 Cnof. Proc.*, 2009.
- [116] W. Pauli. Dear radioactive ladies and gentlemen. *Phys.Today*, 31N9:27, 1978.
- [117] Martin L. Perl, G.J. Feldman, G.S. Abrams, M.S. Alam, A. Boyarski, et al. Properties of the Proposed tau Charged Lepton. *Phys.Lett.*, B70:487, 1977.

- [118] B. Price and L. Bergstrm. Optical properties of deep ice at the south pole: scattering. *Appl.Opt.*, 36:4181, 1997.
- [119] P.B. Price and K. Woschnagg. Role of group and phase velocity in high-energy neutrino observatories. *Astropart.Phys.*, 15:97–100, 2001.
- [120] Soebur Razzaque, Peter Meszaros, and Eli Waxman. Neutrino tomography of gamma-ray bursts and massive stellar collapses. *Phys.Rev.*, D68:083001, 2003.
- [121] Martin J. Rees. Black Hole Models for Active Galactic Nuclei. *Ann.Rev.Astron.Astrophys.*, 22:471–506, 1984.
- [122] D. Rutledge. *A Search for Neutrino-induced Electromagnetic Showers in the 2008 Combined IceCube and AMANDA Detectors*. PhD thesis, 2012.
- [123] Olaf Schulz. The IceCube DeepCore. *AIP Conf.Proc.*, 1085:783–786, 2009.
- [124] Torbjorn Sjostrand. The Lund Monte Carlo for Jet Fragmentation. *Comput.Phys.Commun.*, 27:243, 1982.
- [125] Torbjorn Sjostrand, Leif Lonnblad, and Stephen Mrenna. *PYTHIA 6.2: Physics and manual*, 2001.
- [126] N. Smirnov. Table for estimating the goodness of fit of empirical distributions. *The annals of mathematical statistics*, 19(2):279–281, 1948.
- [127] Floyd W. Stecker. A note on high energy neutrinos from agn cores. *Phys.Rev.*, D72:107301, 2005.
- [128] F.W. Stecker, C. Done, M.H. Salamon, and P. Sommers. High-energy neutrinos from active galactic nuclei. *Phys.Rev.Lett.*, 66:2697–2700, 1991.
- [129] Atsuto Suzuki. (Super-Kamiokande): Next Generation Underground Facility at Kamioka. *CEPP Conf. Proc.*, 1987.
- [130] M. Taiuti, S. Aiello, F. Ameli, I. Amore, M. Anghinolfi, et al. The NEMO project: A status report. *Nucl.Instrum.Meth.*, A626-627:S25–S29, 2011.
- [131] Ignacio Jose Toboada Fermin. *Search for high-energy neutrino induced cascades with the AMANDA B10 detector*. PhD thesis, 2002.
- [132] T. Uchida, W. Shimada, T. Hondoh, S. Mae, and N. Barkov. Refractive-index measurements of natural air-hydrate crystals in an Antarctic ice sheet. *Appl.Opt.*, 34(25):57465749, 1995.

- [133] Bernhard Voigt. *Sensitivity of the IceCube Detector for Ultra-High Energy Electron-Neutrino Events*. PhD thesis, 2008.
- [134] L Wasserman. *All of Statistics: A Concise Course in Statistical Inference*. Springer Science+Business Media, LLC, 2004.
- [135] Eli Waxman and John N. Bahcall. High-energy neutrinos from cosmological gamma-ray burst fireballs. *Phys.Rev.Lett.*, 78:2292–2295, 1997.
- [136] Eli Waxman and John N. Bahcall. High-energy neutrinos from astrophysical sources: An Upper bound. *Phys.Rev.*, D59:023002, 1999.
- [137] Christopher Henrik V. Wiebusch. *The Detection of faint light in deep underwater neutrino telescopes*. PhD thesis, 1995.
- [138] R. Wischnewski. The Baikal neutrino telescope 'NT-200'. *6th International Symposium on Very High-energy Cosmic Ray Interactions Conf. Proc.*, 1990.
- [139] R. Wischnewski. The AMANDA-II neutrino telescope. *Nucl.Phys.Proc.Suppl.*, 110:510–512, 2002.
- [140] G.T. Zatsepin and V.A. Kuzmin. Upper limit of the spectrum of cosmic rays. *JETP Lett.*, 4:78–80, 1966.